

# UC San Diego

## UC San Diego Electronic Theses and Dissertations

### Title

Tectonic and Stratigraphic Controls of the Continental Shelf and Slope, Southern California

### Permalink

<https://escholarship.org/uc/item/0ns410ks>

### Author

Holmes, James John

### Publication Date

2019

Peer reviewed|Thesis/dissertation

UNIVERSITY OF CALIFORNIA SAN DIEGO

**Tectonic and Stratigraphic Controls of the Continental Shelf and Slope, Southern  
California**

A dissertation submitted in partial satisfaction of the  
requirements for the degree  
Doctor of Philosophy

in

Earth Sciences

by

James John Holmes

Committee in charge:

Professor Neal Driscoll, Chair  
Professor Alistair Harding  
Professor Falko Kuester  
Professor David Sandwell  
Professor Peter Shearer

2019

Copyright  
James John Holmes, 2019  
All rights reserved.

The dissertation of James John Holmes is approved, and it is acceptable in quality and form for publication on microfilm and electronically:

---

---

---

---

---

Chair

University of California San Diego

2019

DEDICATION

*To Mayumi, with love.*

## EPIGRAPH

*What was it like then  
When the tsunami came to shore  
I look down and wonder  
Below me spreads the blue sea  
Quiet and perfectly still.*

Akihito, Emperor of Japan (2011)

## TABLE OF CONTENTS

Signature Page	. . . . .	iii
Dedication	. . . . .	iv
Epigraph	. . . . .	v
Table of Contents	. . . . .	vi
List of Figures	. . . . .	x
List of Tables	. . . . .	xiii
Acknowledgements	. . . . .	xiv
Vita	. . . . .	xvi
Abstract of the Dissertation	. . . . .	xvii
Chapter 1	Introduction . . . . .	1
	1.1 Outline of the Dissertation . . . . .	4
Chapter 2	High-Resolution 3D Seismic Imaging of Fault Interaction and Deformation Offshore San Onofre, California . . . . .	6
	2.1 Abstract . . . . .	6
	2.2 Introduction & Geologic Background . . . . .	7
	2.3 Methods . . . . .	12
	2.3.1 3D MCS Acquisition and Processing . . . . .	12
	2.3.2 Age Control . . . . .	18
	2.4 Results . . . . .	20
	2.4.1 Deformation and Fault Characterization . . . . .	20
	2.4.2 Paleochannel Identification . . . . .	29
	2.5 Discussion . . . . .	30
	2.5.1 3D Structure Mapping . . . . .	30
	2.5.2 Seismicity and Through-going Rupture . . . . .	35
	2.6 Conclusions . . . . .	36
	2.7 Acknowledgments . . . . .	38
Chapter 3	Strike-slip Transpressional Uplift Offshore San Onofre, California Inhibits Sediment Delivery to the Deep Sea . . . . .	54
	3.1 Abstract . . . . .	54
	3.2 Introduction . . . . .	55
	3.3 Geologic Setting . . . . .	59

3.3.1	Geomorphology of the Inner California Borderlands . . . . .	59
3.3.2	Strike-slip tectonics offshore San Onofre . . . . .	60
3.3.3	Canyon Systems in the ICB . . . . .	61
3.3.4	Methods . . . . .	63
3.4	Results . . . . .	66
3.4.1	San Onofre North and South (SON and SOS) Canyon-Channel Geomorphology . . . . .	66
3.4.2	Stratigraphy of the San Onofre slope . . . . .	67
3.4.3	San Onofre Sediment Core Lithology and Chronology . . . . .	72
3.4.4	Dana Point Canyon-Channel and Core Stratigraphy . . . . .	74
3.5	Discussion . . . . .	77
3.5.1	Chronology of turbidite and pelagic deposition . . . . .	79
3.5.2	Shelf width controls regional timing of turbidite deposition . . . . .	81
3.5.3	Across-margin deformation controls local turbidite emplacement . . . . .	83
3.5.4	Channel gradient controls morphology and localized differ- ences in turbidite timing . . . . .	85
3.6	Conclusion . . . . .	89
3.7	Acknowledgements . . . . .	90
Chapter 4	New Three-Dimensional P-Cable Seismic Data Image the Geometry and Fault Interaction of the San Mateo and San Onofre Trends Offshore South- ern California . . . . .	92
4.1	Abstract . . . . .	92
4.2	Introduction . . . . .	93
4.3	Methods . . . . .	96
4.3.1	3D Seismic Reflection Acquisition and Processing . . . . .	96
4.3.2	Age Control . . . . .	102
4.4	Results . . . . .	106
4.4.1	Margin Morphology and Structure . . . . .	108
4.5	Discussion . . . . .	113
4.6	Conclusions . . . . .	117
4.7	Acknowledgements . . . . .	118
Chapter 5	Conclusions . . . . .	128
Appendix A	SONGS 3-D High Resolution P-cable Survey Offshore Southern California Cruise Report . . . . .	131
A.1	Executive Summary . . . . .	131
A.2	Introduction . . . . .	132
A.3	Scope and Purpose . . . . .	133
A.4	Survey Instrumentation . . . . .	133
A.4.1	Geophysical Acquisition System . . . . .	134
A.4.2	Positioning . . . . .	137



	A.4.3	Seismic Data Processing . . . . .	138
A.5		Survey Platform . . . . .	138
	A.5.1	Health, Safety and Environment . . . . .	139
	A.5.2	Drills and Muster . . . . .	140
	A.5.3	HSE Safety Meetings . . . . .	141
	A.5.4	Protected Species Awareness . . . . .	141
	A.5.5	Incidents . . . . .	143
A.6		Summary of Survey Operations . . . . .	143
	A.6.1	Mobilization . . . . .	143
	A.6.2	Personnel . . . . .	144
	A.6.3	Survey Methodology . . . . .	146
	A.6.4	Acquisition QC and Onboard Processing . . . . .	148
	A.6.5	Production . . . . .	150
	A.6.6	Deliverables . . . . .	152
	A.6.7	Acknowledgements . . . . .	153
Appendix B		Offshore & Onshore 3D High Resolution Processing Final Report . . . . .	154
	B.1	Introduction . . . . .	157
	B.2	Acquisition & Survey Area . . . . .	159
		B.2.1 Specifications . . . . .	159
		B.2.2 Survey Area . . . . .	161
	B.3	Navigation & 3D Geometry Definition . . . . .	161
		B.3.1 Coordinate System . . . . .	161
		B.3.2 3D Bin Grid Definition Boomer . . . . .	162
		B.3.3 3D Bin Grid Definition Sparker . . . . .	163
		B.3.4 Unrotated Survey Area (Boomer and Sparker) . . . . .	163
		B.3.5 Rotated Survey Area . . . . .	164
	B.4	Acquisition QC and Onboard Processing . . . . .	165
		B.4.1 Amplitude and Frequency Maps . . . . .	166
		B.4.2 Near Trace Gathers . . . . .	167
		B.4.3 Shot Gathers . . . . .	167
		B.4.4 Brute Stacks . . . . .	167
		B.4.5 Channel to Channel Amplitude Diagnostics . . . . .	167
		B.4.6 Offset QC . . . . .	168
		B.4.7 Near Trace Stack . . . . .	168
		B.4.8 3D Raw Stack . . . . .	168
		B.4.9 Binning Control . . . . .	168
		B.4.10 Noise Examples . . . . .	169
	B.5	Onshore Processing . . . . .	171
		B.5.1 Processing Summary . . . . .	171
		B.5.2 Preliminary Processing . . . . .	171
		B.5.3 Static Corrections . . . . .	173
		B.5.4 Pre-migration Processing . . . . .	175

B.5.5	Kirchhoff, post stack time migration . . . . .	179
B.5.6	Post Migration Processing . . . . .	180
B.6	Kirchoff, post stack depth migration . . . . .	184
B.6.1	Initial model building . . . . .	184
B.6.2	Final post-stack depth migration . . . . .	185
B.6.3	Post migration processing . . . . .	186
B.7	Delivery products . . . . .	187
B.7.1	Delivery Address . . . . .	187
B.8	Conclusions . . . . .	188
B.9	Personnel . . . . .	189
B.10	Final Migrated Stack Examples . . . . .	190
B.11	Sail Line Listing . . . . .	192
B.12	Example Observers Log . . . . .	200
B.13	Example Navigation Line Log . . . . .	201
B.14	Example GeoEel Log . . . . .	202
B.15	Example P190 Navigation Header . . . . .	203
B.16	Final EBCDIC Headers . . . . .	204
B.17	Seismic QC displays . . . . .	206
B.18	Acknowledgements . . . . .	214
References	. . . . .	215

## LIST OF FIGURES

Figure 1.1:	Oblique view of coastal bathymetry offshore of San Onofre . . . . .	2
Figure 2.1:	Regional, area, and seismicity maps of the Inner California Borderlands (ICB)	8
Figure 2.2:	Location map of survey area off San Onofre and coastal communities of Dana Point and San Clemente . . . . .	10
Figure 2.3:	Aerial photo of R/V New Horizon . . . . .	13
Figure 2.4:	Uninterpreted stair diagram of Crossline 1790 . . . . .	39
Figure 2.5:	Interpreted stair diagram of Crossline 1790 . . . . .	40
Figure 2.6:	Interpreted stair diagram of Crossline 1945 . . . . .	41
Figure 2.7:	Interpreted stair diagram of Crossline 2038 . . . . .	42
Figure 2.8:	Interpreted stair diagram of Crossline 2252 . . . . .	43
Figure 2.9:	Interpreted stair diagram of Crossline 2457 . . . . .	44
Figure 2.10:	Interpreted stair diagram of Crossline 2763 . . . . .	45
Figure 2.11:	Interpreted stair diagram of Crossline 3400 . . . . .	46
Figure 2.12:	Vertical profile of Crossline 3400 . . . . .	47
Figure 2.13:	Vertical profile of CHIRP line . . . . .	48
Figure 2.14:	Interpreted stair diagram of Crossline 4400 . . . . .	49
Figure 2.15:	Interpreted stair diagram of Crossline 5400 . . . . .	50
Figure 2.16:	Interpreted arbitrary line A-A' . . . . .	51
Figure 2.17:	Mapped segments of the Newport-Inglewood Rose Canyon fault system . .	52
Figure 2.18:	Oblique view of San Onofre shelf and slope bathymetry . . . . .	53
Figure 2.19:	Detail view of timeslice at 285 ms, rendered in curvature attribute . . . . .	53
Figure 3.1:	Maps of study area . . . . .	59
Figure 3.2:	Bathymetric profiles of canyons with channel gradient . . . . .	67
Figure 3.3:	Profile of San Onofre South canyon slope . . . . .	68
Figure 3.4:	Bathymetry and cross-sections of San Onofre North and South canyons . .	69
Figure 3.5:	Sparker seismic dip profiles . . . . .	70
Figure 3.6:	Sparker seismic strike profiles . . . . .	71
Figure 3.7:	Sparker seismic strike profiles . . . . .	73
Figure 3.8:	Schematic of San Onofre cores . . . . .	75
Figure 3.9:	Bathymetry of Dana Point Canyon . . . . .	76
Figure 3.10:	Schematic diagrams of Dana Point cores . . . . .	77
Figure 3.11:	Histograms of sand layer depositional timing offshore San Onofre and Dana Point . . . . .	80
Figure 4.1:	Regional, and area maps of the Inner California Borderlands (ICB) . . . . .	94
Figure 4.2:	Location map of survey areas off San Onofre and coastal communities of Dana Point and San Clemente . . . . .	96
Figure 4.3:	Detailed location map of featured transects and core locations on San Onofre shelf and slope . . . . .	97

Figure 4.4:	Aerial photo of R/V New Horizon underway on NH1323 . . . . .	98
Figure 4.5:	Time-slice view of sparker survey at 1000 ms with fault interpretations . .	109
Figure 4.6:	3D chair view of sparker survey area with fault curtains . . . . .	110
Figure 4.7:	Rose diagrams of San Onofre and San Mateo trend fault segments . . . . .	116
Figure 4.8:	Vertical profile of transect A to A' . . . . .	120
Figure 4.9:	Vertical profile of transect B to B' . . . . .	121
Figure 4.10:	Vertical profile of transect C to C' . . . . .	122
Figure 4.11:	Vertical profile of transect D to D' . . . . .	123
Figure 4.12:	Vertical profile of transect E to E' . . . . .	124
Figure 4.13:	Vertical profile of transect F to F' . . . . .	125
Figure 4.14:	3D map of slope bathymetry . . . . .	126
Figure 4.15:	3D map of slope bathymetry (transparent) with fault curtains . . . . .	127
Figure A.1:	Location map showing survey Areas One and Two . . . . .	134
Figure A.2:	R/V New Horizon with P-cable deployed . . . . .	135
Figure A.3:	The R/V New Horizon underway off Southern California . . . . .	139
Figure A.4:	Location map showing AREA ONE and AREA TWO . . . . .	146
Figure A.5:	Block One bin coverage postplot . . . . .	151
Figure A.6:	Block Two bin coverage postplot . . . . .	152
Figure B.1:	P-Cable 14 Streamer Configuration . . . . .	159
Figure B.2:	P-Cable Aerial View . . . . .	160
Figure B.3:	Offshore southern California, USA with survey areas highlighted (from Google Earth) . . . . .	161
Figure B.4:	Acquired sail lines (all lines) . . . . .	164
Figure B.5:	Acquired source positions (all lines, all shots) . . . . .	164
Figure B.6:	Acquired fold of coverage (all offsets) . . . . .	165
Figure B.7:	Acquired Boomer fold of coverage (nominal=8, all offsets) . . . . .	165
Figure B.8:	Acquired Sparker fold of coverage (nominal=4, all offsets) . . . . .	166
Figure B.9:	Line 1306B (cable 5 brute stack) . . . . .	170
Figure B.10:	Line 1306B with noise attenuation applied (cable 5 brute stack) . . . . .	170
Figure B.11:	Time slice – 300ms (Boomer) . . . . .	190
Figure B.12:	Time slice – 1000ms (Sparker) . . . . .	190
Figure B.13:	Inline – 1755 Enlarged (Sparker) . . . . .	191
Figure B.14:	Crossline – 2746 Enlarged (Sparker) . . . . .	191
Figure B.15:	Raw Shots Display (Line 1114E Cables 1-14) . . . . .	207
Figure B.16:	Reformatted Shots Display (Line 1114E Cables 1-14) . . . . .	207
Figure B.17:	Brute Stack (Line 1114E Cable 5) . . . . .	208
Figure B.18:	Brute Stack Enlarged (Line 1114E Cable 5) . . . . .	208
Figure B.19:	Near Trace (Line 1114E Cable 10) . . . . .	209
Figure B.20:	Near Trace All Cables (Line 1114E Shots 1311-1330) . . . . .	209
Figure B.21:	Whole Window Amplitude Map (Line 1114E) . . . . .	210
Figure B.22:	Whole Window Frequency Map (Line 1114E) . . . . .	210

Figure B.23: Data Window Amplitude Map (Line 1114E) . . . . .	211
Figure B.24: Data Window Frequency Map (Line 1114E) . . . . .	211
Figure B.25: Ambient Amplitude Map (Line 1114E) . . . . .	212
Figure B.26: Deep Amplitude Map (Line 1114E) . . . . .	212
Figure B.27: Sparker Brute Stack (Line 3499A Cable 5) . . . . .	213
Figure B.28: Sparker Brute Stack Enlarged (Line 3499A Cable 5) . . . . .	213

## LIST OF TABLES

Table 2.1:	List of acquisition parameters used for P-Cable 3-D multichannel seismic reflection system . . . . .	14
Table 2.2:	List of onshore processing steps . . . . .	16
Table 2.3:	TN336 Cores, Radiocarbon Ages, and Sedimentation Rates . . . . .	21
Table 4.1:	List of acquisition parameters used for P-Cable 3-D multichannel seismic reflection system . . . . .	101
Table 4.2:	List of onshore processing steps . . . . .	102
Table 4.3:	TN336 Cores, Radiocarbon Ages, & Sedimentation Rates on San Onofre Upper / Middle Slope . . . . .	105
Table 4.4:	TN336 Cores, Radiocarbon Ages, & Sedimentation Rates on San Onofre Lower Slope . . . . .	107
Table A.1:	P-cable Acquisition Parameters . . . . .	136
Table A.2:	Bounding coordinates for survey Area One . . . . .	147
Table A.3:	Bounding coordinates for survey Area Two . . . . .	147
Table B.1:	Boomer Geometry Corner Coordinates . . . . .	162
Table B.2:	Sparker Geometry Corner Coordinates . . . . .	163

## ACKNOWLEDGEMENTS

My eternal thanks and gratitude to my advisor, Neal Driscoll, who always provided me with guidance, humor, and patience. He has taught me so much about stratigraphy, tectonics, geophysics, and seamanship. He showed me that being a good marine scientist goes hand-in-hand with being a good sailor. He kept me on track when I veered off, pushed me when I needed pushing, and gave me much needed support when I dealt with rejection. Neal has given me so many amazing opportunities without asking in return, and this work would not have been even remotely possible without him.

I would also like to take an opportunity to thank my committee, Peter Shearer, Alistair Harding, Dave Sandwell, and Falko Kuester, for agreeing to join this journey with me. The fact that I am blessed with a committee of such staggering intelligence and renown is not lost upon me, and I am forever grateful.

Special thanks to Alistair and Graham Kent for teaching me how to process 2D seismic data, not getting upset when I asked stupid questions, and periodically checking up on me.

I'd like to thank all the amazing faculty I've had at SIO, especially Steve Constable, Geoff Cook, Len Srnka, and Lisa Tauxe. I will always treasure your excitement and enthusiasm about discovering the mysteries of the Earth.

Next I'd like to recognize and thank all the labmates, classmates, and shipmates I've had through the years, but especially Emily Wei, Shannon Klotsko, Jillian Maloney, Boe Derosier, Valerie Sahakian, Lana Graves, and Brian Oller. They are like family to me. They know all of my successes and my failures, and I'm a better person for having met them. Thank you also to Hector Perea Manera, Gülsen Ucarus, Leanne Hirsch, Mackenzie Roberts, Colby Nicholson, Brendan Mendenhall, and Daniel Schwartz. Your friendship and camaraderie mean the world to me.

Thank you to all the friends at SIO and UCSD that I've met, and especially friends I made in GRD: Thomas Martin, John Driscoll, Shelby Jones-Cervantes, Kate Durkin, Alyssa Griffin, and Sarah Maher. You're all amazing people and amazing scientists.

Finally, I'd like to thank my family, both in the U.S. and in Japan, for their love and support during my tenure as a graduate student. I'd especially like to thank my wife Mayumi and my children, Liam, and Grace, for tolerating the highs and lows of the last few years with love, patience, and good humor. All of my love and apologies.

Chapter 2 has been submitted for publication in: Holmes, J.J., Driscoll, N.W., & Kent, G.M., In Review. High-Resolution 3D Seismic Imaging of Fault Interaction and Deformation Offshore San Onofre, California. *Journal of Geophysical Research: Solid Earth*. The dissertation author was the primary researcher and author, and the co-authors listed in this publication directed and supervised the research.

Chapter 3 has been submitted for publication in: Wei, E.A., Holmes, J.J., & Driscoll, N.W., In Review. Strike-slip Transpressional Uplift Offshore San Onofre, California Inhibits Sediment Delivery to the Deep Sea. *Frontiers in Earth Science Special Publication, Sedimentary System Responses to External Forcings: A Process-Based Perspective*. The dissertation author was involved in acquisition, processing, and interpretation of part of the data that forms the basis of this chapter. The dissertation author is secondary author on this publication.

Chapter 4 is being prepared for publication in: Holmes, J.J., Driscoll, N.W., & Kent, G.M., In Prep. New Three-Dimensional P-Cable Seismic Data Image the Geometry and Fault Interaction of the San Mateo and San Onofre Trends Offshore Southern California. The dissertation author was the primary researcher and author, and the co-authors listed in this publication directed and supervised the research.

Appendix A, in part, is a cruise report for NH1323 in: Driscoll, N.W., & Kent, G.M. (2013). SONGS 3-D High Resolution P-cable Survey Offshore Southern California. The dissertation author was a science member of this survey cruise.

Appendix B, in full, is a processing report for data acquired on NH1323 developed by Geotrace, Inc., a Houston, Texas based exploration services company. The dissertation author was a science member of this survey cruise.



## VITA

- 2012 B. S. in Earth Science *magna cum laude*, University of California San Diego
- 2014 M. S. in Earth Science, University of California San Diego
- 2012-2019 Graduate Research Assistant, University of California San Diego
- 2019 Ph. D. in Earth Science, University of California San Diego

## PUBLICATIONS

Holmes, J.J., Driscoll, N.W., Kent, G.M., In Review. “High-Resolution 3D Seismic Imaging of Fault Interaction and Deformation Offshore San Onofre, California”, *Journal of Geophysical Research: Solid Earth*.

Holmes, J.J., Driscoll, N.W., Kent, G.M. Submitted to co-authors. “New Three-Dimensional P-Cable Seismic Data Image the Geometry and Fault Interaction of the San Mateo and San Onofre Trends Offshore Southern California”.

Wei, E.A., Holmes, J.J., Driscoll, N.W., In Review. “Strike-slip Transpressional Uplift Offshore San Onofre, California Inhibits Sediment Delivery to the Deep Sea”, *Frontiers in Earth Science Special Publication, Sedimentary System Responses to External Forcings: A Process-Based Perspective*.

ABSTRACT OF THE DISSERTATION

**Tectonic and Stratigraphic Controls of the Continental Shelf and Slope, Southern California**

by

James John Holmes

Doctor of Philosophy in Earth Sciences

University of California San Diego 2019

Professor Neal Driscoll, Chair

Understanding the tectonic and geomorphic processes that shape continental margins has both scientific and societal relevance. This dissertation uses state-of-the-art 3D seismic reflection, CHIRP, and piston core analysis to investigate the architecture, character, and attendant deformation of the Newport-Inglewood Rose Canyon fault system, San Onofre trend fault system, and San Mateo trend fault system, where all three systems interact off the coast of San Onofre, California.

Using these data, we first describe the fault geometry and subsurface deformation of the Newport-Inglewood Rose Canyon system on the continental shelf based on our analysis of

high-resolution 3D P-Cable multichannel seismic reflection data and CHIRP data. We organize fault segments into three zones based on fault character and describe each zone. We then discuss in detail structures that we observe throughout the survey and propose alternative kinematic models of transpression and then transtension to explain the formation and bisection of a 2 km wide subsurface antiformal dome structure.

Next, using piston core analysis, we compare the grain size and timing of turbidite emplacement from two local off-shelf canyon systems. We describe our models of activity for each canyon system and discuss the tectonic and geomorphic controls that impact sand supply to one of the canyons. The results of this study question the use of turbidites as seismotherms because their emplacement history is controlled by numerous other processes (e.g., shelf width, eustasy, storms, and earthquakes).

Finally, we use high-resolution 3D P-Cable multichannel seismic reflection data and piston core analysis to investigate and categorize the segments of the San Onofre and San Mateo trend fault systems. Using these data, we illuminate structural details observed in both the seismic data and at the seafloor. The structural deformation along this portion of the Californian margin is more consistent with transpression at step overs along strike slip fault systems than compression associated with a regional blind thrust.

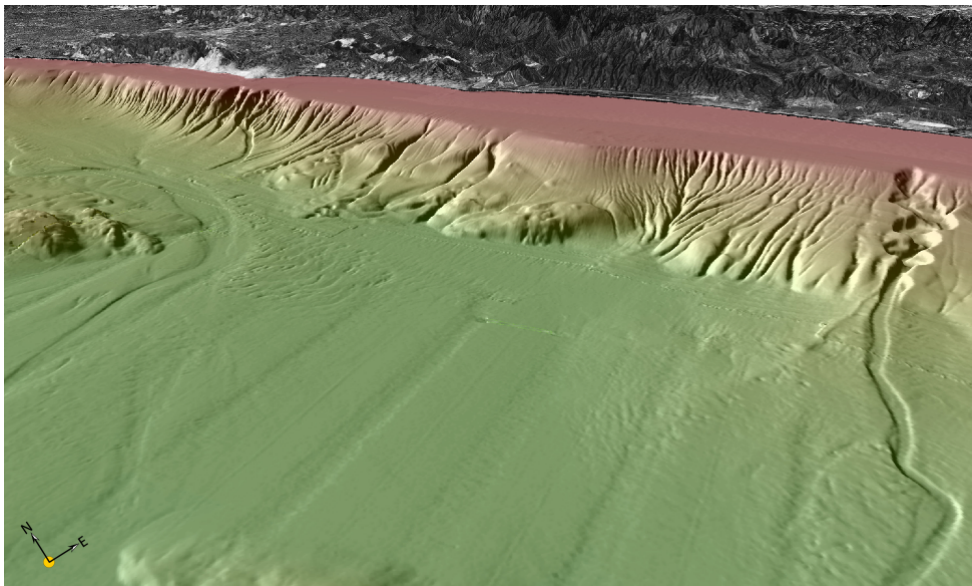
# Chapter 1

## Introduction

All styles of deformation are observed in California, which makes for an ideal geological laboratory. Divided by the boundary between the Pacific and North American plates and sheared by the forces between them, California's own history is written directly into the structures and sediments that renders the state its charming landscapes and stunning coastal views. Over a relatively short distance, California geology covers a wide spectrum of active tectonics— from tilted blocks and subsea level basins due to continental extension, to forearc volcanism, to strike-slip earthquakes along plate-boundary transform faulting that extend over much of the state. The temperate climate, and coastal desert beauty of southern California attracts numerous visitors from all over the world and has contributed to a population density greater than any other coast in North America. Given the large number of coastal residents it is imperative to define the seismic setting to assess the potential hazards to the nearly 20 million people that live, work, and play within the coastal communities of Santa Barbara, Los Angeles, Orange, San Diego, and Tijuana, Mexico (Lee and Normark, 2009).

The coastal margin of southern California is part of a larger geomorphic region called the Inner California Borderlands (ICB). The ICB is a region of extreme structural deformation that records a middle Oligocene ( $\sim 30$  Ma) transition from Farallon plate subduction under an

active margin to large-scale microplate capture causing block rotation between 18 to 12 Ma, and transtension from approximately 12 Ma to 6 Ma (Lonsdale, 1991; Nicholson et al., 1994). Marine stratigraphic evidence reveals that the region was then overprinted by strike-slip deformation starting with the initiation of the San Andreas Fault at 6 Ma, once the southward migrating Rivera triple junction had fully passed and Baja California had completed its fusion with the Pacific plate (Atwater, 1970, 1989; Nicholson et al., 1994; Atwater and Stock, 1998; Axen and Fletcher, 1998; Ingersoll, 2008).



**Figure 1.1:** Oblique view of coastal bathymetry offshore of San Onofre. Modified from Dartnell et al., 2015.

In southern California, geodetic models show that approximately 80% of the 50 mm/yr of movement between the Pacific and North American plates is accommodated by onshore faulting (Becker et al., 2005; Bennett et al., 1996; Dixon et al., 2000; Meade and Hager, 2005). This leaves the remaining 5-10 mm/yr of the slip budget to be distributed amongst offshore faults of the ICB. The ICB has a number of dextral strike-slip fault systems that forms a large diffuse shear zone, including the Newport-Inglewood Rose Canyon, Coronado Bank, Palos Verdes, San Diego Trough, San Pedro Basin, and San Clemente fault systems.

The fault system closest to the coast is the Newport-Inglewood Rose Canyon system, which has a Holocene slip rate of 1.5-2.0 mm/yr along the southern onshore extension of the fault based on paleoseismological trenching (Lindvall and Rockwell, 1995) and 0.35-0.55 mm/yr along its northern onshore extent based on cone penetration tests (CPTs; Grant et al., 1997) and well data (Freeman et al., 1992). Newport-Inglewood Rose Canyon initiates near downtown San Diego, makes a leftward jog at La Jolla, and then runs 120 km offshore on the continental shelf, subparallel to the coastal margin. The system emerges back on shore at Newport, where it causes the deformation that uplifted the San Joaquin Hills and trends up the western Los Angeles Basin until it eventually connects with the Santa Monica fault. Along the way, the system makes four leftward step overs resulting in compressional structures— one of which is Mount Soledad, a subaerial transpressional antiform in La Jolla.

Seismicity tends to be clustered at the two onshore endpoints of the fault system. The most recent historical event was the notorious  $M_L$  6.4 1933 Long Beach Earthquake (Hauksson and Gross, 1991). The quake was particularly destructive, resulting in 120 deaths, US\$40 million in damages, and propelled the passage of legislation mandating new construction of government buildings to be seismically resistant. Offshore seismicity, on the other hand, is limited to relatively diffuse micro-seismicity throughout the region (Grant and Shearer, 2004).

Debate about the post-late Miocene history of deformation in the ICB centers on two competing models, each with evidence reflected in multichannel seismic reflection data: contractual folding and faulting due to a large active blind thrust that previously accommodated regional extension in the Miocene (Crouch and Suppe, 1993; Bohannon and Geist, 1998; Rivero and Shaw, 2000); or transpressional features caused by restraining bends at step-overs along strike-slip faults (Ryan et al., 2012; Maloney et al., 2016). Each model has profound implications for the seismic hazard of the southern California coast.

## 1.1 Outline of the Dissertation

This dissertation focuses on one section of continental shelf and slope off the coast of Southern California, between the communities of San Clemente and Oceanside. At this location, the continental shelf widens from an average of 2 km to 10 km, coincident with a left-step in the Newport-Inglewood Rose Canyon system. Using new high-resolution 3D multichannel seismic (MCS) reflection data along with methods such as CHIRP (high-resolution, swept-frequency, zero-offset seismic reflection) and sediment coring, we investigate the formation and evolution of the southern California margin and assess the potential seismic hazard risk to coastal residents.

In Chapter 2, we explore the geometry and character of the Newport-Inglewood Rose Canyon fault through the use of a new high-resolution 3D MCS array called a "P-Cable Array". We map several of the largest fault segments and describe the complex kinematics and subsurface deformation involved in a leftward step-over coincident with the widest part of the shelf. This manuscript has been submitted to *Journal of Geophysical Research: Solid Earth* and we are addressing reviewers' comments and plan to submit the revised version in December 2019.

Chapter 3 presents numerous gravity and jumbo piston cores along with nested 2D and 3D MCS reflection data to compare how tectonic deformation and shelf width throughout a eustatic sea level cycle governs sediment transfer to the deep sea. We analyze how tectonics, shelf width, gradient, and eustatic sea level influences the timing of turbidite emplacement and grain size. Emplacement history of gravity flows (e.g., turbidites) has important implications for aqueous paleoseismology (Goldfinger, 2009). This manuscript was submitted to *Frontiers in Earth Science Special Publication* and has been revised and resubmitted.

High-resolution 3D MCS reflection data acquired on the California continental margin are presented in Chapter 4 that reveal the interaction of the San Onofre and San Mateo trends. The 3D seismic data image three distinct segments defined on azimuth and character. Finally, we discuss our findings within the context of two end-member models of margin deformation,

and the possibly profound effect on the seismic hazard for much of coastal southern California. This manuscript will be submitted to Bulletin of the Seismological Society of America in January 2020.

Appendices include the cruise report for the 3D P-Cable MCS survey in October 2013 (NH1323), written by Driscoll and Kent (2013) (Appendix A). Appendix B is a complete processing report for NH1323, drafted by Geotrace, Inc. (2013).



## **Chapter 2**

# **High-Resolution 3D Seismic Imaging of Fault Interaction and Deformation Offshore San Onofre, California**

### **2.1 Abstract**

The Inner California Borderlands (ICB) records a middle Oligocene transition from subduction to microplate capture along the southern California and Baja coast. The closest nearshore fault system, the Newport-Inglewood/Rose Canyon (NIRC) fault complex is a dextral strike-slip system that extends primarily offshore approximately 120 km from San Diego to Newport Beach, California. Holocene slip rates along the NIRC are 1.5-2.0 mm/yr in the south and 0.5 mm/yr along its northern extent based on trenching and well data.

High-resolution 3D seismic surveys of the NIRC fault system offshore of San Onofre were acquired to define fault interaction across a prominent strike-slip step-over. The stepover deformation results in transpression that structurally controls the width of the continental shelf in this region. Shallow coring on the shelf yields a range of sedimentation rates from 0.27-0.28

mm/yr. Additionally, a series of smaller anticlines and synclines record subtle changes in fault trends along with small stepovers and secondary splay faults. Finally, sedimentary units onlapping and dammed by the anticline, place constraints on the onset of deformation of this section of the NIRC fault system. Thickness estimates and radiocarbon dating yield ages of 560,000 to 575,000 years before present for the onset of deformation.

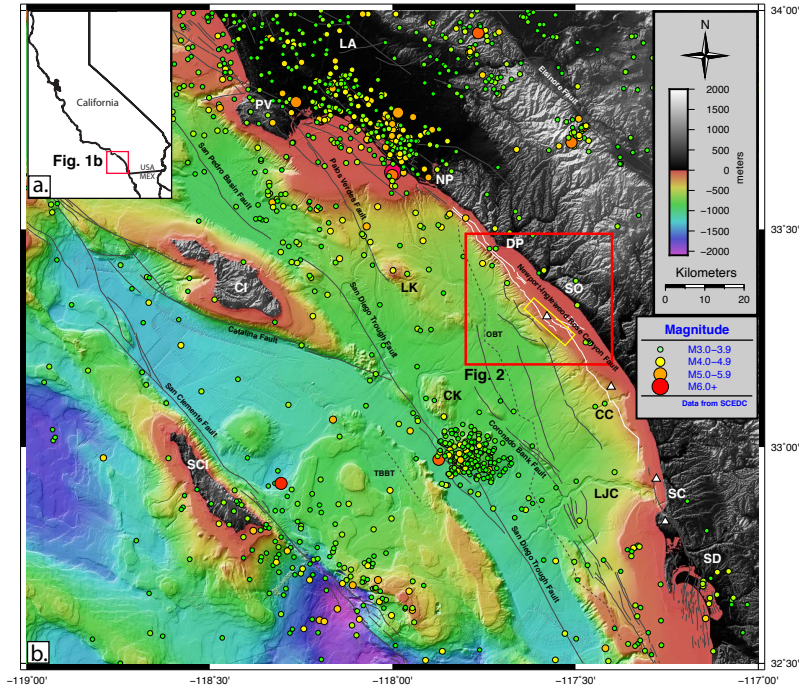
## **2.2 Introduction & Geologic Background**

Prior to the late Oligocene/early Miocene, the western margin of North America was dominated by Farallon plate subduction. The cessation of subduction ushered in a complex tectonic sequence involving block rotation, extension, and then an eventual switch to a transform margin, dominated by the dextral strike-slip San Andreas Fault (e.g., Bohannon and Geist, 1998; Crouch and Suppe, 1993; Legg et al., 1991; Nicholson et al., 1994). In southern California, the San Andreas Fault (SAF) accommodates approximately 18-22 mm/yr of slip between the Pacific and North American tectonic plates (Bennett et al., 1996; Ryan et al., 2012; Sahakian et al., 2017). Not all of the slip, is accommodated by the SAF, San Jacinto (SJF) and Elsinore (EF) systems. Roughly 5-8 mm/yr of the relative plate motion is being taken up by offshore strike-slip fault systems (Platt and Becker, 2010; Bennett et al., 1996; Maloney et al., 2016).

The Inner California Borderlands (ICB) (Figure 2.1) is a region marked by tectonic deformation offshore southern California and northern Baja that records a middle Oligocene transition from a subduction regime to microplate capture. Since the late Miocene to early Pliocene, the margin has been dominated by right-lateral strike-slip faulting, often on reactivated Mesozoic structures (Grant and Shearer, 2004; Freeman et al., 1992). These faults account for approximately 10% of the total slip between the North America and Pacific plates (DeMets and Dixon, 1999; Platt and Becker, 2010). Given the proximity of these offshore faults to the densely populated

coastal communities of southern California and their potential slip rates, it is important to assess their geohazard potential.

The Newport-Inglewood/Rose Canyon (NIRC) fault complex, located closest to shore, is



**Figure 2.1:** (a.) Regional map of California State showing the location of the Inner California Borderlands - red box. (b.) Area map of Inner California Borderlands (ICB) relative to the southern California coast with historical seismicity data represented by colored circles. Seismicity data are from the Southern California Earthquake Data Center (SCEDC). Major fault systems are traced in solid gray, with the exception of the Newport-Inglewood Rose Canyon (NIRC) fault system, traced in solid white. Red box outlines area shown in Figure 2.2. Yellow rectangle outlines the survey area. Scale for topography and bathymetry is shown. Solid and dashed gray faults are from USGS Fault and Fold database (USGS, 2006). Dashed faults denote possible blind thrusts. White faults are from Sahakian et al. (2017). Bathymetry from Dartnell et al. (2015). Major fault systems are labeled. Abbreviations are: CC - arlsbad Canyon; CI - Catalina Island; CK - Crespi Knoll; DP - Dana Point; LA - Los Angeles; LJC - La Jolla Canyon; LK - Lasuen Knoll; NP - Newport; OBT - Oceanside blind thrust; PV - Palos Verdes; SC - Scripps Canyon; SCI - San Clemente Island; SD - San Diego; SO - San Onofre; TBBT - Thirtymile Bank blind thrust. White triangles denote approximate location of "pop-up" compressional structures due to leftward stepping of the fault strands.

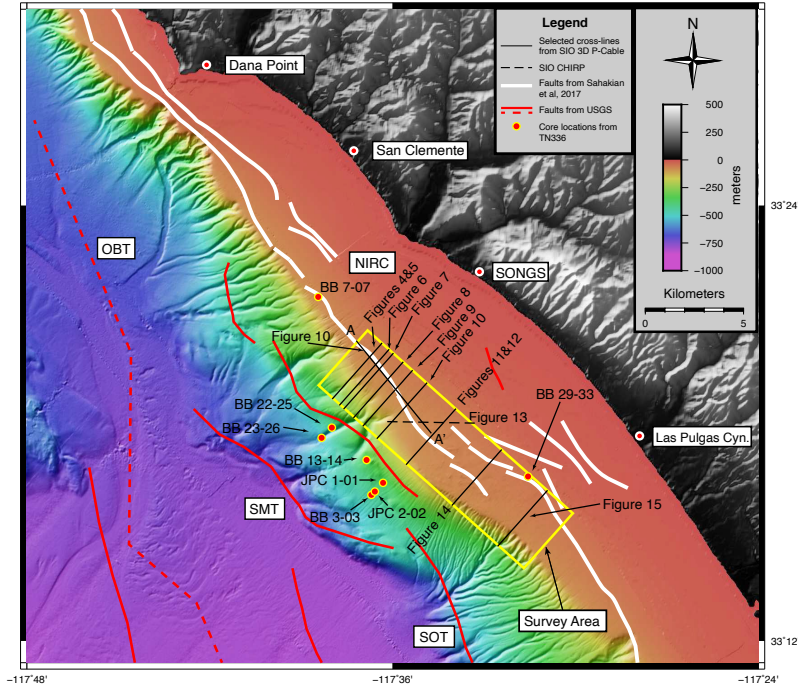
a right-lateral strike-slip system extending from Old Town, San Diego (Rockwell, 2010) to the Cheviot Hills in the Los Angeles Basin (Barrows, 1974). Offshore segments extend approximately 120 km from La Jolla Cove to the San Joaquin Hills near Newport Beach, California (Sahakian et

al., 2017). The Holocene slip rate is 1.5-2.0 mm/yr along the southern onshore extension of the fault based on paleoseismological studies (Lindvall and Rockwell, 1995) and 0.35-0.55 mm/yr along its northern onshore extent based on cone penetration tests (CPTs; Grant et al., 1997) and well data (Freeman et al., 1992). The fault system is comprised of segments belonging to two subsystems: the Newport-Inglewood fault system (NIFZ) terminating in the Los Angeles basin in the north, and the Rose Canyon fault system (RCFZ) starting near Downtown San Diego in the south. The two systems interact and transition between each other at a leftward step-over near Carlsbad Canyon (labeled "CC" in Figure 2.1) (Ryan et al., 2009). Recent geophysical and geological studies of the fault zone reveal the offshore fault system is comprised of four major segments separated by three stepovers (Sahakian et al., 2017).

In the region offshore of San Onofre, the Camp Pendleton splay of the Northern strand interacts with the Carlsbad Canyon strand, following the naming convention of Sahakian et al. (2017). Stepover widths between these strands are all 2 km or less (Figure 2.2; Sahakian et al., 2017). Models and empirical data reveal that an earthquake rupturing the entire offshore length of the NIRC system, could produce an  $M_w$  7.0-7.3 earthquake (Sahakian et al., 2017).

In general, fault geometry and interactions along the NIRC fault system offshore of San Onofre remain poorly constrained compared to the onshore strands. Seismicity also seems to be focused onshore, being relatively diffuse offshore (Figure 2.1) (Fischer and Mills, 1991; Grant and Shearer, 2004). The most recent large seismic events on the fault complex occurred onshore near the ends of the fault system—the 1933 Long Beach Earthquake ( $M_L$  6.4) to the north, and a paleoseismological event dated  $1650 \pm 120$  years near La Jolla, CA (Rockwell, 2010; Lindvall and Rockwell, 1995).

Rivero et al. (2000) and Rivero and Shaw (2011) used legacy industry MCS data to document evidence of a set of large low-angle extensional detachment faults underlying much of the eastern ICB between the Coronado Bank Fault Zone (CBFZ) and NIRC. They hypothesize that these detachment faults have been reactivated as a set of blind thrusts, the Oceanside blind



**Figure 2.2:** Location map of survey area off San Onofre and coastal communities of Dana Point and San Clemente. Location of Las Pulgas Road within Marine Corps Base Camp Pendleton is also shown. Survey area bounds on continental shelf are outlined with a yellow rectangle. Shown here in white are segments of the Newport-Inglewood Rose Canyon (NIRC) fault system from Sahakian et al. (2017). Solid and dashed red fault segments from USGS Fault and Fold database (USGS, 2006). Black solid lines within the survey box denote locations of crosslines and arbitrary line shown in the figures. Black dashed line represents path of SIO CHIRP line displayed in Figure 2.13. Also shown are sampled core locations from TN336 cruise. Cores prefixed "BB" are gravity cores. "JPC" are jumbo piston cores. Bathymetry from Dartnell et al. (2015). Abbreviations are: NIRC - Newport-Inglewood Rose Canyon fault; OBT - Oceanside blind thrust; SMT - San Mateo Trend; SOT - San Onofre Trend.

thrust (OBT) and Thirtymile Bank blind thrust (TBBT) and that these thrusts influence strain distribution between younger local strike-slip and compressional faults. The presence of TBBT was used to identify the location of the 1986 M5.4 Oceanside earthquake (Astiz and Shearer, 2000) and a thrust component to the mainshock fault solution (Rivero and Shaw, 2011). The presence of these blind thrust systems thus has large implications for the seismic hazard of the area, although perhaps not directly related to NIRC.

Fault segments and step-over widths interact to permit or inhibit through-going rupture and act as controls on the maximum possible magnitude of the consequent earthquake. They are

important inputs into models of ground motion. Wesnousky (2006) compiled the properties of 22 historical earthquakes and found that, regardless of the tectonic regime involved (strike-slip, normal, and reverse faulting) the probability of a through-going rupture was higher for a step-over with a width of less than 3-4 km. Sahakian et al. (2017) analyzed re-processed industry 2D multichannel seismic reflection (MCS) profiles acquired along the length of the offshore NIRC system and found a 30-40% possibility of end-to-end rupture on the main segments based on static coulomb stress models. Previous studies have shown a lack of Holocene sediment displacement in offshore segments between Dana Point and Oceanside (Singleton et al., 2019; Sahakian et al., 2017; Klotsko et al., 2015). It is possible that changes in fault geometry and step-over width along NIRC actually act as a barrier to through-going ruptures on this system (Sahakian et al., 2017).

In several places along the coast, multiple strands strike adjacently to each other (Sahakian et al., 2017; Ryan et al., 2009), adding complexity to models of major NIRC strands rupturing together. Recent studies of multi-fault earthquake propagation, as observed in the recent 2016 Kaikōura Earthquake in New Zealand (Hamling et al., 2017; Stirling et al., 2017; Clark et al., 2017; Kaiser et al., 2017), revealed complex and cascading fault linkages that control rupture lengths and potential earthquake magnitudes.

Advances in high-resolution geophysical imaging provide higher resolution of offshore deformation and fault architecture; such technological developments allow for improved imaging of near-vertical fault segments, offsets at stepovers, and fault recency (Nishenko et al., 2018; Kluesner and Brothers, 2016). Three-dimensional seismic data provides improved fault characterization, which is a necessary first step towards assessing the potential geohazard risk to coastal California. In addition, 3D data provide highly accurate imaging of steeply dipping strike slip faults because the data can be projected in cross-section to observe offset stratal layers and in time slice (i.e., map view) to reveal lateral offsets across fault strands in any particular azimuth.

Here we present recently acquired 3D P-Cable seismic reflection data to define NIRC

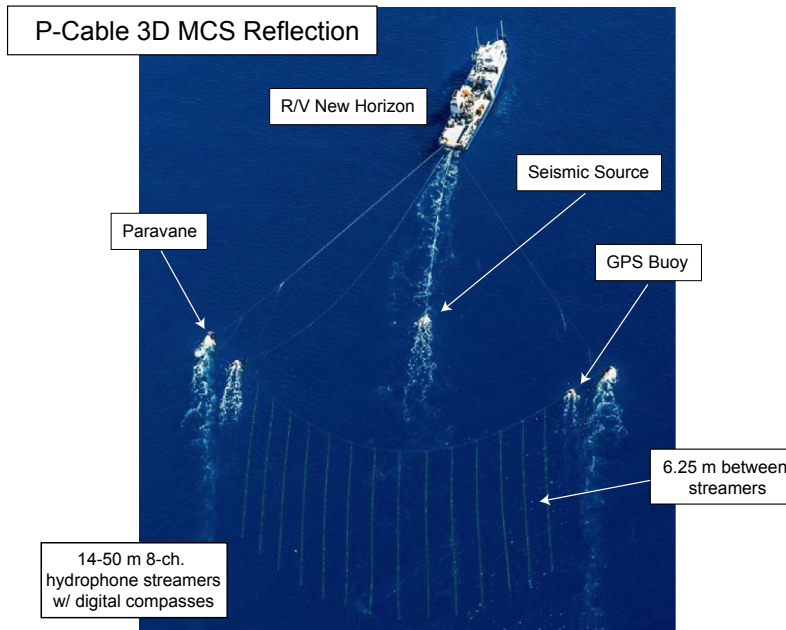
fault segment geometry, segment interaction and attendant deformation at a large stepover ( $\sim 2.8$  km). In addition, we provide evidence that fault segment interaction along this portion of the margin also appears to control the width of the margin, sequestering of sediments on the shelf, and divergence of off-shelf drainage systems.

## **2.3 Methods**

### **2.3.1 3D MCS Acquisition and Processing**

For several decades, 3D MCS data has been acquired by the oil industry for hydrocarbon exploration. Recently, portable state-of-the-art 3D seismic reflection systems have been developed that can be deployed from Ocean-Class research vessels of choice (Ebuna et al., 2013; Eriksen et al., 2015; Crutchley and Kopp, 2018). The 3D P-Cable Seismic Reflection System ("P-Cable") is one such portable high-resolution system. P-Cable employs a cross-cable that is kept under tension by two one-ton paravanes attached to the ends of the cross-cable and to the stern (port and starboard) when the vessel is underway (Figure 2.3). Attached to the cross-cable are fourteen 50 m long streamers, each containing 8 hydrophones, with digital compasses and depth sensors at the head and end of each streamer. Short streamers allow for greater operational maneuverability during acquisition; they also reduce anti-aliasing artifacts, allowing for greater resolution after processing (Brookshire et al., 2016). Differences in hydrophone position caused by the camber of the cross-cable are tracked using a set of GPS transmitters positioned at various points on the system: on the vessel, at the ends of the cross-cable, on the paravanes, and on the seismic source. Tracked changes in system geometry are then corrected during processing.

In late summer/fall 2013, we collected 2D seismic reflection data on the R/V New Horizon (NH1320), which was then processed and analyzed to assist in selecting locations for a later focused 3D survey. Guided by our 2D data observations, we acquired the first high-resolution



**Figure 2.3:** Aerial photo of Scripps Institution of Oceanography’s Research Vessel New Horizon towing the P-Cable 3D Multichannel Seismic Reflection System, with major components of system labeled.

3D data set of the offshore NIRC fault segments in the survey area (Figure 2.1 & 2) using P-Cable (survey acquisition parameters are listed in Table 1 and in Appendix B) towed from the stern of New Horizon (NH1323). Our survey area, a 52.5 km<sup>2</sup> grid with coverage over the continental shelf and shelf-break, was targeted to maximize imaging of the NIRC fault system in a region where the shelf widens anomalously compared to the trend of narrow shelf width between La Jolla and the San Pedro Shelf south of Long Beach (Figure 2.2).

Mapped drainage channels also were targeted, as they would provide piercing points across the NIRC fault system to constrain slip. The survey data were acquired in depths ranging from 44-360 m with 3D bin sizes of 3.125 m. A triple-plate boomer operating at 1.8 kJ was selected as the acoustic source for the continental shelf because of its high-resolution at relatively shallow water depths.

We measured a peak frequency of 175 Hz, allowing us a minimum vertical resolution of 2.1 m. Oscillations produced by the boomer seismic source (termed the "Bubble Effect")



manifested in the data as a very thick series of strong parallel reflectors near the seafloor. Despite post-stack deconvolution during initial processing, the reverberation effect still effectively masks real reflection features in the top of the seismic section, with the result of obscuring feature resolution at shallow depths down 15 ms (11 m) from the seafloor. This problem has also been noted on previous P-Cable surveys conducted with AP3000 boomer sources (Greene, 2014).

A 1000 ms record length was digitized, but after processing the reflectors were resolved to 800 ms (approximately 680 m depth). Much of the analysis of the data, however, was performed between 100 ms and 400 ms (approximately 77-321 m) depth where data resolution and imaging were optimum. Complete acquisition parameters are listed in Table 1.

We collaborated with Geotrace Technologies, a petroleum services company, to process

**Table 2.1:** List of acquisition parameters used for P-Cable 3-D multichannel seismic reflection system.

P-Cable 3-D Acquisition Parameters	
Number of Streamers	14
Streamer Spacing	6.25 meters
Streamer Length	50 meters
Channels per Streamer	8
Group Interval	6.25 meters
Streamer Type	Geometrics GeoEel
Width of Active Spread	87.5 meters
3D Swath Width	43.75 meters
Bin Size	3.125 x 3.125 meters
Nominal Subsurface Fold	8
Sample Rate	0.25 milliseconds
Record Length	0.75 to 1.0 seconds
Recording Format	SEGY
Source Type	AP3000 Triple-Plate Boomer
Source Depth	0.5 m
Shot Interval	3.125 meters
Peak Frequency	175 Hz

the data volume given its enormous size (20 GB per seismic attribute volume) and their experience

with processing 3D P-Cable data acquired from previous surveys (Crutchley and Kopp, 2018). Technicians and science crew conducted on-board QC of both seismic and GPS data during acquisition. On shore, technicians employed a sequence of processing steps to enhance data quality including 1D and 2D surface-related multiple elimination (SRME), normal move-out (NMO) at 1480 meters/sec, 3D stacking, and post-stack migration (processing steps are listed in Table 2; Please see Appendix B for complete processing details). The processed data were compiled into both amplitude-attribute and similarity-attribute products for interpretation. The amplitude volume allows easy identification of reflectors across subsurface stratigraphy based on the relative impedance contrast (i.e., the product of density and velocity) of acoustic reflectors in a trace.

The similarity attribute assigns a value to a bin based on the correlation between the waveform and amplitude of two or more different traces. This attribute is computed as the normalized cross-correlation of all bins within a specified 3D grid (Bahorich and Farmer, 1995). In such a volume, a correlative value of 1 represents the state of "perfectly similar", while a value of 0 represents the state of "completely dissimilar". Similarity attribute volumes are ideal for looking at large-scale discontinuities, such as sharply dipping beds, faults, and paleochannels. These features become readily interpretable especially in the context of an isochron (a "time-slice") view. In amplitude data, these features can often be obscured if they run parallel to strike in a given time-slice. The amplitude volume is instead most useful in vertical profiles, where fault presence and character can be easily identified by analyzing stratigraphic package displacement.

Additional in-house filtering was applied to both the amplitude and similarity data volumes, using OpendTect Seismic Interpretation Suite, and following a workflow described by Kluesner and Brothers (2016), to increase reflector continuity and facilitate data interpretation. A parameterized dip-steered median filter was applied to each volume in order to reduce random noise. The resulting noise from the filtering process was isolated prior to removal and evaluated

**Table 2.2:** List of onshore processing steps.

1	Reformat SEG Y - 0.25 or 0.5 ms raw shot gathers
2	Low cut filter 45(18) Hz(dB/Oct)
3	Temporal resample to 1ms sample rate with anti-alias filter
4	Bad trace edits
5	De-noise with automatic spike removal in Shot domain - 2 iterations
6	2D SRME on common channel/shots
7	Load data to a 3D pre stack volume (3.125m x 3.125m)
8	Apply 1480 m/s primary NMO
9	3D stack
10	Deconvolution After Stack (DAS)
11	1D SRME and subtract
12	Interpolation of empty bins with SNIP
13	Post stack, pre-migration noise attenuation with automatic spike removal, FDNA, and FXY
14	Post stack Kirchhoff migration
15	Dip filtering
16	Amplitude balancing: Measured exponential gain
17	Gun and cable static correction
18	SEG Y - Final Filtered Migrated Stack
19	Scaling: 400ms Iterative AGC - optional
20	SEG Y - Final Filtered Migrated Scaled Stack

for efficacy and potential removal of signal. Finally, a dip-steered diffusion filter was applied to each volume with a symmetric step-out (8x8 for the amplitude volume, and 6x6 for the similarity volume) in both inline and crossline directions and a 0 ms time-gate parameter. This filtering workflow removed randomized noise and enhanced discontinuities to improve fault identification, which increased confidence in our interpretations.

A number of additional seismic attribute volumes were generated using the original amplitude data, in order to facilitate seismic interpretation in specific cases. A seismic attribute is defined as information that can be computed or derived from the original seismic data volume (Chopra and Marfurt, 2005) and is often used in seismic data processing to enhance many aspects of geological information that are not as easily discernable through more conventional processing. Attribute analysis has thus proven to be a very useful tool for geophysicists in the detection and enhancement of fault traces, and paleochannels, as well as illuminating structural details (Kalid et

al., 2016). Using the Rock Solid Attributes toolkit, part of the industry-grade IHS Kingdom Suite software, additional seismic attribute volumes were generated to assist interpretations. These included attributes calculated from geometric properties such as curvature, that greatly improved mapping of structures and paleochannels (Roden et al., 2015).

3D data volumes allow for views using arbitrary azimuths that can be tailored to examine the true strike and dip of structures. In turn, the mapping of interpreted structures in 3D can be accomplished with greater confidence. All of our interpretations were iteratively made by using these arbitrary lines, as well as vertical dipline/strikeline profiles, to identify structures and faults in vertical profiles of the amplitude data. Next, we confirmed our initial interpretations in similarity attribute time-depth slices and correlated our results with other seismic attributes. Finally, we returned to the vertical profiles with our interpretations, to further constrain fault length and character. Although we did not depth migrate our 3D volumes due to a lack of well control, we adopted the following velocity function described by Ryan et al., 2009 to calculate depths for estimations in this paper:

$$V = 1500 + 0.2438t + 8.2659 \times 10^{-5}t^2$$

This function was derived using interval velocities measured from 2D MCS profiles during Jebco cruise J188SC (Triezenberg et al., 2016; MMS, 1997), including profiles acquired within the bounds of our survey area.

Detailed mapping of some paleochannels was accomplished by computing the most negative and most positive curvature seismic attributes on the original data volume. Curvature in this context is defined by geometry: the degree of deviation from a straight line, equivalent mathematically to the reciprocal of the radius of curvature of a stratigraphic bed (Roberts, 2001; Chopra and Marfurt, 2007). There are several properties of curvature that are useful in the application of seismic analysis but the two attributes that we found most useful for identifica-

tion of paleochannels was Most Negative Curvature and Most Positive Curvature. The most negative curvature seismic attribute images synclinal features (e.g., paleochannel thalwegs) as a discontinuity, while the most positive curvature attribute enhances imaging of anticlinal features (e.g., channel overbanks) (Chopra and Marfurt, 2007). Volumetric computation of both curvature properties is computationally inexpensive and could be processed rapidly using Kingdom Suite's Rock Solid Attributes package on a single desktop computer outfitted with a 6-core 2.5 GHz CPU. Once calculated and serialized to disk, the two attributes were coblended into a 60/40 proportion. This imaging method was most successful at revealing paleochannels on the western and eastern edges of the survey area where distortion due to fault damage was minimal.

### **2.3.2 Age Control**

In order to constrain onset of deformation, radiocarbon dating of organic material recovered in cores was performed. The shelf and slope near San Onofre have not been well-sampled. Conrad et al. (2018), however, was able to map the Quaternary boundary in the region using unpublished industry well data acquired as part of the Caldrill program in the 1970s and now held by the US Bureau of Safety and Environmental Enforcement (Conrad et al., 2018).

In January 2016, 64 Gravity (GC) and Jumbo-Piston Cores (JPC) were collected onboard the R/V Thomas G. Thompson (TN336) as part of a regional study designed to provide age constraints on shelf/slope evolution, and recent faulting. Possible piercing points, such as faults and paleochannels were selected as coring targets using previously collected multichannel seismic and CHIRP data. JPC trigger cores were also acquired and logged. In some cases, positional drift caused the cores to be slightly offset from the profiles, in which case the core locations were projected orthogonally onto the profile. Once on-board, intact cores were analyzed for magnetic susceptibility, gamma density, P-wave velocity, and resistivity using a GeoTek Core-logger. Cores were then split and observations of color, grain size, sediment structures, and general lithology

were recorded.

Fourteen samples were selected for radiocarbon dating due to proximity to the survey area. Ten of those samples were analyzed at the National Ocean Sciences Accelerator Mass Spectrometry facility at the Woods Hole Oceanographic Institution (WHOI) and produced an age using the Libby half-life of 5568 years and following the convention of Stuiver and Polach (1977). The other four samples were analyzed at the W.M. Keck Carbon Cycle Accelerator Mass Spectrometry facility at the University of California, Irvine (UCI) following the same conventions.  $^{14}\text{C}$  ages were calibrated using the CALIB program, version 7.0.4 (Stuiver and Reimer, 1993). Non-fragmented planktonic foraminifera that had not undergone diagenesis were preferentially collected.

Ages of planktonic foraminifera of less than 12,000 yr were calibrated with a reservoir age of 800 yr. A reservoir age of 1,100 yr was used for planktonic foraminifera >12,000 yr (Southon et al., 1990; Kienast and McKay, 2001; Kovanen and Easterbrook, 2002) and 1,750 years for a benthic reservoir age similar to Covault et al. (2010). For cores containing more than two dates, age-depth models were generated using the Bacon age-modeling software, version 2.3.3 (Blaauw and Christen, 2011) using these reservoirs as a parameter.

Of the fourteen tested samples, two are from short gravity cores collected on the continental shelf, and the rest were acquired on the continental slope directly southwest of the survey area (Figure 2.2). Two samples, both acquired on the slope below the widest part of the shelf, were greater than 52,000 years old and thus eliminated as radiocarbon dead. Based on analysis of the remaining samples, sedimentation rates (Table 3) were calculated. Sedimentation rates were highly variable, based on sample depth and core location. Cores sampled from the widest part of the continental slope showed extremely low sedimentation rates. The highest sedimentation rates were computed on cores that were taken within drainage channels or on the continental shelf.

Covault et al. (2010) published a sedimentation rate of 0.33 mm/yr for their piston core "H4", located at the toe of the continental slope approximately 10 km northwest of our survey

area, at a sample depth of 374-384 cm. As sediment depositional regimes tend to vary from shelf to slope to abyssal plain, we calculated a sedimentation rate from gravity core BB 29-33 that was collected within the bounds of the survey area on the continental shelf. We sampled between 36 and 44 cm depth. Radiocarbon testing returned an age of 1,460 years with an error of 20 years. Using that value, we calculated a sedimentation rate range of 0.27 mm/yr to 0.28 mm/yr. Although the core was sampled near the bottom, the core length is only 47 cm. Due to the shallow sampling, extrapolating the sedimentation rate to several hundred meters depth introduces much uncertainty.

## **2.4 Results**

### **2.4.1 Deformation and Fault Characterization**

A series of stair diagrams are presented to highlight the three-dimensional architecture of the NIRC fault segments and attendant deformation (Figures 2.4-2.11, 2.14, & 2.15). A stair diagram is a visual depiction of 3D seismic data combining two-time slices (map view) and one cross section (road cut view). In Figures 2.4-2.11, 2.14, & 2.15, cross sections are rendered using data for acoustic amplitude. Time slices in Figures 2.4-2.11, 2.14, & 2.15, are displayed using similarity data at 60% transparency overlying amplitude data, to allow better visualization of discontinuities. The images presented are bounded by an upper timeslice at 125 ms of two-way travel time (TWT) ( $\sim 96$  m) and a lower timeslice at 350 ms TWT ( $\sim 279$  m), with the cross-section point of view moving from north to south. The sections presented here capture the architecture of the fault systems and their along- and across-margin interaction. The locations of vertical profiles presented with respect to the entire data volume are labeled in Figure 2.2.

Figures 2.4 and 2.5 present a vertical profile at crossline 1790. The yellow dashed line

**Table 2.3:** TN336 Cores, Radiocarbon Ages, and Sedimentation Rates.

<b>Core ID</b>	<b>Sample Depth (cm)</b>	<b>Description</b>	<b>Calibrated Radiocarbon Age (yrs)</b>	<b>Age Error (yrs)</b>	<b>Minimum Sedimentation Rate (mm/yr)</b>	<b>Maximum Sedimentation Rate (mm/yr)</b>	<b>Testing Laboratory</b>
BB 3-03	165-170	Planktonic foraminifera	16,300	50	0.103	0.103	WHOI
BB 7-07	26-30	Planktonic foraminifera	2,950	20	0.094	0.096	WHOI
BB 13-14	17-21	Planktonic foraminifera	40,000	960	0.005	0.005	WHOI
BB 13-14	39-43	Planktonic foraminifera	Too old	-	-	-	WHOI
BB 22-25	133-137	Planktonic foraminifera	22,944	78	0.059	0.059	UCI
BB 22-25	256-260	Planktonic foraminifera	38,700	910	0.065	0.068	WHOI
BB 23-26	127-131	Planktonic foraminifera	9,180	25	0.140	0.141	WHOI
BB 23-26	210-214	Planktonic foraminifera	9,840	30	0.215	0.216	WHOI
BB 29-33	36-44	Planktonic foraminifera	1,460	20	0.270	0.278	WHOI
JPC 1-01	15-19	Benthic foraminifera	7,880	25	0.019	0.019	WHOI
JPC 1-01	185-189	Benthic foraminifera	19,950	90	0.092	0.093	WHOI
JPC 2-02	43-47	Planktonic foraminifera	18,043	69	0.025	0.025	UCI
JPC 2-02	157-161	Planktonic foraminifera	39,347	395	0.040	0.041	UCI
JPC 2-02	230-234	Planktonic foraminifera	Too old	-	-	-	UCI



shows the boundary between the crossline (1790) and the timeslice (350 ms). The other dashed lines show locations for crosslines displayed in Figures 2.6-2.10. We will describe the features from north to south. Several fault segments (interpreted in Figure 2.5) enter the survey volume from the northwest; the faults exhibit an along-margin parallel strike. These segments tend to terminate close to the surface; however, seafloor offset in most cases is not observed in the data volume. Prominent changes in slope morphology and subsurface reflector geometry are observed across the two largest fault segments (labeled i and iii, Figure 2.5). Minor surface expression is observed coincident with fault iii. A high-angle ( $\geq 80^\circ$ ) or vertical dip on all the segments is observed in cross section 1790. North of where fault iii exhibits a left lateral jog, a small, semi-circular anticlinal structure is observed in the crossline (1790) and the timeslice (350 ms; Figures 2.4 and 2.5). This structure is bounded by fault vii which exhibits curvilinear character and merges likely as a splay of the larger segment, fault iii. Continuing northeast, the limb of the anticlinal structure is imaged in the crossline and has a northeastward dip. The anticlinal structure is also imaged in the time slice by a circular acoustic reflector pattern that is bounded by fault segments iii to the west (Figure 2.5), and vii to the east. Along the outer shelf upper slope, a seaward thickening wedge is observed in the 3D P-cable cross lines and in the timeslice as a slightly deformed, folded acoustic pattern.

Moving south to crossline 1945 (Figure 2.6), the anticline is dissected by numerous fault segments (e.g., i, ii, and iii; Figure 2.6). The curvilinear nature of fault vii can be observed as the fault bounds the anticline observed in Figure 2.5. Segment vii sharply delineates stratigraphy to the north that is gently dipping seaward, from steeply dipping stratigraphy towards the fault. To the southeast of segment vii, visible in the timeslice, is a synclinal structure likely created by right-lateral pull-apart deformation as strain is distributed from fault iii to fault vii. The western edge of the syncline appears to terminate abruptly into fault iii (Figure 2.6) and the syncline forms a narrow "cusate-like" antiform structure to both the north and the south.

Fault iii is steeply dipping in this region (Figure 2.6); the reflectors imaged to the south

west off fault iii exhibit a synformal geometry. Fault vii is observed north of the northern-most "cusate-like" structure. Farther south of the horn, fault vii curves to the southwest and the stratigraphy transitions laterally from a fault (Figure 2.6) into a fold (labeled in Figure 2.7).

Between faults i and iii— both in the crosslines and time slices —there is an acoustically transparent to semi-transparent and chaotic character with only minor reflectivity. A pronounced change in acoustic reflectivity correlates with the shelf edge in this region; the increase in acoustic amplitude is bounded to the east by fault i. Along the shelf edge east of fault iii there are some concordant reflectors that are flat lying in the crossline and appear to have a lower acoustic character in the time slice. Continuing to the southwest of fault iii, the antiform is dissected by numerous faults, the largest of which are labeled on Figure 2.6 as faults i and ii. Reflectors exhibit increased deformation near the antiform. The wedge of acoustically transparent material along the western slope, also imaged in Figure 2.5, is likely a slump from the shelf break. The irregular nature of the western edge of the time slice reflects the intersection of the data volume with canyon heads on the outer shelf upper slope.

Crossline 1945 (Figure 2.6) is 291 m north of Crossline 2038 (Figure 2.7), but on scales of tens of meters, marked changes in the acoustic reflectors imaged in the 3D data can be observed. North of the horn of the "cusate feature", a fold is observed northeast of fault segment iii. The fold tracks the termination of fault vii. The southwest limb of the anticline to the west of fault iii is highly faulted and deformed. Farther southwest of fault segment i, amplitude reflectors in the limb are steeper, but more continuous and exhibit only some minor folding. The seaward thickening wedge observed to the north is systematically increasing in thickness toward the south.

Moving southeast from crossline 2038 (Figure 2.7) to crossline line 2252 (Figure 2.8), the fold northeast of fault segment iii evolves into a monocline with abrupt increase in dip toward the west near fault iii. Note that several fault segments along the northeastern portion of the data volume bound the "cusate" morphology. Large areas of the volume are acoustically transparent to semi-transparent with broken, chaotic reflectors. Acoustic reflectivity increases along the outer

slope with mild folding near fault segment ii.

A large antiform structure is observed where fault segment vi exhibits a left lateral jog from south to north. Figure 2.9 shows the marked change in acoustic reflectivity with the faulted antiform clearly imaged. Crossline 2457 intersects the time slice in a region where a circular pattern of reflectivity is imaged in the time slice northeast of fault segments v and vi. A faulted anticline, imaged in previous figures, is also well imaged in crossline 2457 (Figure 2.9). The seaward thickening lens observed in Figures 2.6 and 2.7 thins away to the south and is not observed in Figure 2.8 or Figure 2.9. Two large canyons are imaged along the seaward edge of the time slice as large embayments just south of the crossline. Farther south (Figure 2.10), westward dipping reflectors are imaged east of fault segment iii and correlate with a circular reflector pattern in the time slice. High amplitude chaotic reflectors are imaged in the upper portions of the crossline with acoustically transparent to chaotic semi-transparent regions beneath (Figure 2.10).

Crossline 2457 (Figure 2.9) intersects the timeslice between two large canyons on the slope (Figure 2.2). Both canyons are imaged as embayments in the time slice on Figure 2.8 and labeled San Onofre Canyon North and San Onofre Canyon South (Wei et al., 2019). An acoustically transparent region is observed immediately south-east of the crossline making confident interpretation difficult; however, reflector offsets in crosslines and geometry in the time slice allows for potential correlation of the fault segments between faults i and iv and that uncertainty is shown by the dashed fault trace in the region. Farther east in the volume, reflector continuity in both the crossline and the time slice allow for confident correlation of faults iii and v with fault vi (Figure 2.9). Toward the northeast in the data volume the dipping packages observed in cross section are imaged as parallel features with moderate acoustic reflectivity in the lower time slice. Between fault segments i and iii in the crossline, several fold-fault structures are imaged. Southwest of fault i, there is a more uniform dip of the slope reflectors with moderate deformation. The fault geometry along fault vi exhibits a left jog just before the large anticlinal

structure located at the center of the survey area (Figure 2.9). There is a dramatic change in reflector dip across the margin; toward the northeast the stratigraphy is acoustically laminated with a shallow dip, whereas toward the southwest of fault segment ii the dip of the stratigraphy appears to steepen. On the outer shelf, the westward dip of the upper slope reflectors diminishes where the width of the shelf increases (see shelf bathymetry in Figure 2.2).

Fault fold deformation farther to the southeast is observed in crossline 3400 (Figure 2.11). In this region where the shelf is wider, no canyon morphology is observed along the seaward side of the data volume. Fault deformation is very pronounced and focused across a few major fault segments. Crossline 3400 images the eastern limb of a large anticlinal structure near the center of the data volume (Figure 2.2). The anticlinal structure measures roughly 2500 m in diameter and is an E-W elongated structural dome imaged in the lower time slice (Figure 2.17). Two large fault segments, iii and iv, bisect the antiform in the crossline separating the northeast and southwest limbs. Fault iv appears to exhibit a surface expression (Figures 2.6 & 2.7: Sahakian et al., 2017).

Between the cities of Newport and San Diego the continental shelf is relatively narrow, averaging 2.5 km in width (Figure 2.2). The shelf offshore of San Onofre is anomalously wide however, extending to approximately 10 km. The location of the large antiform structure observed in the lower time slice (Figures 2.4-2.11) is spatially coincident with this widest part of the shelf (see crossline locations in Figure 2.2). Stratigraphy to the northeast of the anticline crest, is bounded by the vi segment; the reversal of dip in this region separates the northeast limb of the anticline from the more gently southwest dipping nearshore reflectors. Toward the southwest of the anticline axis, the reflectors are steeply dipping with minor faulted stratigraphy in crossline 3400.

The crossline is truncated at 125 ms ( $\sim 96$  m) in Figure 2.11 for the purpose of showing fault traces along the shelf, but Figure 2.12 shows a full vertical profile of Crossline 3400 with our interpretations. Reflectors in both limbs of the anticline are clearly truncated at the seafloor, likely from transgression of sea level across the continental shelf. A marked change in dip occurs

northeast of the anticline at 200 ms ( $\sim 156$  m) and is outlined with a yellow line in both Figures 2.11 & 2.12. Younger stratigraphy near fault segment vi is undeformed above the line, and thus we infer this boundary to be the onset of fault deformation from vi. In Figures 2.11 & 2.12, the line is dashed to show the inferred boundary where the data is acoustically transparent.

Figure 2.13 shows an east-west line of CHIRP data acquired by Scripps Institution of Oceanography (SIO) in 2008 using a customized EdgeTech X-Star CHIRP sub-bottom reflection sonar with sub-meter vertical resolution. Data were heave-corrected and processed to 200 ms TWT. The line was selected because it passes through the northern limb of the large anticline at the widest part of the shelf and intersects several of the larger fault segments. Due to masking of surficial stratal geometry by oscillations from the bubble effect in the 3D data, this line was selected to investigate any near-surface fault offset. We extended and labeled our fault interpretations into the CHIRP line shown in Figure 2.13 and correlated interpreted sediment horizons with units described by Klotsko et al. (2015). Unit III is an acoustically transparent layer that could be mapped across the entire line and represents a modern marine deposition layer (Klotsko et al., 2015) None of the interpreted fault segments could be mapped into Unit III although the boundary between underlying stratigraphy and Unit III, the transgressive surface, exhibits considerable offset.

Farther southeast of the anticlinal structure, the observed major fault segments outline a large area that is acoustically transparent and approximately 3 km wide. The major fault segments can be divided into two groups based on their strike: fault segments that are parallel to the shelf edge and bisect the anticline (e.g., fault segments iii and iv); versus fault segments that exhibit a more northwest to southeast trend (Figure 2.14). In this region, the fault segments have steep dips, being almost vertical. In Figure 2.14, fault segment xi appears to be the largest segment bounding the acoustically transparent zone to the southwest. Stratigraphy inshore of this fault is acoustically laminated with a dip toward the southwest down to approximately 150 ms, with moderate acoustic reflectivity and is observed in the lower timeslice. The dip of this package

appears to increase markedly with depth.

Fault segment x is the southwestern bounding fault of the acoustic transparent zone (Figure 2.14). Between this fault and the shelf edge, the reflectors tend to parallel the slope with a steep dip. Within these bounding fault segments, there are numerous smaller segments and several zones of deformation associated with these smaller segments. Between the fault segments xii and x, the reflector character is acoustically transparent to acoustically semi-transparent and chaotic with minimal reflector continuity. Southwest of fault segment x, there is higher acoustic reflectivity and reflector continuity. Along the western edge of fault segment x in the middle of the timeslice where the fault jogs to the west there appears to be a small anticlinal structure (Figure 2.14).

Moving south to crossline 5400 (Figure 2.15) near the southeastern limit of the survey area (crossline location shown in Figure 2.2), the shelf width again diminishes and small canyon embayments are observed in the time slice. The continental slope in this location exhibits a maximum slope of  $24^\circ$  at the seafloor (Figure 2.18). Examination of the 3D volume in this region reveals a highly chaotic acoustic character being mostly acoustically transparent to semi-transparent; as such there is much uncertainty in fault location in this region. Our fault interpretations delineate areas with markedly different acoustic character. Where mapped, the fault segments in this location exhibit a predominantly NW-SE trend.

Figure 2.16 shows a vertical display of amplitude data from 0 to 800 ms of an arbitrary line (marked A to A' in Figure 2.2). This line images a sequence of synclines and anticlines from north-northwest to south-southeast. The axes of all the imaged folds is northeast-southwest. The northern limb of the large anticline coincident with the widest part of the shelf is imaged to the far south-southeast and displays steeply dipping stratigraphic bedding. In this location, as in Figure 2.11, bedding terminates at the seafloor. The largest syncline imaged in the arbitrary line, centered around trace 2800, appears to plunge seaward with a west-southwest axis and is coincident with the San Onofre South (SOS) off-shelf drainage channel (Wei et al., 2019). A

smaller syncline to the north, centered at trace 2240, also appears to plunge seaward, towards the San Onofre North (SON) drainage channel (Wei et al., 2019). Separating the two synclines is an asymmetric anticline, measuring 1686 m across at the arbitrary line in Figure 2.16, and narrowing to 1040 m near the shelf edge. Finally, an anticline exhibiting a tight fold, is found to the north centered around trace 1800 suggesting a northwest vergence. This anticline terminates abruptly against fault segment iii. The western limb of the anticline is possibly shifted northwards approximately 252 m along the western side of the fault (northern dashed yellow oval in Figure 2.17). A second possible offset of approximately 116 m is observed along the same fault (fault segment iii) on the next anticline to the south (southern dashed yellow oval in Figure 2.17).

A survey-wide analysis of our interpreted faults reveals two major azimuthal trends of the faults in the study region. Based on these trends and acoustic reflectivity, we divided the study area into three zones, labeled in Figure 2.17.

Fault azimuths in Zone One are oriented roughly towards the northwest. The largest fault segment, iii, bounds an undulating series of smaller synclines and anticlines (shown in cross-section in Figure 2.16). Segment iii delimits Zone One between undeformed sediments trapped from the east and deformed dipping stratigraphy seaward.

Zone Two is dominated by a large structural dome coincident with the widest part of the continental shelf. This antiform structure is bisected by the largest segments (fault segments iii and iv) in the survey area and is bounded on the eastern edge by fault segments vi and vii. As in Zone One, sediments from the east gently dip towards easternmost boundary faults. These boundary faults exhibit a left-ward jog and change trend to a more northwest azimuth as they approach Zone One. Segments iii and iv also exhibit small changes in azimuth to the northwest in the northern part of Zone Two.

In the south (Zone Three), the largest difference in fault azimuth and acoustic character is observed. A marked change in fault trend of  $25^{\circ}$  occurs between Zones Two and Three, and  $32^{\circ}$  between Zones One and Three. Fault segments in Zone Three have a more NW-SE trend and

a small anticline is observed where fault segment x exhibit a small change in trend toward the northwest and interacts with segments ix and xii. As opposed to Zones One and Two, much of Zone Three is acoustically transparent and difficult to interpret except at boundaries where there are large amplitude differences.

Truncated stratigraphy of the large anticline in Zone Two forms an angular unconformity near the seafloor; however, subsurface deformation has a surface expression as shown in a map of bathymetry data (Figure 2.18, line B to B'). The inset shows a transect across the anticline with approximately 5-7 m of surficial relief across the large regional anticline observed in Zone Two (Figure 2.17). Note the small increase in slope along the shelf edge near B on the transect and along the shelf edge to the south of the widest part of the shelf. As expected, the continental shelf and basin floor in this region have low slopes with localized steep slopes coincident with off-shelf channelization. The steepest slopes in the survey area are located above the basin floor at the toe of the slope and are up to 25°. The large canyons in the northern portion of the study region (SON and SOS) incise the shelf edge (Figure 2.18) (Wei et al., 2019).

## **2.4.2 Paleochannel Identification**

In the ICB coastal margin, about half of the regional offshore canyons and most of the smaller gullies appear to be active during the Last Glacial Maximum but were rendered inactive when cut off from canyon heads on the outer shelf during post-glacial transgression (Normark et al., 2009). These bathymetric features make ideal candidates for fault piercing points to measure offset and estimate slip-rate.

Piercing point candidate gullies and canyons on the shelf and slope were identified in timeslices. Several slope features were found to be potentially offset by shore-oblique faults that are likely part of the San Onofre Trend, but there was no observable offset from NIRC segments found in gullies on the shelf. Attempts at mapping channel thalweg horizons below the seismic



signature to determine piercing points were inconclusive due to the presence of chaotic amplitude reflectors in the data.

## **2.5 Discussion**

### **2.5.1 3D Structure Mapping**

Acquiring 3D seismic reflection data is critical to image fault segment interactions especially along steeply dipping strike slip fault systems, such as NIRC. Such a data volume places important constraints on how deformation is communicated to neighboring fault segments, permitting or arresting through-going rupture. Fault analysis in three-dimensions has allowed us to capture the architecture of the NIRC fault segments throughout the survey area and illustrate their curvilinear character (Figure 2.17). Our observations are that distribution and architecture of the fault segments changes throughout the volume. This distribution has implications for rupture behavior and propagation, as well as direct controls on margin architecture such as shelf width, drainage patterns, and tectonic structures. These changes in architecture have allowed us to further assign three separate zones of deformation imaged in the survey area.

Zone One encompasses mapped segments of the Camp Pendleton splay in the north-western section of the survey and the zone is bounded to the south by a large antiform structure (Figure 2.11). In this zone, we observe a transition from a transtensional to transpressional regime accompanying these segments. Ryan et al. (2009), with an industry MCS line only two kilometers north of crossline 1790 shows that transpressional features predominate northward along the Camp Pendleton splay, and eventually disturb the seafloor near Dana Point (Ryan et al., 2009). We attribute this change in stress regime to a series of right and left jogs in fault segments that are expressed in the deformation as a series of synclines and anticlines bounded by the main fault segment, segment iii (Figure 2.2). Given the 3.125 m bin size of the data volume

in all directions, the terminations and transitions of these faults into folds and then eventually monoclines, are well-imaged in the data (Figures 2.6-2.8). These transitions are associated with secondary fault splays and stepovers that creates a "cusplate-style" morphology in the time slice acoustic reflectivity, with the horns of the cusp being antiforms and intervening regions of the cusp being synforms (Figures 2.7 & 2.8). Two major strands of the NIRC fault (iii and v) bound these semi-circular patterns of acoustic reflectivity in the time slice to the southwest (Figure 2.6).

We observe the completion of the transition to transtension in crossline 2457 (Figure 2.9). The faulting and folding of the anticline along the outer shelf exhibit a keystone structure with a negative flower structure, as evidence for transtension in this region. At this location, the damage zone of the fault plane is fairly wide, in contrast to the narrow fault zone of the inshore fault.

The internal structure of the anticline is no longer well-imaged as the point of view moves northwest into the data volume to crossline 2252 (Figure 2.8). Here the anticline exhibits a transparent alternating to semi-transparent acoustic character. We interpret that this loss of acoustic reflectivity may record intense shearing and deformation or possibly fluid flow in the region, which has overprinted the existing acoustic impedance contrasts. Farther north at crossline 2038 (Figure 2.7) and crossline 1945 (Figure 2.6), the acoustic reflectivity of the anticline returns, and the internal deformation is observed with a transtensional, down-dropped geometry.

At crossline 1790 (Figure 2.5), the shelf begins to narrow in this area and the acoustic character has reverted back to transparent and semi-transparent but chaotic. Such changes along the margin are more likely resulting from shearing and overprinting the acoustic character than lateral facies changes with different acoustic impedance contrasts. Our preferred interpretation is the along margin change in acoustic reflectivity is the result of post-depositional processes (i.e., shearing or fluid flow).

An azimuthal change of  $15^\circ$  is observed when moving from the northern zone (Zone One) to the central zone (Zone Two; Figure 2.11). Two segments form a keystone structure from the surface to about 200 ms ( $\sim 156$  m) in depth that bisects the large antiform. Sahakian et al. (2017)

identifies this keystone structure as concomitant with the location of a possible drainage channel.

The faults observed in Zone Three exhibit both fault trends and the changes in trends give rise to an anticline along the northwestern margin of Zone Three (Figures 2.8 & 2.11). A wide zone of acoustically transparent to semi-transparent chaotic character exists in Zone Three and we interpret this acoustic character to record a wide zone of shearing bounded by large faults that strike NW-SE. Problems with acoustic reflectivity persist throughout Zone Three and make interpretation difficult. These problems have been documented previously by Ryan et al. (2009) who found intermittent areas acoustically "wiped out" downwards from the seafloor, just south of our survey area between Las Pulgas Road and Oceanside.

Towards the north these fault segments converge and left-step into the large antiform structure coincident with the widest part of the shelf and near the center of the survey. The boundary between observed acoustic reflectors and transparent to semi-transparent character are interpreted to be shear zones at segment locations. These shear zones probably represent the step-over between more northwestwardly striking segments on the eastern edge of the data volume and the coast-parallel segments on the western edge of the data volume. It is possible that strain in this location is being partitioned through duplexing structures (light green segments in Figure 2.17). These structures are the end of segments that change strike from northwest to more northerly. Strain appears to be transferred to several large segments in the step-over that, in turn, then crosscut the large antiform structure.

Leftward steps on a right-lateral system result in localized compression and frequently form deformational structures such as pressure ridges (or "pop-up structures"). There are three other documented left-ward jogs on NIRC, each resulting in pressure ridge structures. The Torrey Pines strand interacts with the Carlsbad Canyon strand just to the north of Carlsbad Canyon and creates a northwest trending ridge that extends for 15 km (Ryan et al., 2009). Another pop-up structure occurs from a jog between the Torrey Pines strand and the La Jolla strand offshore of Torrey Pines State Reserve (white triangles in Figure 2.1) (Hogarth et al., 2007; Le Dantec et

al., 2010). Finally, onshore segments of the Rose Canyon Fault left jog to the offshore La Jolla strand near the neighborhood of La Jolla in northern San Diego and create Mount Soledad, with approximately 150 m of uplift (Hogarth et al., 2007). The large antiform in Zone Two is in the shape of a structural dome, roughly egg-shaped, and approximately 2 km wide at the deepest point in the data volume. The structure is transpressional and coincident with left-stepping right-lateral segments between the Carlsbad Canyon strand and Camp Pendleton splay (Sahakian et al., 2017).

Strike-slip fault planes often transition into extensional fractures before terminating (Corbett et al., 1991) and despite the overall transpressional regime controlling the uplift of this antiform, two large fault segments bisect the middle of the antiform and display evidence of transtension including a negative flower structure also previously documented by Sahakian et al., (2017). Fault architecture provides further evidence of transtension at the antiform. Terminating fault segments from the northwest and from the southeast tend to curve around the eastern half of the antiform feature in a hook pattern similar to that observed in en-passant linkages observed at scale in loaded granite microcracks (Kranz, 1979). En-passant linkages occur when the stress field at the tip of a propagating fracture deflects the tip of an approaching fracture away from it. Both tips deflect around each other until each is removed from the influence of the other's stress field. Then the tips curve towards the opposite fracture and connect (Kranz, 1979; Corbett et al., 1991). En-passant fracture linkages tend to be associated with extension or transtension (Corbett et al., 1991).

The antiform creates a local bathymetric high in the area, which can be observed in profile in Figure 2.18. The relief on the seafloor in this region exhibits a 5-meter difference as shown between points B and B' in the profile. In fact, east of the bathymetric high, the seafloor dips slightly landwards towards the margin. The uplift and consequent bathymetric relief acts to divert offshore drainage flow to the north and south, around the main portion of the antiform structure. The bathymetry data show a lack of canyons and gullies on the slope to the west of the observed antiform (Figure 2.18). A lack of sedimentation due to diversion of drainage is further supported

by a shallow gravity core from the slope (BB 13-14; location shown in Figure 2.2). We discovered that this core contained extremely old sediments at only 40 cm depth.

The relatively undeformed reflectors with lower acoustic reflectivity observed to the east are recording sediments trapped against the eastern limb of the anticline (Figure 2.11). Given the thickness of the sediment overlying the highly deformed and faulted reflectors together with extrapolated sediment rates yields the onset of more recent faulting along this segment of the NIRC to be 560,000 to 575,000 years before present. Unfortunately, shallow penetration of cores contributes to a great deal of uncertainty into the extrapolated sedimentation rates and age of onset of faulting.

The sediment transport deflected to the north by the anticline is captured by two large drainage channels northwest of the antiform structure that incises the shelf edge (in Zone One). The main fault segment continues northwestward along the margin; however, several smaller fault segments appear to control these channels with right-lateral offset visible at the surface. A dendritic-shaped network of small channels accommodates flow diverted to the south by the large anticlinal structure. Typical dips of the seafloor along continental slopes are approximately 4-6°; however, at the location of the channels south of the anticline exhibits slopes along the shelf/slope break of 12-21°. This scarp is aligned with several fault segments striking parallel to the margin. The greatest slopes are observed at the toe of the slope (~ 25°) and are interpreted to be pop-up structures associated with left steps along right lateral fault segments.

Sahakian et al. (2017) noted that the NIRC segments in the vicinity of SONGS showed no displacement of the transgressive surface, consistent with our observations. Despite deformation recorded at the seafloor in the survey area, CHIRP data acquired over the large antiform at the widest part of the shelf shows large fault segments terminate very close to the transgressive surface, but no displacement of modern marine sediments were imaged (Figure 2.13).

In the acoustic amplitude data, paleochannel thalwegs were difficult to confidently identify; however, the uncertainty was reduced when the data were rendered using most negative

and most positive curvature seismic attributes (Figure 2.19). By coblending the two attributes paleochannels are enhanced in the time-slice view. Using these attributes, gullies extending to the base of the slope can be imaged down to 545 ms ( $\sim 446$  m), and traces of the largest off-shelf drainage channels are imaged in Zone One at depths down to 440 ms ( $\sim 355$  m). Reflectors tended to become chaotic with depth due to fault shear and possible fluid flow, so candidate paleochannels on the shelf could only be confidently imaged to a shallow depth, approximately 160 ms ( $\sim 124$  m). Chaotic reflections also made mapping of shelf thalwegs impractical and thus we were unable to confidently locate offset across mapped fault segments.

## **2.5.2 Seismicity and Through-going Rupture**

No large earthquakes have been recorded on any segment mapped in the survey area in the recent past; epicenters recorded since the 1930s for earthquakes greater than a M3.0 show a lack of recent activity along the San Onofre portion of the NIRC system (Figure 2.1) and a general gap in recent major seismicity along the entire fault system southwards into San Diego (Anderson et al., 1989). The area has experienced only low rates of microquake (M1.0-2.0) activity in recent times (Grant and Shearer, 2004). Large earthquakes, however, have been recorded near the fault system's endpoints. The most recent event is the  $M_L$  6.4 1933 Long Beach Earthquake, epicentered on the northern end of the system. At the time of that rupture, epicenters were not precisely known, and had to be calculated by hand based on seismogram and shake reports from the area (Hauksson and Gross, 1991). The most likely epicenter for the mainshock has been on a segment offshore of the city of Newport Beach. Conversely, in the southern onshore segments there have been no large seismic events on main segments of the system since the founding of Mission San Diego in 1769 but trenching surveys in San Diego show a surface rupture, dated at AD  $1650 \pm 120$  years, which caused 2-3 m of slip (Lindvall and Rockwell, 1995; Rockwell, 2010).

Magnitude tends to scale with fault length and recent modeling of an end-to-end rupture of the offshore segments from La Jolla cove to Newport Beach system could potentially generate a M7.3 earthquake (Sahakian et al., 2017; Wells and Coppersmith, 1994). In the 3D volume, mapped step-over widths between fault segments are mostly equal to or less than 1 km. Wesnousky (2006) observed that there was a high likelihood of through-going rupture between fault segments when step-over distances were 3 km or less (Wesnousky, 2006; Biasi and Wesnousky, 2016). This suggests that all the segments mapped in our survey area, along with segments from north of Carlsbad Canyon (south of the survey area) and onshore segments north of the survey area, could rupture together in a single event (Singleton et al., 2019). The largest step-over in the survey area is associated with the large anticline observed in Zone Two. This structure would likely not inhibit through-going rupture based on step-over width alone.

## **2.6 Conclusions**

High-resolution 3D P-Cable seismic reflection data provide unprecedented imaging of fault segments off the coast of San Onofre, California. Such imagery allows us to define how fault segments interact laterally and at depth and the importance of small stepovers and secondary fault splays in how deformation is communicated to neighboring faults. Understanding fault-fold deformation by peeling back a combination of crosslines, inlines, and arbitrary lines for a given time slice, as well as observing sequences of time slices and horizons provides for a true 3D examination of deformation features. Interactions between individual segments of the NIRC have been imaged at the scale of deformation and have revealed the curvilinear character of many of the fault segments on this system.

Based on fault orientation and acoustic reflectivity, the data volume has been divided into three zones, with the northerly most two zones having more continuous reflectivity. Zone Three

to the south is characterized by transparent to chaotic semi-transparent acoustic reflectivity. In Zone Two, the faults are oriented in a more northwest azimuth engendering transpression and the consequent anticline.

Zone One illustrates the marked variability in acoustic reflectivity that appears to be post-depositional in nature and is associated with intense shear deformation and/or fluid flow. Along the eastern portion of Zone One, the data volume images the transition from a monocline, into a fold, and finally into a fault in response to small changes in fault orientation and secondary fault splays. The consequent deformation created a "cusped" geometry in the acoustic reflectivity patterns in the time slice with the "horns" being anticlines.

The large anticline observed in Zone Two traps sediments to the east, which creates a 10 km wide shelf in this region. The anticline has bathymetric expression diverting drainage to the north and south. Fault-controlled canyons that incise the shelf edge capture the northward-deflected flow. Thickness of trapped sediments to the east of the anticline suggests that the deformation of the NIRC fault system in region began 560,000 to 575,000 years before present. Age estimates from shallow penetration core data were used to extrapolate sedimentation rates, which introduced uncertainty in age estimates for the onset of deformation in this region. Future well sampling and/or longer cores are necessary to properly constrain the age and magnitude of deformation in the region.

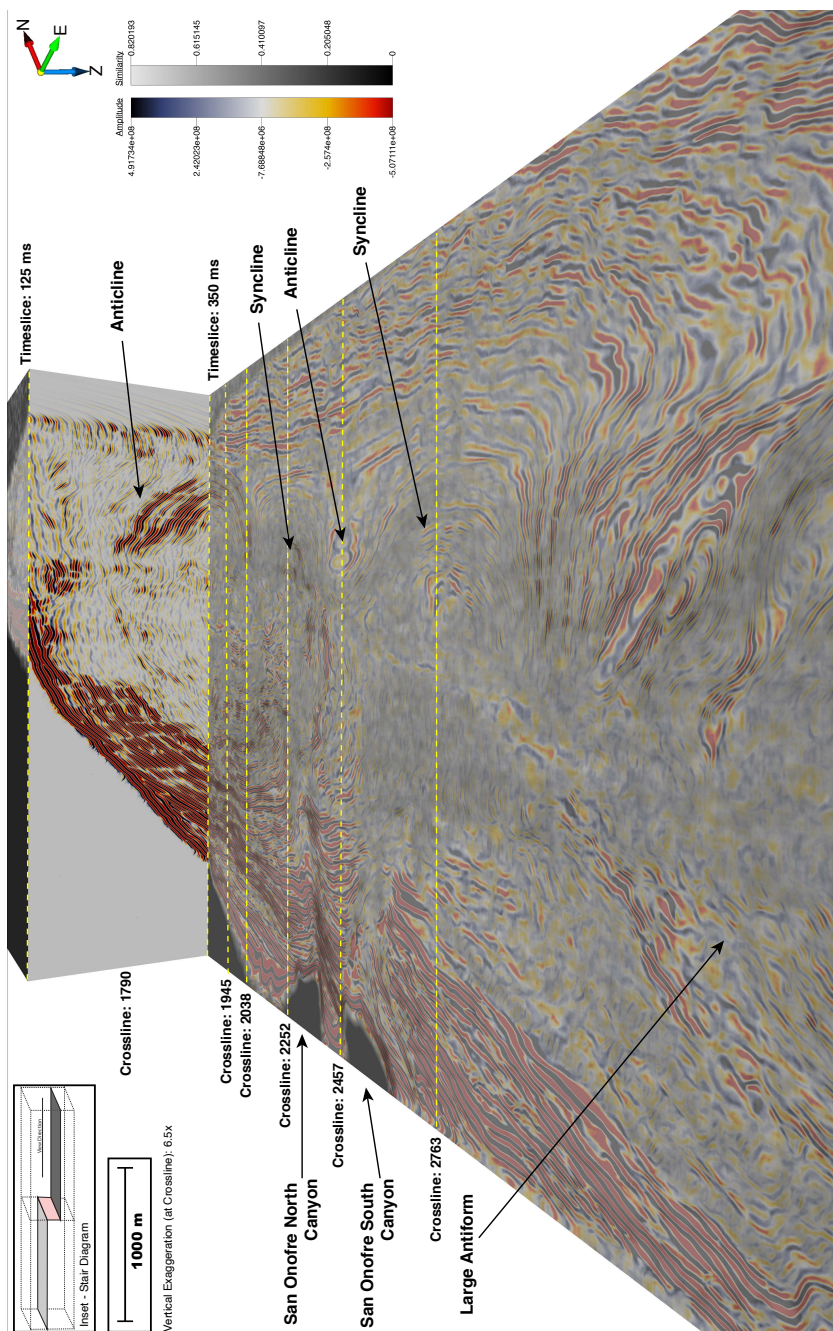
Finally, the main strands of the NIRC fault system bound a large acoustically transparent region in Zone Three. This transparent region appears to be bounded by large fault segments suggesting the transparent region may be caused by complex shear zone. Several duplex structures are observed partitioning strain and causing compression with resulting pressure ridges.



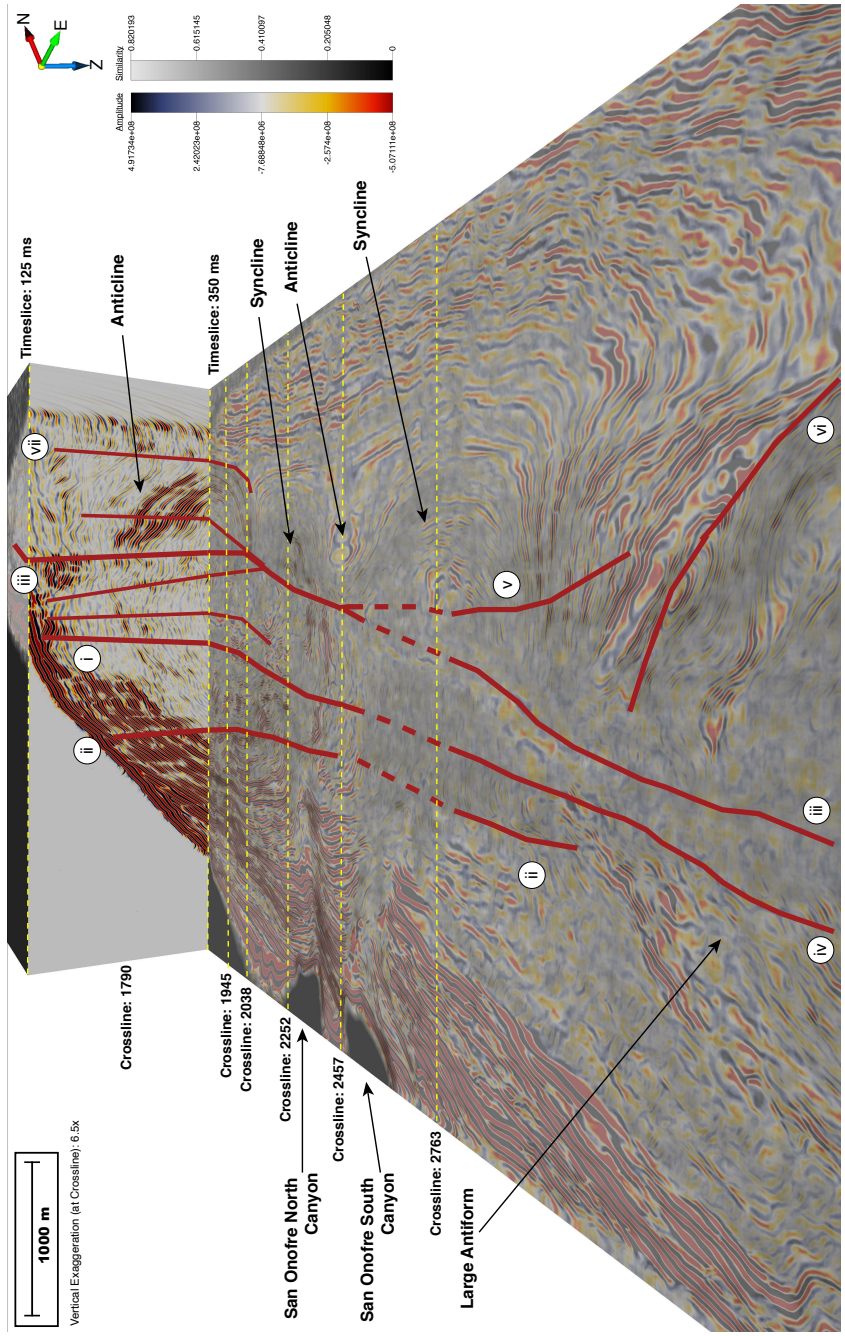
## 2.7 Acknowledgments

The authors wish to acknowledge the assistance of Mike Barth of Subseas Systems, the sailing and science crews of the R/V New Horizon (NH1320, and NH1323) and R/V Thomas G. Thompson (TN336), Geotrace Technologies, and NCS Subsea, Inc. for their roles in data acquisition and processing. Our thanks in particular to Hector Perea and an anonymous reviewer who provided valuable input on enhancing and clarifying an early version of the manuscript. Funding for this research was provided by a grant from Southern California Edison funded through the California Public Utility Commission (CPUC). Figures were generated using Generic Mapping Tools, version 5 (Wessel et al., 2013), Kingdom Suite 2018 (IHS Markit), OpendTect (dGB Earth Sciences), and Fledermaus (QPS B.V.). Cruise information for NH1320 (2D MCS; <https://doi.org/10.7284/902996>), NH1323 (3D P-Cable MCS; <https://doi.org/10.7284/903024>), and TN336 (Coring; <https://doi.org/10.7284/906644>) are accessible via the Rolling Deck to Repository (R2R) web interface. Seismic data are archived with Marine Geoscience Data System repository.

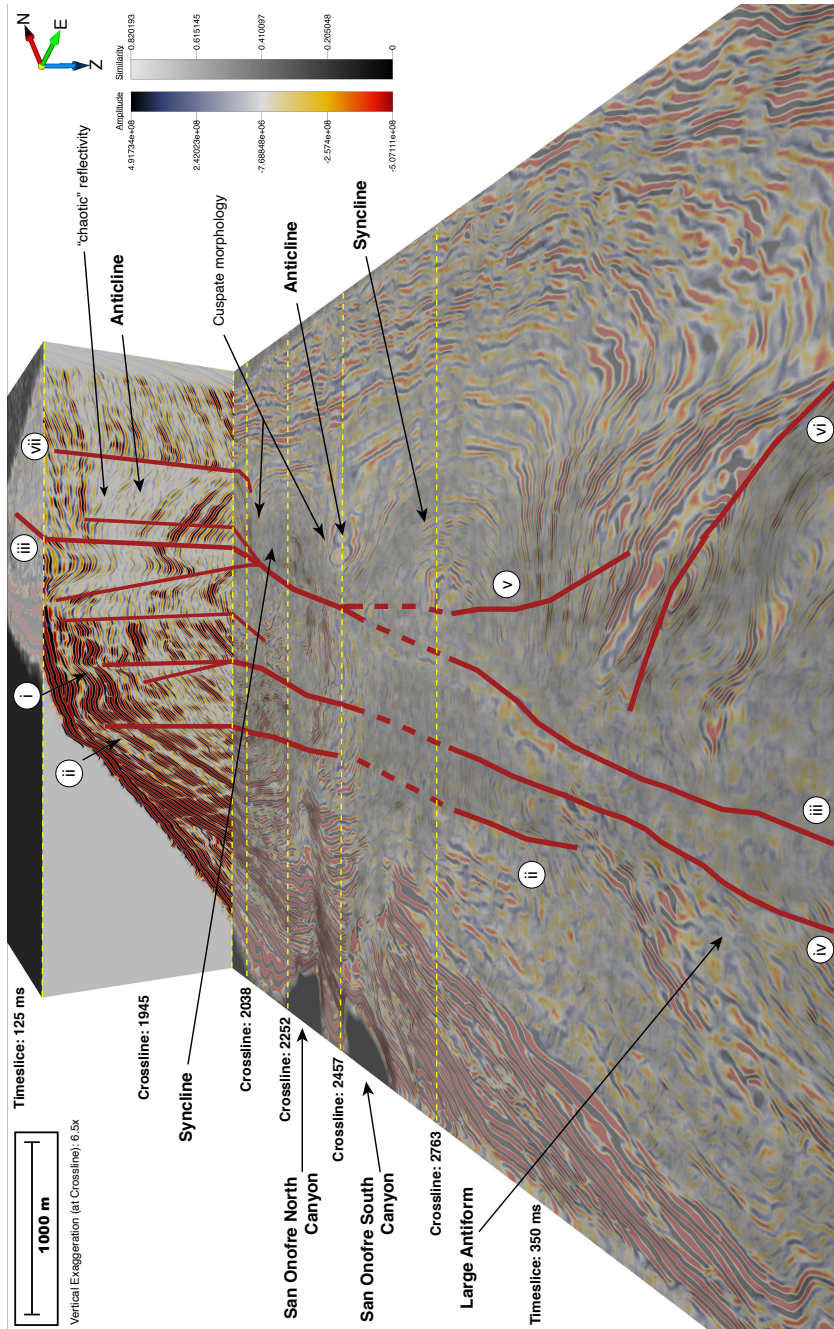
This work has been submitted for publication in: **Holmes, J.J., Driscoll, N.W., and Kent, G.M., In Review. High-Resolution 3D Seismic Imaging of Fault Interaction and Deformation Offshore San Onofre, California. *Journal of Geophysical Research: Solid Earth*.** The dissertation author was the primary researcher and author, and the co-authors listed in this publication directed and supervised the research.



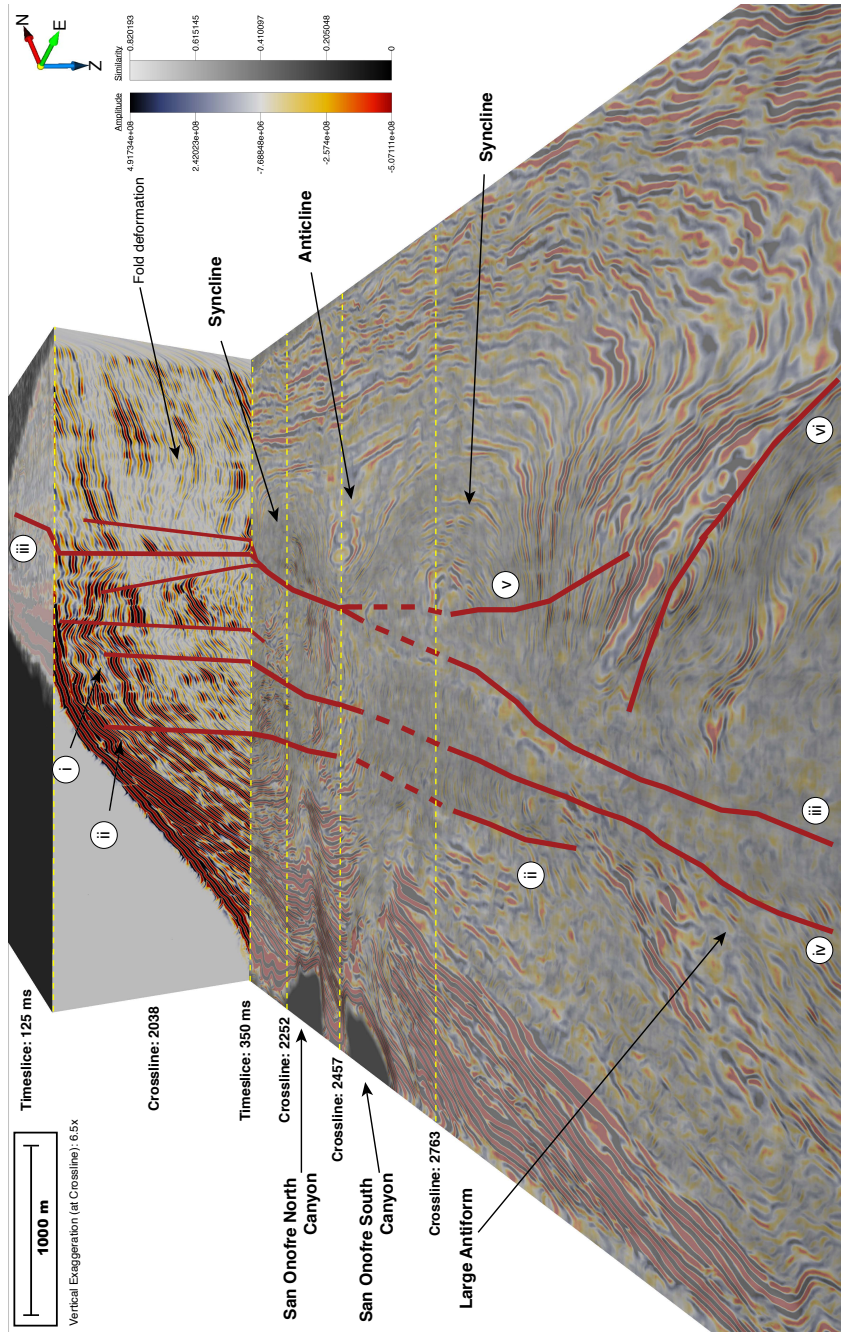
**Figure 2.4:** Uninterpreted stair diagram showing crossline 1790 in vertical profile with reflectors in amplitude display. Location of the crossline, relative to the survey area, is shown in Figure 2.1. All crosslines shown in stair diagrams are bounded by timeslices at 125 ms, and 350 ms. Both timeslices for all stair diagrams in Figures 2.4-2.11, 2.14 & 2.15 are rendered using a combination of similarity data and amplitude data at 60% transparency. View direction is towards the northwest. Color scales are displayed for both amplitude and similarity seismic attributes. Yellow dashed lines show locations of crosslines shown in other figures. Black areas in the southwest part of the lower timeslice represent shelf incisions from channelization. (Inset) Schematic view of data volume depicting view angle of stair diagrams used in this paper.



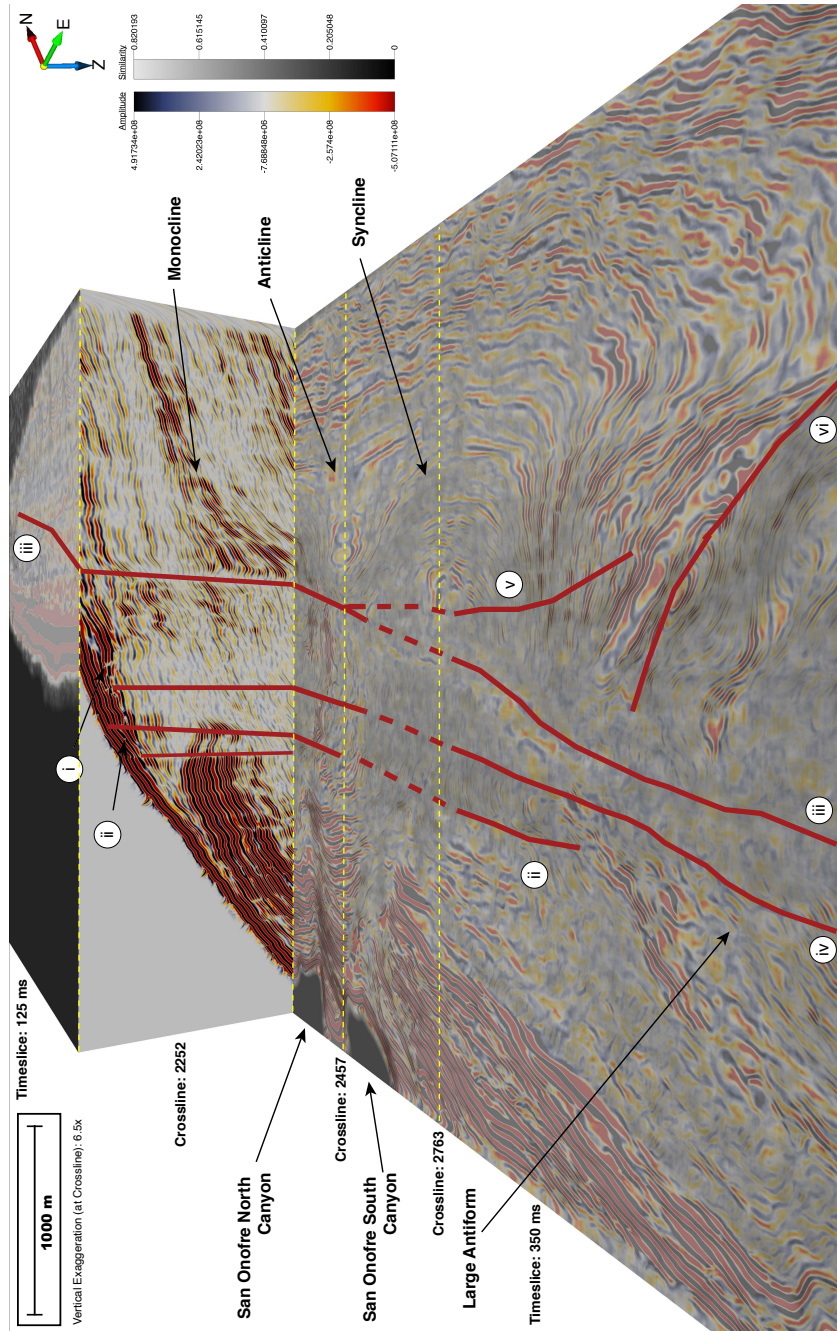
**Figure 2.5:** Stair diagram of crossline 1790 showing fault interpretations in solid red. Location relative to the survey area, is shown in Figure 2.1. Thick lines denote major fault segments i, ii, and iii. Thin lines denote secondary fault systems no; faults are dashed in the lower (350 ms) timeslice, where there is more uncertainty. Alternating anticline/syncline sequence can be observed in the lower timeslice. The outline of a large structural dome, labeled as a large antiform, is observed towards the bottom of the figure in the lower timeslice.



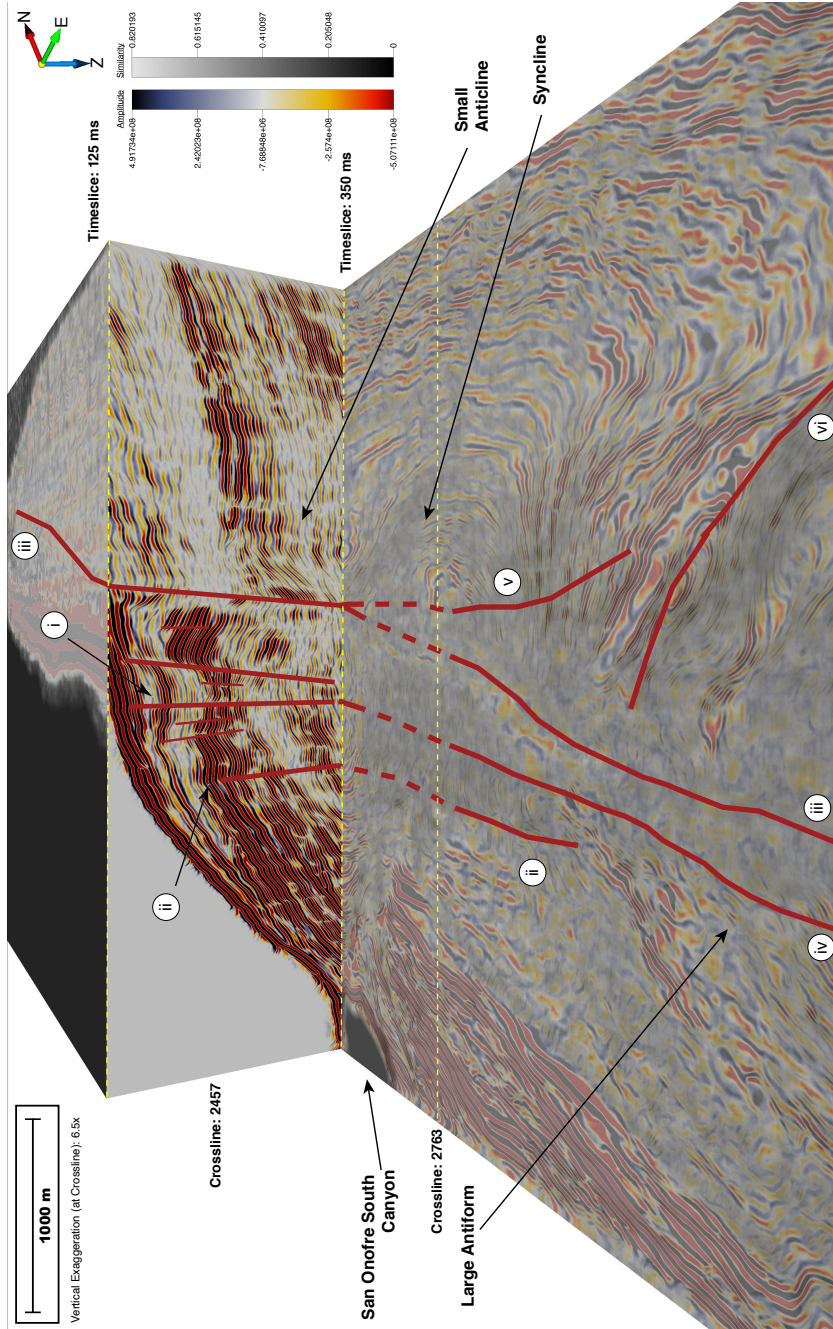
**Figure 2.6:** Stair diagram of crossline 1945 with interpreted faults displayed using solid red lines. Location relative to the survey area, is shown in Figure 2.1. Fault interpretations with more uncertainty are shown as dashed red lines in lower (350 ms) timeslice. Much of the minor faulting and deformation shown is bounded between fault segments ii and iii along the outer shelf edge. In the crossline, deformation between fault segments iii and vii is narrower than in Figure 2.5, as the plane of fault segment viii moves closer to splays of segment iii. Segment iii represents the main fault plane and is the only plane shown that extends upwards past the upper (125 ms) timeslice.



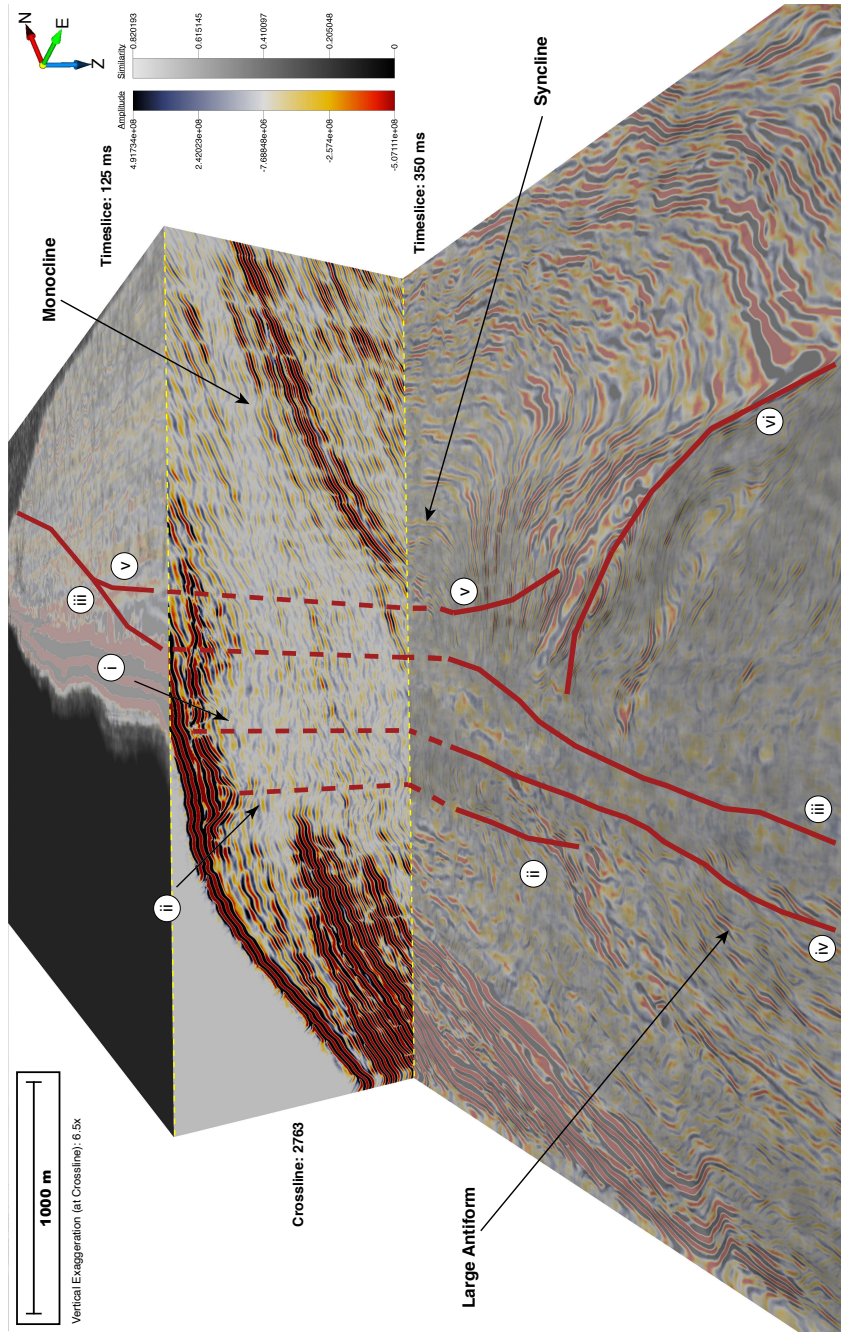
**Figure 2.7:** Stair diagram of crossline 2038 with interpreted faults shown with solid red lines. Location relative to the survey area, is shown in Figure 2.1. Faults are dashed where there is acoustic transparency, which introduces uncertainty. Fault plane of segment vii has terminated and been replaced with fold deformation. Sediment from northeast is laminar and acoustically transparent until fault segment iii. Reflector amplitude is visibly more prominent on southwestern side of segment iii.



**Figure 2.8:** Interpreted stair diagram of crossline 2252. Fault interpretations shown with solid red lines; dashed where interpretations have more uncertainty. Fault fold shown in Figure 2.7 has been replaced by a monocline terminating at fault segment iii. Yellow dashed lines in lower (350 ms) timeslice represent locations of crosslines shown in other figures. Location relative to the survey area, is shown in Figure 2.1.

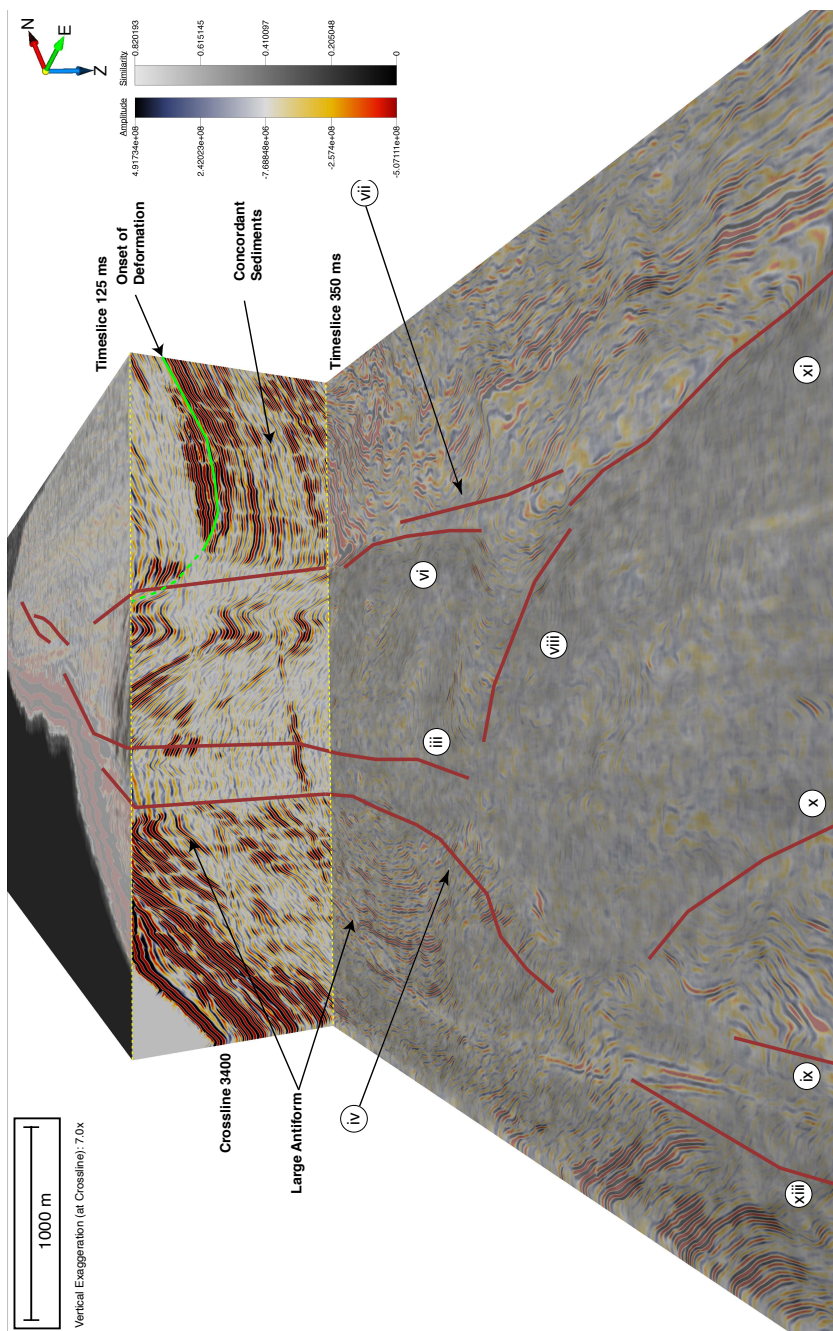


**Figure 2.9:** Stair diagram of crossline 2457. Crossline is rendered in amplitudes and shows a seismic cross-section very near San Onofre South Canyon, and north of large antiform structure. Acoustic and deformation character both visibly changes on either side of fault segment iii. Yellow dashed line shows location of crossline 2763.

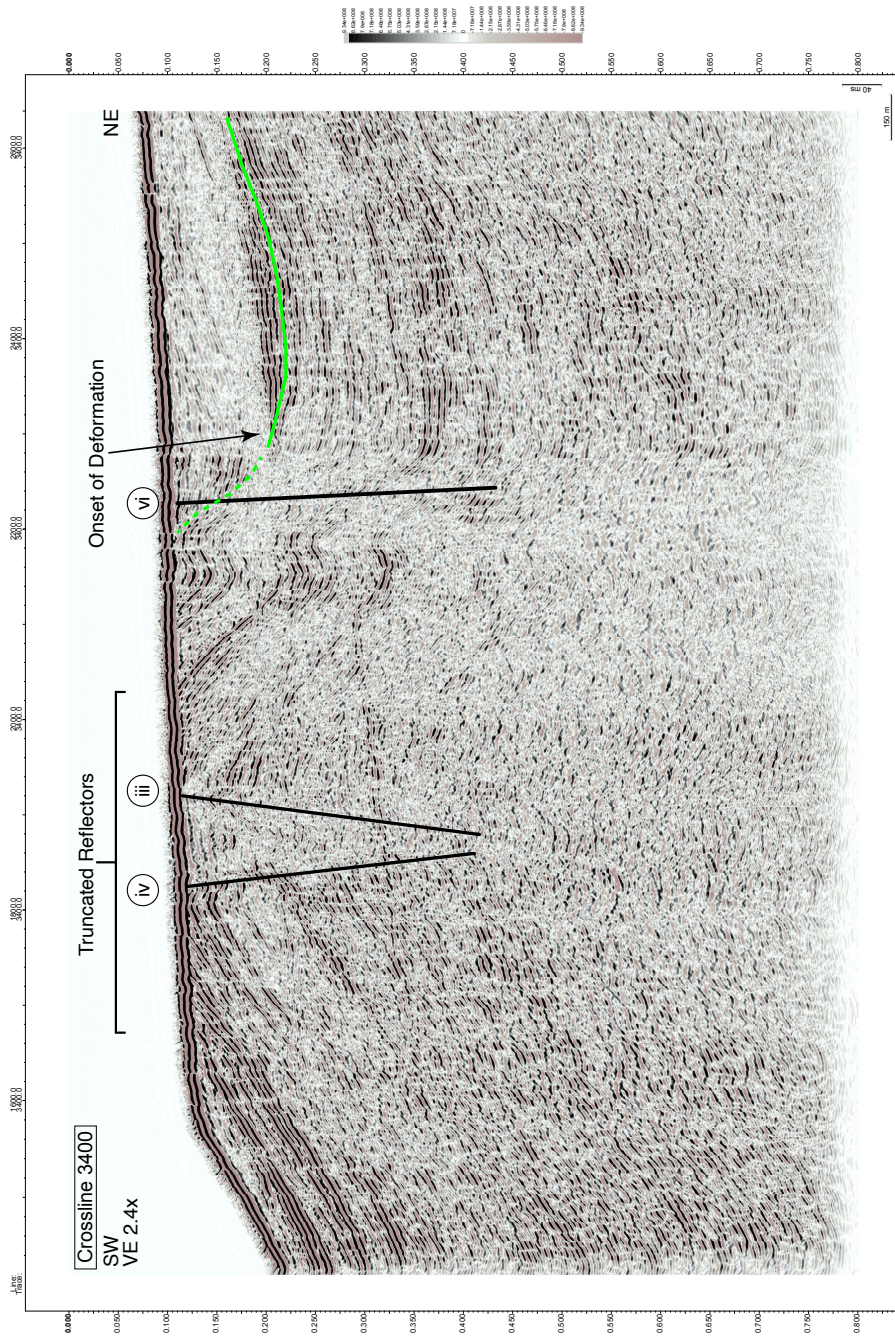


**Figure 2.10:** Stair diagram of crossline 2038 with interpreted faults shown with solid red lines. Location relative to the survey area, is shown in Figure 2.1. Faults are dashed where there is acoustic transparency, which introduces uncertainty. Fault plane of segment vii has terminated and been replaced with fold deformation. Sediment from northeast is laminar and acoustically transparent until fault segment iii. Reflector amplitude is visibly more prominent on southwestern side of segment iii.

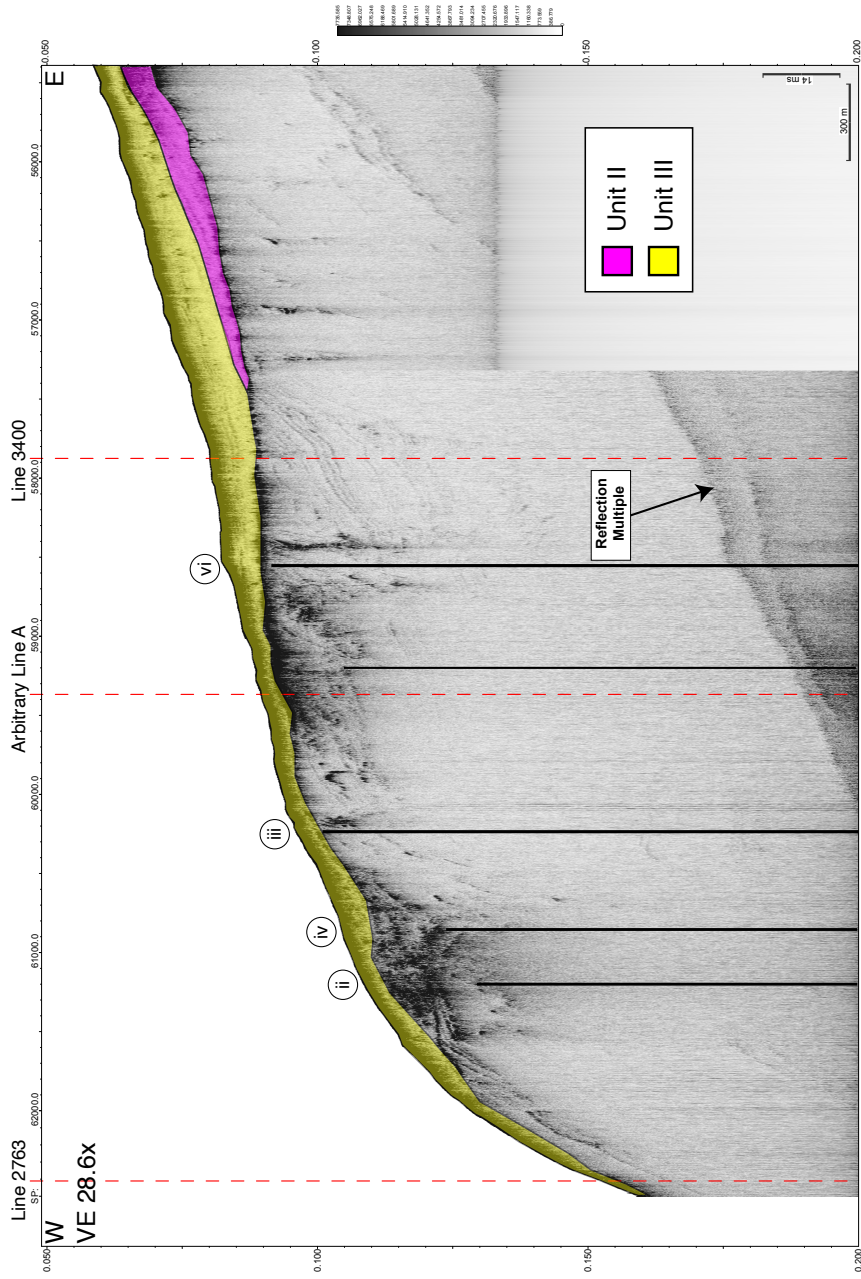




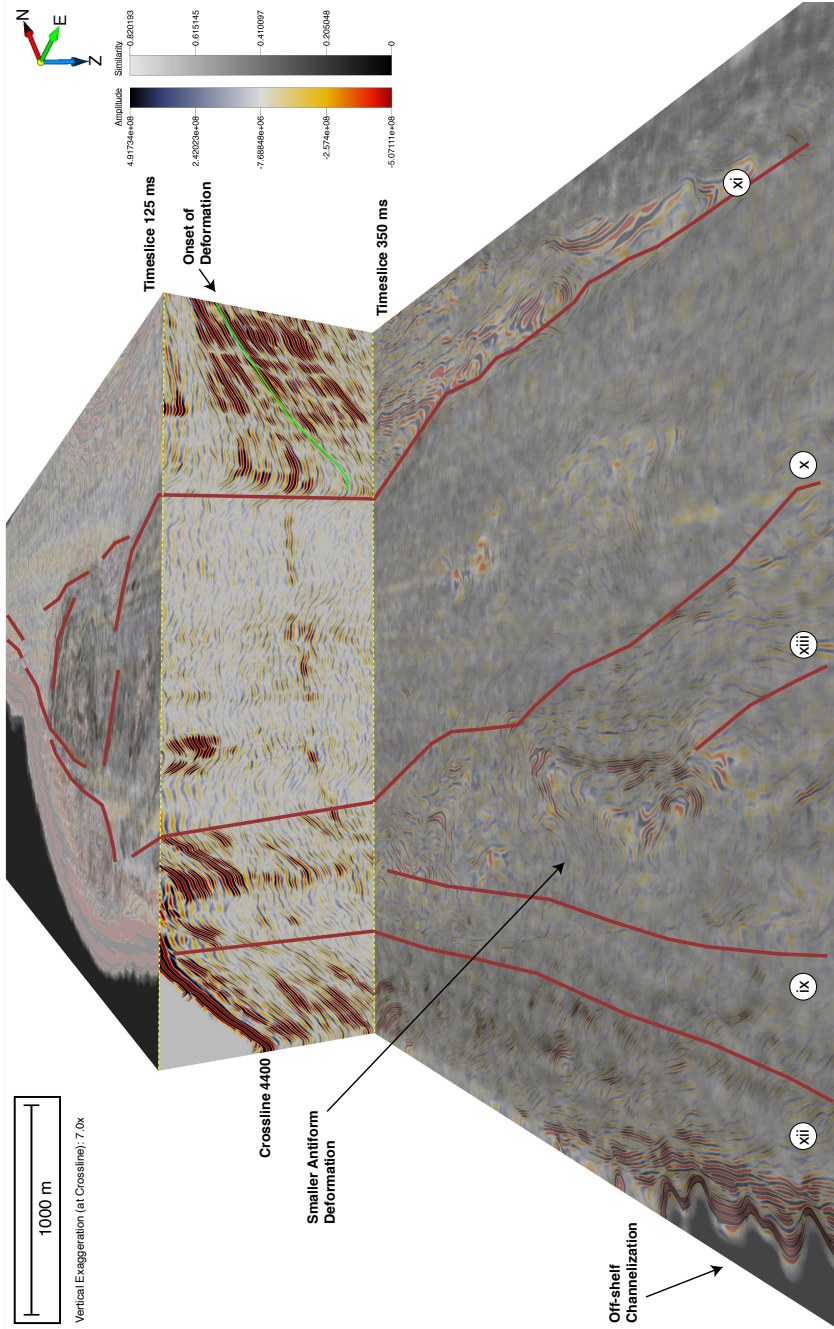
**Figure 2.11:** Interpreted stair diagram of Crossline 3400 bounded by timeslices at 125 ms, and 350 ms. Timeslices are displayed as a combination of similarity data and amplitude data at 60% transparency. Major fault segments are labeled. This crossline cuts through the middle of the large anticline structure observed in Zone Two of the survey area. Lower timeslice shows fault segments delineating an acoustically transparent to semi-transparent region in the middle of the timeslice. Note some of the faults exhibit a more northwesterly trend in this region. Solid green line delineates stratigraphic horizon recording the onset of deformation (lowest depth is 200 ms or ~ 156 m). Dashed green line shown where horizon is inferred. Locations of seismic lines are shown in Figure 2.1.



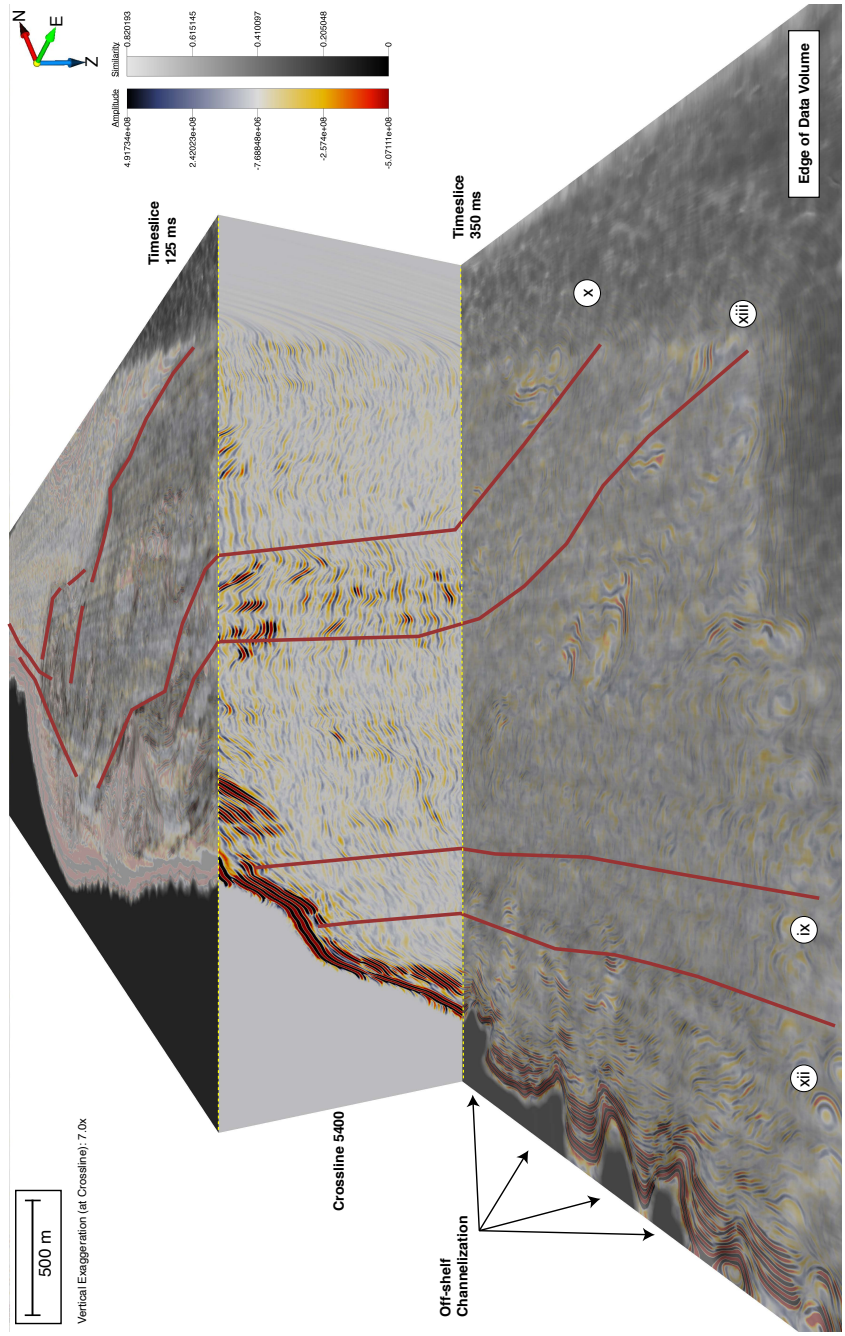
**Figure 2.12:** Vertical seismic profile of crossline 3400 from full record length, 0 to 800 ms (~ 679 m) depth, with interpretations. View is from southwest to northeast. Data shown are amplitude reflectors. Color has been desaturated for ease of interpretation. Major fault segments are labeled. Reflectors of large antiform are truncated at the seafloor. Solid green line marks stratigraphic horizon that tracks the onset of deformation (lowest depth is 200 ms), where dashed interpretation is more uncertain.



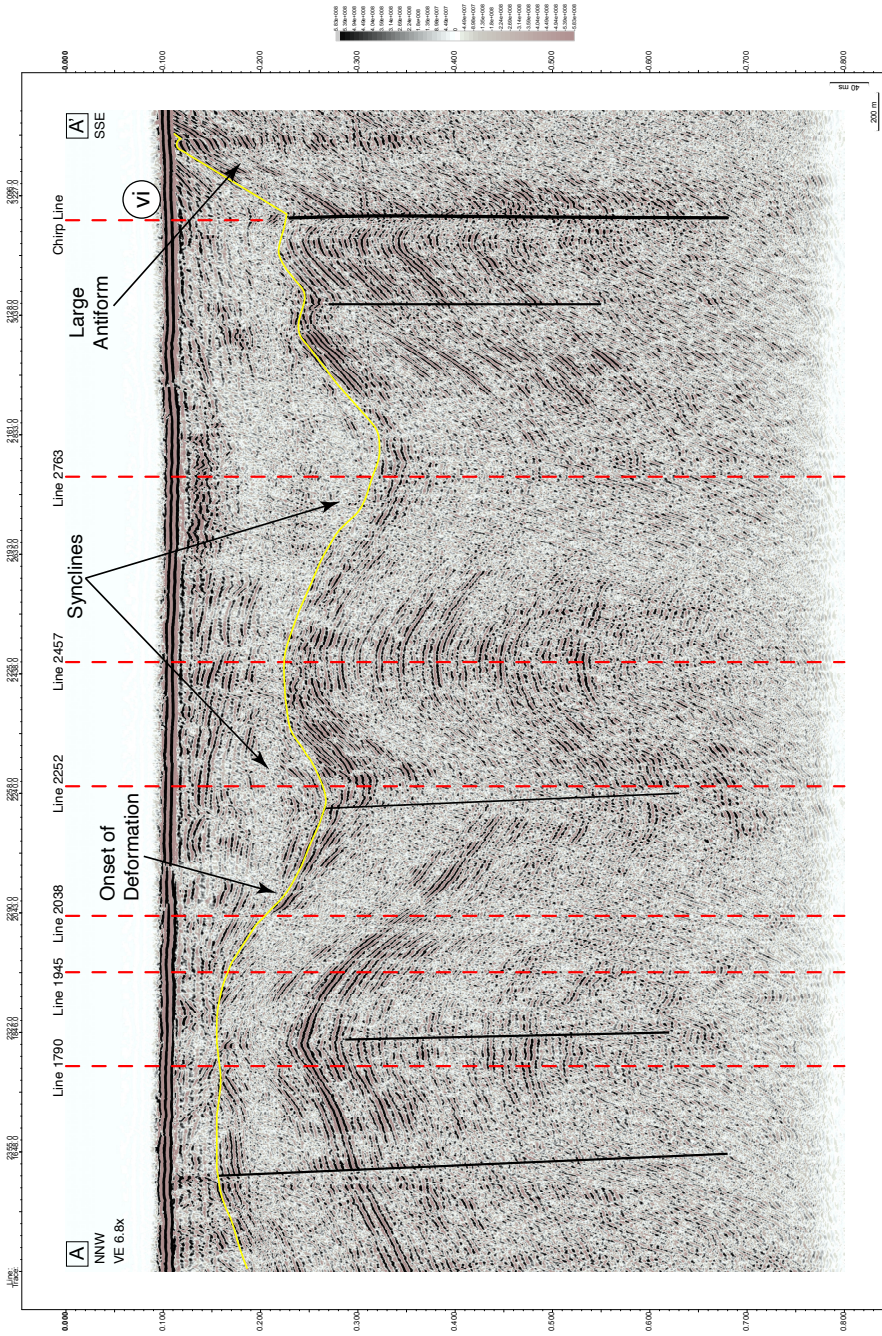
**Figure 2.13:** CHIRP seismic profile from 50 to 200 ms (~ 38 – 156 m) depth. Red dashed vertical lines show locations of other crosslines and arbitrary line. Major faults shown in black are labeled. Mapped units II and III are correlated to interpretations published by Klotsko et al., 2015. Multiple is labeled.



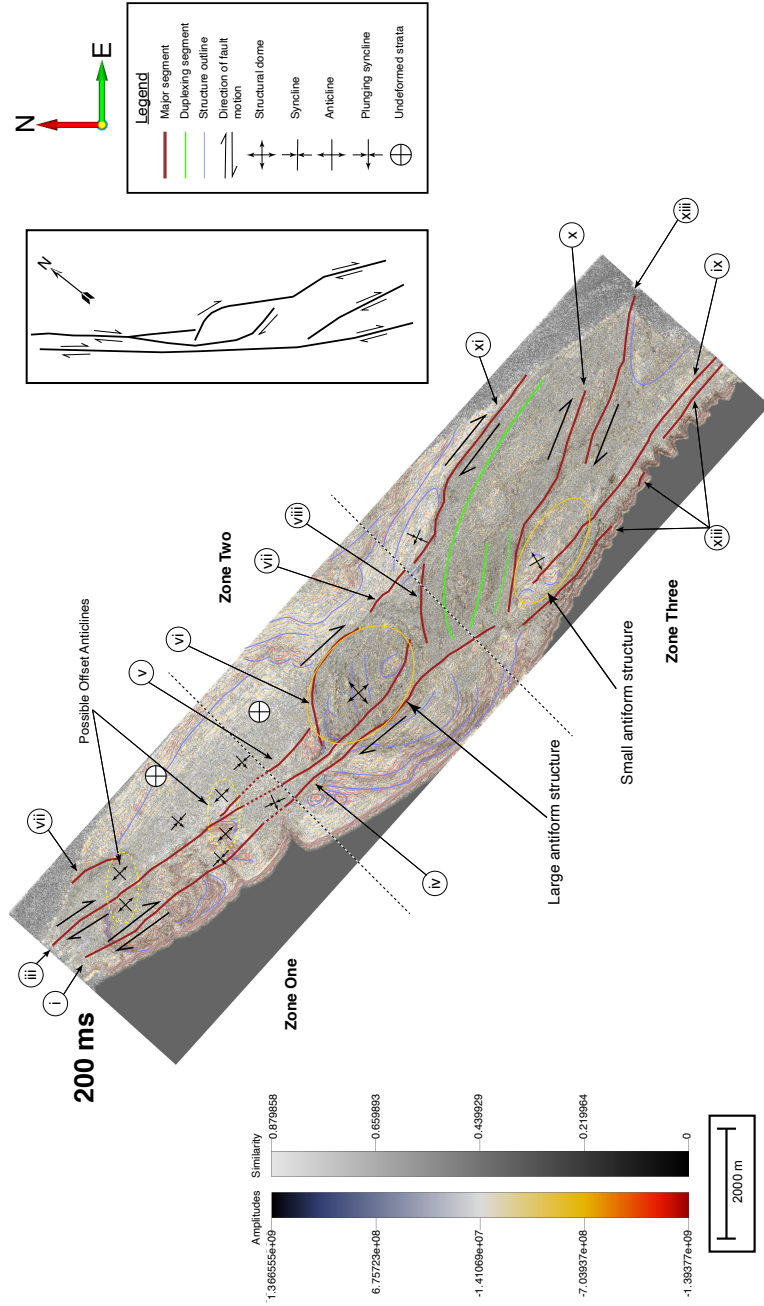
**Figure 2.14:** Interpreted stair diagram of Crossline 4400 with major fault segments labeled. Crossline is bounded by timeslices at 125 ms and 350 ms ( $\sim 96$  m and  $\sim 279$  m), rendered using similarity data combined with amplitude data at 60% transparency. A smaller anticline is observed in the lower (350 ms) timeslice west of fault segment x. Note the monocline in the crossline north of fault segment xi. Green line traces stratigraphic horizon that records onset of deformation. Locations of seismic lines are shown in Figure 2.1.



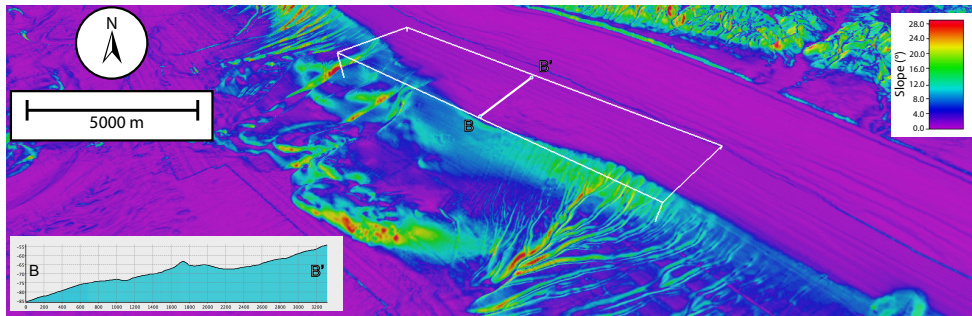
**Figure 2.15:** Interpreted stair diagram of Crossline 5400 bounded by timeslices at 125 ms and 350 ms (~ 96 m and ~ 279 m). Timeslices are similarity reflectors combined with amplitude seismic attribute at 60% transparency. Major fault segments are labeled. The timeslice and crosslines have an acoustically transparent character, which makes it difficult to identify the faults in this region and are projected from adjacent lines in the data volume. Locations of seismic lines are shown in Figure 2.1.



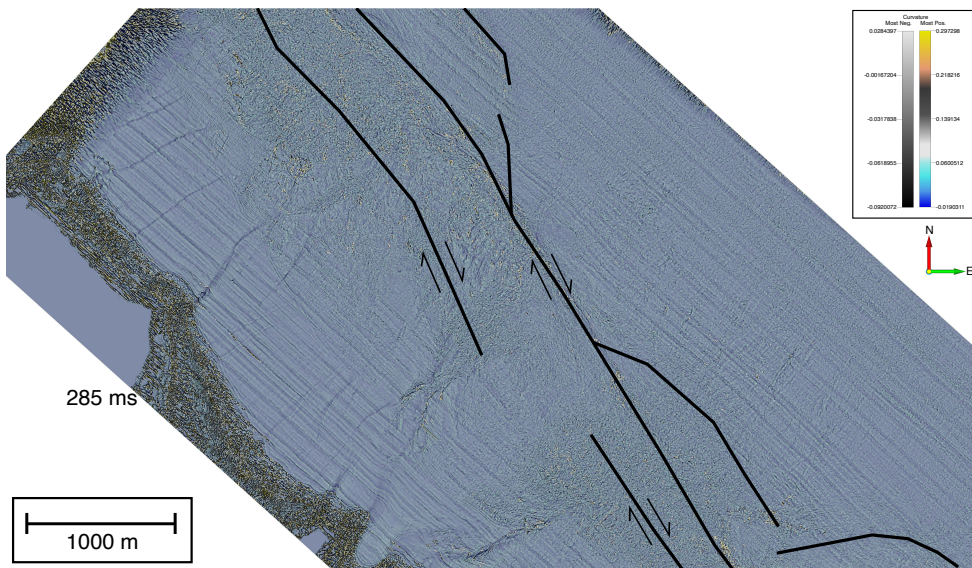
**Figure 2.16:** Interpreted arbitrary line across northern section of survey are from A to A'. Location of seismic line is shown in Figure 2.1. Minor faults are shown with thin black lines. Major faults are shown with thick black lines and labeled. The view is to the northeast, towards the coastline. Reflector color has been desaturated for ease of interpretation. Red dashed lines trace locations of crosslines shown in previous figures. A sequence of anticlines and synclines is imaged across the arbitrary line, terminating at the northern limb of the large mid-shelf antiform structure (labeled).



**Figure 2.17:** Map view of timeslice 200 ms (~ 156 m) showing major fault interpretations and right-lateral movement. Timeslice is a combination of amplitude data, overlapped with similarity attribute data at 60% transparency. The survey area is divided into three zones based on fault character and acoustic facies. Solid yellow ovals outline area of large and small anticlines in Zones Two and Three. In Zone One an alternating sequence of anticlines and synclines is imaged. Dashed yellow ovals group possible offset anticlines. Green lines denote possible duplex faulting. Light purple lines outline structures and patterns in the amplitude data. Inset shows a simplified kinematic diagram of the major faults in the survey area.



**Figure 2.18:** Oblique view of continental shelf and slope bathymetry off the coast of San Onofre and San Clemente, showing location of survey in white 3D box. Colors denote slope angle. Inset shows slope along an arbitrary cross-section from B to B' passing through large antiform coincident with widest part of the shelf.



**Figure 2.19:** Detail map view of Zone One using an interpreted timeslice at 285 ms (~ 225 m). Fault segment interpretations are shown as solid black lines. North is towards the top of the Figure. Timeslice is rendered using coblended Most Negative and Most Positive Curvature seismic attributes to enhance paleochannel identification.



# Chapter 3

## Strike-slip Transpressional Uplift Offshore San Onofre, California Inhibits Sediment Delivery to the Deep Sea

### 3.1 Abstract

The Inner California Borderlands is a complex margin where sediment delivery to the basin floor is largely routed through canyon-channel-gully systems. Using nested geophysical surveys, piston and gravity cores from the Eastern Gulf of Santa Catalina, this study compares two canyon systems and investigates how tectonics, shelf width, gradient, and autogenic processes influence turbidite emplacement timing and grain size. One end-member canyon is the Dana Point Canyon, which is  $\sim 2$  km from the San Juan Creek drainage and has a concave-up channel profile. The other endmember system consists of the San Onofre North and South (SON and SOS) canyons that are detached from San Mateo Creek by a wide 10 km shelf and they traverse a tectonically-deformed slope with multiple ponded basins. Radiocarbon ages sampled from 8 cores reveal that turbidite deposition at Dana Point persists during the sea-level lowstand of Marine Iso-

tope Stage (MIS) 2 through the subsequent transgression and highstand. On the contrary, turbidite emplacement adjacent to the SON and SOS canyons occurs mostly during MIS 2 and ceases around 8 ka. The main regional control on turbidite timing is the wide shelf adjacent to the SON and SOS canyons that is formed by a broad uplifted anticline. This anticline separates the SON and SOS canyons from a riverine source during the sea-level transgression. Much of the tectonic deformation offshore of San Onofre was created by transpression along the right-lateral Newport Inglewood-Rose Canyon Fault Zone. Second-order controls on local turbidite emplacement include small synclines and anticlines that form ponded basins and accommodate deformation on the San Mateo Fault Zone. These basins engender deposition and intervening steep slopes promote sediment bypass. Complex bathymetry offshore San Onofre also affects channel gradient by either accelerating or decelerating flow. Turbidity flow dynamics modified by gradient changes offshore of San Onofre have the ability to modulate channel architecture and grain size. The implications of this work are that tectonically-deformed morphology complicates the timing of turbidite emplacement throughout a sea level cycle and the interpretation of turbidites as paleoseismic records in such regions.

## **3.2 Introduction**

Studying submarine channels has both societal and scientific relevance. Not only do they serve as conduits for terrigenous material across margins to the deep sea (Allen, 2008), but fan deposits at the base of the submarine channels can serve as significant hydrocarbon reservoirs when filled with sand- or silt-prone sequences (Mayall and Stewart, 2000; Stow and Mayall, 2000; Pettingill and Weimer, 2002; Mayall et al., 2006). Large catastrophic flows through channels in the eastern Gulf of Santa Catalina (GoSC) can be a significant geohazard to marine infrastructure (Paull et al., 2003; Xu et al., 2010). For these reasons, it is important to understand

the evolutionary processes that shape channel morphology and stacking patterns through time in sedimentary basins.

The Inner California Borderlands (ICB) is a complex, tectonically active margin that is characterized by narrow continental shelves dissected by numerous canyon-channel systems (Normark et al., 2009). As distances between river mouths and canyon heads are short, the ICB is an ideal place to study source-to-sink processes and sediment routing (Normark et al., 2009; Covault et al., 2010; Romans et al., 2016). Sediment flux to submarine canyons can occur either as particles that settle out of suspension or flows that move downslope as turbidites. Turbidity currents can transport large quantities of sediment (Talling et al., 2007); nevertheless, they have not been observed to traverse entire submarine canyon-channel systems (Symons et al., 2017; Fildani et al., 2017). Plausible triggers for turbidity currents include river floods, storm events, tsunami wave loading, sediment loading, internal tides, and earthquakes (Goldfinger et al., 2007; Xu et al., 2010). Storm waves can rework shelf sediment and advect it to canyon heads as a turbid layer in the Hueneme and Mugu Canyons (Xu et al., 2010). Since multiple causes are capable of producing turbidites, it can be difficult to distinguish seismo-turbidites from those produced by tsunamis, storms, and sediment loading. Some studies have argued that seismo-turbidites can be distinguished by wide areal extent, multiple coarse-fraction pulses, variable mineralogical provenance, greater depositional mass, and coarser texture than the storm-generated events (Nakajima and Kanai, 2000; Goldfinger et al., 2007; Goldfinger, 2011). Other studies cite concerns for using turbidites as records of paleoseismic activity, as geologic dating lacks the time resolution to determine whether a fault ruptured as a whole or whether it ruptured in segments over a time period of days, years, or even decades (Nelson et al., 1995; Atwater et al., 2014). Furthermore, Sumner et al. (2013) and Atwater et al. (2014) have discussed uncertainties with methods used to evaluate paleoseismic deposits, such as the confluence test (Goldfinger et al., 2003), synchronous turbidite deposition in multiple basins (Gracia et al., 2010), large turbidite volumes (Talling et al., 2007), and correlating turbidites to historically recorded earthquakes (Sumner et al., 2013).

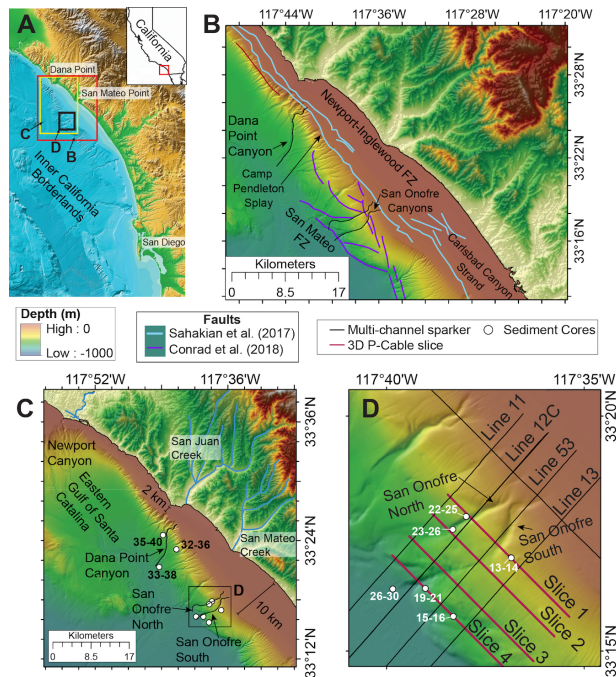
As such, there is still debate as to whether deep-sea turbidites are reliable paleo-seismometers (Sumner et al., 2013; Atwater et al., 2014). As the ICB is tectonically active, turbidite records have the potential to provide insight on past earthquake activity; nevertheless, this study finds that tectonically-controlled morphology dominates the turbidite depositional record and hinders our ability to tease out morphologic signals from past earthquake activity.

In addition to hydrodynamic regimes, morphologic factors such as bathymetry, shelf width, and ponded basins may exert important controls on sediment flux to canyons (Xu et al., 2010; Damuth and Olson, 2015). Factors such as distance from a river source and shelf width may change throughout sea-level cycles. Sequence stratigraphic models predict that the greatest delivery of sediment to canyons and basin floor occurs during sea-level lowstands when rivers deposit directly into the canyon-channel system (e.g., Vail et al., 1977; Mitchum, 1985; Posamentier et al., 1991). Nonetheless, many recent studies have proposed that sea-level is subordinate to the distance between the canyon head and shoreline (Covault et al., 2010; Blum et al., 2013; Gamberi et al., 2015) and proposed that distances  $< 5$  km result in canyons characterized by active sand transport (Sweet and Blum, 2016). In addition, secondary factors can exert controls on sediment flux to the deep sea, including strength and location of littoral cells and the presence of shelf clinothemms that sequester sediment (Sweet and Blum, 2016). Ponded basins may serve as local depocenters that trap flow deposits (Prather et al., 1998; Damuth and Olson, 2015). Tectonic deformation likely plays a role in the morphology of submarine canyons, as canyon trends have been documented to follow trends in bathymetry caused by intraslope basins and diapirs (Damuth, 1994; Damuth and Olson, 2015; Qin et al., 2019).

This study area was chosen to evaluate the controls of tectonically-controlled wide shelves and ponded basins on canyon-channel sedimentation, as architecture of the Newport-Inglewood/Rose Canyon fault zone has been characterized by recent studies (Klotsko et al., 2015; Maloney et al., 2016; Sahakian et al., 2017). Furthermore, this study fills a gap in existing knowledge about submarine canyons in the Eastern GoSC, as the Newport, Oceanside, Carlsbad,

and La Jolla canyon-channel systems have been studied extensively by Covault et al., (2007; 2011) and Normark et al. (2009). This study presents extensive seismic surveys, sediment cores, and radiocarbon ages from this region and focuses on the San Onofre North (SON) and South (SOS) canyon-channel systems. While much of the ICB margin, such as the shelf offshore of Dana Point, has widths  $\sim 2$  km, the shelf offshore of San Onofre has a maximum width  $\sim 10$  km (Fig. 3.1C). By comparing the Dana Point to the SON and SOS canyon-channel systems, the overarching goal of this research is to test the hypothesis that the wide shelf exerts the largest control on the timing of turbidite emplacement to the deep basins. Additionally, this study investigates the role of secondary controls such as across-margin deformation and changes in gradient on depositional timing.

The main findings of this study are that Dana Point Canyon has remained active during lowstands, transgressions, and highstands in sea-level due to its short  $\sim 2$  km connection to San Juan Creek with less tectonic deformation along this portion of the margin. In contrast, the SON and SOS canyon-channel systems are complicated by jogs on the right-lateral strike-slip Newport-Inglewood/Rose Canyon (NIRC) Fault that create broad anticline uplift (Klotsko et al., 2015; Sahakian et al., 2017). Smaller-scale anticlines and synclines in the across-margin direction may be deformed by crosscutting faults in the San Mateo Fault Zone (Conrad et al., 2018). Much of this deformation pre-dates post-glacial sediment deposition (Sahakian et al., 2017; Conrad et al., 2018). The broad along-margin anticline widens the shelf, which in turn caused sand delivery to the slope to cease around 8 ka during the last sea-level transgression. Most of the sand delivery to the deep offshore San Onofre occurred during sea-level lowstands such as Marine Isotope Stage (MIS) 2.



**Figure 3.1:** A) The Inner California Borderlands (ICB) is a tectonically active region located offshore of Southern California. This study focuses on the portion of the margin with the wide continental shelf. The locations of insets B, C, and D are shown. B) Previously mapped active faults within the study area are shown. Blue faults are from Sahakian et al. (2017) and purple faults are from Conrad et al. (2018). FZ = Fault Zone. C) Location of Dana Point and San Onofre North and South canyons. The area shown in inset D is outlined by the black box. D) The study area offshore of San Onofre. This study uses 2D Sparker Multi-channel seismics shown by the black lines and slices of 3D P-cable Sparker seismics shown by the red lines. Gravity Cores (GC) and Jumbo Piston Cores (JPC) are labeled with white circles. Bathymetry from Dartnell et al. (2015).

### 3.3 Geologic Setting

#### 3.3.1 Geomorphology of the Inner California Borderlands

The Inner California Borderlands is a complex seismically active region off Southern California that is highly deformed (Ehlig, 1977; Crouch, 1979; Legg, 1991; Crouch and Suppe, 1993; Magistrale, 1993; Nicholson et al., 1994; Bohannon and Geist, 1998; Meade and Hagar, 2005; Ryan et al., 2009, 2012; Maloney et al., 2016). Such deformation is responsible for the characteristic basin and ridge basement structure observed in the ICB bathymetry. The main

basins within the ICB are the GoSC and the San Diego Trough (SDT). Our coring locations focus on the Eastern GoSC (Fig. 3.1).

### **3.3.2 Strike-slip tectonics offshore San Onofre**

Much of the complex tectonic deformation in the ICB occurred during the Oligocene to the late Miocene, when the ICB underwent block rotation, extension, and transcurrent faulting associated with microplate capture and formation of the Transverse Ranges (Lonsdale, 1991; Nicholson et al., 1994; ten Brink et al., 2000). As plate motion became more northerly during the late Miocene, deformation of this region created a vast system of basins and ridges that dominates ICB bathymetry (Atwater and Stock, 1998; Maloney et al., 2016). After the late Miocene, deformation in the ICB decreased dramatically and changed in style (Maloney et al., 2016).

Two active faults that dominate the GoSC region are the Palos Verdes Fault in the western GoSC and the Newport-Inglewood/Rose-Canyon (NIRC) Fault along the eastern basin (Fig. 3.1B; Ryan et al., 2009). Sediment dispersal in our study area is affected most by the NIRC Fault (Fig. 3.1B; Klotsko et al., 2015; Sahakian et al., 2017). The right-lateral strike-slip NIRC Fault trends northwest-southeast, has been active since at least the Miocene in the north, and it is estimated to accommodate  $0.5\text{-}2\text{ mm a}^{-1}$  of Pacific-North American plate boundary motion (Freeman et al., 1992).

The NIRC fault exhibits much variability from south to north. The NIRC Fault Zone is characterized by compression offshore of San Onofre and to the south near La Jolla, whereas it is characterized by extensional deformation and divergence near Carlsbad (Maloney et al., 2016). Where the shelf is wide, two segments of the NIRC fault are separated by a stepover of 1 km (Fig. 3.1B). The left lateral jog between these two segments engenders transpression and forms an anticlinal feature responsible for the widening of the shelf in this region (Sahakian

et al., 2017). The anticlinal feature is overlapped by younger sediment (Sahakian et al., 2017). Deformation offshore San Onofre is older than on other locations to the north or south on the NIRC fault (Sahakian et al., 2017), as the transgressive surface is not displaced (Klotsko et al., 2015). It is estimated that fault activity pre-dates 100 ka (Sahakian et al., 2017). Furthermore, it is possible that the central section of the NIRC fault has not experienced surface rupture from recent historical events such as the 1933  $M_L$  6.4 Long Beach earthquake (Sahakian et al., 2017). The study area on the slope offshore San Onofre coincides with the San Mateo (SM) Fault Zone, which consists of steeply to moderately northeast-dipping fault strands (Maloney et al., 2016; Conrad et al., 2018). Deformation within the SM Fault Zone includes strike-slip, normal, and reverse offset, with the greatest amount of deformation on the lower slope (Conrad et al., 2018). Many of these faults exhibit crosscutting relationships and are difficult to resolve, which explains multiple interpretations of faults across this region (Conrad et al., 2018).

### **3.3.3 Canyon Systems in the ICB**

South of Dana Point, the San Juan Creek has an annual sediment discharge of 98 Mt  $a^{-1}$  (Warrick and Farnsworth, 2009) and contributes to the Dana Point Canyon. Just north of San Onofre, the San Mateo Creek discharges 2.7 Mt  $a^{-1}$  of sediment (Warrick and Farnsworth, 2009) and is detached from the head of San Mateo Canyon. Previous studies speculate that sediment discharge from the San Mateo Creek was higher in the past, as evidenced by the creek's construction of a subaerial delta (Kennedy and Tan, 2007). Sediment discharge to canyons in the ICB likely increased during the Last Glacial Maximum, when creeks would directly discharge sediment to the canyon head (Covault and Romans, 2009).

Main canyons in the Eastern Gulf of Santa Catalina include the Newport, Oceanside, Carlsbad, San Mateo, and La Jolla canyon-channel systems as well as numerous small gullies (Prins and Potsma, 2000; Covault et al., 2007; Covault and Romans, 2009; Normark et al., 2009;



Covault and Graham, 2010). It is estimated that about half of the canyons and most of the small gullies were active during the LGM and became inactive during the post-glacial transgression when canyon heads were stranded on the upper slope (Normark et al., 2009). One eastern canyon head of the Newport Canyon remains active in the present day, as it is fed directly by the Santa Ana River, the San Diego Creek, and indirectly by littoral drift from other rivers (Warrick and Farnsworth, 2009; Normark et al., 2009). Cores acquired near the channel recover recently-deposited turbidites and they lack a hemipelagic drape (Normark et al., 2009). Another canyon that is presently active is the La Jolla Canyon, which is sourced by littoral drift (Normark et al., 2009). The La Jolla Canyon represents the end of the littoral cell, as it is bounded to the south by resistant Cretaceous rocks that trap sediment (Inman and Brush, 1973; Normark et al., 2009; LeDantec et al., 2010). During the post-glacial transgression, erosion of the La Jolla Canyon head kept pace with sea-level rise (Normark et al., 2009). Both the Oceanside and Carlsbad canyons were active during the LGM but were drowned during the post-glacial transgression (Normark et al., 2009). Nonetheless, during lowstand intervals such as MIS 2, the Oceanside Canyon may have potentially intercepted littoral drift before it could reach the Carlsbad or La Jolla canyons (Normark et al., 2009). Carlsbad Canyon is not fed directly by any river system and as a result contributed less sediment to the seafloor than the Newport or Oceanside canyons when it was active during MIS 2 (Normark et al., 2009). Its location on a relatively narrow portion of the shelf may have allowed the Carlsbad Canyon to keep pace with shoreline transgression during the early stages of the MIS 2-1 transition (Normark et al., 2009). Gullies on the margin are not necessarily connected to rivers and creeks onshore (Piper et al., 1990) and it is proposed that they could form where coastal geomorphology focuses rip currents during storms (Normark et al., 2009). Denudation rates from river catchments illustrated that catchment erosion is much less than the rate of fan deposition (Covault et al., 2011). To account for additional sources of sediment to fans, Covault et al. (2011) proposed that additional contributors are littoral transport, sea cliff erosion, and mass wasting of shelf and slope deposits.

Even though previous studies (e.g., Covault et al., 2011) propose that shelf width is an important control on sediment delivery through submarine canyons, few studies have examined the timing of deposition offshore of San Onofre, a wide shelf in the ICB. Since the publication of Covault et al. (2007, 2011), additional marine seismic surveys have investigated the complex sedimentation and tectonic regimes offshore of San Onofre (e.g., Klotsko et al., 2015; Maloney et al., 2016; Sahakian et al., 2017; Conrad et al., 2018; Bormann et al., in press). Neither the San Onofre North and South canyons nor the Dana Point canyons have been studied in detail; the goal of this study is to understand how deformation on varying spatial scales modulates the timing of sand delivery to the deep sea.

### **3.3.4 Methods**

2D multi-channel seismic reflection data were collected in August 2013 on the R/V New Horizon and R/V Melville using a 2 kJ three-tip EG&G sparker source and 48-channel streamer. Group spacing of 6.25 m and 6.25 m shot spacing allows reflectors to be resolved to approximately 1.5 s two-way travel time (Sahakian et al., 2017). Data were stacked at 1500 m/s and processing included poststack f-k migration using a water velocity of 1500 m/s (Driscoll et al., 2013; Sahakian et al., 2017). Based on observations from the 2D dataset, a high-resolution 3D data set was acquired using a 3D P-Cable system with 14 streamers with 8 channels per streamer, 6.25 m group spacing, 3.125 m shot spacing, and a 2 kJ three-tip EG&G sparker source. This study uses a data grid of 39 km<sup>2</sup> collected over the continental slope and the data are published in Driscoll et al. (2013) and Sahakian et al. (2017). 3D data were processed by Geotrace Technologies, a petroleum services company, due to the large size of the data volume.

High-resolution bathymetry from Dartnell et al. (2015) was visualized in ArcMap 10 to examine canyon geomorphology. Gradient maps were constructed using the Slope tool in ArcMap and these maps were used to delineate thalwegs of the canyon-channel systems. Two-dimensional

profiles starting at the canyon head were taken through the canyon-channel thalwegs using the 3D analyst toolbox. At intervals of 0.5 km from the canyon head, across-channel profiles were oriented perpendicular to the channel. These across-channel profiles were used to calculate channel relief.

In January 2016, 64 Gravity (GC) and Jumbo-piston cores (JPC) were collected onboard the R/V Thompson as part of a study designed to evaluate hazards such as recent faulting. Additionally, 546 km of Compressed High Intensity Radar Pulse (CHIRP) data were collected near coring targets. The survey and coring targets were designed to image faults and paleochannels that could potentially serve as piercing points. Trigger cores were deployed with the JPCs. GC and JPC targets were selected from previously-collected Sparker and Boomer Multichannel as well as CHIRP seismic profiles. In some cases, drift in ship position caused the cores to be offset from the profiles, in which case the core locations were projected orthogonally onto the profile. On board, whole intact cores were scanned for magnetic susceptibility, gamma density, P-wave velocity, and resistivity using a GeoTek Core-logger. Cores were split and observations of color, grain size, sediment structures, and general lithology were recorded.

A total of 116 samples were collected for radiocarbon dating, preferentially from planktonic foraminifera (Table 1). As some samples did not contain sufficient planktonic foraminifera for age dating, mixed benthic foraminifera were used in these samples. Fragmented foraminifera and foraminifera that showed signs of diagenesis were avoided. For 20 samples, both planktonic and benthic samples were collected in order to define a reservoir age. 110 samples were analyzed at the National Ocean Sciences Accelerator Mass Spectrometry facility at the Woods Hole Oceanographic Institution and produced an age using the Libby half-life of 5568 years and following the convention of Stuiver and Polach (1977). 6 samples were analyzed at the WM Keck Carbon Cycle Accelerator Mass Spectrometry facility at the University of California Irvine following the same conventions.  $\delta^{13}\text{C}$  values were not reported and the radiocarbon result was corrected for isotopic fractionation using unreported values measured  $\delta^{13}\text{C}$  values measured on

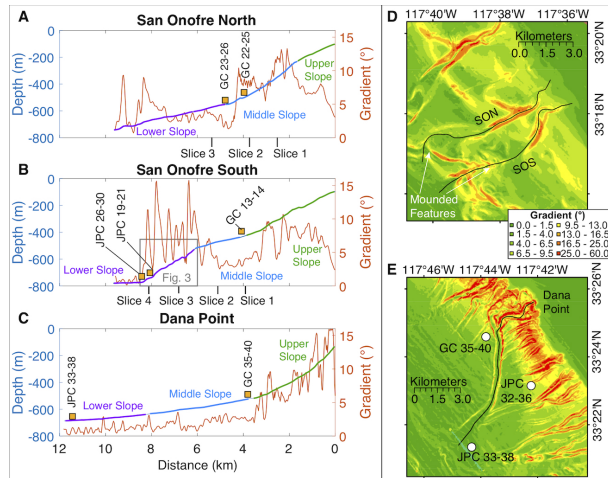
the accelerator. The  $^{14}\text{C}$  ages were converted using the CALIB program version 7.0.4 (Stuiver and Reimer, 1993) with a reservoir age of 800 for planktonic foraminifera  $<12,000$  yr and a reservoir age of 1100 for planktonic foraminifera  $>12,000$  yr (Southon et al., 1990; Kienast and McKay, 2001; Kovanen and Easterbrook, 2002). Based off the 20 samples that acquired ages for both benthic and planktonic foraminifera, we calculated an average difference in reservoir age of 900 years. For this difference in reservoir age, benthic foraminifera  $<12,000$  year would have a reservoir age of 1700 yr, which is comparable to the reservoir age of 1750 for benthic foraminifera used by Mix et al. (1999), Covault et al. (2010), Brothers et al. (2015), and others. Thus, we used this value of 1750 years for a benthic reservoir age. Age-depth models for cores containing more than 2 dates were constructed using the Bacon software version 2.3.3 (Blaauw and Christen, 2011) using the reservoir ages as mentioned above and calibrated using the Marine 13 curve (Supplementary Fig. 3.1). The Bacon software divided each core into 20 cm thick vertical sections and estimated accumulation rates for each section through millions of Markov Chain Monte Carlo iterations (Blaauw and Christen, 2011). This version of the Bacon software allows users to input abrupt events of sedimentation such as slumps and turbidites (Blaauw and Christen, 2011). Nevertheless, the software assumes that there are no hiatuses between these rapid sedimentation events (Blaauw and Christen, 2011) and does not account for sediment reworking in cores. The bounding depths of sand layers with abrupt basal contacts were inputted into the software as rapid periods of deposition in the age-depth models. If sand layers were bound by radiocarbon dates, the date of the sand layer was taken as an average of the corrected dates. If the sand layers were lacking bracketing radiocarbon ages, the age of the middle of the sand layer was determined using the age-depth model produced by the Bacon software. In sections where turbidites are amalgamated, turbidites were distinguished by their erosive basal boundary and the age of the center of each turbidite was extrapolated using the age-depth model.

## 3.4 Results

### 3.4.1 San Onofre North and South (SON and SOS) Canyon-Channel Geomorphology

Bathymetric profiles through the SON and SOS canyons reveal marked variability in gradient (Figs. 3.2A and B). The SON Canyon-channel is characterized by a steep concave-up profile (average  $\sim 13^\circ$ ) in the middle slope between the depths of 240-680 m (Fig. 3.2A). The characteristic feature of the SOS Canyon-channel is the gently-sloping and smooth terraced feature (average  $\sim 4.5^\circ$ ) in the middle slope between the depths of 430-480 m, above and below which the average gradient increases to  $\sim 7^\circ$  (Fig. 3.2B). The lower slope has higher rugosity than the upper or middle slopes due to mounded features between 500-800 m that increase channel gradient for short distances (Figs. 3.2B and 3.3). On the slope map, these mounded features are crescentic in plan-view, are perpendicular to the SOS canyon, and exhibit higher slopes (Fig. 3.2D). We fit a linear regression to the morphology and subtracted the average slope from the bathymetric profile to reveal five mounded features, with three low-amplitude mounds with wavelengths of  $\sim 260$  m and two larger mounds with higher wavelengths (Fig. 3.3).

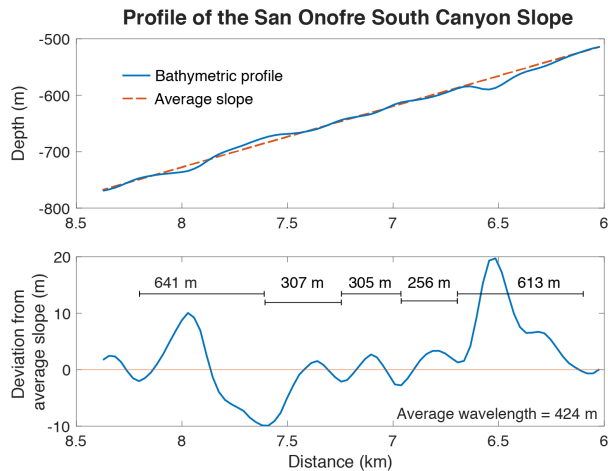
The SON and SOS canyon-channels are narrow and v-shaped in the middle slope and widen in the lower slope (Fig. 3.4C and D), consistent with other canyon-channel systems on the California margin and worldwide (e.g., Menard, 1955; Normark, 1970; Covault et al., 2011). In both the SON and SOS canyon-channels, deeper channel depths are spatially coincident with steeper channel gradients (Fig. 3.4B).



**Figure 3.2:** A, B, C) Bathymetric profiles of the San Onofre North, San Onofre South, and Dana Point Canyons are plotted with channel gradient. The channel profiles are subdivided into the Upper, Middle, and Lower slope. The locations of sediment cores are projected onto profiles as yellow squares. The intersections of Sparker 3D seismic slices are shown by the vertical black lines. In B, the location of Figure 3.3 is highlighted. D, E) Gradient maps offshore of San Onofre and Dana Point. SON = San Onofre North, SOS = San Onofre South. Green colors represent gentler gradients and red colors represent steeper gradients. The bathymetric profile through the channel is shown by the black line.

### 3.4.2 Stratigraphy of the San Onofre slope

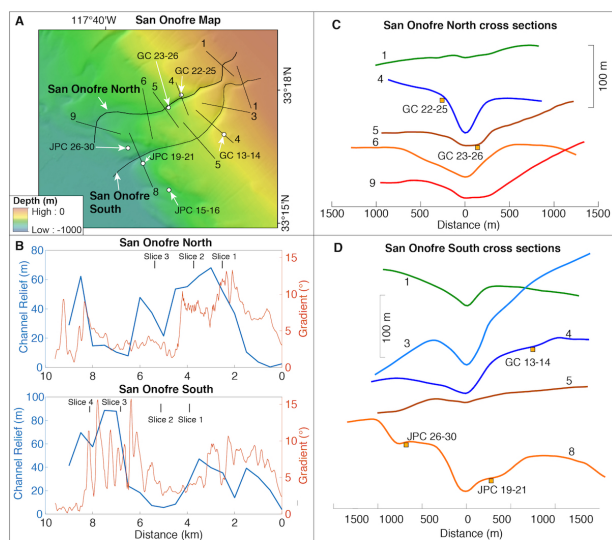
Sparker dip profiles through the study area reveal the internal structure of sediment packages along the slope. Four sediment units were delineated based on sequence stratigraphic principles (e.g., Vail et al., 1977; Mitchum et al., 1977; Christie-Blick and Driscoll, 1995). The upper boundaries of many of the packages can be defined by toplapping reflectors against the base of the overlying unit. The uppermost sediment package on the slope is the Pink Unit that infills local bathymetric lows in all dip profiles and pinches out where there are local bathymetric highs (Fig. 3.5). In strike profiles, the Pink Unit exhibits continuous high-amplitude reflectors that distinguish it from the underlying Blue Unit (Figs. 3.6A and B). In dip profiles, the underlying Blue Unit also infills local bathymetric lows and is not present everywhere on the slope (Fig. 3.5). Low-amplitude reflectors within the Blue Unit exhibit toplap in strike profiles, especially over bathymetric highs (Figs. 3.6A and B). Orange Unit reflectors exhibit toplap in dip Line 11 against



**Figure 3.3:** Top: the bathymetric profile from the lower slope of the San Onofre South Canyon is plotted in blue and has undulatory features. The dashed orange line is the average slope for this length of the canyon. Bottom: Subtracting the average slope from the bathymetric profile reveals undulatory features with amplitudes ranging from 2-15 m and wavelengths ranging from 228-729 m.

the Blue Unit (Fig. 3.5A), and in dip Line 53, flat-lying reflectors in the Blue Unit terminate against the Orange Unit (Fig. 3.5C). Green Unit reflectors exhibit some top lap against the overlying Orange Unit around 5 km in dip Line 53 and around 7 km in dip Line 13 (Figs. 3.5C and D). The lower boundary of the Green Unit is delineated by a high amplitude reflector in strike Slice 1 and the northwest portion of Slice 3 (Figs. 3.6A and C) and this lower boundary truncates underlying reflectors in Slice 4 (Fig. 3.6D). Sediment packages below the Green Unit were not interpreted.

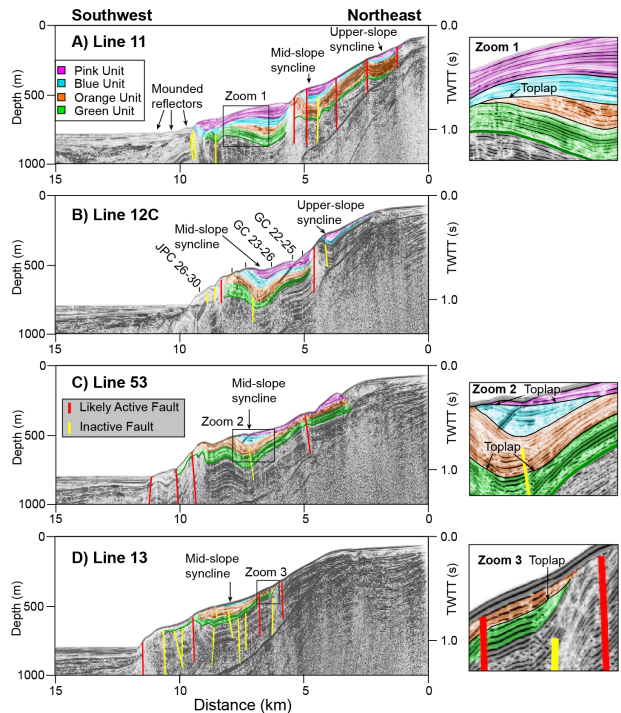
Dip profiles through the survey area (Fig. 3.5) reveal that in general, portions of the slope with steep gradients are along anticline limbs. Conversely, portions of the slope with gentler gradients correspond to infilled synclines. Upper slope synclines appear only in the two northern dip profiles (Fig. 3.5A and B). Some faults bounding the upper-slope syncline appear to offset reflectors just below the seafloor (Fig. 3.5A). The upper-slope syncline is separated from a mid-slope syncline by an anticline that is cross-cut by a recent fault and obscured by gas-wipeout (Figs. 3.5A and B). In contrast to the upper-slope syncline, the mid-slope syncline is



**Figure 3.4:** A) Bathymetry of the San Onofre North (SON) and South (SOS) Canyons. Cross-sections numbers correspond to their distance from the start of the bathymetric profile and are shown in C and D. Sediment cores are labeled. B) Channel relief is plotted relative to channel slope for the two canyons. The intersections of the 3D Multichannel Sparker slices with the canyons are indicated at the top of the plots. C and D) Cross sections through the SON and SOS canyon- channels are plotted. Horizontal and vertical scales are shown. Sediment cores were projected onto cross-sections and are indicated by yellow boxes.

observed in all dip profiles (Fig. 3.5). Note that the local mid-slope and upper-slope synclines are completely infilled by sediment (Fig. 3.5). Deformation within the mid-slope syncline appears to have along-margin variability. Faults at the syncline boundaries in lines 12C, 53, and 13 appear to deform the uppermost reflectors; nevertheless, faults cross-cutting the mid-slope syncline appear to have deformed only the Green and Orange units (Figs. 3.5A, B, and C). In these three lines, only Green and Orange units exhibit sediment thickening towards cross-cutting faults in the mid-slope syncline (Figs. 3.5A, B, and C). At the slope-basin transition, recent sediment onlaps slope deposits (Fig. 3.5B). This recent sediment has an undulatory bathymetric expression and appears to step northeast through time (Fig. 3.5A). The most seaward undulatory feature is onlapped by aggrading reflectors (Fig. 3.5A). Four slices from 3D P-Cable data oriented along-strike to the margin reveal that the most prominent feature shaping the slope offshore of San Onofre is a prominent anticline that is clearly imaged in Slice 2 (Fig. 3.6B). Sediment thins

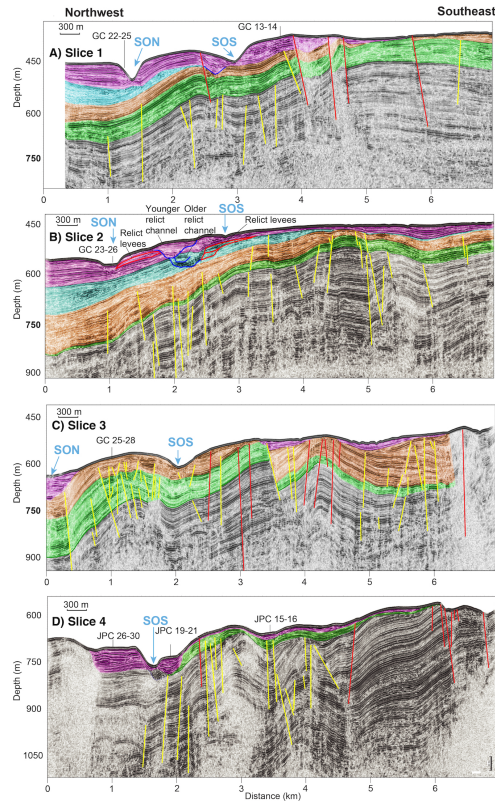




**Figure 3.5:** Sparker seismic dip profiles offshore San Onofre reveal the internal structure of the slope and are organized with the northernmost profile at the top and southernmost profile at the bottom. The continental slope is characterized by a mid-slope syncline that decreases gradient that is bound by anticlines that increase gradient. Lines 11 and 12C contain upper slope synclines. The mid- and upper-slope synclines act as ponded basins that trap sediment. Mounded features are shown at the slope-basin transition in Line 11. Colors of Units are shown in panel A. Active faults offset reflectors just below the seafloor are shown in red. Inactive faults offset deeper reflectors and are shown in yellow. Sediment cores are projected onto seismic lines. Locations of lines are shown in Figure 3.1. At right are enlargements of areas that show toplap relationships. Vertical Exaggeration = 5.6x.

across the anticline crest and thicken away from the crest (Fig. 3.6B).

Channel and overbank deposit geometry appear to correspond to variations in channel gradient. Pink Unit deposits adjacent to the SON channel have aggradational reflector character in Slices 1, 2, and 4 (Figs. 3.6A, B, and D). The SON channel overlies over 16 m of aggradational Pink Unit deposits in Slice 1 and the channel truncates horizontal reflectors within the upper Pink Unit (Fig. 3.6A). In Slice 2, the SON channel overlies over 18 m of Pink Unit deposits, above which a u-shaped feature is infilled with discontinuous, wavy reflectors (Fig. 3.6B). Overbank



**Figure 3.6:** Strike slices along the San Onofre margin reveal the internal architecture of the slope and channel elements. The along-margin architecture in Slices 1 and 2 is characterized by a broad anticline. This anticline controls the location of the SON and SOS canyons as well as the thickness of Pink, Blue, Orange, and Green units. The shallowest (easternmost) slice is at the top and the deepest slice (westernmost) is at the bottom. Sediment cores are projected onto seismic slices. Locations of lines are shown in Figure 3.1. Vertical Exaggeration = 5.1x.

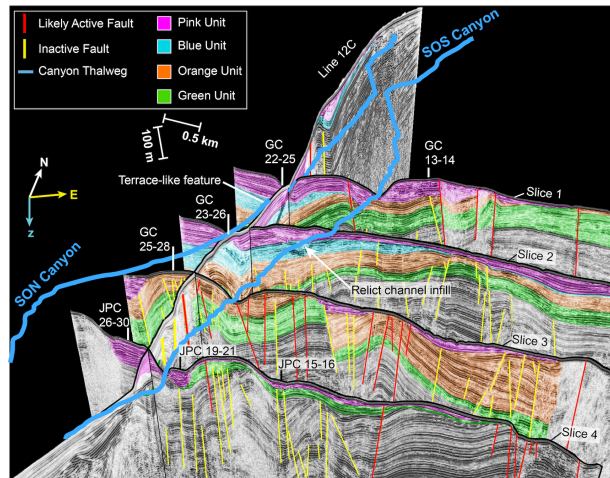
deposits with gull-wing geometries that converge away from the channel are defined as channel levees, after Qin et al. (2016). Pink Unit levees bounding the SON channel to the northwest have maximum thicknesses of 82 m in Slice 1 and 87 m in Slice 2 and diminish in thickness to the southeast (Fig. 3.6B). Broadening in Slice 3, the SON channel has a base of a thick Pink Unit deposit that unconformably aggrades into a NW-SE trending synform (Fig. 3.6C). The SON channel is not present in Slice 4 (Fig. 3.6D). Levees bounding the SOS channel exhibit more variability. In Slice 1, the SOS channel has an asymmetric v-shape that is adjacent to dipping wavy reflectors in the northwest levee and conformable reflectors in the southeast levee (Fig. 3.6A). In Slice 2, the SOS channel is extremely narrow and shallow, and is bordered to the

northwest by discontinuous, wavy reflectors (Fig. 3.6B). The SOS channel in Slice 3 appears to be located in a local syncline and truncates reflectors in the Orange Unit (Fig. 3.6C). In Slice 3, note the lack of Pink Unit channel levees. In the lower slope Slice 4, the SOS channel exhibits asymmetry, with thick levees to the northwest and thinner levees to the southeast that form a bench-like feature (Fig. 3.6D).

Deformation on this margin is complex, as evidenced by the multiple synclines imaged in dip profiles that create local accommodation (Fig. 3.5), anticlines imaged in dip profiles that increase gradient (Fig. 3.5), and a prominent anticline imaged in strike slices that appears to exert control on SON and SOS locations as well as Pink Unit levee thickness (Fig. 3.6). 3-dimensional seismic fence diagrams provide an unprecedented view of the synclines and anticlines (Fig. 3.7). Overall, the SON and SOS channels are located on the flank of the broad NW-SE trending antiform in Slices 1 and 2 in the middle slope (Figs. 3.6A, B, and 3.7). The SON channel is located at deeper depths than the SOS channel (Figs. 3.6A, B, and 3.7). In contrast, accommodation for the SOS channel is limited, as it is located proximal to the antiform. The lack of accumulation adjacent to the SOS channel in Slices 1-2 is coincident with its v-shape and as the SOS channel moves into a synform in Slices 3-4, channel width increases (Figs. 3.6A, B, and 3.7).

### **3.4.3 San Onofre Sediment Core Lithology and Chronology**

Cores offshore of San Onofre can be grouped by their depth on the middle slope (300-600 m) or on the lower slope (600-1000 m). Note that few cores were recovered on the upper slope due to poor recovery (Figs. 3.2A and B). With the exception of JPC 15-16, the upper portions of most of the cores offshore of San Onofre are capped by tens of cm to meters of clay or silty clay (Fig. 3.8). This clay cap is commonly homogenous and bioturbated. In JPC 26-30, the base of the upper clay section is dated to approximately 13.2 kyr, 23.3 kyr in GC 22-25, and 44.4 kyr in GC 13-14 (Fig. 3.8). Below this cap, silty clay or silt layers are interbedded with thin (< 1 cm)



**Figure 3.7:** A 3D seismic fence diagram with a Sparker 2-D seismic profile and Sparker 3D slices. The locations of the two canyons are traced in blue. Colors denote sediment units, with the Pink unit as the youngest and the Green unit as the oldest. Likely active faults are shown in red and inactive faults are shown in yellow. Locations of cores are plotted as white or black lines. Vertical Exaggeration = 6.

to thick (10's of cm) sand layers. Many of these sand layers are observed to fine upward, with sands at the base of the layer ranging from fine sand to coarse sand. Sand layers in the cores are commonly observed to have sharp, erosive basal boundaries and gradational upper boundaries; however, the basal boundary was occasionally diffuse. Often, sand layers are characterized by color changes, as noted by the change from olive green to tan in the photo of JPC 19-21 (Fig. 3.8 photo inset). Nevertheless, some of the sand layers, such as those shown in the photo inset of JPC 15-16, exhibit only slight color changes. Some of the sand layers also contained shell hash in GCs 22-25 and 23-26 from the middle slope (Fig. 3.8).

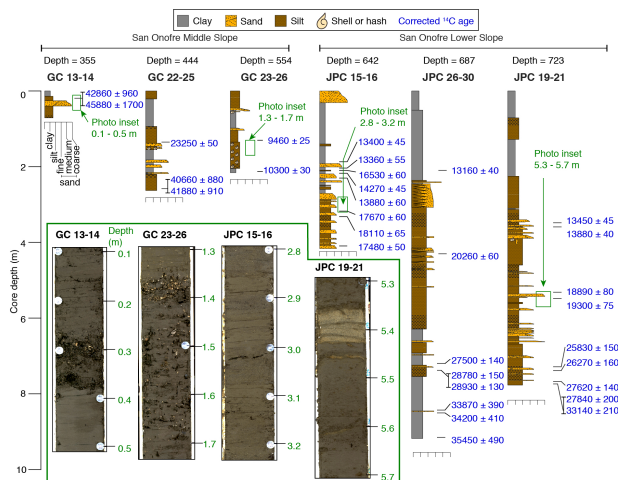
GC 13-14 was recovered from the southeast end of a channel levee on the middle slope and it contains only one sand layer (Figs. 3.6 and 3.8). This layer has a sharp basal boundary and is composed of a mud matrix with unsorted medium sand, gravel, and shell hash (Fig. 3.8 photo inset). Above and below this sand layer is homogenous, bioturbated mud (Fig. 3.8 photo inset). The sand and shell hash layer was likely deposited before the overlying layer with a radiocarbon age of 44.5 ka. Approximately 90 m downslope, the middle portion of GC 22-25 contains 5 sand

layers that fine upward with grain sizes ranging from fine to coarse sand. Radiocarbon dates bracketing the five sand layers suggest that they were deposited between 22.3-41.3 ka (Fig. 3.8). GC 23-26, recovered from the SOS channel thalweg (Fig. 3.5B), is composed of an upper silt cap, two sand layers composed of fine sand that are separated by 40 cm of clay, and blocky silt with shell hash in the lower sections of the core. Shell hash is interbedded with silt in GC 23-26 and the concentration of shell hash decreases downsection beginning at 1.4 m (Fig. 3.8 photo inset).

JPCs 15-16, 26-30, and 19-21 were recovered from the lower slope (Figs. 3.6D and 3.8) and are longer cores that contain 13, 14, and 23 sand layers respectively. The upper 30 cm of JPC 15-16 contains an upward-fining sand layer with coarse sand at the base. The lower 2.5 m of JPC 15-16 is characterized by sand layers with fine to medium sand that are interbedded with silt and clay. Sand layers increase in frequency and thickness in the lower 1.5 m in the core with ages ranging between 17.8 and 18.2 ka. Constraining the exact timing of sand layer deposition is difficult in this core, as ages are inverted. As such, dating of the layers was conducted using age models calculated by the R Bacon package (Supplementary Figure 3.1). In the lower portion of JPC 26-30, sand layers are less frequent and separated by longer intervals than those in JPCs 15-16 or 19-21 and these sand layers predate MIS 2. Overall, sand layers within JPC 19-21 at 5.3 m depth have a lighter color than the surrounding silt and exhibit sharp basal and upper contacts (Fig. 3.8 photo inset). Around 6 m, sand layers are closer together and thicken until the bottom of JPC 19-21, where sand layers are spaced farther apart and consist of fine sand (Fig. 3.8).

### **3.4.4 Dana Point Canyon-Channel and Core Stratigraphy**

The narrow shelf (~ 2 km) offshore of Dana Point separates the head of Dana Point Canyon from San Juan Creek (Fig. 3.1C). Dana Point Canyon has two branches at the head of the canyon and one broad meander (Figs. 3.2E and 3.9A). Three cores, GCs 35-40, and JPCs 32-36 and 33-38 were collected adjacent to the Dana Point Canyon (Figs. 3.1C and 3.9A).

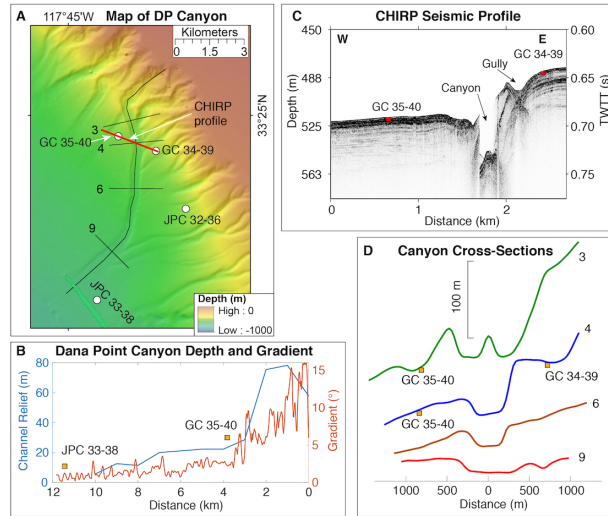


**Figure 3.8:** Schematic diagrams of San Onofre cores. Labeled grain size scale is shown under GC 13-14 and unlabeled scales are shown under all other cores. Corrected radiocarbon ages are shown to the right of the cores. At the bottom left, photo insets of select cores are plotted with their depth. The locations of the photo insets are shown relative to core diagrams by the outlined green rectangles.

Sparker seismic surveys do not extend into this area and therefore, most of our interpretations on geomorphology are based off limited CHIRP seismic coverage and multibeam bathymetry.

The bathymetric profile of the Dana Point Canyon is generally concave-up with a steep upper slope ( $5 - 15^\circ$ ), and gentler gradients on the middle and lower slopes ( $0 - 3^\circ$ ; Fig. 3.2C). Steep gradients in the upper slope coincide with greater channel relief and canyon-channel depth dramatically decreases between 3-4 km as gradient decreases (Fig. 3.9B). This transition occurs at the intersection of the canyon head branches and at the inner bend of the canyon's only meander (Figs. 3.9A and B). A CHIRP seismic profile through this transition reveals that the canyon has higher walls to the east (Fig. 3.9C). Unlike the SON and SOS canyons, the Dana Point Canyon maintains a u-shaped channel with a wide valley floor throughout the slope (Fig. 3.9D).

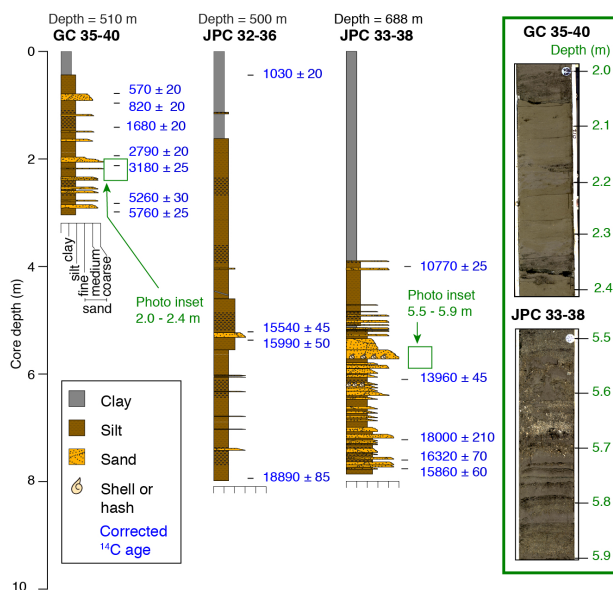
JPC 32-36 and GC 35-40 are located on the middle slope at depths of 500 and 510 m, whereas JPC 33-38 is located on the lower slope at depths of 688 m. GC 35-40 was recovered from the Dana Point channel flank and is located at the transition from higher to lower channel



**Figure 3.9:** A) Bathymetry of the Dana Point Canyon. The location of the CHIRP profile shown in B is highlighted in red. Cross-sections numbers correspond to their distance from the start of the bathymetric profile and are shown in D. Sediment cores used in this study are also labeled. B) Channel relief is plotted relative to channel gradient. Yellow boxes indicate the location of sediment cores along the bathymetric profile. C) CHIRP seismic profile through GCs 35-40 and 34-39. D) Cross sections through the DP canyon-channel are plotted. Numbers at right correspond to the distance along the bathymetric profile. Horizontal and vertical scales are shown. Sediment cores were projected onto cross-sections and are indicated by yellow boxes.

gradient (Figs. 3.9B and C). JPC 33-38 is located at the slope-basin transition where the canyon widens (Fig. 3.9A). Cores in Dana Point are capped by an upper layer of clay and silt that varies from  $< 1$  to 4 m thick (Fig. 3.10). In GC 35-40, the age of the clay and silt cap is  $< 570$  years BP,  $< 10.8$  ka in JPC 33-38, and cannot be constrained by available ages in JPC 32-36 (Fig. 3.10). Below this, silty clay and sandy silt are interbedded with fine sand. Sand layers in GC 35-40 are a few cm's thick, whereas sand layers in JPC 32-36 are thin and most are  $< 1$  cm (Fig. 3.10). The 12 sand layers in GC 35-40 exhibit ages between 570-5760 years BP and this range of ages is limited by the short core recovery. JPC 32-36, which is farthest core from the Dana Point Canyon, has the thinnest and fewest sand layers (7) that are dated between 15.5-18.9 ka (Fig. 3.10). Thick and thin sand layers in JPC 33-38 are amalgamated and can be distinguished by erosive lower boundaries (Fig. 3.10). JPC 33-38 has the most abundant (37) and thickest sand layers that range in age from 10.7 to 15.9 ka (Fig. 3.10). Sand color ranges from olive-gray in the photo of GC

35-40 to light tan in the photo of JPC 33-38 (Fig. 3.10). Some sand layers in JPC 33-38 contain shell hash, which can be observed between 5.6-5.7 m in this core's photo inset (Fig. 3.10).



**Figure 3.10:** Schematic diagrams of Dana Point cores. Grain size scale is shown under GC 35-40. Unlabeled grain size scales are shown below all other cores. Corrected radiocarbon ages are shown to the right of the cores. At right, photo insets of select cores are plotted with their depth. The location of the photo insets are shown relative to core diagrams by the outlined green rectangles.

### 3.5 Discussion

Deposition on the continental slope predominantly occurs by two main modes: gravity-driven turbidites during intervals with high terrigenous supply or hemipelagic sedimentation when terrigenous supply is low (Stow and Piper, 1983; Walsh and Nittrouer, 2003; Maier et al., 2017). Turbidites were identified in sediment cores by fining-upward sand layers (i.e., graded beds) with erosional bases (Stow and Piper, 1984). While many of the turbidites have sharp, erosive basal contacts and gradational upper contacts, some basal boundaries were occasionally diffuse. Turbidites were treated as instantaneous events, based on studies by Talling et al. (2015)



and Symons et al. (2017) that found that the depositional timing of turbidites is much shorter than that of hemipelagic background sedimentation. Multiple turbidites in amalgamated beds were identified and counted as separate events.

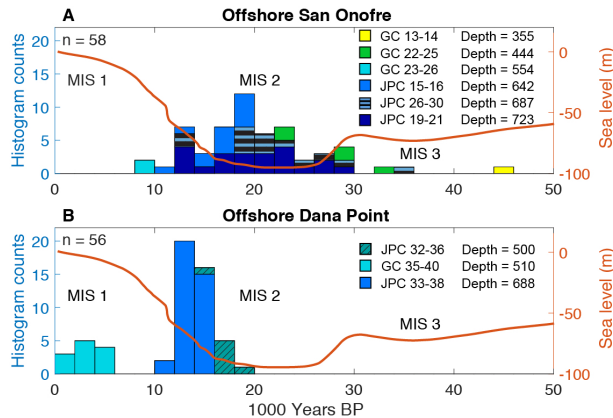
The homogenous, upper clay section observed in most cores (Figs. 3.8 and 3.10) is interpreted as hemipelagic sediment drapes that accumulate slowly and follows interpretations of Stow and Piper (1984), Piper and Normark (2001), and Normark et al. (2009). Such deposits are also observed draping inactive canyons that halted deposition  $\sim 15 - 20$  kyr ago (Sweet and Blum, 2016), such as the Mississippi (Normark et al., 1986), Amazon (Milliman et al., 1975; Normark et al., 1997), and Nile (Ducassou et al., 2009). Thus, the hemipelagic mud that drapes the levee deposits are interpreted to have been deposited after terrigenous supply to the canyon-channel declined. While recent papers in the ICB have interpreted mud deposits interbedded with turbidites as hemipelagic background sedimentation (e.g., Maier et al., 2017), some studies in the Gulf of Mexico interpret grey-brown muds interbedded with turbidites as hemiturbidites, or thin fluid-mud flows moving continuously downslope (Damuth, 1977; Damuth and Olson, 2015). It is difficult for us to discern their exact origin, as laminations were obscured by bioturbation. As such, we treated mud interlayers in the age model as constant-rate deposition. We did not test whether interbedded mud layers are deposited at constant rates, as radiocarbon ages were sampled in order to constrain turbidite depositional timing.

Most of the cores in the study, with the exception of GC 23-26, recovered deposits from channel levee deposits. The histogram of turbidite emplacement records the relative timing of high-volume turbidity currents that overtopped levees. Comparing levee deposits still allows us to investigate broad patterns that distinguish the San Onofre Canyons (SON and SOS) from the Dana Point Canyon. Additionally, these patterns shed light on whether high-volume flows can reach the lower slope. In order to accurately evaluate the most recent emplacement of turbidites in these canyon-channel systems, cores should be acquired along transects across a channel, following Maier et al. (2017) and Symons et al. (2017). This method requires the use of ROV-collected

vibracores, which was not available to us in this study. Based on broad patterns, we propose that large-scale shelf-width differences and ponded basins constructed by strike-slip tectonics affect sediment supply and hence the timing of turbidite emplacement, whereas flow dynamics and channel geomorphology influence the relative number of turbidites.

### **3.5.1 Chronology of turbidite and pelagic deposition**

Reservoir ages for foraminifera vary with depth; ages can range from 1000-2000 years and have errors as large as 40‰  $\Delta^{14}\text{C}$  ( $\sim 320$  years) along the Southern California margin (Roach et al., 2013; C. Charles, pers. comm.). As a result, uncertainties exist and precise age estimates for turbidites are not feasible. Such uncertainties for radiocarbon dating on the Southern California margin are associated with the effects of vertical ocean mixing and migration of benthic foraminifera species from the depth of calcification to the depth of deposition (Roach et al., 2013). Furthermore, Bayesian constructions of age-depth models have limitations, as these models do not consider hiatuses or sediment reworking (Blaauw and Christen, 2011). In some sections of JPCs 15-16 and 33-38, inverted radiocarbon ages are within 1000-year error windows found by Roach et al. (2013). When the inverted ages are outside of the 1000-year error window, we hypothesize that inverted ages may be caused by turbidity currents or mass wasting events that mobilize sediment with older foraminifera re-deposited downslope. As such, we examined broad patterns in turbidite depositional timing, such as MIS 3, MIS 2, the post-LGM transgression, and MIS 1. Histograms for turbidite ages offshore of San Onofre and Dana Point employ a 2000-year bin in order to account for large uncertainties in radiocarbon dating (Fig. 3.11). Broad patterns in the histogram reveal that turbidites are emplaced to the Dana Point continental slope throughout lowstands and highstands in sea-level (Fig. 3.11). Conversely, turbidites transported to the slope offshore of San Onofre show a marked decrease around 12-13 ka with the last few emplacements at approximately 8 ka (Fig. 3.11).



**Figure 3.11:** A) Histograms of sand layer depositional timing offshore San Onofre and Dana Point have bins of 2000 years. A) The number of sand layers recovered from cores offshore San Onofre. B) The number of sand layers recovered from cores offshore Dana Point. In orange, the Southern California sea level curve from Muhs et al. (2012) versus time.

The large uncertainties for radiocarbon dating turbidite deposits in Southern California with  $^{14}\text{C}$  makes using turbidites to reconstruct paleoseismicity difficult. Some studies have argued that seismically triggered turbidites can be distinguished by synchronous turbidites emplaced over a wide area (Goldfinger, 2011; Sumner et al., 2013). Many of these studies, such as Goldfinger et al. (2007), aim to use seismoturbidites to constrain earthquake recurrence intervals on the order of 100's of years; nevertheless, constraining turbidite ages to 100's of years has much uncertainty along the Southern California margin. Depending on deposit depth,  $\Delta^{14}\text{C}$  could exhibit wide variability and may be influenced by El Niño Southern Oscillation patterns (Roach et al., 2013). Radiocarbon dating lacks the time resolution to constrain whether a fault ruptured over days or even decades (Nelson et al., 1995; Atwater et al., 2014). In Southern California, uncertainties with radiocarbon ages preclude the required accuracy for events spaced by 100's of years, let alone for a single earthquake event. Sumner et al. (2013) suggested that the most reliable records of seismoturbidites were recovered within a few years of a major earthquake event and could be dated using multiple methods, such as  $^{14}\text{C}$  and  $^{210}\text{Pb}$ .

### **3.5.2 Shelf width controls regional timing of turbidite deposition**

The San Onofre and Dana Point canyons have three main differences that may affect the emplacement of turbidites, namely i) shelf width is  $\sim 10$  km offshore San Onofre versus  $\sim 2$  km offshore of Dana Point (Fig. 3.1C); ii) Dana Point canyons were likely attached to San Juan Creek during the sea-level lowstand and during the ensuing transgression, whereas the San Onofre canyons were likely not attached to a creek source during the post-glacial transgression; and iii) the slope offshore Dana Point is relatively smooth and concave-up in comparison to a more rugose slope offshore of San Onofre. As shelf width is known to be an important control on sediment supply to the slope and basin, widening of the shelf caused by the NW-SE trending anticline may contribute to decreased sediment delivery to the slope in that region (Covault et al., 2007; 2010). We propose that broad tectonic and structural controls influence the timing of turbidite deposition regionally (San Onofre versus Dana Point). In section 5.4, we discuss why there are local variances in the timing turbidite emplacement (e.g., different depths on the slope and distances from the channel) that are affected most by ponded basin and channel geomorphology.

This paper addresses multiple scales of the SON, SOS, and Dana Point canyons. Large-scale features such as shelf width and slope gradient are predominantly controlled by tectonic deformation. The broad anticline along the outer shelf imaged by Sahakian et al. (2017) is a first-order tectonic feature that has increased shelf width offshore of San Onofre. Second-order features include the anticlines and synclines imaged in dip and strike profiles along the slope (Figs. 3.5 and 3.6). The ponded basins and anticlines are related to transpression and transtension along faults in the SM Fault Zone (Maloney et al., 2016; Conrad et al., 2018). Third-order features such as channel levees are geomorphic features that are influenced by properties of turbidity flows, such as flow velocity and entrainment.

The paucity of turbidites offshore San Onofre that are younger than 8 ka suggests that the most favorable conditions for turbidite deposition offshore of San Onofre are sea-level lowstands

and the early transgression (Fig. 3.11). Older turbidites within the San Onofre cores dating back to 40 ka may have a high potential for recovery within JPCs because sedimentation rates are lower offshore San Onofre than in Dana Point; that is, the cores are condensed. It appears that the cores located on the middle slope, GC 13-14 and GC 22-25, have the oldest turbidite ages whereas cores on the middle and lower slopes have slightly younger turbidite ages (Fig. 3.11). This may be related to ponded basins, channel gradient, and geomorphology, which will be discussed in Sections 5.3 and 5.4.

The narrower shelf width at Dana Point and its potential connection to San Juan Creek may facilitate the emplacement of turbidites during sea level lowstands, transgressions, and highstands. JPC 33-38 recovered from 688 m depth recovered turbidites spanning the interval from 13-18 ka, whereas GC 35-40 from slightly shallower depths of 510 m recovered turbidites spanning the interval from 1-6 ka (Figs. 3.10 and 3.11). Thick clay deposits in the upper 4 m of JPC 33-38 are interpreted as hemipelagic sediment deposited during the sea-level transgression and highstand when terrigenous supply was lower. This contrasts with the timing of turbidite deposition in GC 35-40, where most of the core is characterized by turbidites interbedded with silt. Only the upper 0.5 m of GC 35-40 is capped by clay. This difference between highstand turbidite deposition in GC 35-40 and lowstand deposition in JPC 33-38 may be related to channel dynamics and core location explored in Section 5.3. Turbidites within JPC 32-36 span the interval of 15-19 ka (Fig. 3.10). This suggests that Dana Point Canyon remained active during the lowstand, subsequent transgression, and highstand. Timing differences between core locations are likely due to local variability in turbidity flow discussed in Section 5.3.

Comparisons of the SON and SOS canyons to the Dana Point Canyon draw similarities to studies that contrast coast-disconnected canyons versus connected canyons along the same active margin (*sensu* Gamberi et al., 2015). A study on the Sicilian margin observed that canyons with heads close to the coast are active during the present highstand and are sourced by hyperpycnal flows or longshore currents that rework shelf sands (Gamberi et al., 2015). In contrast, sediment

supply to coast-disconnected canyons ceased during the post-glacial transgression (Gamberi et al., 2015).

### **3.5.3 Across-margin deformation controls local turbidite emplacement**

Deformation across the San Onofre slope exerts three main influences on turbidite emplacement: i) NW-SE trending anticlines and synclines form ponded basins that either trap sediment or cause bypass (Figs. 3.5 and 3.7), ii) NW-SE trending anticlines and synclines dictate the morphology of SON and SOS channel levees, and iii) structural controls influence slope gradient, which in turn affect canyon-channel dynamics and geomorphology (discussed further in Section 5.3). Models predict that ponded basins exert controls on grain size, as these basins are predicted to fill with thick, sand-rich deposits, whereas slope deposits tend to contain less sand (Prather, 2000). This model may explain why GCs 22-25 and 23-26 recovered  $\sim 4 - 5$  turbidites from the mid-slope syncline/ponded basin (Figs. 3.7 and 3.8).

On the slope, the only mechanism of generating basins/synclines may be tectonic deformation (Covault et al., 2012) such as right jogs on the right-lateral strike-slip NIRC and SM Fault Zone that form transtensional basins (Ryan et al., 2009; Maloney et al., 2016; Conrad et al., 2018). Recent deformation of the middle slope ponded basin may be observed in Line 11 (Fig. 3.5A); however, recent deformation of Blue and Pink unit sediment is not observed south of Line 11 (Fig. 3.5). Thus, it appears that deformation within the ICB occurred on timescales much longer than the timescales of recent deposition; on this margin, there was no recent renewal of accommodation in local ponded basins. Thick Pink, Blue, and Orange units infilling the mid-slope ponded basin have diminished relief on the continental slope in dip profiles (Line 12C; Fig. 3.5B) as well as SON and SOS channel relief on the intersecting Slice 2 (Slice 2; Figs. 3.6B and 3.7). Nested U-shaped bodies that truncate underlying deposits and are infilled with aggrading Blue and Pink units are suggestive of relict channels (Fig. 3.6B). As these nested U-shaped bodies are

bound by gull-wing shaped levees, we interpret these U-shaped bodies as relict channels rather than localized deformation or draping infill. The older and deeper relict channel was infilled and this aggradational sediment was subsequently truncated by a younger relict channel located to the northwest with shallower channel depths (Fig. 3.6B). After the complete infilling of the younger relict channel, the present-day SOS channel is deflected to the southeast of the relict channels and maintains a shallow depth (Fig. 3.6B). The infilled relict channels serve as an example of how the formation of such ponded basins affect the flow dynamics of channels and channel element architecture.

When ponded basins in the upper, middle, and lower San Onofre slope became completely infilled with thick sediment, sediment likely bypassed these basins and deposited turbidites on the lower slope and basin floor (Figs. 3.5, 3.6, 3.7). The radiocarbon age below the mud cap in GC 22-25 could imply that turbidite emplacement to the ponded basin ceased before 23.25 ka as the basin infilled. Shortly after, bypass of the ponded basin and pelagic sedimentation may have commenced. This hypothesis is supported by abundant turbidites on lower slope JPCs 15-16, 19-21, and 26-30 that post-date 23 ka (Fig. 3.11). The formation of ponded basins and intervening anticlines influences the channel profile and channel gradients, as discussed below.

The NW-SE trending anticlines and synclines imaged in the dip and strike profiles (Figs. 3.5 and 3.6) exert controls on the levee morphology adjacent to the SON and SOS canyon-channels. On the middle slope, levees thin towards the anticline crest adjacent to the SOS canyon-channel and thicken away from the anticline crest (Figs. 3.6A and B). Levees located closer to the anticline crest may have less frequent deposition than those located at deeper depths away from the anticline. For example, GC 13-14 has one turbidite that is  $\sim 20$  kyr older than multiple turbidites in GC 22-25. While GC 13-14 is located on a shallower levee close to the anticline crest, GC 22-25 is located in deeper water away from the anticline crest. On the lower slope, the SOS channel migrates into a NW-SE trending syncline as the channel widens (Figs. 3.6C and D). Thus, deformation on the San Mateo Fault Zone appears to influence turbidite em-

placement and timing over lateral distances  $< 1$  km by creating ponded basins that trap sediment, forming anticlines that cause sediment bypass in the cross-margin direction, and affecting levee architecture in the along-margin direction.

### **3.5.4 Channel gradient controls morphology and localized differences in turbidite timing**

Channel gradient exerts controls on turbidity flow behavior and morphology, as the force of turbidity flows is proportional to gradient (McHargue et al., 2011). Therefore, steep gradients along broader scales are often related to greater incision, whereas gentler gradients are related to deposition (Prather et al., 2000; McHargue et al., 2011; Brothers et al., 2015; Maier et al., 2017). Without tectonic deformation, canyon-channel systems on a continental slope would trend towards an equilibrium profile just like fluvial systems (McHargue et al., 2011). A smooth concave-up profile is observed through the Dana Point Canyon, whereas tectonic deformation offshore of San Onofre has created bathymetric irregularities that disrupt the equilibrium profile for the SON and SOS canyons (Fig. 3.2). In this manner, the SON and SOS canyons exhibit similarities to the Palos Verdes Channel, where strike-slip tectonics that create local uplift or pull-apart basins that have prohibited channels from developing an equilibrium profile (Maier et al., 2017). In the Palos Verdes Channel, local uplift abruptly increases channel gradient, leading to hydraulic jumps that can cause subsequent scouring or bypass; breaks in gradient may lead to deposition (Maier et al., 2017).

Turbidity current flow dynamics influence architectural elements of channel systems such as width, depth, and confinement by levees or erosion (Piper and Normark, 2009; McHargue et al., 2011; Talling et al., 2013, 2015). Offshore of Palos Verdes, regions of steep gradients and sediment bypass are characterized by overbank deposits, whereas regions characterized by breaks in gradient are characterized by depocenters (Maier et al., 2017). Such variability in turbidity



current flow may further overprint the influence of shelf width on turbidite emplacement. While we attempt to address the overlapping influences of shelf width and current dynamics on the turbidite record, these signals cannot be unambiguously teased out, as multiple processes can form similar deposits (Talling et al., 2012).

Though the concave-up bathymetric profile of the Dana Point Canyon suggests less tectonic deformation in this area than the SON and SOS canyon-channels, changes in downslope gradient may cause local variances in the timing of turbidite emplacement. The gradient changes from  $5 - 15^\circ$  in the upper slope to  $< 5^\circ$  in the middle slope (Fig. 3.2C); GC 35-40 is located at this break in gradient and here deposition may be favored over bypass. As a result, it records recent turbidites within the past 600 years (Fig. 3.10). JPC 33-38 is located at the slope-basin transition where the channel levees decrease in height and the channel becomes unconfined (Fig. 3.9B). Despite the decrease in channel gradient, turbidites have not been emplaced within the past 10 kyr. It is plausible that turbidity currents are less capable of reaching the basin floor during intervals of lower sediment supply, such as sea-level highstands, as short-term observations in other canyons have yet to record modern turbidity currents propagating throughout entire systems (Fildani, 2017). JPC 32-36 recovered fewer turbidites and may be related to its location farther from the channel axis (Fig. 3.9A).

Of the San Onofre canyons, the SON canyon profile trends the most towards equilibrium whereas the SOS canyon profile is punctuated by the mid-slope ponded basin (Figs. 3.2A and B). The recency of turbidite emplacement and the SON and SOS channel gradient do not exhibit a one-to-one relationship. Much of this could be attributed to the recovery of cores along channel levees rather than thalwegs, as levee cores record high-volume turbidity currents capable of overtopping levees. Additionally, complex geomorphic features that are constructed in response to accelerating or decelerating turbidity flow may further complicate the timing of turbidite emplacement.

Offshore San Onofre, breaks, or abrupt changes in channel gradient (*sensu* Maier et al.,

2017) are observed at the transitions from the upper to middle and middle to lower slopes (Fig. 3.2). Where these breaks occur, thick, aggradational channel levees flank the SON and SOS channels (Fig. 3.7). These breaks coincide with GC 23-26 on the SON canyon mid-slope, at GC 13-14 on the SOS canyon mid-slope, and JPC 26-30 on the SOS canyon lower slope (Figs. 3.2A and B). While GC 23-26 exhibits recent turbidite emplacement as young as 8 ka, JPC 26-30 exhibits turbidite emplacement as recent as 14 ka, and there was no turbidite emplacement at GC 13-14 since > 44 ka (Figs. 3.8 and 3.11).

Steep gradients in the lower slope facilitate faster turbidity currents that potentially caused bypass and thinning sediment cover. In Slice 3, a small NE-SW trending anticline separating the SON and SOS canyons appears to have no Pink or Blue unit sediment cover and the SOS channel appears to incise the southwest flank of the anticline (Figs. 3.6C and 3.7). The only core recovered from a portion of the slope with a steep gradient is GC 22-25, and a lack of turbidites < 23.3 ka in this core (Figs. 3.8 and 3.11) may be indicative of either bypass due to steep channel gradient or sediment starvation caused by infilling of the upslope ponded basin.

On the lower slope, deformation on short length scales (< 1 km) may trigger hydraulic jumps that produce the mounded bathymetry shown in Fig. 3.3 and also observed in the slope map in Fig. 3.2D. The northern extent of these mounds was imaged by dip Line 11 (Fig. 3.5A) as landward-migrating mounded reflectors (Fig. 3.5A). Note that the landward-migrating mounds are observed just landward of the basin deposits. These mounds are similar to crescentic bedforms located at the channel-lobe transition zone in the adjacent San Mateo Canyon and have been interpreted as cyclic steps (Kostic, 2011; Covault et al., 2014; Covault et al., 2017). Cyclic steps are large-scale, upstream-migrating, wave-like bedforms with wavelengths of 100's to 1000's of m and are typically observed in unconfined submarine environments (Covault et al., 2017). In the San Mateo Canyon (Covault et al., 2014) and in model simulations (Kostic, 2011), cyclic steps are located at the decrease in gradient at the channel-lobe transition zone (Covault et al., 2017). Cyclic steps that are oriented orthogonal to the canyon, such as the ones observed here,

are typically initiated by large turbidity currents (Normark et al., 2002; Covault et al., 2017). In this study area, cyclic steps are observed in the lower kilometer of the SON profile (Fig. 3.2A), as the SON channel widens (Fig. 3.2D). In contrast, cyclic steps are observed throughout the steep lower slope in the SOS profile (Figs. 3.2B and 3.3) and the gradient map of the SOS lower slope exhibits much more variability in downslope gradient (Fig. 3.2D). In a manner similar to the San Mateo Canyon, subsurface folding observed in dip Line 12C (Fig. 3.5B) caused by deformation along the San Mateo Fault Zone (Conrad et al., 2018) may create rugose bathymetry that causes turbidity currents to undergo hydraulic jumps necessary for the formation of cyclic steps (e.g., Ryan et al., 2009; Covault et al., 2017). The increased bathymetric rugosity caused by deformation and cyclic steps may play an important role in deposition along submarine channels, as has been documented in Brazil (Qin et al., 2016; Gamboa et al., 2015).

The levee deposits recovered in our core dataset may additionally be affected by flow filtering, which is the process by which overbank deposition contributes to the loss of mud and the increase in relative sand concentration downslope (McHargue, 2011). It is plausible that turbidites in downslope cores exhibit increases in grain size due to flow filtering; however, our levee cores are located at varying distances from the channel thalweg and direct comparisons cannot be made.

When autogenic processes such as flow filtering are complicated by allogenic elements such as gradient, ponded basins, and wide shelves, the record of turbidite emplacement becomes increasingly difficult to disentangle. As such, paleoseismology studies that rely on turbidite emplacement records (e.g., Goldfinger et al., 2003, 2007) should be approached with caution. The most conclusive results of this study confirm findings of regional scales from Covault et al. (2007, 2010) and Normark et al. (2009) and the effects of local ponded basins *sensu* Prather (1998) and Damuth and Olson (2015). The wide shelf offshore San Onofre likely prevents terrigenous supply to the deep sea during the post-glacial transgression and highstand, whereas the narrow shelf offshore Dana Point remains connected to sediment sources and has allowed for the recent

emplacement of turbidites within the past 1000 years. On scales finer than 1 km, the dynamics of tectonic deformation and gradient can explain variances in depositional timing from individual cores. Despite recent advances in linking modern flow processes to their deposits (e.g., Xu et al., 2010; Symons et al., 2017; Maier et al., 2019), we still do not completely understand down-canyon variability in turbidity current flow and the preservation of facies adjacent to canyons. Even though the margin offshore of Dana Point has likely experienced less deformation than offshore San Onofre, the record of turbidite emplacement is difficult to disentangle due to channel gradient and autogenic processes. As such, individual core records from the much more complex margin offshore of San Onofre are affected not only by breaks in channel gradient, but also by tectonically-controlled ponded basins. Turbidites offshore this tectonically active margin could theoretically record recent deformation. Nevertheless, turbidites offshore of San Onofre are  $> 8$  ka and fail to record historical earthquakes such as the 1933 Long Beach earthquake. This also supports the hypothesis of Sahakian et al. (2017) that the San Onofre segment has been inactive for much longer ( $> 10$  ka) than other segments the NIRC Fault Zone.

A disconnect persists between the ages of the cores, the recovered length of the cores, and the resolution of the Sparker 2D and 3D profiles. Despite advances in coring technology, piston cores and gravity cores are still not able to recover cores long enough to resolve sediment packages older than the Pink Unit or sediment offset by faulting. Without deeper cores, it is difficult to constrain margin evolution on the timescales imaged in the seismic reflection data.

### **3.6 Conclusion**

This study draws comparisons between small end-member canyons within the ICB. Dana Point Canyon can be considered a shore-proximal canyon with minimal tectonic deformation on the continental slope. As evidenced from dated turbidite deposits, this canyon has remained

active during the most recent lowstand, sea-level transgression, and highstand. In contrast, the San Onofre North and South canyons are separated from the coast by a wide  $\sim 10$  km shelf that is characterized by extensive deformation. Shelf widening offshore of San Onofre is caused by a left step along the right-lateral Newport Inglewood/Rose Canyon Fault (e.g., Maloney et al., 2016; Sahakian et al., 2017). This broad feature inhibits sand supply to the SON and SOS canyons after 8 ka and these canyons are predominantly active during MIS 2. Over lateral distances  $< 1$  km, variability in turbidite emplacement timing can be attributed to ponded basins, small anticlines that promote bypass, and increases in gradient. These basins were likely formed by crosscutting faults in the San Mateo Fault Zone. Gradient and autogenic processes of turbidity flows may play an important role controlling the grain size of turbidites. Thus, allogenic processes acting on a range of scales muddies interpretations of the turbidite record as paleoseismic indicators.

### **3.7 Acknowledgements**

This project was funded by the California Public Utility Commission through Southern California Edison. Many thanks to the crew of the R/V Thompson and core technicians at Oregon State University for assisting with the collection of these cores, the crew of the R/V New Horizon and R/V Melville for assisting with the acquisition of seismic profiles and swath bathymetry, Geotrace Technologies and NCS Subsea Inc. for processing seismic data, and Alex Hangsterfer at Scripps for aiding with core curation. Leanne Hirsch, Mackenzie Roberts, and Lana Graves processed the cores and sampled benthic and planktonic foraminifera for radiocarbon age dating. Funding for six radiocarbon ages was provided by the Scripps Institution of Oceanography Department Graduate Student Excellence Research Award.

This work has been submitted for publication in: **Wei, E.A., Holmes, J.J., and Driscoll, N.W., In Review. Strike-slip Transpressional Uplift Offshore San Onofre, California In-**

**hibits Sediment Delivery to the Deep Sea. *Frontiers in Earth Science Special Publication, Sedimentary System Responses to External Forcings: A Process-Based Perspective.*** The dissertation author was involved in acquisition, processing, and interpretation of part of the data that forms the basis of this chapter. The dissertation author is secondary author on this publication.

## **Chapter 4**

# **New Three-Dimensional P-Cable Seismic Data Image the Geometry and Fault Interaction of the San Mateo and San Onofre Trends Offshore Southern California**

### **4.1 Abstract**

Compressional deformation observed along the San Mateo (SMT) and San Onofre trends (SOT) in southern California has been explained by two opposing structural models, which have very different hazard predictions for the coastal region. One model predicts that the deformation is transpressional in a predominantly right lateral fault system with left lateral step-overs. Conversely in the alternative model, the deformation is predicted to be compressional associated with a blind thrust that reactivated detachment faults along the continental margin. State-of-the-art

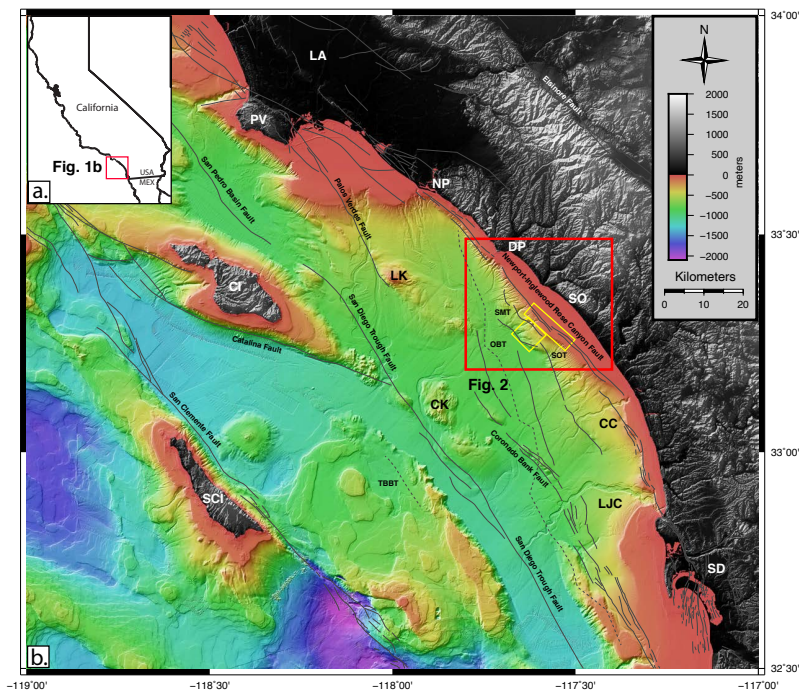
3D P-Cable seismic data were acquired to characterize the geometry and linkage of faults in the SMT and SOT. New observations gained from these data provide evidence that deformation along the slope is more consistent with step-over geometry than a regional blind thrust model. For example, regions in the SOT exhibit small scale compressional structures that deflect canyons along jogs in the fault segments across the slope. The deformation observed in the SMT along northwesterly trending faults has a mounded, bulbous character in the swath bathymetry data with steep slopes ( $\sim 25^\circ$ ) separating the toe of the slope and the basin floor. The boundary between the toe of the slope and the basin floor is much more gradual away from this region. The faulting and folding in the SMT are very localized and occur where the faults trend more northwesterly (average trend  $\sim 285^\circ$ ) with the deformation dying away both towards the north and east. The SOT faults trend more northerly (average trend  $\sim 345^\circ$ ) and the boundary between these fault systems is abrupt. Shorter faults with an average trend of  $\sim 40^\circ$  are observed in the boundary zone between the SMT and SOT and appear to be rotated bookshelf faults recording right lateral displacement. Onlapping undeformed turbidite layers reveal that the deformation is inactive and radiocarbon dating suggests deformation ceased in the middle to late Pleistocene. In summary, tectonic deformation along the SMT and SOT is best explained by left lateral step-overs along the predominantly strike-slip fault systems. The lack of evidence for a blind thrust underlying the southern California margin reduces the hazard for coastal regions because there would be no hanging wall effects during an earthquake and nearby slip rates would be reduced.

## 4.2 Introduction

Southern California's complex tectonic evolution is recorded in the offshore basins and deformation of the Inner California Borderland (ICB). From the late Oligocene/early Miocene, the cessation of Farallon plate subduction ushered in a tectonic sequence of block rotation and ex-



tension. Since the late Miocene to early Pliocene the margin has been overprinted by right-lateral strike-slip motion, often on reactivated Mesozoic structures. The majority of the slip budget between North America-Pacific plates is accommodated by onshore faulting (primarily the San Andreas, San Jacinto, and Elsinore fault systems); however, approximately 5-8 mm/yr, or nearly 15% of relative plate motion, is partitioned offshore between a network of northwest-trending strike-slip faults complexes ranging from just east of San Clemente Island to the coastline (Bennett et al., 1996; Ryan et al., 2012; Sahakian et al., 2017) (Figure 4.1).

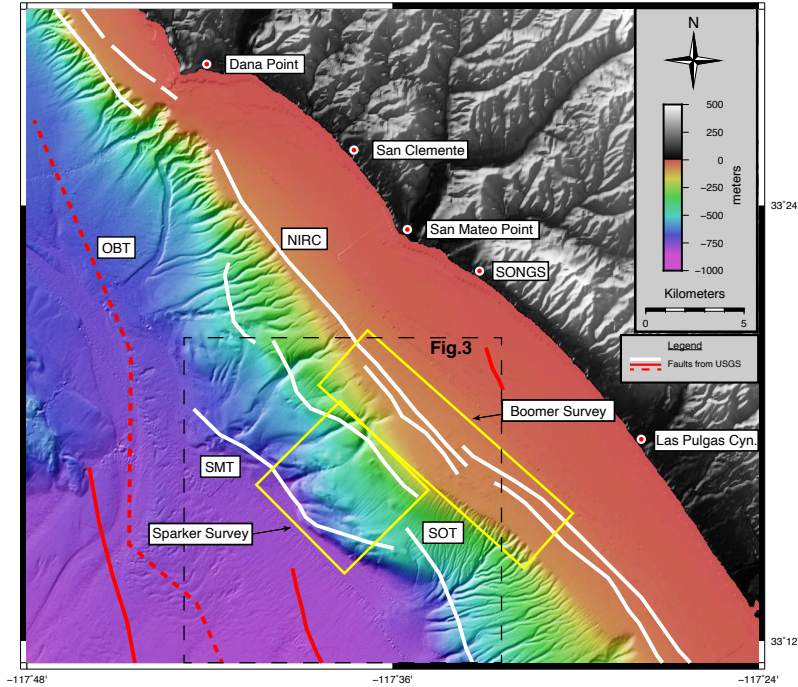


**Figure 4.1:** (a.) Regional map of California State showing the location of the Inner California Borderland - red box. (b.) Area map of Inner California Borderland (ICB) relative to the southern California coast. Red box outlines area shown in Figure 4.2. Yellow rectangle outlines the survey areas. Scale for topography and bathymetry is shown. Solid and dashed gray faults are from USGS Fault and Fold database (USGS, 2006). Dashed faults denote possible blind thrusts. Bathymetry from Dartnell et al. (2015). Major fault systems are labeled. Abbreviations are: CC - Carlsbad Canyon; CI - Catalina Island; CK - Crespi Knoll; DP - Dana Point; LA - Los Angeles; LJC - La Jolla Canyon; LK - Lasuen Knoll; NP - Newport; OB - Oceanside blind thrust; PV - Palos Verdes; SC - Scripps Canyon; SCI - San Clemente Island; SD - San Diego; SMT - San Mateo Trend; SO - San Onofre; SOT - San Onofre Trend; TB - Thirtymile Bank blind thrust.

Legg and Kennedy (1979) divided the major strike-slip fault systems of the ICB into four distinct subparallel groups. The group passing closest to the southern California coast, the Newport-Inglewood Rose Canyon fault system, consists of several discontinuous segments characteristic of wrench faulting (Moody and Hill, 1956). The Newport-Inglewood Rose Canyon system is a vertical right-lateral strike-slip system that runs nearly 120 km along the continental margin. The system runs onshore from downtown San Diego to La Jolla, then strikes roughly northwestward about 10 km off the coast until reemerging onshore at the San Joaquin Hills near the community of Newport Beach (Sahakian et al., 2017) (Figure 4.1). Paleoseismological work published by Lindvall and Rockwell (1995) reveals a Holocene slip rate of 1.5-2.0 mm/yr on the southern onshore segment. The slip rate for the northern onshore segment is 0.35-0.55 mm/yr based on cone penetration tests (Grant et al., 1997) and well data (Freeman et al., 1992).

ICB fault systems are in close proximity to the California cities of Los Angeles, Orange, San Diego, and Tijuana, Mexico. With a combined population of greater than 15 million people (Wilson et al., 2010), these communities together constitute some of the most densely populated coastline in North America. Accurate determination of seismic hazard relies on a comprehensive understanding of several fault parameters including slip-rate, geometry, and kinematics (Conrad et al., 2018). In recent years, high-resolution seismic data acquisition targeting specific fault systems has added considerable information to models of fault segmentation and constraints in the region, but there are still fault systems in the ICB region that remain poorly constrained today, including systems located near populated areas.

We conducted a high-resolution 3D multichannel seismic (MCS) survey of the San Onofre and San Mateo trends offshore southern California to determine if these features are caused by low-angle thrusting and compression or transpression along steeply dipping strike slip faults. This paper presents the results of our analysis of these data. (Figures 4.2 & 4.3)

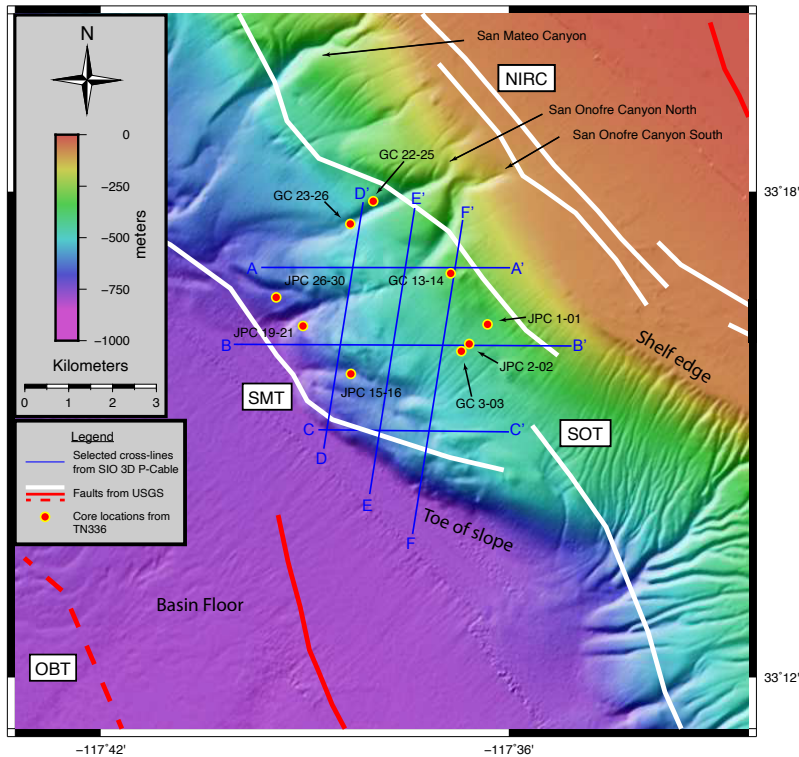


**Figure 4.2:** Location map of survey area off San Onofre and coastal communities of Dana Point and San Clemente. Location of Las Pulgas Canyon within Marine Corps Base Camp Pendleton is also shown. Survey area bounds on continental shelf and slope are labeled and outlined with yellow rectangles. Shown here in white are segments of the Newport-Inglewood Rose Canyon (NIRC) fault system, San Mateo trend fault system (SMT), and San Onofre trend fault system (SOT). Black dashed line outlines area shown in Figure 4.3. All fault segments from USGS Fault and Fold database (USGS, 2006). Bathymetry from Dartnell et al. (2015). Location with respect to ICB is shown in Figure 4.1. Abbreviations are: NIRC - Newport-Inglewood Rose Canyon fault; OBT - Oceanside blind thrust; SMT - San Mateo trend; SOT - San Onofre trend.

## 4.3 Methods

### 4.3.1 3D Seismic Reflection Acquisition and Processing

3D multichannel seismic reflection (MCS) has been the ideal method of data acquisition of the oil and gas industry for several decades. 3D data permits a more complete visualization of fault geometry and subsurface structure and recently technological advances have allowed for the development of portable state-of-the-art 3D MCS systems that can be deployed from Ocean-class research vessels of choice (Ebuna et al., 2013; Eriksen et al., 2015). These systems promise

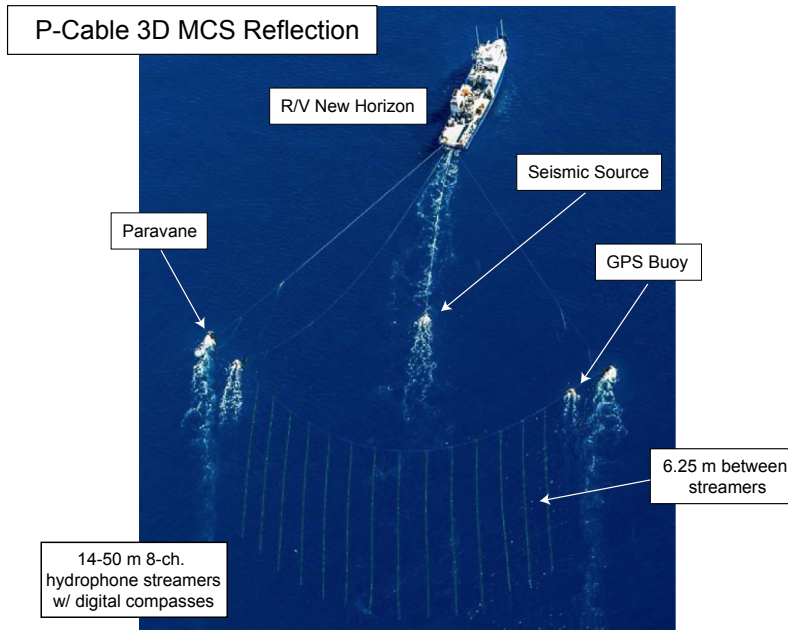


**Figure 4.3:** Detailed location map of survey area off San Onofre, California, with local offshore submarine canyons, and geomorphic features labeled. White solid lines represent segments of Newport-Inglewood Rose Canyon (NIRC) fault system, San Mateo trend fault system (SMT), and San Onofre trend fault system (SOT). All fault segments from USGS Fault and Fold database (USGS, 2006). Bathymetry from Dartnell et al. (2015). Dark blue solid lines denote locations of transects shown in the figures. Also shown are sampled core locations from the TN336 cruise. Cores prefixed "BB" are gravity cores. "JPC" are jumbo piston cores. Location with respect to Abbreviations are: NIRC - Newport-Inglewood Rose Canyon fault; OBT - Oceanside blind thrust; SMT - San Mateo trend; SOT - San Onofre trend.

high-resolution data at lower costs than that of standard 3D MCS deployments (Planke et al., 2009a, 2009b).

One such portable high-resolution system, the P-Cable system developed by Geometrics, Inc., employs 14 short (50 m) streamers attached to a cross-cable (Figure 4.4) (Crutchley and Kopp, 2018). The cross-cable is kept under tension by two one-ton paravanes attached to the ends of the cable and both port and starboard sides of the stern via a tow cable. Attached to the cross-cable are fourteen 50 m long solid-core digital streamers, each containing eight hydrophones. At the head and end of each streamer are digital compasses with depth sensors. The target data

horizontal resolution, based on bin size and fold, was 6.25 m. This was dictated by spacing between streamers and spacing between hydrophones in each streamer (Ebuna et al., 2013).



**Figure 4.4:** Aerial photo of Scripps Institution of Oceanography’s Research Vessel New Horizon towing the P-Cable 3D MCS array during NH1323 in the eastern Gulf of Catalina, with major components of system labeled.

The use of short streamers in the P-Cable array allow for greater operational maneuverability during acquisition and reduce operation concerns such as time spent in deployment and recovery. In post-processing, short streamers can result in decreased aliasing artifacts and higher resolution due to smaller crossline spacing (Brookshire et al., 2016). Shorter streamers are insufficient for extracting rock acoustic velocity via processes such as seismic inversion (Ebuna et al., 2013), however, and this must be kept in mind when designing a survey.

Although we did not depth migrate our 3D volumes due to a lack of well control, we adopted the following velocity function described by Ryan et al. (2009) to calculate depths for

estimations in this paper:

$$V = 1500 + 0.2438t + 8.2659 \times 10^{-5}t^2$$

This function was derived using interval velocities measured from 2D MCS profiles during Jebco cruise J188SC (Triezenberg et al., 2016; MMS, 1997), including profiles that crossed our survey areas.

Survey array geometry was tracked by using a set of GPS transmitters positioned at several points on the system: on the paravanes, on the ends of the cross cable, on the seismic source, and on the vessel itself. Tracked changes in system geometry were then corrected during processing.

We collected 2D seismic reflection data of the continental shelf and slope off the coast of San Onofre, California in late 2013 aboard the R/V New Horizon (NH1320). This 2D data was processed and analyzed to assist in selecting candidate locations for a focused 3D survey. Guided by our 2D data observations, we acquired the first high-resolution 3D data set that images the fault segments offshore of this region of southern California (Figures 4.1 & 4.2), using a P-Cable array (survey acquisition parameters are listed in Table 1 and complete acquisition report is included in Appendix B) towed from the stern of R/V New Horizon (NH1323).

We acquired data in two survey areas: a 52.5 km<sup>2</sup> rectangular grid with coverage over the continental shelf and self-break, and a 39 km<sup>2</sup> square grid, targeted to maximize imaging over the continental slope, and located due west of the rectangular grid. The continental shelf grid was designed to provide maximal coverage of the Newport-Inglewood Rose Canyon fault system in a region where the shelf widens anomalously compared to the trend of narrow-width shelf along the margin between La Jolla and the San Pedro Shelf, south of Long Beach (Figures 4.1 & 4.2).

The shelf survey data were acquired in depths ranging from 44-360 m, while the shelf data was acquired in deeper waters from 182 m to nearly 800 m. Due to the differing depth profiles of each survey, two low-energy (2-2.4 kJ) acoustic sources were employed, one for each survey. For

the shelf survey, a boomer source was employed, and a sparker source was used as an acoustic source on the slope survey. Shot intervals for the boomer survey constrained a bin size of 3.125 m, while the sparker survey acquired data with a bin size of 6.25 m.

For the boomer survey, a 1000 ms record length was digitized, however after processing, reflectors were resolved to 800 ms two-way traveltime (TWT). A 2000 ms record length was digitized for the sparker volume, but much of the data analysis was performed between 0 and 1600 ms TWT where data resolution and imaging were optimum. Complete acquisition parameters are listed in Table 1.

We measured a peak frequency of 125.025 Hz (full frequency response graph shown in supplemental material), which allowed us a minimum vertical resolution of 3 m. Shallow structure and deformation was overprinted and masked by the strong reflectors inherent in the seismic source signature.

The 3D data was processed by Geotrace Technologies, a petroleum services company, given the enormous size of the data volume (20 GB per seismic attribute volume) and their previous experience with processing 3D P-Cable data acquired on previous surveys (Crutchley and Kopp, 2018). Technicians and science crew conducted on-board real-time QC of both seismic reflection and GPS data during acquisition. Once on shore, technicians employed a sequence of processing steps to improve and enhance data quality including multiple elimination, normal move-out (NMO) at 1480 m/s, post-stack migration, and application of a post-stack time-variant filter (TVF) to remove high-frequency noise (processing steps are listed in Table 4.2; Complete processing details are located in Appendix B).

Processed data were compiled into amplitude and similarity-attribute volumes for interpretation. Amplitude volumes image reflectors based on the relative impedance contrast in a trace, while similarity attribute assigns a decimal value to a bin based on the correlation between waveform and amplitude of two or more different nearby traces (Bahorich and Farmer, 1995). In

**Table 4.1:** List of acquisition parameters used for P-Cable 3-D multichannel seismic reflection system.

P-Cable 3-D Acquisition Parameters	
Number of Streamers	14
Streamer Spacing	6.25 meters
Streamer Length	50 meters
Channels per Streamer	8
Group Interval	6.25 meters
Streamer Type	Geometrics GeoEel
Width of Active Spread	87.5 meters
3D Swath Width	43.75 meters
Bin Size	3.125 x 3.125 meters
Nominal Subsurface Fold	8
Sample Rate	0.25 milliseconds
Record Length	0.75 to 1.0 seconds
Recording Format	SEGY
Source Type	AP3000 Triple-Plate Boomer
Source Depth	0.5 m
Shot Interval	6.25 meters
Peak Frequency	125.025 Hz

similarity data, a correlative value of 1 represents the state of "perfectly similar", while a value of 0 represents the state of "completely dissimilar". While amplitude volumes are useful for imaging and mapping stratigraphic offset within a vertical section, a similarity attribute dataset is valuable for imaging large-scale discontinuities, such as sharply dipping beds, faults, and paleochannels, in an isochron ("time-slice") view.

Additionally, a parameterized dip-steered median filter was applied to the amplitude volume using OpendTect Seismic Interpretation Suite, and following a workflow described by Kluesner and Brothers (2016). This had the effect of increasing reflector continuity and facilitating data interpretation, which in turn, increased confidence in our interpretations.

We followed an iterative process for interpretation. Initial interpretations were made by interpreting on every 20-50 dipline and strikeline vertical profiles of the amplitude data. We used



**Table 4.2:** List of onshore processing steps.

1	Reformat SEG Y - 0.25 or 0.5 ms raw shot gathers
2	Low cut filter 45(18) Hz(dB/Oct)
3	Temporal resample to 1ms sample rate with anti-alias filter
4	Bad trace edits
5	De-noise with automatic spike removal in Shot domain - 2 iterations
6	2D SRME on common channel/shots
7	Load data to a 3D pre stack volume (3.125m x 3.125m)
8	Apply 1480 m/s primary NMO
9	3D stack
10	1D SRME and subtract
11	Interpolation of empty bins with SNIP
12	Post stack, pre-migration noise attenuation with automatic spike removal, FDNA, and FXY
13	Post stack Kirchhoff migration
14	Time Variant filtering
15	Amplitude balancing: Measured exponential gain
16	Gun and cable static correction
17	SEG Y - Final Filtered Migrated Stack
18	Scaling: 400ms Iterative AGC - optional
19	SEG Y - Final Filtered Migrated Scaled Stack

lines with arbitrary azimuths on occasion to verify segment trends and picks. Next, we confirmed our initial interpretations in similarity attribute time-depth slices, and finally we restarted the process to further constrain fault length and character. In some cases, fault smoothing, and pick decimation was necessary in order to remove outliers.

This paper is mainly concerned with our analysis of fault segments imaged in the sparker survey only. Faults imaged in the boomer survey on the continental shelf are discussed only briefly and reported on in more detail in Holmes et al. (in review).

### 4.3.2 Age Control

Historically, the shelf and slope near San Onofre have not been well-sampled. Conrad et al. (2018), however, was able to map the Quaternary boundary in the region using unpublished

Caldrill program well data acquired by industry in the 1970s and now held by the US Bureau of Safety and Environmental Enforcement.

At various locations throughout the ICB we collected 64 Gravity (GC) and Jumbo-Piston Cores (JPC) in 2016, as part of a regional study designed to provide age constraints on shelf/slope evolution, and recent faulting (TN336). Possible piercing points, such as faults and paleochannels were selected as coring targets using previously collected 2D multichannel seismic and CHIRP data. Trigger cores were also acquired and logged. In some cases, positional drift caused the cores to be slightly offset from the profiles, in which case the core locations were projected orthogonally onto the profile. Once on-board, intact cores were analyzed for magnetic susceptibility, gamma density, P-wave velocity, and resistivity using a GeoTek Core-logger. Cores were then split and observations of color, grain size, sediment structures, and general lithology were recorded.

Forty samples were selected for radiocarbon dating due to proximity to the survey areas. Thirty-four of those samples were analyzed at the National Ocean Sciences Accelerator Mass Spectrometry facility at the Woods Hole Oceanographic Institution (WHOI) in Massachusetts and resulted in ages using the Libby half-life of 5568 years, based on the convention described by Stuiver and Polach (1977). The other six samples were analyzed at the W.M. Keck Carbon Cycle Accelerator Mass Spectrometry facility at the University of California, Irvine (UCI) following the same convention. Non-fragmented planktonic foraminifera that had not undergone diagenesis were preferentially collected. All  $^{14}\text{C}$  ages were calibrated using the CALIB software, version 7.0.4 (Stuiver and Reimer, 1993).

Ages of planktonic foraminifera of less than 12000 yr were calibrated with a reservoir age of 800 yr. For planktonic foraminifera greater than 12000 yr a reservoir age of 1100 yr was used (Southon et al., 1990; Kienast and McKay, 2001; Kovanen and Easterbrook, 2002) and 1750 years for a benthic reservoir age as also used by Covault et al. (2010). For cores containing more than two dates, age-depth models were generated using the Bacon age-modeling software package, version 2.3.3 (Blaauw and Christen, 2011) using these reservoirs as parameters.

Of the forty tested samples, twelve are from a collection of short gravity cores and jumbo piston cores collected on the middle to upper continental slope, and the rest were jumbo piston cores acquired on the lower slope within the survey area (Figure 4.3). Two samples, both acquired on the slope below the widest part of the shelf, were greater than 52,000 years old and thus eliminated as radiocarbon dead. Based on analysis of the remaining samples, sedimentation rates (Table 3 & 4) were calculated. Sedimentation rates were highly variable, based on sample depth and core location. Cores sampled from the widest part of the upper continental slope showed extremely low sedimentation rates. The highest sedimentation rates were computed on cores that were taken within drainage channels or on the continental shelf.

Covault et al. (2010) reported a sedimentation rate of 0.33 mm/yr for their piston core "H4", located at the toe of the continental slope approximately 10 km northwest of our survey area, at a sample depth of 374-384 cm. Using extrapolated sedimentation rates calculated from JPC 15-16, located about 1.8 km from the slope-basin interface, we calculated a sedimentation rate of approximately 0.25 mm/yr at the toe of the continental slope within the survey area.

**Table 4.3:** TN336 Cores, Radiocarbon Ages, & Sedimentation Rates on San Onofre Upper / Middle Slope.

Core ID	Sample Depth (cm)	Description of Foraminifera	Calibrated Radiocarbon Age (yrs)	Age Error (yrs)	Minimum Sedimentation Rate (mm/yr)	Maximum Sedimentation Rate (mm/yr)	Testing Laboratory
GC 3-03	165-170	Planktonic	16,300	50	0.103	0.103	WHOI
GC 13-14	17-21	Planktonic	40,000	960	0.005	0.005	WHOI
	39-43	Planktonic	Too old	–	–	–	WHOI
GC 22-25	133-137	Planktonic	22,944	78	0.059	0.059	UCI
	256-260	Planktonic	38,700	910	0.065	0.068	WHOI
GC 23-26	127-131	Planktonic	9,180	25	0.140	0.141	WHOI
	210-214	Planktonic	9,840	30	0.215	0.216	WHOI
JPC 1-01	15-19	Benthic	7,880	25	0.019	0.019	WHOI
	185-189	Benthic	19,950	90	0.092	0.093	WHOI
JPC 2-02	43-47	Planktonic	18,043	69	0.025	0.025	UCI
	157-161	Planktonic	39,347	395	0.040	0.041	UCI
	230-234	Planktonic	Too old	–	–	–	UCI

## 4.4 Results

The San Mateo trend (SMT), San Onofre trend (SOT), and Carlsbad trend (CT) are contractional structures (anticlines and faulted anticlines) that have been attributed to the Oceanside blind thrust (OBT; Rivero and Shaw, 2011), or alternatively to localized contraction associated with strike-slip faulting on the Newport Inglewood-Rose Canyon fault zone (Crouch and Bachman, 1989; Fisher and Mills, 1991). The San Mateo and San Onofre trends are mapped west of the Newport-Inglewood-Rose Canyon fault zone, offshore from San Onofre, whereas the Carlsbad trend extends farther south and terminates offshore north of Del Mar. Rivero and Shaw (2011) interpret these trends as being soling into the Oceanside blind thrust at depth and interpreted the structures as forethrusts. These trends have been identified as active structures that produce bathymetric relief on the seafloor (Rivero and Shaw, 2011; Maloney et al., 2016).

An alternative to the blind thrust model is transpression along strike-slip fault systems where left lateral step-overs occur. Ryan et al. (2012) concludes that the 1986 Oceanside earthquake was located in an area of transpression associated with a restraining bend in the right-lateral, strike-slip San Diego Trough fault. Additionally, Ryan et al. (2009) put forth an alternative explanation for the observed compressional deformation associated with the Oceanside blind thrust that involves a clockwise rotating block located between the Coronado Bank fault zone and Newport Inglewood-Rose Canyon fault zone. They reported areas of both extension and compression in seismic data acquired within the ICB region and therefore propose that changes in deformation are explained better by rotation associated with large strike-slip faults versus regional thrust systems. Here we present new high-resolution 3D seismic reflection data across the San Mateo and San Onofre trends to discern between the two end member models: (1) the deformation is caused by a splay of the Oceanside blind thrust (Rivero et al., 2011) or (2) transpression along jogs in the offshore strike slip fault systems explains the deformation (e.g., Maloney et al., 2016).

**Table 4.4:** TN336 Cores, Radiocarbon Ages, & Sedimentation Rates on San Onofre Lower Slope.

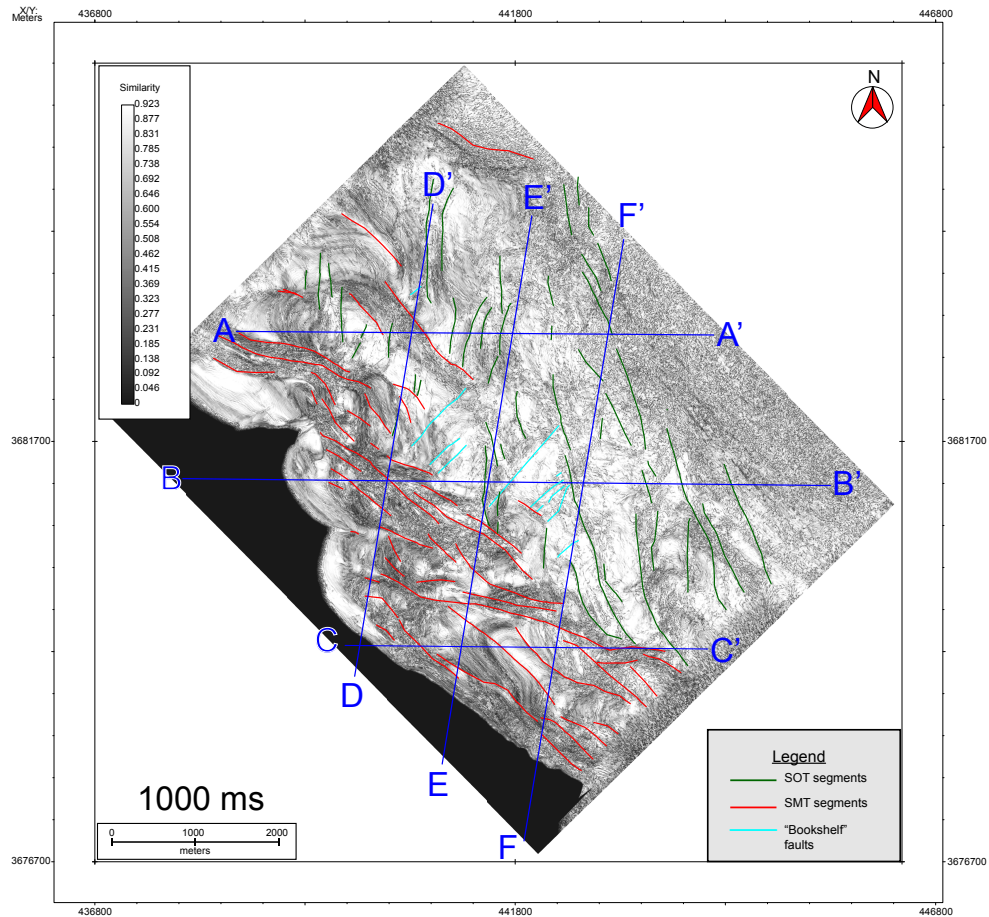
Core ID	Sample Depth (cm)	Description of Foraminifera	Calib. Radiocarbon Age (yrs)	Age Error (yrs)	Min. Sed. Rate (mm/yr)	Max. Sed. Rate (mm/yr)	Testing Laboratory
JPC 15-16	185-189	Benthic	13700	45	0.14	0.14	WHOI
	202-205	Benthic	13650	55	0.15	0.15	WHOI
	207-213	Benthic	35500	620	0.06	0.06	WHOI
	207-213	Planktonic	14800	60	0.14	0.14	WHOI
	214-218	Benthic	14450	45	0.15	0.15	WHOI
	228-232	Benthic	14150	60	0.16	0.16	WHOI
	315-320	Planktonic	15600	55	0.20	0.20	WHOI
	315-320	Benthic	16650	65	0.19	0.19	WHOI
	330-334	Benthic	17100	65	0.19	0.19	WHOI
	330-334	Planktonic	15950	60	0.21	0.21	WHOI
JPC 19-21	407-411	Benthic	16500	50	0.25	0.25	WHOI
	346-350	Benthic	13750	45	0.25	0.25	WHOI
	357-361	Benthic	14150	40	0.25	0.25	WHOI
	530-533	Benthic	17800	80	0.30	0.30	WHOI
	546-550	Benthic	18150	75	0.30	0.30	WHOI
	727-730	Benthic	23700	150	0.31	0.31	WHOI
	737-740	Benthic	24200	160	0.30	0.31	WHOI
	766-769	Benthic	25600	140	0.30	0.30	WHOI
	772-776	Benthic	25900	200	0.30	0.30	WHOI
	772-776	Planktonic	30100	320	0.25	0.26	WHOI
JPC 26-30	208-212	Benthic	12890	72	0.16	0.16	UCI
	428-432	Benthic	19959	85	0.21	0.22	UCI
	718-722	Benthic	25400	140	0.28	0.29	WHOI
	736-740	Benthic	26900	150	0.27	0.28	WHOI
	736-740	Planktonic	26000	130	0.28	0.29	WHOI
	842-844	Benthic	31900	390	0.26	0.27	WHOI
	849-852	Benthic	32300	410	0.26	0.27	WHOI
	913-916	Benthic	33700	490	0.27	0.28	WHOI

#### 4.4.1 Margin Morphology and Structure

The bathymetry data reveal a complex pattern of structural troughs and highs that are predominantly bounded by large fault systems (Figure 4.1). Toward the north, the shelf is wide offshore Palos Verdes/Long Beach with an abrupt change in shelf width moving south. Continuing south the shelf systematically widens from 2 km wide off Dana Point to 10 km wide offshore San Onofre; where the width diminishes to Carlsbad Canyon (Figure 4.1). Farther south, the shelf once again widens markedly south of the La Jolla Canyon. Along much of the margin the slope gradually grades into the basin floor (Figures 4.2 and 4.3). Southwest of the broad shelf offshore San Onofre, the slope exhibits a steep gradient at the juncture with the basin floor, with dips up to 25°. These steep dips are very localized and observed along features with a northwest trend. Also note the bulbous character of the seafloor just inboard of the toe of the slope; the bulbous morphology dies quickly away from this region with steep slopes. Furthermore, gullies in the region appear deflected away from this mounded seafloor (Figure 4.3).

Incised regions observed toward the northwest in the time slice at 1000 ms correlate with canyons imaged in the bathymetry data along the slope (Figure 4.5). The faults are identified based on reflector terminations and offset of acoustic packages (Figure 4.5). Faults have been color-coded according to their trends. Fault architecture and intersections are imaged by the 3D data volume. This portion of the margin is dominated by two major fault trends; the San Onofre trend faults are shown in green and San Mateo trend faults are shown in red. The turquoise faults exhibit a more easterly trend and are usually shorter. Note the abrupt boundary between SOT and SMT. SMT is mostly confined to the outer slope/toe of the slope with a more northwest orientation. SOT has a northerly trend towards the continental shelf with many fault segments. Deformation systematically increases with the greatest amount of deformation and folding at the intersection of toe of the slope and basin floor. In this manuscript, the flat-lying region at the toe of the slope is referred to as the "basin floor". Also shown are locations of arbitrary lines

extracted from the 3D volume featured in Figures 4.7 - 4.12. Lines were selected to be orthogonal to SMT and SOT segments and subparallel to the margin.

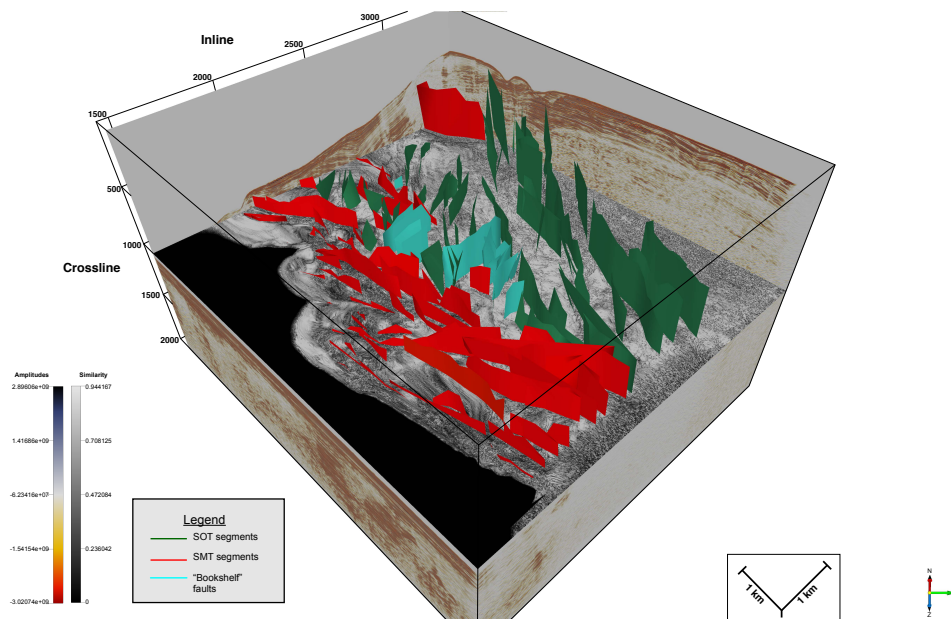


**Figure 4.5:** Time-slice view of sparker survey at 1000 ms. Time-slice is rendered using similarity attribute that highlights discontinuities such as faults, sharply dipping beds, and paleochannels. Interpreted fault segments are shown with solid lines and color-coded according to azimuth and character. Dark green faults trend northward, with steeply vertical dip in the San Onofre trend fault zone. Red fault segments trend towards the northwest, exhibit transpressional features, and are within the San Mateo trend fault zone. Light blue segments trend to the northeast and appear to accommodate rotation between the two fault zones. Dark blue lines with labels denote locations of vertical profile transects shown in later Figures.

Fault curtains can be constructed by tracing the faults throughout the 3D seismic volume, which captures how the fault plane changes across the margin, along the margin, and with depth trends (Figure 4.6). As shown in the time slice (Figure 4.5), SMT trends more to the northwest,



and the SOT trends more northerly; the curtains show that the trends exhibit minor variation with depth (Figure 4.6). In addition, 3D fault curtain figures help image fault segments and how they structurally relate to adjacent faults. Strike slip faults with steep dips are not well imaged in 2D vertical sections; however, in 3D data volumes, fault terminations and changes in acoustic character are also imaged in the time slice (e.g., map view). By examining faults in both vertical sections and in the timeslice, it further reduces the uncertainty of fault mapping, which increases the ability to define the fault architecture and interaction of neighboring segments.



**Figure 4.6:** 3D chair view of sparker survey area. View is due north, oblique to the continental shelf. Dipline and strikeline amplitude vertical profiles frame a timeslice at 1000 ms rendered in similarity attribute. Dipline and strikeline vertical profiles below timeslice are rendered in amplitude data. Green faults - San Onofre Trend fault system and trend towards the continental shelf where they intersect with Newport-Inglewood Rose Canyon (NIRC) fault system. Red faults - San Mateo trend fault system trending towards the northwest, subparallel to the continental margin.

Arbitrary line transects were constructed from the 3D data volume to image structures in dip sections (Figures 4.7, 4.8, and 4.9; downslope - orthogonal to structure) and strike sections (Figures 4.10, 4.11, and 4.12; along slope - parallel to structure). We will first describe the dip

sections from west to east (Figure 4.5). In arbitrary line D - D', there is a change in dip of the imaged reflectors just to the northeast of cross-line A - A'; that is, the reflectors along the margin exhibit a slight dip to the southwest before being folded and deformed with the regional dip being toward the northeast. The southwest dipping reflectors along the margin show little signs of folding and faulting. Continuing to the southwest the deformation increases with a broad antiform - synform pair. Along the northeast limb of the anticline, the stratigraphy is truncated at the seafloor and small gullies are imaged on the northeast limb and crest of the anticline. The antiform - synform pair is bounded to the southwest by a fault system near cross-line B-B'. Southwest of the fault there are acoustically transparent zones (Figure 4.10). Reflector continuity increases toward the southwest and is faulted and folded. Another fault system separates faulted and folded stratigraphy toward the northeast from flat lying reflectors toward the southwest.

Farther east, arbitrary line E-E' crosses the same two deformational structures (Figures 4.5 and 4.11). Once again there is a reverse in dip near crossline B-B'; however, the amplitude of the antiform - synform pair is less. Uprturned reflectors are fault bounded to the southwest and appear truncated at the seafloor. Continuing southwest, a well-developed antiform is imaged with its crest near cross line C-C'. The northeastern limb is faulted with small scale folds. Flat lying reflectors to the southwest are separated from the antiform by an eastward dipping fault (Figure 4.11). A reversal in reflector dip is also imaged by arbitrary line F-F' just to the northeast of cross-line C-C' (Figure 4.12). A faulted antiform - synform - antiform structure is observed in this region; the folding is tighter toward the toe of the slope in this region than imaged on the other arbitrary dip lines D-D' and E-E' (Figures 4.10, 4.11, and 4.12). An acoustic transparent zone separates the faulted anticline from the more flat-lying reflectors to the southwest. The reflectors terminate in this region and display a marked change in dip across the acoustically transparent zone.

The arbitrary strike lines (Figures 4.7, 4.8, and 4.9) image the antiform and change in dip of the reflectors, which occurs just east of cross-line D-D'. East of the change in dip the

reflectors are more continuous with minor faulting along the margin (Figure 4.7); west of the change in dip, fault and fold deformation increases markedly. The reflectors are truncated at the seafloor; a wedge of truncated reflectors infills the structural low where the reflectors change dip just east of cross-line D-D'. Onlapping reflectors are observed toward the west. Continuing south, the deformation is broader on arbitrary line B-B' with no clear change in dip (Figure 4.8). There is a slight decrease in slope moving from the margin in the east until the bathymetric high near cross-line D-D', where the slope again increases. Farther west, a package of acoustically laminated reflectors onlap the faulted and folded reflectors. Arbitrary line C-C' is farthest south and once again images the regional change in dip. A broad antiform is imaged in the central portion of the profile but is bounded to the east and west by regions that are more acoustically transparent introducing uncertainty.

Rose diagrams were generated to display the fault trends and dips in the data volume (Figure 4.13). In Figure 4.13a, the polar axis is fault azimuth and the radial axis is number of faults with this trend, fault trends were mapped in  $10^\circ$  bins. The radial axis for Figures 4.13b - 4.13d plots is the dip of the mapped faults in the 3D data volume. Three main fault trends emerge from the rose diagrams. The SMT faults have an average azimuth of  $\sim 285^\circ$ , with the SOT faults trending more northerly with an average azimuth of  $\sim 345^\circ$ . The turquoise faults have an average azimuth of  $\sim 40^\circ$  (Figure 4.13a). Most of the faults mapped in the 3D volume are steeply dipping (Figures 4.13b-4.13d), with dips ranging between  $63.9^\circ$  to  $90^\circ$ .

Bathymetry data of the region show the influence of these fault trends on the gullies and morphology (Figure 4.14). Scarps of the SOT faults are observed in the bathymetry data as well as uplifted regions where fault segments have left lateral jogs. The trend of the fault scarps observed in the bathymetry are consistent with the trend of the fault curtains from the 3D data volume (Figure 4.15). The large mounded features at the toe of slope are bounded by faults of the SMT trend and are oriented more toward the northwest than the SOT faults (Figures 4.15 and 4.16). The boundary between these features and the basin floor is extremely steep dipping at

almost  $25^\circ$  and they are spatially localized to this region of the margin. The boundary between the SOT and SMT faults is rather abrupt and the faults in either domain exhibit consistent strikes (Figures 4.13 and 4.15). The turquoise faults are oriented to the northeast with an average strike of  $\sim 40^\circ$  and occur within the domain of the SOT faults (Figure 4.15).

## 4.5 Discussion

The width of the continental shelf in southern California from Palos Verdes to La Jolla exhibits marked variability (Figure 4.1). The wider portions of the shelf offshore Mount Soledad, Penasquitos Lagoon (Hogarth et al., 2007; LeDantec et al., 2010), San Onofre (Holmes et al., in review), and Palos Verdes are regions where left lateral jogs occur along the predominantly right lateral fault systems offshore. Left lateral jogs along right lateral strike slip faults engenders transpression, often referred to as constraining bends. In contrast, a right lateral jog along a right lateral strike slip fault system creates transtension. The wide shelf offshore San Onofre is spatially coincident with a large anticline, which acts as a large dam to sediment traversing the inner shelf (Wei et al., in review; Holmes et al., in review). The large anticline also diverts sediment transport to the south where it appears to be trapped by the Oceanside and Carlsbad canyons (Figure 4.1). The littoral transport of sediment in this region of the shelf is to the south (LeDantec et al., 2010). Note that the Oceanside and Carlsbad canyons exhibit a more sinuous nature than the surrounding more linear canyons. The Oceanside and Carlsbad canyon heads intersect the shelf where its width is diminishing rapidly from north to south (Figure 4.1). Along-shore sediment transport intersecting the shelf edge as the shelf width diminishes might explain the location and morphology of the Oceanside and Carlsbad canyons. In a similar manner, sediment is shunted offshore into La Jolla Canyon due to the uplift of Mount Soledad, which acts as a natural groin to southerly sediment transport. The morphology of these sinuous canyons (e.g., La Jolla, Carlsbad,

and Oceanside) appears to occur where long-shore transport intersects the shelf edge and spawn gravity flows that sculpt and shape the canyons.

The smaller canyons imaged in the swath bathymetry are more linear (Figures 4.2 and 4.3). The slope offshore San Onofre where the 3D sparker data were acquired, appears to be less well incised by canyon systems, which is consistent with sediment damming and southward deflection by the anticline (Figure 4.3). In this region, the seafloor has a mounded, bulbous morphology. There is a large change in inclination near the deformed features at the toe of the continental slope, with angles reaching  $25^\circ$ . The steep slopes imaged in the bathymetry are extremely localized; other regions along the margin exhibit a more gradual transition from the toe of the slope to the basin floor (Figures 4.1-4.3). The localized nature of these features will be discussed further in a following section.

The 3D sparker survey was acquired along the continental slope to test between the two hypotheses to explain the observed deformation. As mentioned previously, the deformation observed along the slope has been proposed to record deep seated thrusting with eastward dipping splays shoaling off the main detachment (i.e., Oceanside Blind Thrust; Rivero and Shaw, 2011). Conversely, the observed compressional deformation also has been explained by a left lateral jog along the right lateral faults in the San Mateo trend (Crouch and Bachman, 1989; Fisher and Mills, 1991; Ryan et al., 2009; Maloney et al., 2016). The fault azimuth of the San Onofre and San Mateo trends is markedly different (Figures 4.5 and 4.6), with the San Mateo trend faults exhibiting a more northwest trend (average trend  $\sim 285^\circ$ ). Most of the fault planes mapped throughout the 3D volume (Figure 4.6) show little change in fault dip and trend with depth (Figure 4.6). The change in slope of the acoustic reflectors and degree of deformation observed in arbitrary lines D, E, F (Figures 4.10, 4.11, 4.12) is a direct result of the two orientations of the SOT and SMT.

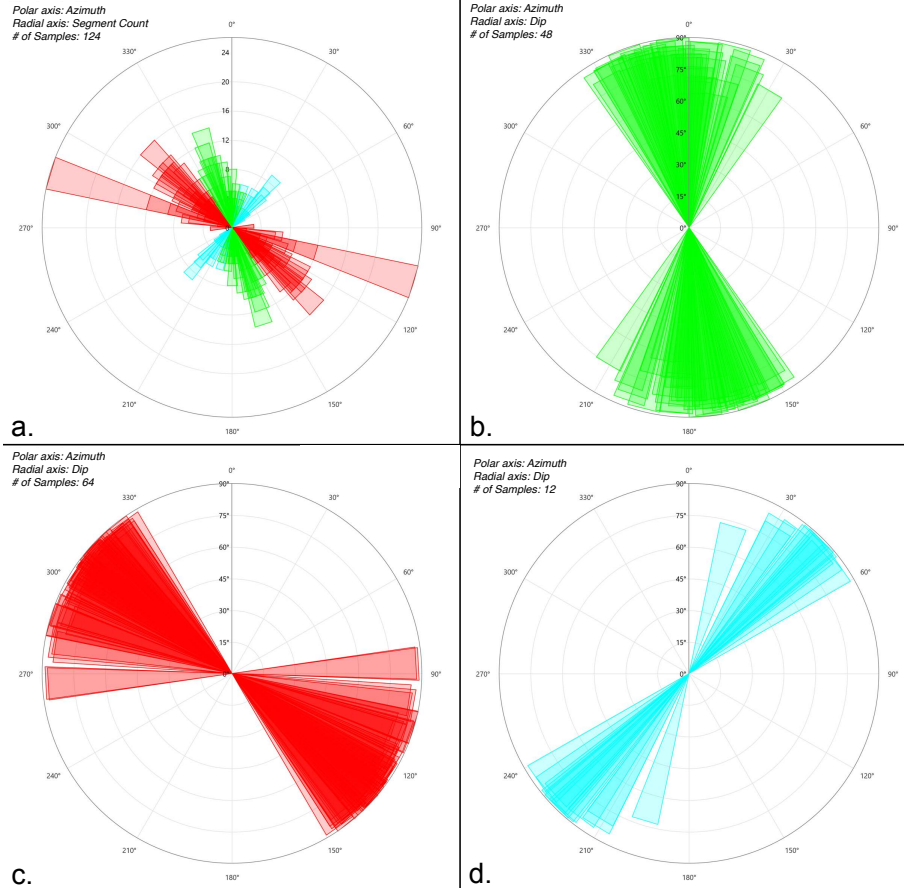
The arbitrary dip lines are oriented north-northeast (lines D, E, and F; Figure 4.5) roughly subparallel to the orientation of the SOT faults (average azimuth of  $\sim 345^\circ$ ) and more orthogonal

to the faults in the SMT (average azimuth of  $\sim 285^\circ$ ; Figure 4.13). Compressional faulting and folding are recorded by the acoustic reflectors imaged in the SMT region. The width of the anticline-syncline pair fold axis diminishes to the east from line D to arbitrary line F near the toe of the slope (Figures 4.10 - 4.12). Arbitrary strike lines A, B, C are more subparallel to the SMT faults and folds, thus the apparent wavelength of the deformation appears longer (Figures 4.7, 4.8, and 4.9). Note that along the arbitrary dip lines D, E, and F (Figures 4.10 -4.12), there are large dominant northeast dipping faults that bound the regional deformation and subordinate faults that appear to accommodate the localized deformation. These large faults extend close to the seafloor; however, there is no clear seafloor offset across the faults.

Constraining the relative age of deformation is difficult as the present-day seafloor exhibits erosional and structural truncation resulting from slumping, block rotation, and downslope canyon erosion. Nevertheless, flat lying deposits on the basin floor appear to onlap the deformation and suggest the deformation is moribund; an interpretation that is consistent with previous research (Figures 4.10 and 4.11; Maloney et al., 2016). Using an extrapolated sedimentation rate of 0.25 mm/yr, we measured the thickness of basin floor turbidites imaged on arbitrary line transects D-D', E-E', and F-F' and calculated the relative age of deformation to be between 360,000-438,000 yrs.

The SMT faults are oriented more northwest than the SOT faults and that difference in fault trend correlates closely with the change in the style and magnitude of the deformation (Figures 4.14 and 4.15). The NW trending mounded features at the toe of the slope are 2-4 km in length and 1-2 km in width recording a NE shortening direction. The mounded features are very localized along the margin and occur where there is marked change in trend (Figure 4.2). The localized deformation abruptly terminates at the basin floor with steep dips (up to  $25^\circ$ ). Such a steep contact with the basin floor is not observed elsewhere along the margin (Figure 4.1).

Localized deformation that correlates with an average fault azimuth of  $285^\circ$  along the SMT (Figure 4.15) is more consistent with a left lateral jog along a right lateral fault system than a regional blind thrust with splays that have surface expression. Rivero and Shaw (2011)



**Figure 4.7:** Rose diagrams of fault segments interpreted in the sparker survey data volume. (a.) Azimuth vs. number of fault picks for all interpreted faults. Fault picks are on radial axis, azimuth is on polar axis. Picks were made every 50 lines, so unbroken fault length can be inferred on radial axis. Fault segments were color-coded into three different categories depending on azimuth. Green faults - San Onofre trend (SOT). Red faults - San Mateo trend (SMT). Blue faults represent segments of rotational faults between the two fault systems. Fault segments lengths were largely consistent; however, SMT system contained longest fault segments at toe of slope. (b.) Graph showing azimuth vs. dip of segments categorized as belonging to the SOT. Measured fault dips ranged from  $63.9^{\circ}$  to  $89.8^{\circ}$  for 48 segments. (c.) Graph showing azimuth vs. dip of segments categorized as belonging to the SMT. Measured fault dips ranged from  $72.6^{\circ}$  to  $90^{\circ}$  for 64 segments. (d.) Graph showing azimuth vs. dip of segments categorized as belonging to connector faults between SMT and SOT. Measured fault dips ranged from  $73^{\circ}$  to  $89.3^{\circ}$  for 12 segments.

propose that the Oceanside blind thrust, and attendant splays extend from south of San Diego Bay to north of Dana Point. The deformation observed here is very localized with a lateral extent of approximately 12 kilometers.

Fault scarps in the SOT can be observed in the swath bathymetry data with compression pop-ups occurring along left lateral jogs, which appear to deflect canyons and gullies along the margin (Figure 4.14). Continuing northeast the SOT faults appear to connect up with faults mapped along the shelf edge in the 3D boomer data (Holmes et al., in review). In our preferred interpretation, the faults along the slope are the horse tail splay termination of the Newport Englewood Fault as the deformation is deflected westward away from the zone of compression on the shelf. Such a hypothesis is consistent with the lack of deformation and offset of the transgressive surface imaged in CHIRP and Sparker multichannel seismic data acquired offshore San Onofre (Sahakian et al., 2017; Klotsko et al., 2016).

## 4.6 Conclusions

Newly acquired 3D P-Cable MCS and bathymetry data along the slope offshore southern California place important constraints on the timing and architecture of the San Onofre and San Mateo trends. Conceptual models to explain the offshore deformation need to honor the following observations:

1. Mounded, bulbous morphology with steep slopes ( $\sim 25^\circ$ ) are observed at boundary between the toe of the slope and the basin floor; the deformation is very localized. The style and magnitude of the deformation is greatest along the SMT and dies away toward the north/northeast.
2. The steeply dipping faults in the SMT and the SOT exhibit markedly different trends and the boundary between the two trends is abrupt.
3. Localized compression in the SOT occurs as predicted at fault bends and step-overs (i.e., un-named faults). The transpressional features are observed in the swath bathymetry data



and appear to deflect canyons/gullies along the slope.

4. The SOT faults on the slope appear to be splays off the Newport Inglewood fault mapped on the shelf.
5. Shorter faults with an average trend of  $\sim 40^\circ$  are observed in the boundary zone between the SMT and SOT and appear to be rotated bookshelf faults recording right lateral displacement.
6. The lack of deformation in the flat lying onlapping sequences suggest deformation in the region is old (Late Pliocene/Pleistocene).

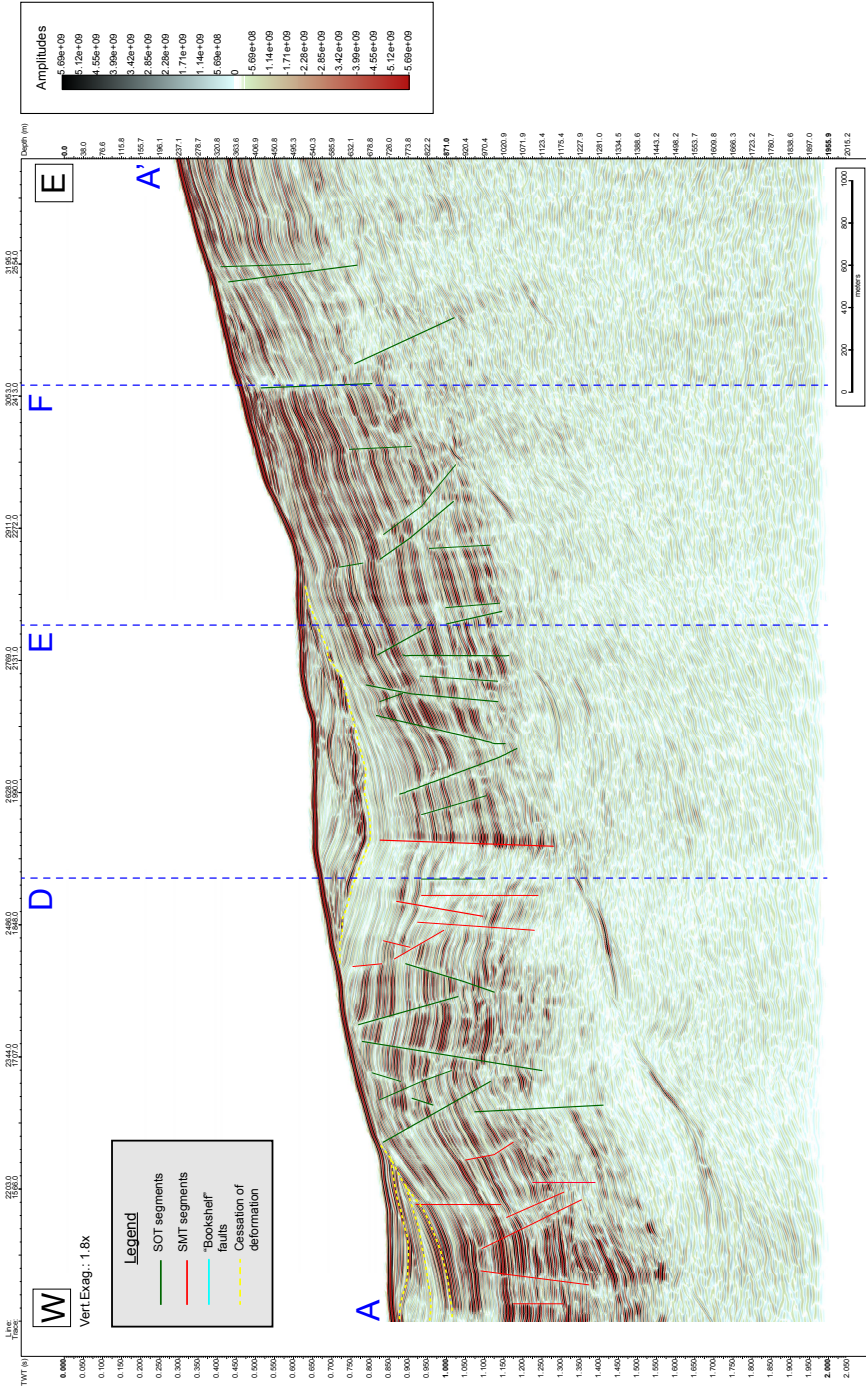
In summary, the timing and style of deformation observed in the SOT and SMT are better explained by left lateral jogs along right lateral fault systems that engenders transpression than splays off a master regional detachment (i.e., OBT). The coastal hazards in southern California are reduced because the predicted deformation associated with the OBT is not observed in the region and the deformation at the toe of slope is onlapped by flat lying turbidites that indicate the deformation in this region is moribund. Based on these observations, the  $\sim 0.62$  mm/yr of slip predicted by Field et al., (2014 - UCERF3) along the OBT under the Southern California coast does not appear to exist.

## **4.7 Acknowledgements**

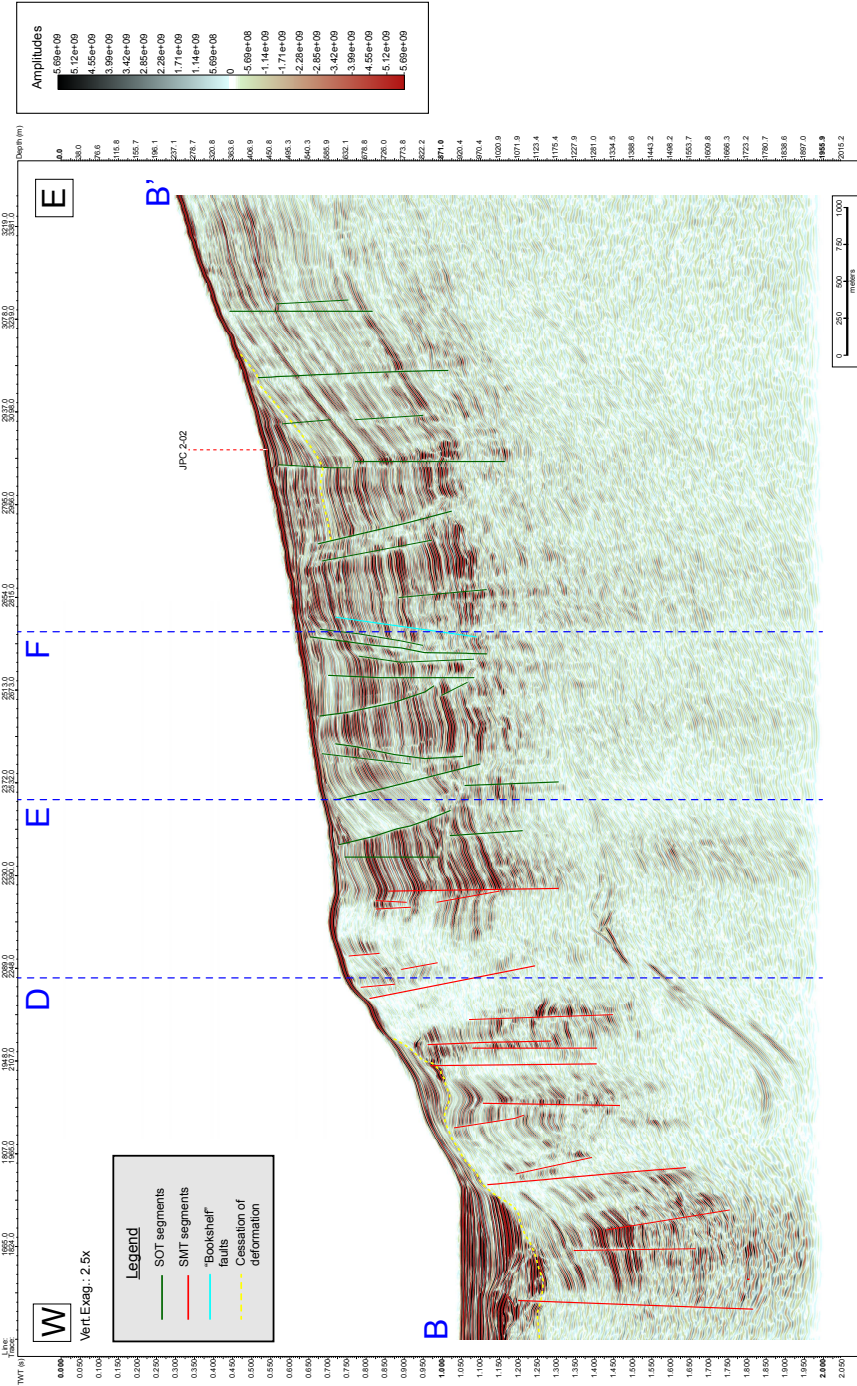
The authors wish to acknowledge the assistance of Mike Barth of Subseas Systems, the sailing and science crews of the R/V New Horizon (NH1320, & NH1323) and R/V Thomas G. Thompson (TN336), Geotrace Technologies, and NCS Subsea, Inc. for their roles in data acquisition and processing. We'd also like to thank Emily Wei for her assistance in core processing and analysis. Funding for this research was provided by a grant from Southern California Edison

funded through the California Public Utility Commission (CPUC), and the Maxwell J. Fenmore Memorial Fellowship. Figures were generated using Generic Mapping Tools, version 5 (Wessel et al., 2013), Kingdom Suite 2019 (IHS Markit), and OpendTect 6.4.4 (dGB Earth Sciences). Cruise information for NH1320 (2D MCS; doi: 10.7284/902996), NH1323 (3D P-Cable MCS; doi: 10.7284/903024), and TN336 (Coring; doi: 10.7284/906644) are accessible via the Rolling Deck to Repository (R2R) web interface. Seismic data are archived with Marine Geoscience Data System repository.

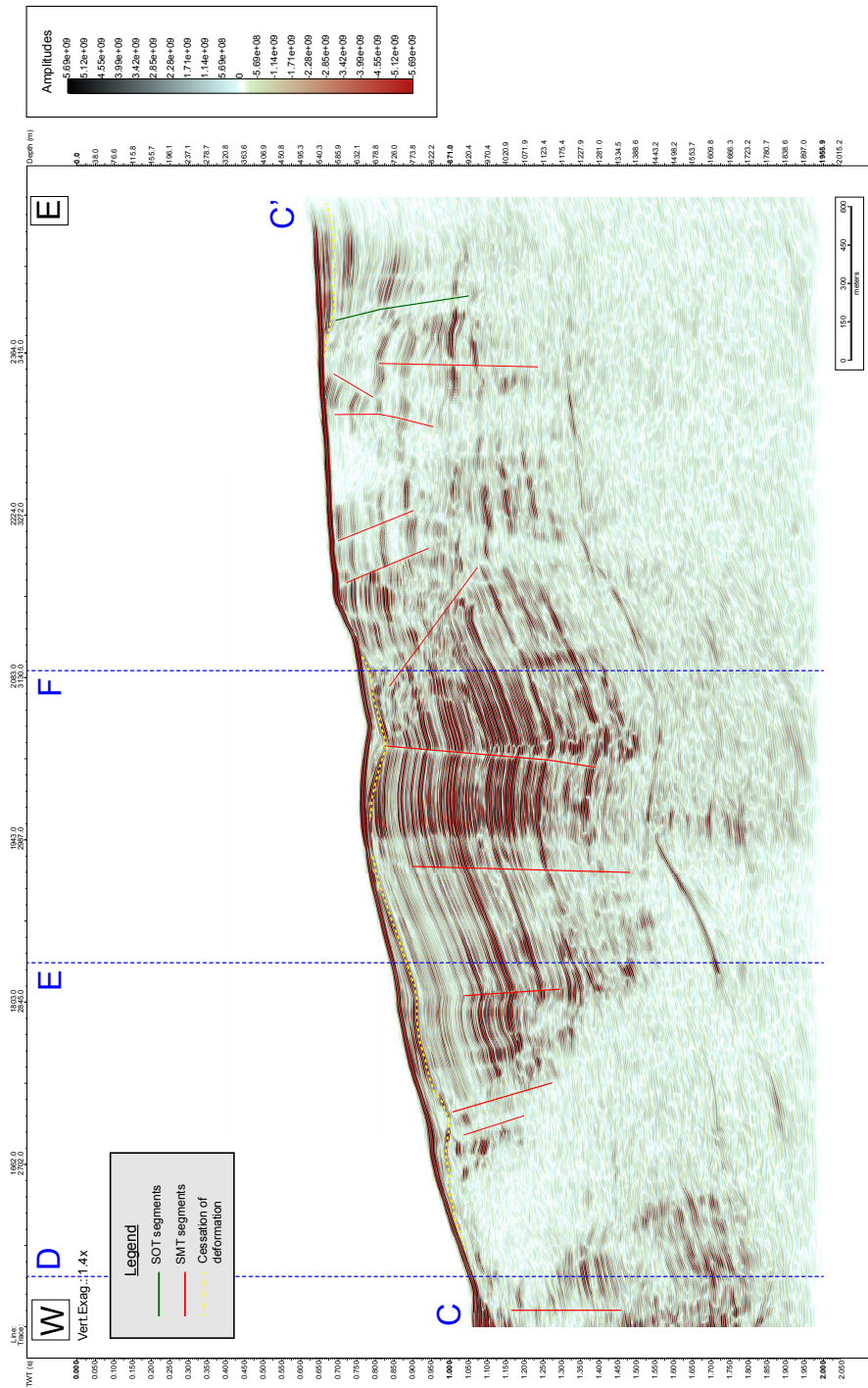
This work is being prepared for publication in: **Holmes, J.J., Driscoll, N.W., and Kent, G.M., In Prep. New Three-Dimensional P-Cable Seismic Data Image the Geometry and Fault Interaction of the San Mateo and San Onofre Trends Offshore Southern California.** The dissertation author was the primary researcher and author, and the co-authors listed in this publication directed and supervised the research.



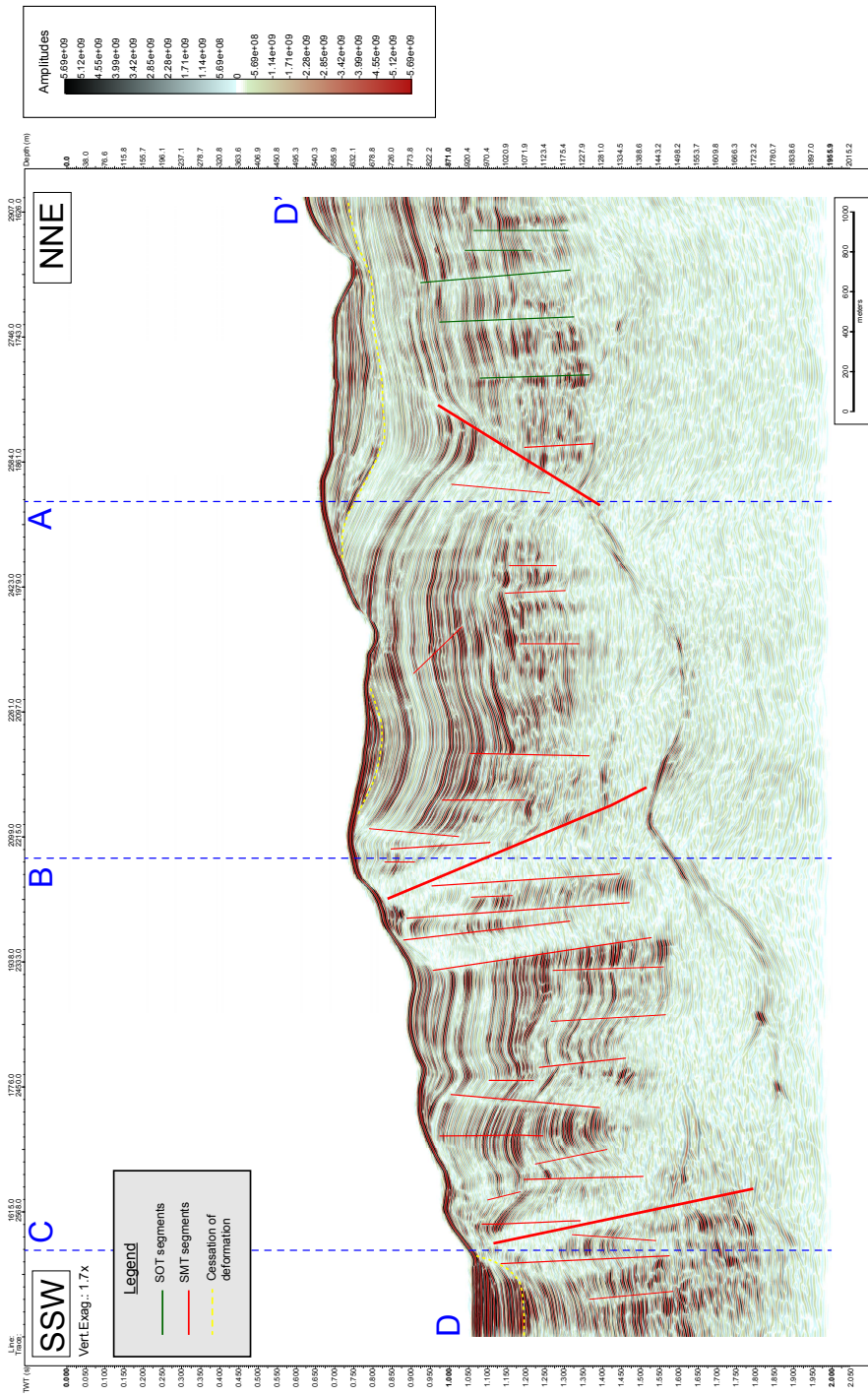
**Figure 4.8:** Vertical profile in amplitudes showing transect from A to A' (location shown in Figure 4.3). Faults color-coded according to azimuth and character. Red faults - San Mateo trend fault system (SMT). Green faults - San Onofre trend fault system. Minor fault segments (segments that can't be mapped for more than 50 lines) are shown with thin lines. Yellow dashed line marks base of sediment fill packages. Blue dashed lines show intersections between other transects in Figures.



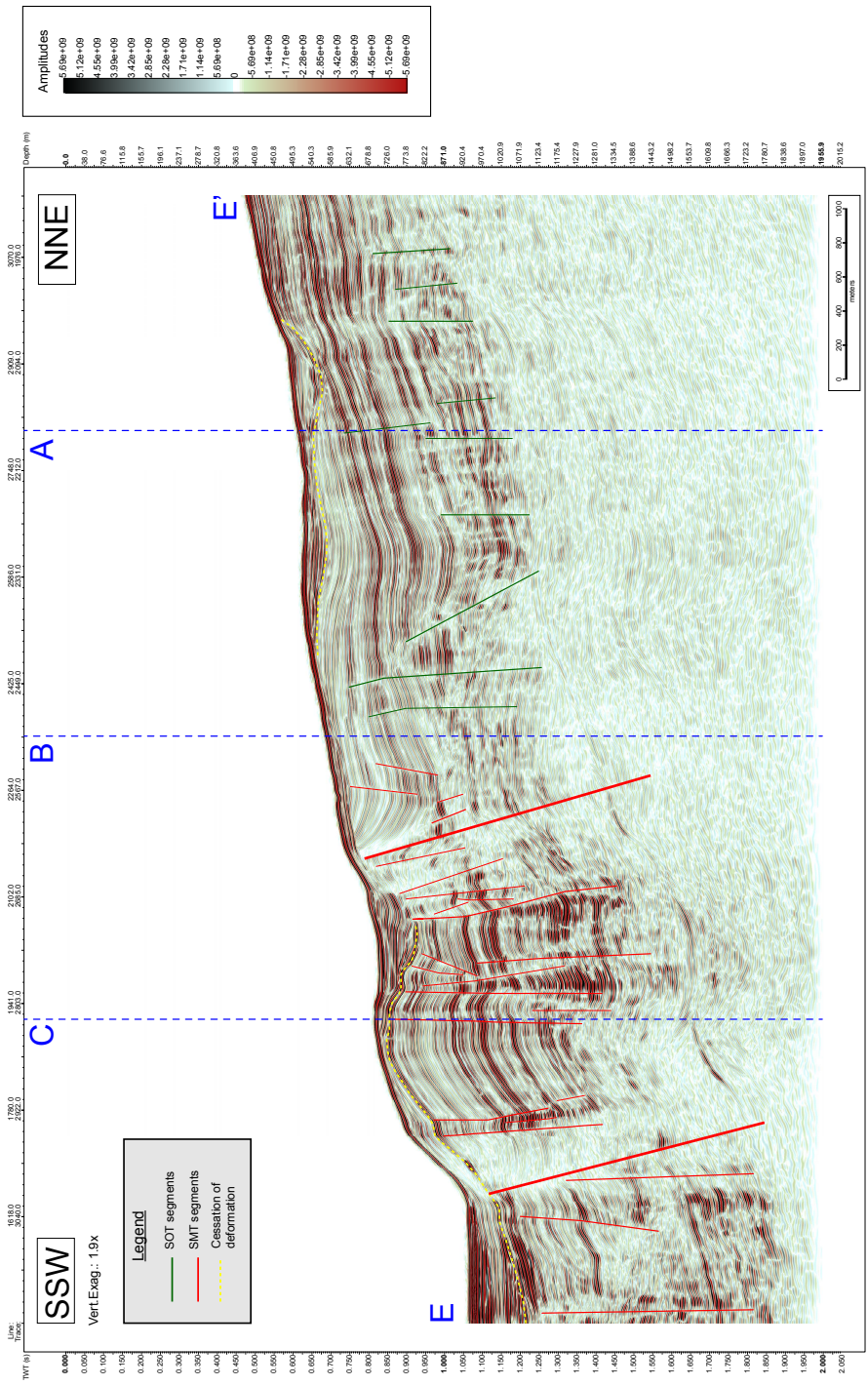
**Figure 4.9:** Vertical profile in amplitudes showing transect from B to B' (location shown in Figure 4.3). Faults color-coded according to azimuth and character. Red faults - San Mateo trend fault system (SMT). Green faults - San Onofre trend fault system. Turquoise faults denote faults that strike orthogonal to the margin ( $\sim 40^\circ$ ). Minor fault segments (segments that can't be mapped beyond 50 lines) shown with thin lines. Yellow dashed line marks base of sediment packages that represent cessation of deformation. Blue dashed lines show intersections between other transects in Figures. Short red dashed line denotes location of mid-slope jumbo piston core (JPC) 2-02.



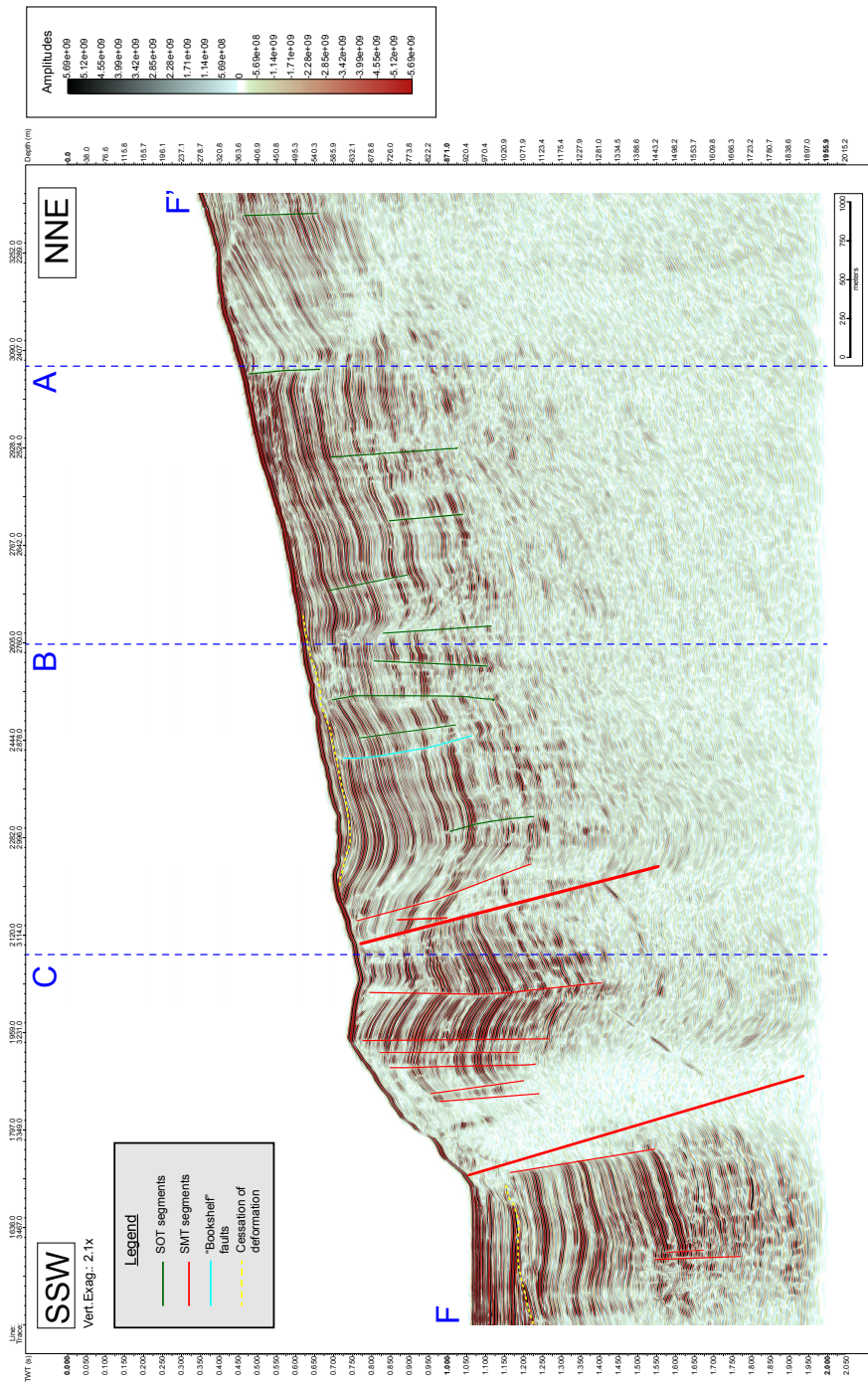
**Figure 4.10:** Vertical profile in amplitudes showing transect from C to C' (location shown in Figure 4.3). Faults color-coded according to azimuth and character. Red faults - San Mateo trend fault system (SMT). Green faults - San Onofre trend fault system. Minor fault segments (segments that can't be mapped beyond 50 lines) shown with thin lines. Yellow dashed line marks base of sediment packages that represent cessation of deformation. Blue dashed lines show intersections between other transects in Figures.



**Figure 4.11:** Vertical profile in amplitudes showing transect from D to D' (location shown in Figure 4.3). Faults color-coded according to azimuth and character. Red faults - San Mateo trend fault system (SMT). Green faults - San Onofre trend fault system. Minor fault segments (segments that can't be mapped beyond 50 lines) shown with thin lines. Yellow dashed line marks base of sediment packages that represent cessation of deformation. Blue dashed lines show intersections between other transects in Figures.

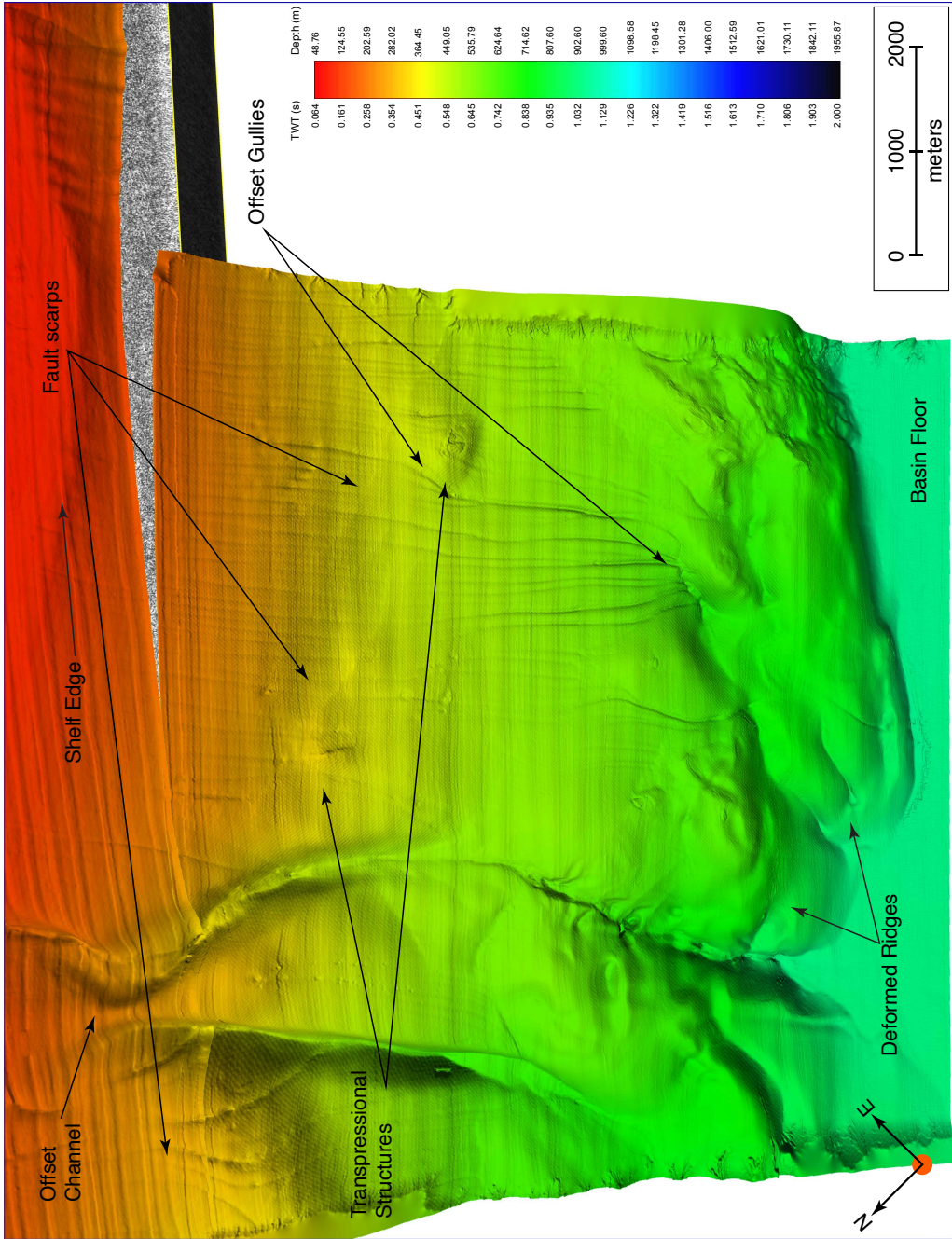


**Figure 4.12:** Vertical profile in amplitudes showing transect from E to E' (location shown in Figure 4.3). Faults color-coded according to azimuth and character. Red faults - San Mateo trend fault system (SMT). Green faults - San Onofre trend fault system. Minor fault segments (segments that can't be mapped beyond 50 lines) shown with thin lines. Yellow dashed line marks base of sediment packages that represent cessation of deformation. Blue dashed lines show intersections between other transects in Figures.

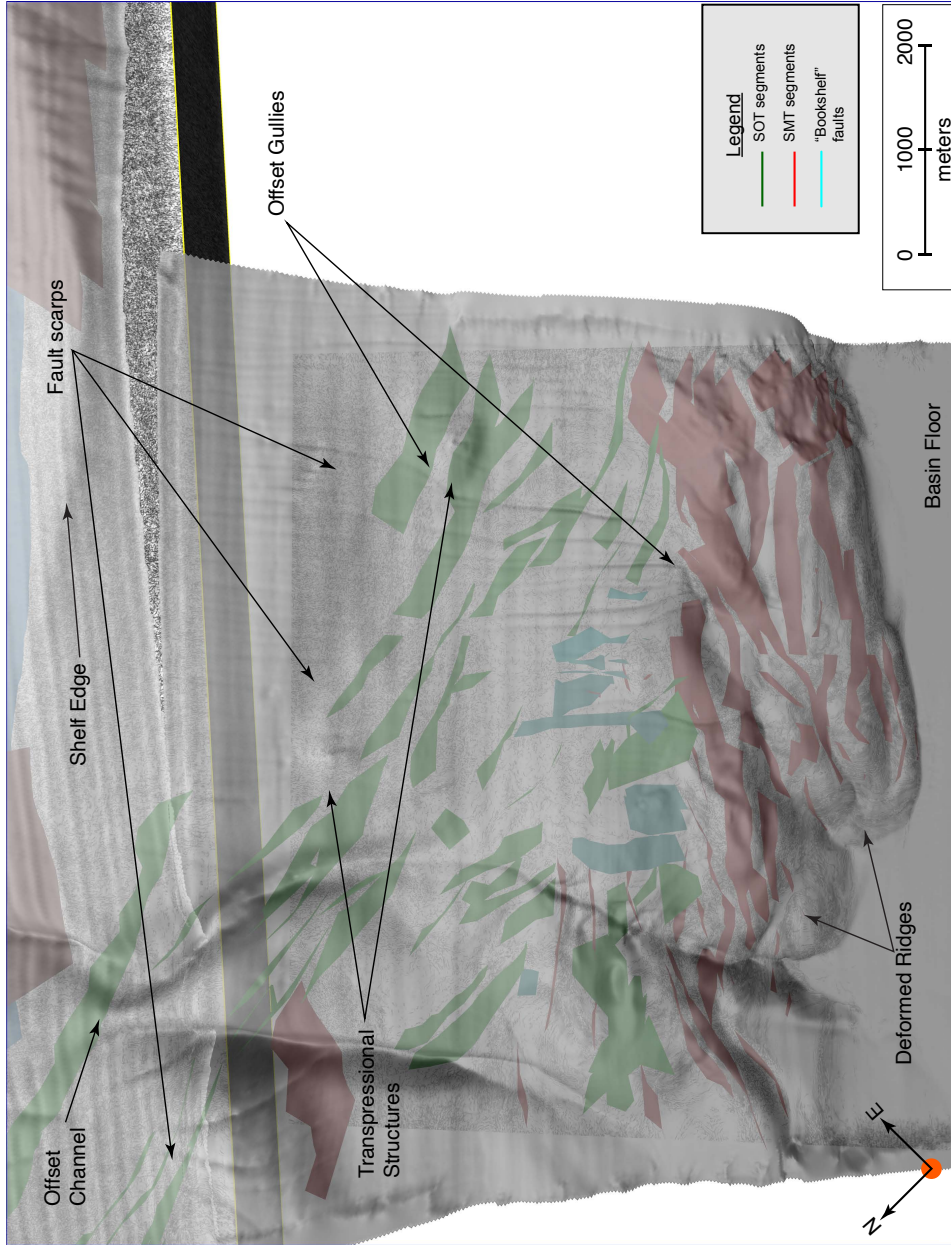


**Figure 4.13:** Vertical profile in amplitudes showing transect from F to F' (location shown in Figure 4.3). Faults color-coded according to azimuth and character. Red faults - San Mateo trend fault system (SMT). Green faults - San Onofre trend fault system. Turquoise faults denote faults that strike orthogonal to the margin (~40°). Minor fault segments (segments that can't be mapped beyond 50 lines) shown with thin lines. Yellow dashed line marks base of sediment packages that represent cessation of deformation. Blue dashed lines show intersections between other transects in Figures.





**Figure 4.14:** Depth-colored map view of seafloor bathymetry computed from 3D data amplitude volumes in both boomer and sparker. Continental margin is towards the top of image. Toe of slope is largely deformed at interface with the basin floor. Transpositional structures, gullies and canyons appear offset by fault scarps at the seafloor.



**Figure 4.15:** Map view of seafloor bathymetry from same viewpoint at Figure 4.14. Bathymetry is colored in shades of gray and 20% transparent. 3D fault planes are plotted below seafloor and color-coded according to strike and character. Green faults - San Onofre trend (SOT). Red faults - San Mateo trend (SMT). Blue faults represent segments of rotational faults between the two fault systems.

# Chapter 5

## Conclusions

The resolution of marine 3D P-Cable seismic reflection data provides new insights into fault geometry, kinematics, and subseafloor deformation. Such technology that was previously restricted to use by industry for hydrocarbon exploration because of cost is now available to the marine community for margin studies. Computing techniques in data processing and visualization, formerly the province of massively parallel supercomputers, can now be accomplished by general-purpose desktop workstations further improving the resolution of 3D P-Cable data.

Employing these techniques provides new constraints on the structural evolution of the southern California margin. These new data directly impact our knowledge of fault segments offshore and their interaction with neighboring fault segments, which have important implications for assessing the seismic hazard along the southern California coast. We have focused our studies on the margin offshore of San Onofre to understand the tectonic deformation of the region and to test between two end member models developed to explain the deformation; transpression at a left lateral step-over along a right-lateral strike-slip fault system verses compression along splays associated with a westward verging thrust system.

High-resolution 3D P-Cable data were acquired to image the Newport-Inglewood Rose Canyon (NIRC) fault system and reveal a buried 2 km wide antiform dome structure along a left

lateral jog on the right lateral fault system. Continuing north, a series of synclines and anticlines result from small changes in fault azimuth; that is, fault segments with a more northwest trend ( $\sim 285^\circ$ ) appear transpressional, while more northward trending fault segments ( $\sim 345^\circ$ ) appear transtensional. Such an observation is consistent with those from other studies of faults in the ICB region (e.g., Coronado Bank, San Diego Trough, and Descanso faults)(Ryan et al., 2009; Maloney et al., 2016; Conrad et al., 2018; Bormann et al., in review).

Examining piston cores from the continental slope and basin floor within a 3D seismic reflection data framework, we assessed how shelf width impacts turbidite delivery to the slope and basin floor throughout the last eustatic sea level cycle. Turbidite emplacement history was analyzed for two nearby canyon systems, one where the shelf width was narrow (2 km - Dana Point Canyon) and the other where the shelf was wide (10 km - San Onofre North/South canyons). Shelf width appears to play an important role in turbidite emplacement throughout a eustatic sea level cycle. For example, the San Onofre canyon systems were most active when eustatic sea level was low with a marked decrease in turbidite emplacement to the slope and basin floor during the eustatic sea level rise beginning about 13 ka. In contrast, the Dana Point canyon was active during times of eustatic sea level low and also during times of sea level rise (transgression). Short distance variation in turbidite emplacement history appears to be largely controlled by shelf width. Local influences such as channel gradient may also modify the turbidite flow and introduce variability in the deposit. Emplacement history of turbidites along continental margins has important implications for their use in aqueous paleoseismology (Goldfinger, 2009).

In addition, we imaged the San Onofre and San Mateo trend fault zones with high-resolution 3D seismic reflection data and swath bathymetry along the slope to test between the two end member models . The mapped fault segments revealed two predominant fault zones; the San Onofre trend with an average strike of  $\sim 345^\circ$  and the San Mateo trend with an average strike of  $\sim 285^\circ$ . The boundary between these two trends is very abrupt with different styles of deformation. The more northwest trending San Mateo trend exhibits much greater deformation

with folded and faulted acoustic reflectors. Smaller fault systems with an average trend of  $\sim 40^\circ$  are observed along the boundary between the two trends. These short faults appear to be rotated clockwise due to the shearing between the two trends and as such are interpreted to be left lateral bookshelf faults. Segments of the San Onofre trend fault zone observed on the slope merge with the Newport-Inglewood Rose Canyon system on the shelf.

Finally, localized transpressional features observed in the swath bathymetry data appear to deflect canyons and gullies along the slope. Mounded steeply sloping morphology ( $\sim 25^\circ$ ) at the base of the slope appears to be entirely localized within the area of the northwest trending San Mateo trend. Undeformed onlapping sequences at the slope-basin interface suggest that the deformation is old, with our estimate of late Pliocene to mid-Pleistocene, based on extrapolated sedimentation rates.

Based on our analysis of the high-resolution 3D data, our preferred hypothesis is the timing and style of deformation along the slope is caused by leftward jogs along right lateral faults that generate transpression as opposed to the alternative model of splays off of an underlying regional detachment fault (i.e., Oceanside blind thrust model). Several observations support our preferred model: the predicted deformation associated with an active blind thrust is not observed; the observed transpressional deformation appears to be localized not regional as would be predicted by the OBT model; and finally flat lying turbidites onlapping the toe of the continental slope indicates that deformation in the region is moribund not an active thrust front with westward vergence.

Blind thrust models, such as the Oceanside blind thrust, carry with them seismic risk due to the ability to support larger earthquakes on low-angle reverse detachments. Our observations suggest that the 0.62 mm/yr of slip predicted along the Oceanside blind thrust are not observed in the new 3D P-Cable MCS data and thus the seismic hazard to the highly populated southern California coast is reduced.

# **Appendix A**

## **SONGS 3-D High Resolution P-cable Survey Offshore Southern California Cruise Report**

### **A.1 Executive Summary**

The 35-day 3-D P-cable seismic survey campaign was conducted from October 3rd, 2013 through November 6th, 2013. The Scripps Institution of Oceanography (SIO) subcontracted Subsea Systems, Inc. (SSI) to provide geophysical survey services in support of the geophysical project. In addition, SIO contracted support services NCS-SubSea to provide navigation and positioning and Geotrace Technologies to access the geophysical data in real time and onshore process the 3-D P-cable seismic data.

The survey was conducted onboard the Scripps Institute of Oceanography's R/V New Horizon. Following mobilization of all survey and support instrumentation at Scripps's Nimitz Marine Facility, the New Horizon made the 80 km transit north to begin survey operations.

A P-cable acquisition system was employed to acquire nearly 3,000 line-kilometers of

3-D data over two offshore survey areas lying between Oceanside and San Clemente, California. Two seismic sources, a triple plate boomer and a spark-array, were used as a sound source for the survey areas; the boomer at Area One and the spark-array at the deeper water site, Area Two.

The two surveyed areas, designated Area One and Area Two, comprised a series of 101 and 161 roughly shore parallel sail lines respectively. Area One measured a notional 14.2 km by 3.7 km covering an area of 52.5 km<sup>2</sup> while Area Two measured approximately 6.6 km by 6.0 km and enclosed an area of 39 km<sup>2</sup>.

Seismic reflection data acquired for the two survey areas totaled 2,975 line-kilometers or 1,682 line-kilometers for the Area One survey and 1,293 line-kilometers for the Area Two survey inclusive of re-shoots and infill lines.

On completion of survey operations all digital seismic reflection data and associated navigation files were turned over to the UCSD/SIO Chief Scientist. The entire 35 day project, from mobilization through survey operations and demobilization, was completed with zero incidents, near hits or other safety issues.

## **A.2 Introduction**

Scripps Institution of Oceanography (SIO) at University of California, San Diego (UCSD) subcontracted Subsea Systems Inc. (SSI) to provide geophysical survey services in support of their 3-D P-cable seismic reflection project.

SSI provided geophysical seismic equipment and personnel and subcontracted NCS-Subsea, Inc. (NCS) of Stafford, Texas to provide positioning equipment and personnel. Under separate contract directly with UCSD/SIO Geotrace Technologies Ltd. was engaged to provide shipboard QA/QC and seismic data processing.

High-resolution 3-D seismic reflection data were acquired within two survey blocks

offshore Southern California between San Clemente and Oceanside from 10 October through 05 November, 2013 (Figure A.1). The survey blocks, Area One and Area Two, are located approximately 12 and 18 kilometers offshore in water depths ranging from 44 m to over 790 m. Nearly 3000 line-kilometers of high-resolution 3-D data were acquired over a 25-day period. The entire survey was confined to US federal waters with no production occurring inside the 3-mile boundary demarcating California state waters. The weather during survey operations was mild and the seas were calm yielding very high quality seismic reflection data.

### **A.3 Scope and Purpose**

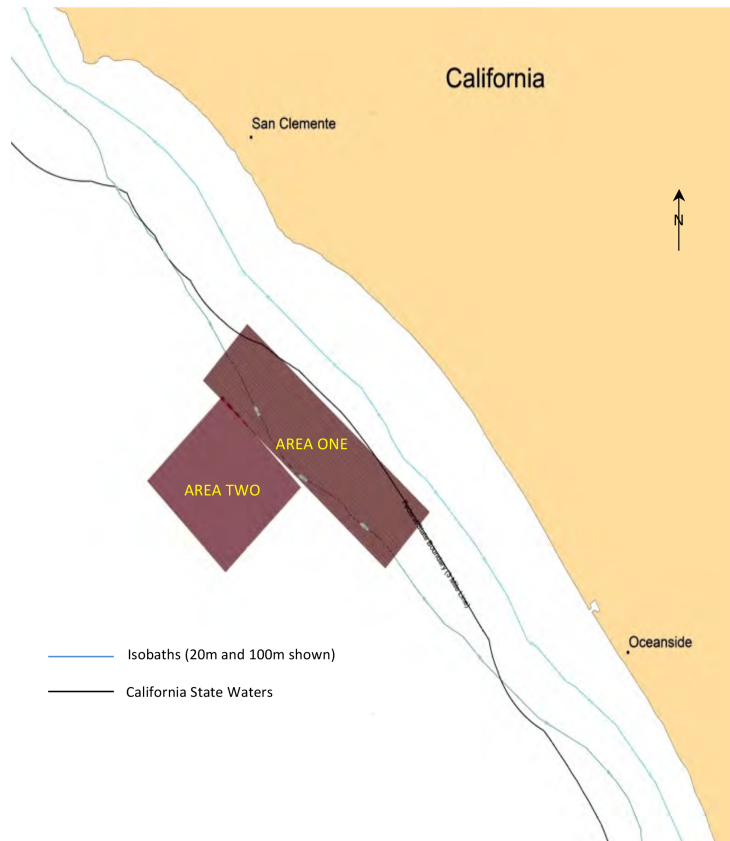
The survey was designed to collect 3-D seismic reflection data on the subsurface faults offshore of a portion of southern California's coastline between San Clemente and Oceanside, approximately 80 km (43 nmi) north of San Diego, California. A low energy sparker and a boomer seismic source were employed to collect the reflection data during a 25-day campaign in October and early November of 2013.

This report presents a summary account of the field survey effort and provides daily documentation of the survey.

### **A.4 Survey Instrumentation**

A brief description of the survey instrumentation that was mobilized aboard the New Horizon for the SONGS 3-D P-cable seismic reflection project is provided in the following sections.





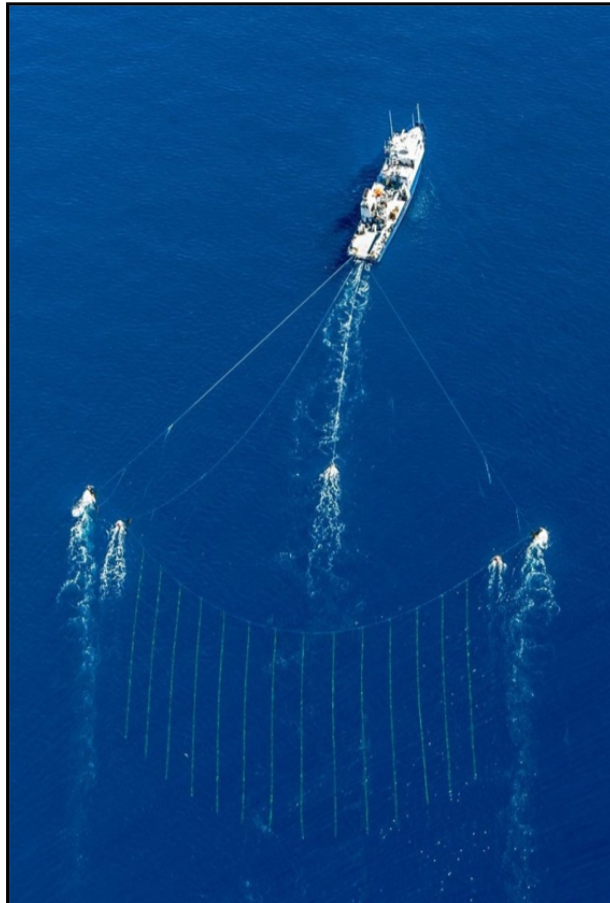
**Figure A.1:** Location map showing survey Areas One and Two

### **A.4.1 Geophysical Acquisition System**

The 3-D offshore survey employed the following basic components: a P-Cable comprised of 14 streamers each with 8 channels @ 6.25 m group intervals and deployed from a single transverse cable, a Triple-Plate Boomer (AP3000) seismic source by Subsea Systems Inc., a 2kJ sparker seismic source also by Subsea Systems, Inc. and a Knudsen Engineering, Chirp Model 3260 Echo Sounder.

The P-Cable consists of an array of short streamers used to acquire many closely spaced seismic lines simultaneously. The streamers are supported by a transverse cross-cable deployed between two paravanes. The systems relative slightness of weight makes it easy to deploy and use aboard most research and industry survey vessels.

In order to achieve the small bin size requirements, SSI deployed a P-Cable with 14 streamers separated by a distance of 6.25 meters. Each 50-meter streamer consisted of 8 channels at a group interval of 6.25 meters. With this configuration 112 channels of data were acquired. Data were acquired at a sample rate of 250 microseconds and a record length of up to 1.0 second. This provides a Nyquist frequency of 2 kHz, which spans the bandwidth of most high-resolution marine acoustic energy sources. Subsurface swath width was 43.75 meters for the sail lines spacing of 37.5 meters.



**Figure A.2:** R/V New Horizon with P-cable deployed.

The seismic source was selected based on the acoustic tests and results from our earlier 2-D test cruise completed in August of this year. For the 3-D cruise, SSI provided both the

AP3000 boomer and a 3-tip Sparker Array. Both of these systems are capable of operating at a power level of 2000 joules, while the Sparker Array can operate at higher energy levels. Based on water, the boomer was deployed in Area One and the sparker was used in Area Two.

Data from the P-Cable system are sent via Ethernet to the topside recording computers. These data are converted to SEG Y format and stored on the computer hard drive. The SEG Y formatted data are backed up to a server after each seismic line is completed. The Geometrics CNT software also allows many QA/QC features. These include complete calibration of the streamer electronics, leakage and capacitance testing of hydrophones, display of all seismic channels, gathers of selected channels and signal/noise measurements. Comprehensive logs recording streamer depths, shot information and any errors that occurred along line were also kept. Table 3.1 below documents the acquisition parameters of the system used for the 3-D survey.

**Table A.1:** P-cable Acquisition Parameters

P-CABLE 3-D ACQUISITION PARAMETERS	
Number of Streamers	14
Streamer Spacing	6.25 meters
Streamer Length	50 meters
Channels per Streamer	8
Group Interval	6.25 meters
Streamer Type	Geometrics GeoEel
Width of Active Spread	87.5 meters
3D Swath Width	43.75 meters
Bin Size	3.125 x 3.125 meters
Nominal Subsurface Fold	8
Sample Rate	0.25 milliseconds
Record Length	0.75 to 1.0 seconds
Recording Format	SEG Y or SEG D
Source Type	AP3000 Boomer or 2KJ Sparker Array
Source Depth	0.5 m
Shot Interval	3.125 meters or 6.25 meters

The 3-D high resolution P-Cable array is a surface towed spread and the resulting data

quality can be severely compromised with increasing sea states. The general limitations to survey operations due to weather are commonly defined in terms of the Beaufort Scale. Acceptable data quality can be achieved in seas up to about Beaufort Force 3-4 (as whitecaps appear and small crests begin to break). System deployment and recovery operations become a safety issue for personnel in sea states greater than a low Beaufort Force 5 as well as a damage risk to the towed survey equipment.

#### **A.4.2 Positioning**

SIO subcontracted NCS-SubSea of Houston, Texas (NCS) to provide navigational services. The positioning for the survey vessel, streamers and seismic source used Differential Global Positioning System (DGPS) as the primary and secondary navigation systems. The DGPS survey navigation system was capable of achieving vessel, paravane and buoy surface position accuracy of better than 1 meter. The navigation system uses survey-grade DGPS with real-time, differentially-corrected positions passed to the onboard integrated navigation and data management computer. The integrated navigation system was interfaced with the onboard and in-water DGPS receivers. Compass and depth devices embedded in the cross cable and streamers provide additional positioning information. The DGPS system on the sound source was also wired directly to the navigation system. DGPS data from these positions are input to the navigation computers to model the source and hydrophone locations for the streamer.

The NavPoint Integrated Navigation System used during P-Cable seismic surveys consists of three primary components. These components are two online programs, NavPoint Main and NavPoint Trawler, and one offline program, NavPoint Processing. Final navigation data processing was conducted onboard using the NavPoint Processing software that converts the P2/94 file into a P1/90 data file format. Two such sets of files were logged and subsequently processed to produce the P1/90 files for the boomer and sparker data sets.

### **A.4.3 Seismic Data Processing**

Geotrace provided onboard QC and seismic data processing. A behemoth computer was mobilized aboard the New Horizon to facilitate near-real time processing of the acquired seismic reflection data. Hardware components of the processing unit included 60 Linux CPUs (15 Quad nodes), 2GB memory per Linux node, a 50TB external hard disk, 2 x 3595 tape drives and CD and DVD drives. Two PC workstations each with dual 30" monitors were part of the Q/C effort.

Software used during QA/QC and data processing comprised Complete DIAMOND™ parallel processing software package including Seismic Data Viewer and Velocity Work Bench. Specifics of the onboard QA/QC procedures is provided in section 6.2 of this report.

## **A.5 Survey Platform**

The R/V New Horizon, owned and operated by the Scripps Institution of Oceanography, University of California, San Diego, was used to perform the geophysical survey. The New Horizon (Figure A.3) is a 52 m long purpose built research vessel operated by SIO Ship Operations. She was built in 1978 with a registered gross tonnage of 297 tons, a beam of 11 m and a maximum draft of 3.7 m. The New Horizon is propelled by two D398, 850hp Caterpillar diesel engines driving two variable pitch screws making her acoustically very quiet and ideal for seismic survey operations. Her two 230kW service generators supply ample electrical servicer for all survey instrumentation. A fuel capacity of over 40,000 gallons and an average consumption rate of 1,000 gallons per day push her range out to 9,600 miles with endurance to 40 days.

She carries a complement of 12 crew members and has berthing accommodations for



**Figure A.3:** The R/V New Horizon underway off Southern California.

an additional 19 scientific personnel. Ample work space aboard the New Horizon included 117m<sup>2</sup> of laboratory space on the main deck and additional lab/office space on the 01 deck. The 160 m<sup>2</sup> main deck work area easily accommodated the three P-cable system winches and a platform extension to the 01 deck provided the additional space required for the three tow winches. One meter of freeboard made for easy deployment and recovery of the in-water P-cable system components. The aforementioned vessel attributes made the R/V New Horizon ideally suited to the SONGS project.

### **A.5.1 Health, Safety and Environment**

Scripps Institution of Oceanography and Subsea Systems Inc. is committed to provide a healthy and safe workplace for all personnel on the SONGS project. Our commitment is based on the conviction that accidents are preventable.

In the event of an emergency at sea the captain and his crew constitute the initial emergency services. In the event of an emergency, all crew will report directly to the ship's captain and assist/proceed as directed in accordance to the ship's emergency procedures.

Subsea Systems Inc. commissioned the creation of a safety manual entitled General

Offshore Safety Manual for the project that was noted and maintained onboard the vessel. Several additional supporting safety documents were also assembled and available shipboard. SIO's published R/V New Horizon Handbook complemented the General Offshore Safety Manual with vessel-specific information also outlined in UNOLS documents.

## **A.5.2 Drills and Muster**

An orientation tour and safety meeting was held on 11 October once the R/V New Horizon was on the work site and all extraneous mobilization personnel had disembarked the vessel. A second orientation tour and safety meeting was conducted following a crew change on the 22nd of October. Topics discussed included:

- Boat Stations / Abandon Ship
- Fire
- Man Over Board
- Location of fire extinguishers
- Location of Life Preservers
- Station Bill and Alarms
- Emergency Staging Areas
- First Aid and Eyewash Stations
- Identify First Aid and CPR Trained Responders
- Back Deck / PPE Restricted Area
  
- Exclusion Zones

Four weekly general muster and drills were held during the survey. Instruction was also presented on the use and location of Emergency Breathing Apparatus (EBA), EPIRBs and emergency flares.

### **A.5.3 HSE Safety Meetings**

Toolbox Safety meetings were held every morning during mobilization prior to any activities to discuss who would be involved in what activities and what support might be needed. Once the R/V New Horizon was underway Toolbox Safety meetings were held prior to any back deck activity. During these meetings discussion was focused on but not limited to environmental conditions, individual responsibilities, details of the expected activity, any additional PPE requirements. A total of 12 Toolbox meetings were held relating to back deck activities and 6 related to mobilization/demobilization.

All attending these meetings were required to sign the Toolbox Meeting Log.

### **A.5.4 Protected Species Awareness**

Four marine turtle species, 24 cetaceans (whales, dolphins, and porpoises), six pinnipeds (seals and sea lions), and one fissiped (southern sea otter) have been recorded along the southern California coast. Seasonal abundance of these taxa varies, with marine turtles, pinnipeds and some dolphins being considered year-round residents, while other species are migratory (i.e. gray whales, *Eschrichtius robustus*) and are more common during specific months (i.e. blue and humpback whales, *Balaenoptera musculus*, and *Megaptera novaeangliae*, respectively, in the summer and fall months). Within the project area, both resident and migrant taxa were expected.

Encounters with these species during survey operations were anticipated and as a precaution certain actions and mitigations that are designed to reduce or eliminate adverse impacts to the marine mammals were implemented.

Accordingly, the operating seismic source was shut down if a marine mammal approached or entered an exclusion zone (safety zone). For both the sparker and boomer surveys, the safety zone was set at 100 m.



Survey activity did not resume until the marine mammal had cleared the exclusion zone. Mitigations are initiated by vessel-based Protected Species Observers (PSOs). The size of the exclusion and safety zones were modeled according to specific sources used during the operation. During the SONGS 3D P-cable survey, 3 PSOs were tasked with watching for marine mammals. When a mammal sighting was made, the following information was recorded on Effort and Detection Forms by the on-duty PSO:

- Time
- Location (GPS coordinates)
- Speed and activity of the vessel
- Sea state
- Visibility
- Sun glare
- Species
- Group size
- Behavior when first sighted and after initial sighting
- Heading
- Distance from the source and the vessel
- Apparent reaction to activities.

During SONGS P-cable survey, the operating source was shut down during marine mammal entries to the 100-m safety zone and was not started until the mammal group cleared the exclusion zone. Information regarding sightings was logged by the PSO in an Effort and Detection form and have been recorded and documented by the PSOs.

## **A.5.5 Incidents**

Safety was a prime concern throughout the SONGS project and was borne out by the project's safety record. The SONGS survey campaign commenced with the initiation of mobilization efforts on October 3rd, 2013 and was completed with all demobilization activities on November 6th, 2013. During the 35-day project, including on-site survey operations, mobilization and demobilization, there were zero incidents, near hits or safety issues.

## **A.6 Summary of Survey Operations**

### **A.6.1 Mobilization**

A Pre-mobilization meeting at UCSD's Nimitz Marine Support Facility (MarFac) was held on September 4th, 2013 to discuss operational details related to the survey and to discuss prefabrication and modifications to the New Horizon that were needed prior to mobilization.

Prior to mobilizing and throughout survey operations the P-cable system was subject to a barrage of calibration and validation tests. Performed by Geometrics at their San Jose, California facility, Geometrics' pre-mobilization testing and calibration included analog performance tests, depth sensor and hydrophone validation tests. It should be noted that field capacitance and leakage were also performed during survey operations.

Mobilization activities aboard the R/V New Horizon began on the morning of October 4th, 2013 and were completed by mid-afternoon on October 9th, 2013. She was mobilized for the 3-D survey effort at her UCSD MarFac home port facility in San Diego, California. Subsea Systems personnel traveled to San Diego on October 3rd, 2013 and commenced locating and inventorying survey equipment previously shipped to MarFac. The vessel was made available for mobilization on October 4th, 2013 and installation of geophysical, navigational and data processing instru-

mentation began. The first few days activities focused mainly on deck related issues; spotting and securing winches, hanging tow blocks and installing a prefabricated 01 deck extension. NCS SubSea personnel were engaged in installing and testing positioning instrumentation, calibrations and documenting system offsets. A systems engineer from Geotrace was also present to oversee the on-loading, installation and configuration of their behemoth data processing computer.

## **A.6.2 Personnel**

The survey team was comprised of 17 scientific and technical personnel from Subsea Systems, Inc., NCS SubSea, Geotrace Technologies, Ltd., Lamont-Dorhety Earth Observatory (LDEO) and Scripps Institute of Oceanography (SIO). A crew change out involving five technical staff was effected on October 22nd, 2013. A listing of scientific and technical personnel and their affiliation for the two survey periods includes:

**10 Oct - 22 Oct**

M. Barth, Subsea Systems, Inc.	M. Angel, Geotrace
C. Chamberlain, Subsea Systems, Inc.	N. Driscoll, Chief Scientist, SIO
R. Steinhaus, LDEO	J. Holmes, SIO
J. Gaytan, NCS SubSea	M. Lande, SIO
M. Hall, NCS SubSea	G. Ucarkus, SIO
A. Parish, NCS SubSea	V. Sahakian, SIO
S. Traceski, NCS SubSea	S. Klotsko, SIO
D. Fontenot, NCS SubSea	J. Bormann, UNR
F. Landers, Geotrace	

**10 Oct - 22 Oct**

M. Barth, Subsea Systems, Inc.	N. Driscoll, Chief Scientist, SIO
C. Chamberlain, Subsea Systems, Inc.	J. Holmes, SIO
R. Steinhaus, LDEO	M. Lande, SIO
J. Gaytan, NCS SubSea	G. Ucarkus, SIO
M. Hall, NCS SubSea	V. Sahakian, SIO
A. Parish, NCS SubSea	S. Klotsko, SIO
S. Traceski, NCS SubSea	J. Bormann, UNR
D. Fontenot, NCS SubSea	
F. Landers, Geotrace	
M. Angel, Geotrace	

**22 Oct - 05 Nov**

M. Barth, Subsea Systems, Inc.	G. Kent, Chief Scientist, SIO
C. Chamberlain, Subsea Systems, Inc.	J. Holmes, SIO
R. Steinhaus, LDEO	A. Harding, SIO
B. Mattox, NCS SubSea	G. Ucarkus, SIO
M. Hall, NCS SubSea	T. Seaman, SIO
A. Parish, NCS SubSea	J. Maloney, SIO
S. Traceski, NCS SubSea	J. Bormann, UNR
D. Fontenot, NCS SubSea	
F. Landers, Geotrace	
M. Angel, Geotrace	

The *R/V New Horizon's* 12 person crew included:

I. Lawrence, Captain	T. Schuler, Chief Engineer
P. Redmond, 1st Mate	J. Garcia, Wiper
J. Irza, 3rd Mate	W. Brown, A/E
D. Haddon, A/B	W. Bouvier, Oiler
E. Collier, A/B	E. Lograsso, Sr. Cook
D. Weaver, A/B	M. Stein, Cook

### A.6.3 Survey Methodology

High-resolution 3-D seismic reflection data were acquired within two survey blocks offshore Southern California between San Clemente and Oceanside (Figure A.4). The survey activities extended from October 10th, 2013 through November 5th, 2013. The entire survey was confined to US federal waters with no production occurring inside the 3-mile boundary demarcating California state waters.

Seismic reflection data were acquired along 262 pre-plotted sail lines traversing the two survey blocks. A sparker source was employed for lines within AREA TWO and a three-plate boomer was utilized as the sound source in AREA ONE. Data were acquired with the P-cable system and observer logs were maintained to document the acquisition and recorded file data parameters.

Daily Progress Reports (DPRs) were also created to provide additional details of each day's activities.



**Figure A.4:** Location map showing AREA ONE and AREA TWO.

Area One is a rectangular survey block of approximately 52.5 km<sup>2</sup>, comprised of 101 survey lines with a notional line length of 14 km. Bounding coordinates for the Area One block

are provided in Table 6.1 below. Roughly shore parallel, the sail lines were oriented along an azimuth of 312° and the reciprocal of 132° and spaced 37.5 m apart. Area One is the shallower of the two survey areas with depths ranging from less than 44m to nearly 360m. Approximately 1682 line-kilometers of reflection data were acquired with the boomer source at a 2kJ power setting in Area One.

**Table A.2:** Bounding coordinates for survey Area One.

<b>X</b>	<b>Y</b>	<b>Latitude</b>	<b>Longitude</b>
442,892.06m	3,689,447.97m	33° 20' 33.7237"	-117° 36' 49.3535"
440,383.92m	3,686,661.21m	33° 19' 02.7485"	-117° 38' 25.7580"
450,786.91m	3,677,293.43m	33° 14' 00.4650"	-117° 31' 41.5558"
453,296.23m	3,680,080.33m	33° 15' 31.3591"	-117° 30' 05.1176"

Area Two is a nearly square survey block contiguous to Area One toward the southwest. Area Two covers approximately 39 km<sup>2</sup> and is consists of 161 pre-plotted survey lines of a nominal 6.6 km length. Bounding coordinates for the Area Two block are provided in Table 6.2 below. The sail lines were spaced 37.5 m apart along an azimuth of 315° and a reciprocal of 135°. Area Two lies in generally deeper water with depths ranging from 182 m to more than 790 m. In the deeper water, Area Two block the sparker sourced was operated at 2000j to 2400j to acquire approximately 1262 line-kilometers of 3-D seismic reflection data.

**Table A.3:** Bounding coordinates for survey Area Two.

<b>X</b>	<b>Y</b>	<b>Latitude</b>	<b>Longitude</b>
441,482.32m	3,685,849.10m	33° 18' 36.5971"	-117° 37' 43.0512"
437,179.77m	3,681,623.76m	33° 16' 18.5275"	-117° 40' 28.3800"
441,640.91m	3,677,080.92m	33° 13' 51.9244"	-117° 37' 34.8843"
445,943.53m	3,681,306.33m	33° 16' 09.9317"	-117° 34' 49.5558"

## A.6.4 Acquisition QC and Onboard Processing

Geotrace performed full data acquisition QC. Products and examples are described in this section. QC products were created after the acquisition of each line when the SEG-Y data and P190 navigation data were available. The parameterisation and production of the QC displays take into account the specifications for the acquisition and the local geology and conditions.

Amplitude and Frequency Maps - Amplitude and frequency analyses were conducted as part for the standard QC for every line acquired. The following design windows were used:

### **Ambient Window:**

Measured above direct arrival - Amplitude measured in microbars

Boomer Near chan: 2 to 60ms Far chan: 2 to 60ms

Sparker Near chan: 2 to 60ms Far chan: 2 to 60ms

### **Data Window:**

Measured over area of best S/N or target. Amplitude and dominant frequency measured- RMS and Hz.

Boomer Near chan: 300 to 400ms Far chan: 300 to 400ms

Sparker Near chan: 1250 to 1500ms Far chan: 1250 to 1500ms

### **Deep Window:**

Measured over last 500ms of trace. Amplitude and dominant frequency measured- microbars and Hz.

Boomer Near chan: 700 to 800ms Far chan: 700 to 800ms

Sparker Near chan: 1900 to 2000ms Far chan: 1900 to 2000ms

### **Whole Trace:**

Measured over full trace length, RMS and Hz.

Boomer Near chan: 2 to 800ms Far chan: 2 to 800ms

Sparker Near chan: 2 to 2000ms Far chan: 2 to 2000ms

Near Trace Gathers - Four near trace gathers (streamers 1, 5, 10 and 14), were generated for each sail line. These displays were useful in quickly determining any possible errors with acquisition. They reveal source changes, bad records, time break problems and misfires not reported by the recording system. They also provided a good indication of the geological conditions including the strength of water bottom multiples and swell noise contamination.

Shot Gathers - The raw 0.25 ms and the re-sampled, filtered 1.0 ms shot volumes stored

for further processing could be viewed after acquisition and was used to monitor overall data quality and general noise contamination.

Brute Stacks - Two brute stacks, for streamers 5 and 10, were created during the acquisition of each sail line. A constant velocity of 1480 m/s was applied as the brute function to create the stacks.

Channel to Channel Amplitude Diagnostics - Similar to the shot to shot diagnostics, a single RMS value for each channel was calculated from the "data" window RMS. For each channel, every shot RMS contributes to the mean RMS amplitude value for that channel, giving a mean value for each receiver. These values were then displayed adjacently to highlight noisy channels or those with low recording sensitivity.

Offset QC - A check was carried out to comparing the 3D offset assignment derived from the modelled receiver co-ordinates with the expected direct arrival time. The offset QC was created for every channel (all cables and all shots, e.g. Chan 1, 9, 17, ...105; Chan 2, 10, 18, ...106, etc).

Any errors in navigation data processing were highlighted from this QC. This allowed subsequent re-processing of the P190 navigation data to be performed where appropriate.

Near Trace Stack - A near trace stack volume was created to verify further the integrity of the seismic data. The stack was created at a 25 m CDP interval thereby giving a nominal fold of 1. The volume was stacked with a single water velocity of 1480 m/s. Normalized time slice, in-line and cross-line displays were created to QC the volume.

The near trace stack was updated after every accepted sequence acquired.

3D Raw Stack - A brute 3D stack volume was created to verify further the integrity of the seismic data. The stack was created at a 3.125 m CDP interval thereby giving a nominal fold of 8 for the Boomer source (3.125 m shot spacing) and a nominal fold of 4 for the Sparker source (6.25 m shot spacing). The volume was stacked with a single water velocity of 1480 m/s. Normalized time slices, in-lines and cross-lines displays were created to QC the volume. The 3D



stack was updated after every accepted sequence acquired.

Binning Control - The binning process is monitored by comprehensive printed diagnostics and optional colour displays detailing:

- Acquired fold of coverage - all offsets.
- Fold following trace rejection.
- Fold following trace re-allocation.
- Final fold of coverage - all offsets.
- Mean radial distance to bin centre.
- Standard deviation of the distance from bin centre.
- Mean inline distance to bin centre.
- Mean crossline distance to bin centre.
- Number of traces rejected.
  
- Fold of coverage plots - Colour displays of both acquired and final fold of coverage of both restricted and full offset ranges are used to check proposed fold and offset distribution.

### **A.6.5 Production**

Survey operations occurred over a 26-day period from October 10th to November 5th, 2013. During that period 3-D seismic reflection data were acquired within two areas of interest and production for these areas is summarized below. Post plots charts illustrating the bin coverage for each of the surveyed areas are shown in figures A.5 and A.6 below. A summary by sequence was generated onboard during acquisition.

Postplot bin coverage maps are illustrated in Figures A.5 and A.6 below.

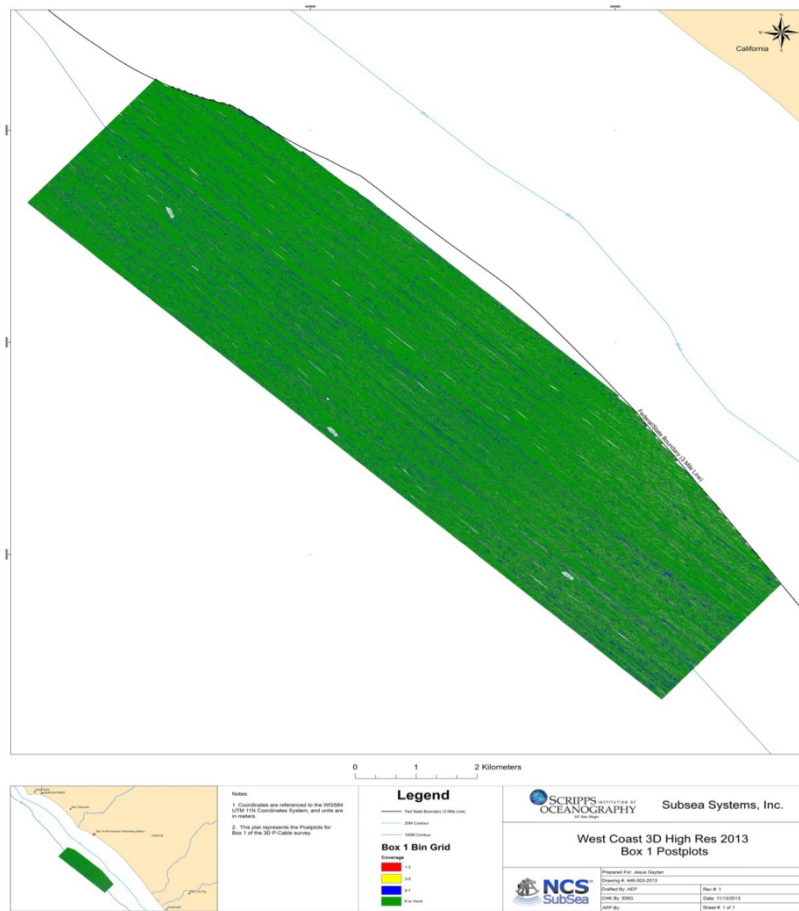
**Area One**

Primary Survey Lines 101  
Re-shot and Infill Lines 48  
Total Line-kilometers 1,660.50

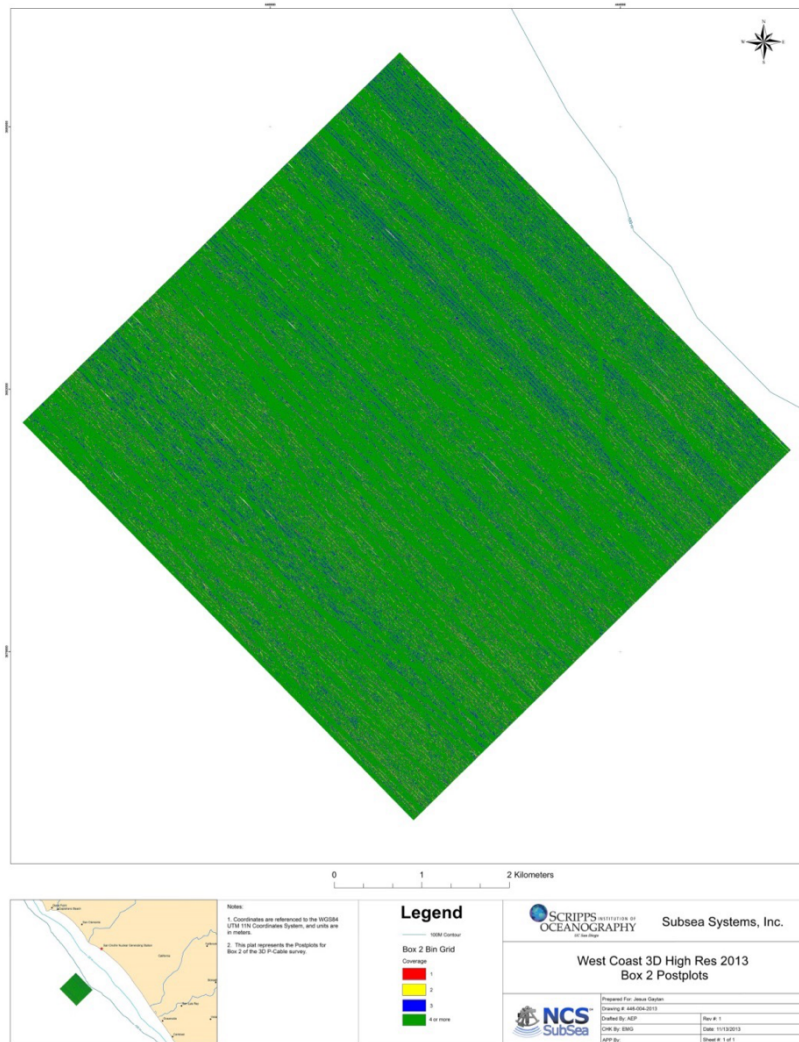
**Area Two**

Primary Survey Lines 161  
Re-shot and Infill Lines 34  
Total Line-kilometers 1,289.31

**Total line-kilometers 2,950**



**Figure A.5:** Block One bin coverage postplot.



**Figure A.6:** Block Two bin coverage postplot.

## A.6.6 Deliverables

On completion of survey operations all digital seismic reflection data in SEGy format and associated navigation files in P1/90 format were turned over to the UCSD/SIO Chief Scientist. GeoTrace performed seismic QA/QC onboard and is processing the P-Cable 3D data. This Field Report outlines the operations onboard the R/V New Horizon.

## **A.6.7 Acknowledgements**

This work, in part, is a cruise report for NH1323 in: **Driscoll, N.W., and Kent, G.M. (2013). SONGS 3-D High Resolution P-cable Survey Offshore Southern California.** The dissertation author was a science member of this survey cruise.

## **Appendix B**

### **Offshore & Onshore 3D High Resolution**

### **Processing Final Report**



**Geotrace**<sup>®</sup>  
TECHNOLOGIES

**SCRIPPS / UNR**

**Survey: SONGS**

**Area: Offshore Southern California**

**Offshore & Onshore 3D High Resolution Processing Final Report**

Geotrace Project No.: 5800411

Date: April 2014  
Geotrace Contact: Frank Landers  
Addressee: Dr. Graham Kent

Geotrace Technologies  
12141 Wickchester Lane, Suite 200  
Houston, Texas 77079  
Tel: (281) 497 8440 Fax: (281) 497 4619

# **Seismic Data Processing Report**

Area : San Onofre Nuclear Generating Station (SONGS) Offshore southern California, USA  
Date acquired: October 2013 – April 2014

## **Prepared by:**

**Geotrace Technologies**  
12141 Wickchester Lane, Suite 200  
Houston, Texas 77079  
USA

## **For:**

**Scripps University California San Diego**  
**University Nevada Reno**

## **B.1 Introduction**

This report describes the onboard and onshore high resolution data processing carried out on behalf of Scripps Institute of Oceanography UCSD and UNR during the period October 2013 to April 2014, by Geotrace Technologies, onboard the academic research vessel New Horizon operated by Scripps Institute of Oceanography.

The survey was acquired over the SONGS area, offshore southern California, USA. The area covered by the 3D seismic survey totals approximately 100 km<sup>2</sup>.

The survey was acquired using the P-Cable acquisition configuration. This comprised a single source and 14 streamers attached to a cross cable. The survey was acquired at both a 0.25ms and 0.5ms sample rate. The native bin size was 3.125m inline and 3.125m crossline separation for acquisition. The final data was processed using a 3.125m inline and 3.125m crossline separation. Full details of the acquisition parameters can be found in Section B.2 of this report and a full inventory of the lines processed is provided in Section B.10.

This report covers the development and application of an appropriate data processing scheme, including the tests performed and a summary of the processing sequence adopted. The report also details the quality control products generated both as part of the acquisition QC and the processing QC.

The main objectives of the processing were to provide Scripps and UNR with a raw 3D stack that could be produced onboard and maintained alongside acquisition. Further processing would then be carried out onshore to produce a final migrated volume.

Testing was conducted prior to the start of the acquisition phase using supplied 2D data acquired August 2013 prior to the start of acquisition of the 3D surveys in October 2013. The testing then continued during the acquisition of the 3D surveys. Part of the testing was performed on the vessel and was followed by the onshore stage involving Scripps and UNR in all important stages of processing to provide confirmation of any major parameter decisions.



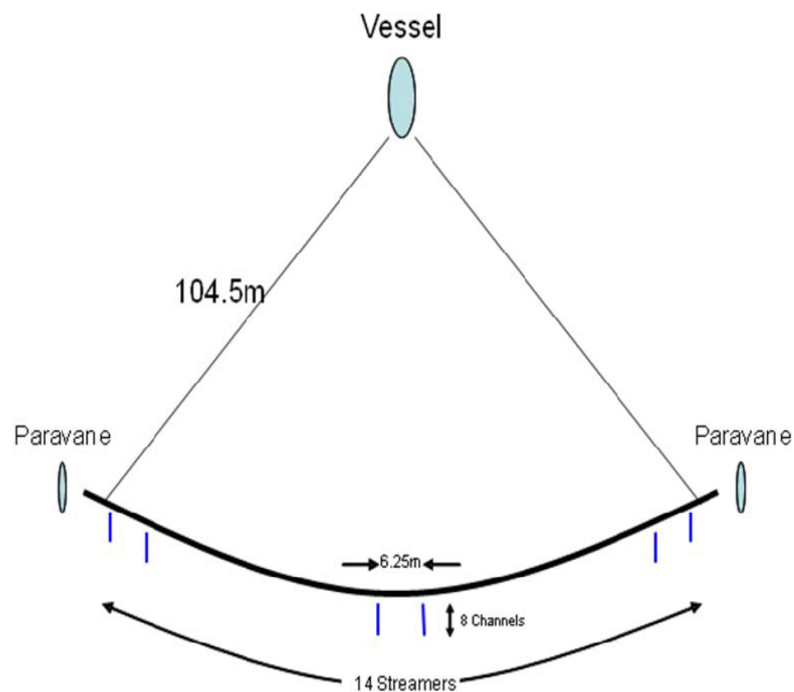
The report concludes with a qualitative assessment of the project, together with a list of the personnel involved. Data and test examples are also included in the report.

## B.2 Acquisition & Survey Area

### B.2.1 Specifications

The survey was acquired by R/V New Horizon (Scripps Institute of Oceanography) from October 2013 to November 2014. The acquisition geometry comprised a single source and a cross cable with 14 small streamers attached, each with 8 channels. This is the P-Cable acquisition system details of which are summarised below.

#### B.2.1.1 P-Cable 14 Streamer Configuration:



**Figure B.1:** P-Cable 14 Streamer Configuration



**Figure B.2:** P-Cable Aerial View

**B.2.1.2 Energy source:**

Types	Boomer (using 3 plates)
Sparker	(using 3 tips)
Shot interval	3.125m (B) 6.25m (S)
Direction of shooting	132 or 312 degrees (B) and 135 or 315 degrees (S)
Source depth	0.5m (B) and 2m (S)

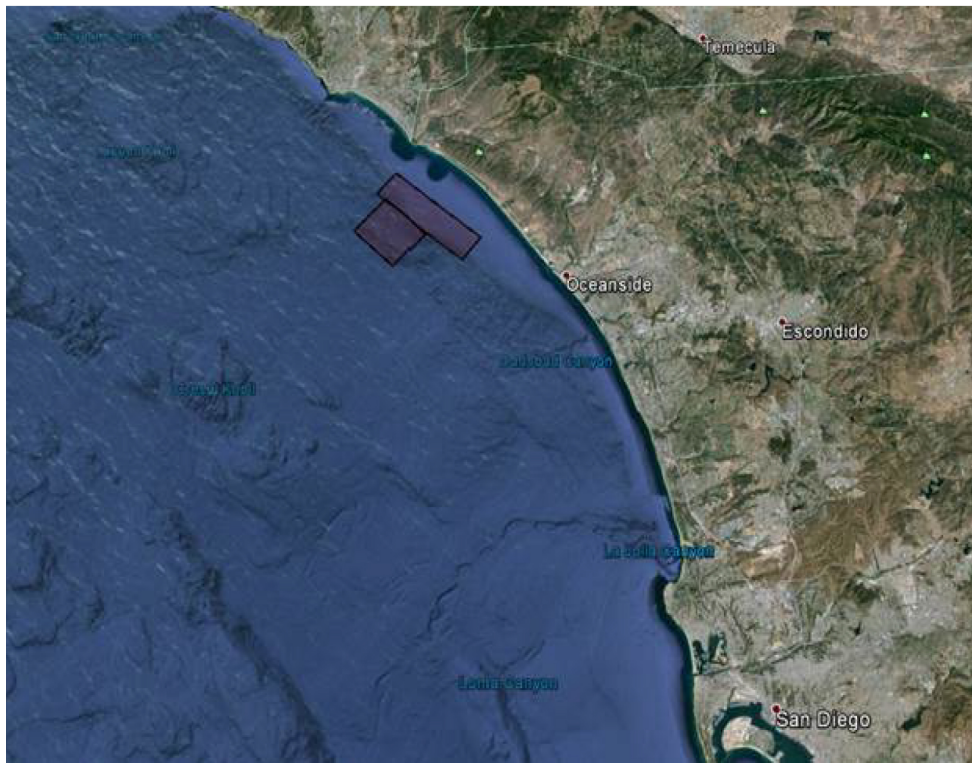
**B.2.1.3 Receiving arrangements:**

No. of groups	8 *14
Group interval	6.25m
Cable depth	2m

**B.2.1.4 Instrumentation:**

Format	SEGY
Recording length	800ms (B) and 2000ms (S)
Sample rate	0.25ms (B) and 0.5ms (S)
Recording polarity	Normal (SEG convention)
Recording delay	0ms

## B.2.2 Survey Area



**Figure B.3:** Offshore southern California, USA with survey areas highlighted (from Google Earth)

## B.3 Navigation & 3D Geometry Definition

### B.3.1 Coordinate System

Processed navigation data in UKOOA P1/90 format was created onboard for the paravane and source positions. The following projection and datum were used:-

Geodetic Datum: WGS84  
 Spheroid: WGS84  
 Longitude of Central Meridian: 129° West  
 Projection Type: 001 TM North Orientated  
 UTM Projection Zone: 11 N

### B.3.2 3D Bin Grid Definition Boomer

Grid Origin : Inline 1000 Crossline 1000  
 (“local” coordinate x,y = 0,0m)  
 Defined at Co-ordinate Point : Easting : 438370.4 E  
 Northing : 3686647.4 N  
 (centre of bin)  
 Grid Bearings : inline direction 132°  
 Local Rotation Angle : -42° (anti clockwise rotation)

#### 3D Processing Geometry:

Bin Size : Inline spacing : 3.125m  
 Crossline spacing : 3.125m  
 Numerical Bin Increment: Inline separation : 1  
 Crossline separation : 1  
 Total Number of Bins : Inlines : 2100  
 (1001,1002,1003, .....3100)  
 Crosslines : 5400  
 (1001,1002,1003.....6400)  
 Local Rotation Angle: -42°

**Table B.1:** Geometry Corner Coordinates:

Cross line	Inline	Easting	Northing
1001	1001	438370.40	3686647.40
1001	3100	442759.48	3691521.97
6400	3100	455927.73	3680232.48
6400	1001	450908.65	3675357.91

### B.3.3 3D Bin Grid Definition Sparker

Grid Origin : Inline 1000 Crossline 1000  
 (“local” coordinate x,y = 0,0m)  
 Defined at Co-ordinate Point : Easting : 435186.3 E  
 Northing : 3681633.1 N  
 (centre of bin)  
 Grid Bearings : inline direction 135.52°  
 Local Rotation Angle : –45.52° (anti clockwise rotation)

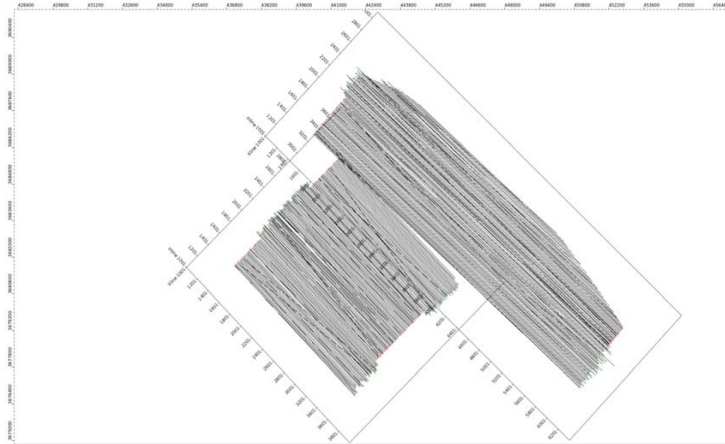
#### 3D Processing Geometry:

Bin Size : Inline spacing : 3.125m  
 Crossline spacing : 3.125m  
 Numerical Bin Increment: Inline separation : 1  
 Crossline separation : 1  
 Total Number of Bins : Inlines : 2800  
 (1001,1002,1003, .....3800)  
 Crosslines : 3000  
 (1001,1002,1003.....4000)  
 Local Rotation Angle: –42°

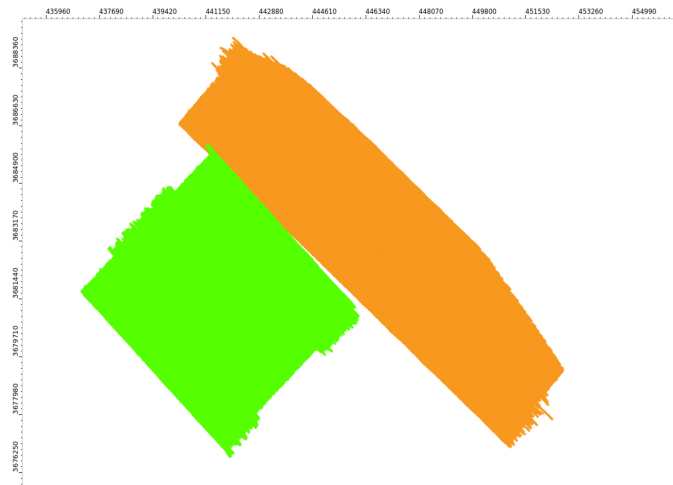
**Table B.2:** Geometry Corner Coordinates:

Cross line	Inline	Easting	Northing
1001	1001	435186.30	3681633.10
1001	3800	441314.89	3675392.25
4000	3800	448001.67	3681958.75
4000	1001	441873.09	3688199.60

### B.3.4 Unrotated Survey Area (Boomer and Sparker)

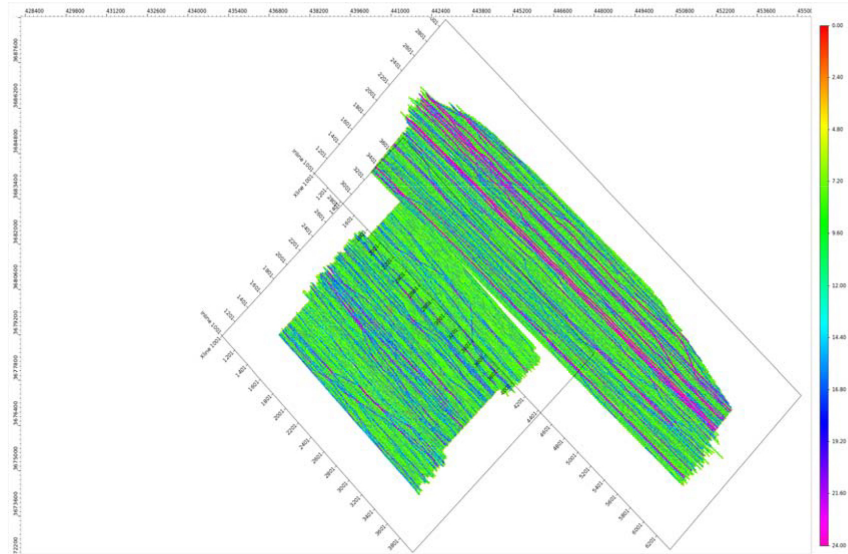


**Figure B.4:** As acquired sail lines (all lines)

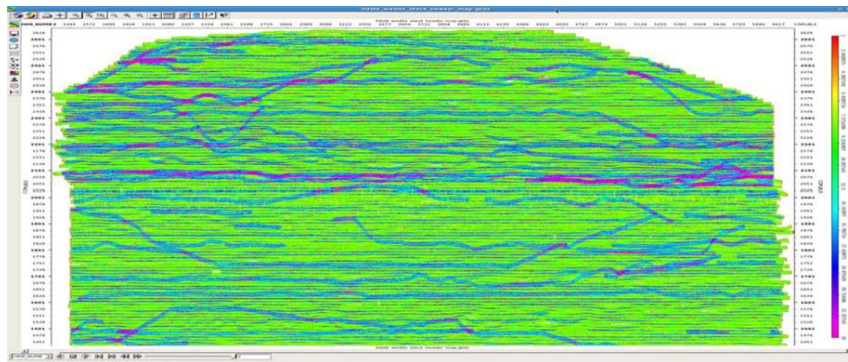


**Figure B.5:** As acquired source positions (all lines, all shots)

### B.3.5 Rotated Survey Area



**Figure B.6:** As acquired fold of coverage (all offsets)



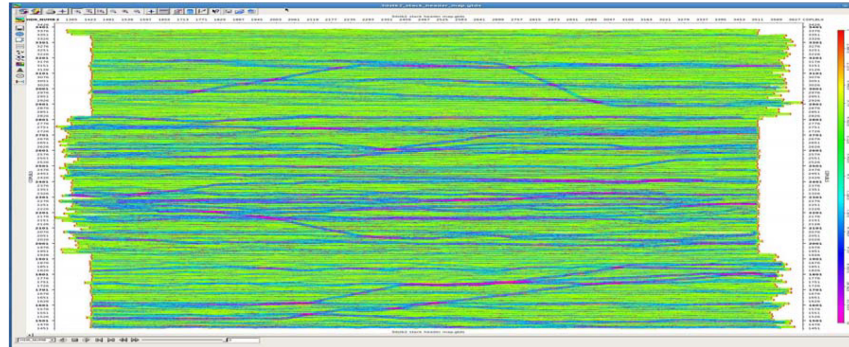
**Figure B.7:** As acquired Boomer fold of coverage (nominal=8, all offsets)

## B.4 Acquisition QC and Onboard Processing

Geotrace Technologies performed full data acquisition QC. Products and examples are described in this section. QC products were created after the acquisition of each line when the SEG-Y data with the modelled receiver co-ordinates were available.

The parameterisation and production of the QC displays take into account the specifications for the acquisition and the local geology and conditions.





**Figure B.8:** As acquired Sparker fold of coverage (nominal=4, all offsets)

### B.4.1 Amplitude and Frequency Maps

Amplitude and frequency analyses were conducted as part for the standard qc for every line acquired. The following design windows were used:

**Ambient Window:** Measured above direct arrival – Amplitude measured in microbars

Boomer Near chan: 2 to 60ms Far chan: 2 to 60ms

Sparker Near chan: 2 to 60ms Far chan: 2 to 60ms

**Data Window:** Measured over area of best S/N or target. Amplitude and dominant frequency measured- RMS and Hz.

Boomer Near chan: 300 to 400ms Far chan: 300 to 400ms

Sparker Near chan: 1250 to 1500ms Far chan: 1250 to 1500ms

**Deep Window:** Measured over last 500ms of trace. Amplitude and dominant frequency measured- microbars and Hz.

Boomer Near chan: 700 to 800ms Far chan: 700 to 800ms

Sparker Near chan: 1900 to 2000ms Far chan: 1900 to 2000ms

**Whole Trace:** Measured over full trace length, RMS and Hz.

Boomer Near chan: 2 to 800ms Far chan: 2 to 800ms

Sparker Near chan: 2 to 2000ms Far chan: 2 to 2000ms

## **B.4.2 Near Trace Gathers**

Four near trace gathers (streamers 1, 5, 10 and 14), were generated for each sail line. These displays were useful in quickly determining any possible errors with acquisition. They reveal source changes, bad records, time break problems and mis-fires not reported by the recording system. They also provided a good indication of the geological conditions including the strength of water bottom multiples and swell noise contamination.

## **B.4.3 Shot Gathers**

The raw 0.25ms and the resampled, filtered 1.0ms shot volumes stored for further processing could be viewed after acquisition and was used to monitor overall data quality and general noise contamination.

## **B.4.4 Brute Stacks**

Two brute stacks, for streamers 5 and 10, were created during the acquisition of each sailline. A constant velocity of 1480m/s was applied as the brute function to create the stacks.

## **B.4.5 Channel to Channel Amplitude Diagnostics**

Similar to the shot to shot diagnostics, a single RMS value for each channel was calculated from the “data” window RMS. For each channel, every shot RMS contributes to the mean RMS amplitude value for that channel, giving a mean value for each receiver. These values were then displayed adjacently to highlight noisy channels or those with low recording sensitivity.

## **B.4.6 Offset QC**

A check was carried out to comparing the 3D offset assignment derived from the modelled receiver co-ordinates with the expected direct arrival time. The offset qc was created for every channel (all cables and all shots, eg. Chan 1, 9, 17, ...105; Chan 2, 10, 18, ...106, etc).

Any errors in navigation data processing were highlighted from this qc. This allowed subsequent re- processing of the P190 navigation data to be performed where appropriate.

## **B.4.7 Near Trace Stack**

A near trace stack volume was created to further verify the integrity of the seismic data. The stack was created at a 25m CDP interval thereby giving a nominal fold of 1. The volume was stacked with a single water velocity of 1480m/s. Normalised timeslices, inlines and crosslines displays were created to QC the volume.

The near trace stack was updated after every accepted sequence acquired.

## **B.4.8 3D Raw Stack**

A brute 3D stack volume was created to further verify the integrity of the seismic data. The stack was created at a 3.125m CDP interval thereby giving a nominal fold of 8 for the Boomer source (3.125m shot spacing) and a nominal fold of 4 for the Sparker source (6.25m shot spacing). The volume was stacked with a single water velocity of 1480m/s. Normalised timeslices, inlines and crosslines displays were created to QC the volume.

The 3D stack was updated after every accepted sequence acquired.

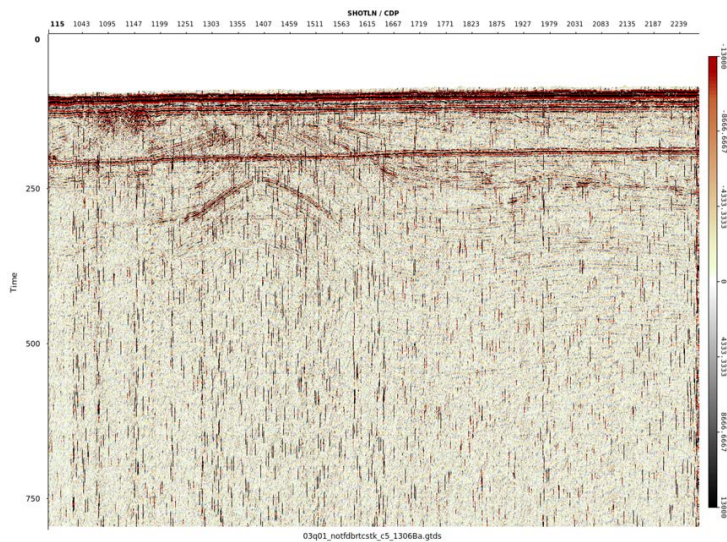
## **B.4.9 Binning Control**

The binning process is monitored by comprehensive printed diagnostics and optional colour displays detailing:

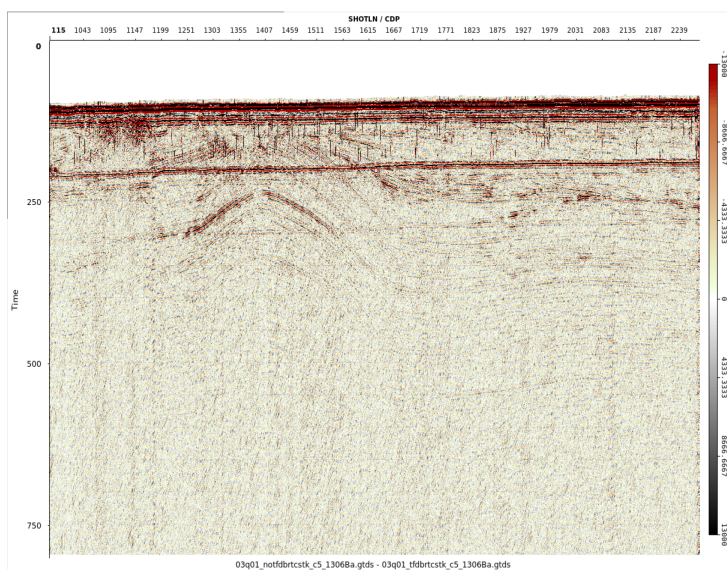
- Acquired fold of coverage – all offsets.
- Fold following trace rejection.
- Fold following trace re-allocation.
- Final fold of coverage – all offsets.
- Mean radial distance to bin centre.
- Standard deviation of the distance from bin centre.
- Mean inline distance to bin centre.
- Mean crossline distance to bin centre.
- Number of traces rejected.
  
- Fold of coverage plots - Colour displays of both acquired and final fold of coverage of both restricted and full offset ranges are used to check proposed fold and offset distribution.

## **B.4.10 Noise Examples**

### **B.4.10.1 Random noise bursts (possible swell noise)**



**Figure B.9:** Line 1306B (cable 5 brute stack)



**Figure B.10:** Line 1306B with noise attenuation applied (cable 5 brute stack)

### B.4.10.2 Swell Noise

There was inevitably some swell present during the survey but only light or moderate and not considered to be problematic for final processing. The swell noise attenuation applied is described in Section B.5.2.5.

## **B.5 Onshore Processing**

### **B.5.1 Processing Summary**

The onshore processing sequence was derived after the acquisition finished. Processing was carried out at Geotrace's Houston office.

1. Reformat SEGY– 0.25 or 0.5 ms raw shot gathers
2. Low cut filter 45(18) Hz(dB/Oct)
3. Temporal resample to 1ms sample rate with anti-alias filter
4. Bad trace edits
5. De-noise with automatic spike removal in Shot domain – 2 iterations
6. 2D SRME on common channel/shots
7. Load data to a 3D pre stack volume (3.125m x 3.125m)
8. Apply 1480m/s primary NMO
9. 3D stack
10. Deconvolution After Stack (DAS) – (Boomer data only)
11. 1D SRME and subtract
12. Interpolation of empty bins with SNIP
13. Post stack, pre-migration noise attenuation with automatic spike removal, FDNA, and FXY
14. Post stack Kirchhoff migration
15. Dip filtering (Boomer data only)
16. Time Variant Filter (Sparker data only)
17. Amplitude balancing: Measured exponential gain
18. Gun and cable static correction
19. SEGY – Final Filtered Migrated Stack
20. Scaling: 400ms Iterative AGC - optional
21. SEGY – Final Filtered Migrated Scaled Stack

### **B.5.2 Preliminary Processing**

#### **B.5.2.1 Low Cut Filter**

Application of a 45(18) Hz (dB/oct) zero phase low cut filter was applied.

### **B.5.2.2 Signature / Debubble**

No far field was available for the Boomer or Sparker sources used in the acquisition. Therefore no designation or debubble was applied in the final processing with the data being left at acquired or minimum phase.

### **B.5.2.3 Temporal resample**

A 375(96) Hz (dB/Octave) anti-alias minimum phase filter was applied prior to resampling from 0.25ms (or 0.5ms) to 1ms.

### **B.5.2.4 Bad trace editing**

Geotrace confirmed the single trace edits flagged during the onboard QC processing for removal.

### **B.5.2.5 Noise Attenuation**

Swell noise attenuation (TFD) was tested as required but was in general not a serious issue for this project. TFD performs noise suppression with sub spectral balancing using sample-wise median thresholds within frequency sub-bands in time-frequency space. It is ideally suited to removing low- frequency noise bursts and swell noise in marine data, whilst preserving the signal amplitudes.

The initial TFD testing was conducted onboard the vessel for sequence 2 which contained minimal swell. Due to the particular setup the standard approaches of TFD (shot or receiver domains) were unsuitable.

Alternately an automatic spike removal process was tested. The program locates high amplitude spikes and noise bursts within seismic data and replaces the affected samples with data averaged from the surrounding traces. Spikes are found by comparing the ratio between the each

sample amplitude on the input trace to the RMS average. Whenever the ratio exceeds a given threshold level, that input sample is defined as a spike. The spike definition can be extended to a user-specified number of samples in time before and after the current sample. For each input trace the program sums together a number of adjacent traces to form a reference trace (after first squaring their values). The reference trace is smoothed over a time gate by applying a running average. After normalization and application of a square root, the sample values stored in the reference trace form the 2-dimensional window averages to be used in the comparisons. Amplitude despiking was applied in the shot domain.

### **B.5.3 Static Corrections**

The raw 3D stack provided evidence of possible static shifts. Much of these were seen to be line to line statics.

#### **B.5.3.1 Offset Corrections**

The 3d offsets derived from the modelled receiver locations were checked by comparing the predicted direct arrival time with that measured in the data. To do this, displays were produced of common channel sections for specific cables within selected lines. Using the predicted arrival times the data were shifted to a nominal reference time (100ms). Any deviations of the 3d offset are seen as shifts in the data away from this time. It could be seen only a few minor errors in the modelled receiver positions existed.

Further static shifts were also apparent. These occurred at the boundaries of sail lines and therefore were assumed to originate from variations in the water column.

#### **B.5.3.2 Tidal Static Corrections**

Predicted tidal tables, covering the period of acquisition, were provided by NCS. From these, timing shifts were extracted and applied to the data based on the time header. The



application of the tidal statics was tested by creating a near trace stack.

The decision was made not to apply the tidal static corrections due to the erroneous shifts the extracted values were introducing into the data.

### **B.5.3.3 Water Column Statics**

Line to line statics thought to originate from variations in the water column such as temperature changes, currents etc were evident.

To correct for these statics the following methodology was tested.

- Pick water bottom times over an nmo corrected 3D near trace cube for every inline.
- Convert picked times to a gridded 3D surface.
- Smooth raw surface using a Gaussian 11point filter to create an ideal surface.
- Subtract smoothed surface from raw to derive statics.
  
- Apply statics.

The decision was made not to apply any water column based static corrections in order to prevent smearing of possible faults and other natural geologic structures.

### **B.5.3.4 Displays of Static Corrections – Near Trace Stacks**

### **B.5.3.5 Trim Statics**

After sorting to CDP gathers, the gathers were investigated for time-variant trim statics.

It was apparent after examination of the CP sorted gathers that trim statics were not a problem and thus the decision was made not to test or apply any time-variant trim static corrections.

## **B.5.4 Pre-migration Processing**

### **B.5.4.1 Surface Related Multiple Elimination (SRME)**

Surface Related Multiple Elimination was applied to coincident shots and receivers each 3.125m (B) or 6.25m (S) apart. SRME is a pre-stack technique designed to attenuate surface generated multiples following studies made by Verschuur et. al. and described in a number of publications including the Journal of Seismic Exploration, 1, Jan. 1992. The method utilises the general wave equation boundary condition and makes no assumptions regarding wave behaviour in the earth. No prior model or knowledge of the sub-surface is therefore necessary.

In addition, traces were extrapolated to zero offset within the shot records.

Three iterations of SRME were performed on the data. A multiple estimate is made and subtracted from the input data. Both the results of this subtraction and the unchanged input data are passed on for further processing. Subsequent iterations use the result of the previous subtraction as input to the multiple prediction. After the final iteration, the final multiple estimate is adaptively subtracted from the original input data.

The adaptive subtraction was performed within common channel records. The multiple model was matched and subtracted as follows:

- (i) Match the gross amplitude difference between the input data and the multiple model. This is designed on the whole record and applied as a single point filter.
- (ii) Filter to match the phase.
- (iii) Filter to match the amplitudes.

### **B.5.4.2 3D Volume Load**

Before the stack and migration processing the data were loaded to a 3D pre-stack volume using the grid definition defined in Section B.3.3. The data was left on the acquired natural

3.125m CDP spacing within the load giving a final nominal fold of 8 for the Boomer data and 4 for the Sparker data.

#### **B.5.4.3 Velocity Analysis**

Due to the relative lack of fold a conventional velocity analysis was not possible. Trials were performed using a constant velocity of 1480m/s.

#### **B.5.4.4 Final Stack**

The final data were stacked and 1/N normalisation was applied where N is the number of live samples stacked.

#### **B.5.4.5 Deconvolution After Stack (DAS) - Boomer data only**

Due to the depth of the water bottom the Boomer data was suitable for deconvolution. A water bottom gap (predictive) deconvolution after stack (DAS) was tested and found to be successful at removing interbed multiples just below the water bottom.

Various operator lengths and gaps were tested and displayed with stacks. The chosen one window deconvolution was a 10/250ms (gap/total operator length) filter applied in the space-time (X-T) domain.

Water bottom gap deconvolution was tested and confirmed for production using the following parameters:-

#### **B.5.4.6 1D Surface Related Multiple Elimination (SRME)**

Following the stack and before the migration processing a multiple estimate was again made and adaptively subtracted from the input data. The results of this subtraction were then passed on for further processing.

Minimum Prediction Lag	10 ms
Maximum Prediction Lag	250 ms
Water bottom time	50ms
Design windows	1
	Near trace 50 ms – 750 ms
	Far trace 50 ms – 750 ms
Application windows	1
	Near trace 100 ms – 750 ms
	Far trace 100 ms – 750 ms
Water bottom time	500ms
Design windows	1
	Near trace 50 ms – 750 ms
	Far trace 50 ms – 750 ms
Application windows	1
	Near trace 200 ms – 750 ms
	Far trace 200 ms – 750 ms

#### **B.5.4.7 Interpolation of empty bins**

An interpolation method was applied post stack to fill any remaining areas that lacked coverage.

SNIP is basically a signal to noise enhancement tool, it determines signal by finding the dipping plane of maximum semblance centered on the output point. It determines noise with an amplitude median/trim process within each plane.

On the same principle, data interpolation can be done. Instead of noise attenuation, the dip filter can estimate the data in missing locations. The SNIP was run in the crossline direction to fill in inlines within the crosslines.

#### **B.5.4.8 Post stack noise attenuation**

Following the interpolation of empty bins, Frequency Dependent Noise Attenuation (FDNA) was tested in an attempt to prevent unwanted migration artifacts during the imaging step.

FDNA (frequency domain noise attenuation) focuses more on any high frequency remnant noise remaining after stack. At the high frequency level, it can be used effectively to attenuate

diffracted noise such as multiples based on discrimination of frequency content between primary and non-primary events.

FDNA operates on one ensemble at a time. Each ensemble is transformed into time-frequency space using a short time Fourier transform algorithm. The transform is separated into amplitude and phase components for each frequency sub-band. If auto-thresholding is requested then the median spectral amplitude within each requested frequency sub-band is calculated for the ensemble.

The median of these medians becomes the threshold for that ensemble. Each sample of each requested sub-band is compared against this threshold. If the sample amplitude exceeds the threshold then the median spectral amplitude of the adjacent samples within that sub-band is computed and installed at this location.

**Boomer data**

Number traces	10 (rolling window)
Threshold	1 x the median value
Frequency bandwidth* attacked	20-250 Hz
Taper	100 ms
Start-time	Inline 1417 100ms (contoured to water bottom time) Inline 2639 150ms

**Sparker data**

Number traces	5 (rolling window)
Threshold	2 x the median value
Frequency bandwidth* attacked	20-250 Hz
Taper	100 ms
Start-time	Inline 1600 100ms (contoured to water bottom time) Inline 3300 150ms

FXY was also tested to attenuate any pure random noise throughout the section.

Within a 2D stack (Inline or Crossline), flat events appear as complex sinusoidal oscillations in the F-X domain. By designing and applying complex one-step-ahead predictive operators within a sliding trace gate, the sinusoidal oscillations may be separated from the random noise which contaminates them. The width of the trace gate is selected such that curved data appear locally linear.

In 3D, the linear model is extended to include locally planar surfaces. The spatial distribution of the F-X- Y filter coefficients provides for better preservation of low amplitude events and curved surfaces than either 2D or two-pass approaches.

Frequencies	1-500Hz
Iterations	1
White noise	0%
Gate Overlap	33% each in inline, crossline, & time directions

**Boomer data**

Filter design widths	3 traces in both inline and crossline directions
Autocorrelation Window	lengths 41 traces in both inline and crossline directions

**Sparker data**

Filter design widths	8 traces in both inline and crossline directions
Autocorrelation Window	lengths 21 traces in both inline and crossline directions

### **B.5.5 Kirchhoff, post stack time migration**

A zero offset post stack Kirchhoff algorithm was used to migrate the data. A series of Impulse responses were performed initially to establish suitable migration parameters.

An aperture of 1km with a time varying dip limit was selected for the final migration.

The single constant velocity function tested and applied in Section B.5.4.3 was used as the migration velocity field.

The following parameters were chosen for production :-

### **Boomer data**

Input & Output trace length	800ms	
Input & Output sample rate	1ms	
Input & Output grid	3.125m x 3.125m bins	
Half Aperture	1km	
Pre-conditioning	None	
Dip Limit:	Time (ms)	Angle (degrees)
	1	90
	500	80
	800	70

### **Sparker data**

Input & Output trace length	2000ms	
Input & Output sample rate	1ms	
Input & Output grid	3.125m x 3.125m bins	
Half Aperture	1km	
Pre-conditioning	None	
Dip Limit:	Time (ms)	Angle (degrees)
	1	90
	1500	80
	2000	70

## **B.5.6 Post Migration Processing**

### **B.5.6.1 Dip Filtering - Boomer data only**

To further attenuate the water bottom multiple a post stack dip filter was applied to the PSTM stacks. A  $\pm 4$  ms / trace F-k dip filter was applied after migration.

### **B.5.6.2 Time Variant Filter - Sparker data only**

A post stack time variant filter was applied based upon a start time header which varied spatially depending upon the water depth along each line. Filtering the high frequency noise in the deepest sections of the lines enhanced the stack response of the lower frequency primary events. The filter applied was defined as follows:

Water bottom time=400ms:

Time(ms)	High Cut (dB/Oct.)
300	500 (36)
500	150 (36)
2000	100 (36)

Water bottom time=800ms:

Time(ms)	High Cut (dB/Oct.)
700	500 (36)
900	150 (36)
2000	100 (36)

Water bottom time=1600ms:

Time(ms)	High Cut (dB/Oct.)
1500	500 (36)
1700	150 (36)
2000	100 (36)

### B.5.6.3 Amplitude Balancing: Measured Exponential gain

The final migrated section was balanced by the application of the following measured exponential gain.

#### Boomer data

Water bottom time=50ms:

Time (ms)	Gain (dBs)
0	0
50	7
250	10
400	11
800	15

#### Sparker data



Water bottom time=250ms:

<b>Time (ms)</b>	<b>Gain (dBs)</b>
0	0
250	10
400	11
600	13
800	15

Water bottom time=450ms:

<b>Time (ms)</b>	<b>Gain (dBs)</b>
0	0
250	10
400	11
600	13
800	15

Water bottom time=500ms:

<b>Time (ms)</b>	<b>Gain (dBs)</b>
0	0
500	4
800	8
1000	13
1200	12

Water bottom time=700ms:

<b>Time (ms)</b>	<b>Gain (dBs)</b>
700	0
800	2
1000	6
1200	10
1400	11

Water bottom time=1100ms:

<b>Time (ms)</b>	<b>Gain (dBs)</b>
1100	0
1200	5
1400	11
1600	14
1800	16

#### **B.5.6.4 Gun and cable static**

A correction for the source and receiver depths was made applying a +1.7 ms bulk shift to all Boomer data and +2.7ms bulk shift to all Sparker data.

#### **B.5.6.5 Scaling: AGC**

An iterative 400ms AGC was tested and optionally applied to the data.

## **B.6 Kirchoff, post stack depth migration**

### **B.6.1 Initial model building**

The Initial model was built using a Dix conversion of the smoothed RMS velocities derived for the migration from the 2013 2D SONGS PSTM processing as follows:

The RMS field was produced as part of the 2013 2D SONGS PSTM processing flow. Straight ray (2nd order) Kirchhoff pre-stack time migration was performed. The PSTM data was used to pick a manual RMS field.

Careful attention was paid to picking these analyses in a relatively smooth consistent manner suitable for the Kirchhoff migration process. The accurate nature of the velocities was confirmed by the migrated imaging of each 2D line, together with the “flat” NMO corrected nature of the main events across diagnostic 2D CDP gathers.

The validity of the interpreted velocity functions for the velocity line was confirmed by inspection of the following QC displays:

- Isovelocity display
- Stack section plus NMO corrected CMPs at both the velocity locations and intermediate points
- Colour areal plots of the velocities at selected isotimes were produced to verify the integrity of the 2D interpolation of the velocity field

The RMS velocity field was converted to an interval velocity field using Dix conversion. This procedure involved the following steps:

- Grid RMS velocity into 3D section
- Rotate and cut to individual Boomer and Sparker 3D geometries
- Smooth with time variable smoother
- Via DIX to time/interval
- Convert to depth
- Smooth again with depth variable smoother.

## B.6.2 Final post-stack depth migration

Geotrace Technology's Kirchhoff 3D depth migration is a highly efficient target-oriented or full volume pre- or post-stack migration algorithm for production of accurate depth images in areas of strong lateral velocity variation.

The algorithm is a standard Kirchhoff integral formulation incorporating temporal and spatial anti-alias protection and providing user-specified dip (including turning ray capability) and aperture control. Travel time calculation is accomplished using proprietary 2D ray tracing software based on a Wavefront Construction algorithm. The algorithm can use maximum energy, 1st arrival or shortest-path, but generally speaking we use maximum energy.

The migration implementation includes state-of-the-art enhancements for amplitude preservation during migration. Amplitude preservation incorporates a variety of weight functions that compensate for obliquity angle and geometric spreading.

Amplitude preservation follows Thierry et al (1999) and incorporates a variety of weight functions which compensate for:

- geometric spreading
- obliquity and slowness
- acquisition irregularities (Jousset et al 1999)
- ray path bending caused by a complex overburden (Beylkin determinants, Thierry et al, 1999)

Pre-computed travel-time and geometrical spreading factors are derived by a wavefront construction scheme. The approach is an implementation based on the ideas presented by Alkalifah et al (1996) and provides multi-valued travel times. Ray selection and summation is based on either first arrivals or shortest travel path / maximum energy. Alternatively, in complex areas dominated by wavefront triplications, ray selection can be abandoned and multi-branch migration operators can be constructed using all the travel time information.

The anti-aliasing is described as Lumley's triangle filtering (Anti-aliased Kirchhoff 3D migration – Lumley, Claerbout and Beve 1994, 64th Annual meeting) with Abma et al correction (Abma, Sun and Bernitas, 1999, Geophysics 64).

The Parameters used in the final migration were:

Algorithm	Kirchhoff
Input & output grid	3.125m x 3.125m bins
Maximum depth	2km
Maximum radial aperture	1km
Depth step	1m
WFC mode:	Maximum Energy

### **B.6.3 Post migration processing**

Following the migration, a similar sequence to the PSTM processing was used, as described earlier in this report:

- Stretch to time domain using final velocity model
- High Cut filter (water depth dependent)
- Application of Exponential Gain
  
- Stretch to depth domain

The only significant differences between the time and depth post-migration sequences were the stretching between time and depth domains.

## **B.7 Delivery products**

The following were confirmed as the required deliverables:-

<b>Description</b>	<b>Output Medium</b>	<b>Number of copies</b>
Final PSTM Migrated Stack	SEG-Y format on USB disk	1
Final PSDM Migrated Stack	SEG-Y format on USB disk	1
Final Report	CD	1

### **B.7.1 Delivery Address**

**Reno, Nevada**

Attn: Dr. Graham Kent

University of Nevada Reno (UNR) Reno, Nevada

USA

## B.8 Conclusions

The first objective with this project was to provide QC after acquisition of every line and a raw 3D QC stack. This was achieved with the raw stack being shown soon after acquisition completed.

The main challenge with this survey was the novel acquisition configuration of the P-cable method.

One drawback of the P-cable method is the lack of fold of coverage. This is not suited to multi-channel processing particularly many demultiple processes such as Radon demultiple and Taup transforms. This wasn't a problem with the SONGS survey as a suitable demultiple scheme was developed using both 1D and 2D SRME along with Deconvolution to attenuate much of the first water bottom multiple thru energy in order to prevent migration smearing or artifacts during the final imaging.

Another problem is that the lack of fold makes velocity estimation difficult. The use of known velocities from the 2D processing acquired over the same survey area helped in this project and allowed a final PSDM migration to be created. Over such short offsets the move out was relatively low which made the use of trim statics unnecessary for the final stack response.

The P-Cable method gives good 3D coverage for high-resolution surveys but requires modelling to be conducted for locating the receiver positions. Fortunately NCS Subsea provided accurate enough modelling of the receiver positions to not need any large corrections which would have seriously degraded the final stack due to the high sample rate and size of the errors. The high sample rate also means that water column and tidal statics have the potential to become a significant problem as well.

The noise attenuation and demultiple methods derived in the onshore phase of the processing to address the problem of noise worked very well and provided a final stack that was of higher quality than the raw onboard stack.

Examples of the key processing steps and comparisons of the raw onboard un-processed and onshore processed data can be seen in the following enclosures;

## **B.9 Personnel**

### **Scripps/UNR**

Dr. Graham Kent Director, Nevada Seismological Laboratory | State Seismologist Professor,  
Department of Geological Sciences and Engineering UNR  
Neal Driscoll Professor Geological Research Division  
Scripps Institution of Oceanography UCSD

### **Geotrace Onshore**

David Bannister Technical Manager, Marine Worldwide  
Joel Latchman Processing Manager, Marine US  
Frank Landers Onshore Senior Project Geophysicist  
Michael Angel Onshore Geophysicist

### **Geotrace Offshore**

Frank Landers Chief Marine Geophysicist  
Michael Angel Marine Geophysicist  
Brian Joiner Systems Administrator, Houston



## B.10 Final Migrated Stack Examples

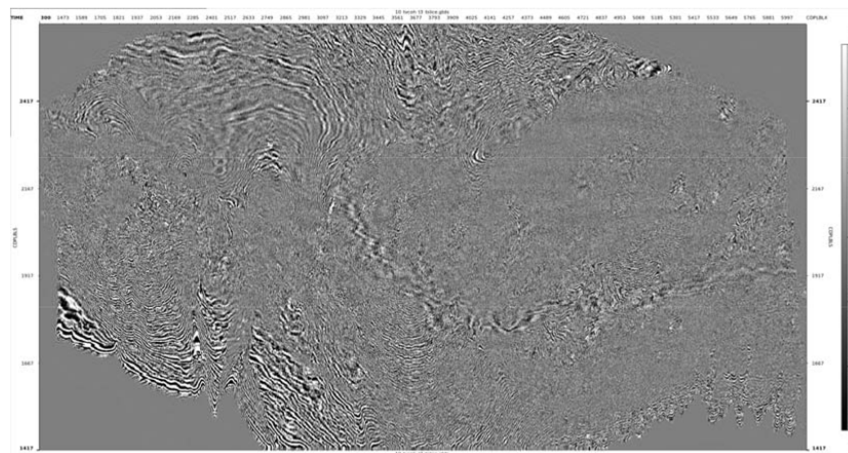


Figure B.11: Time slice – 300ms (Boomer)

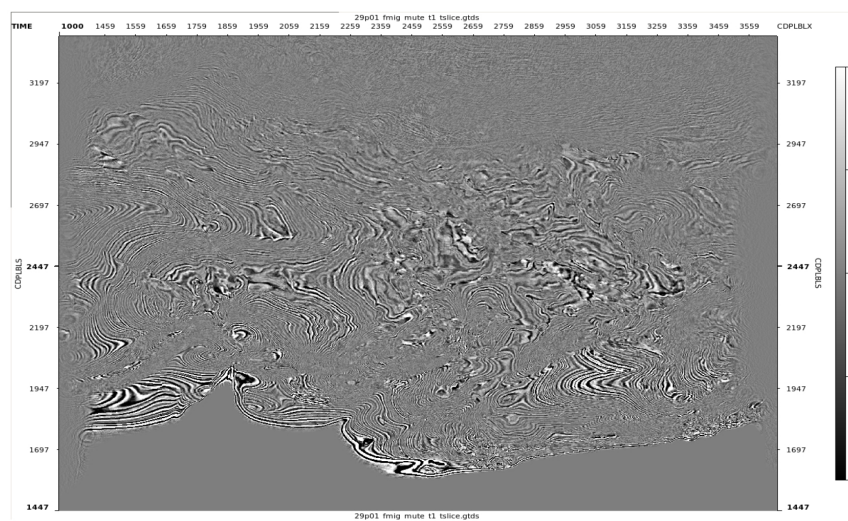
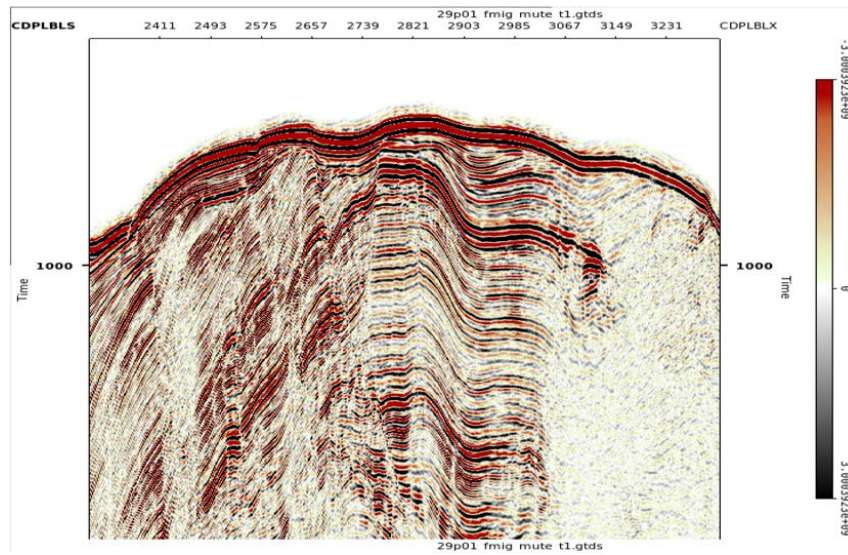
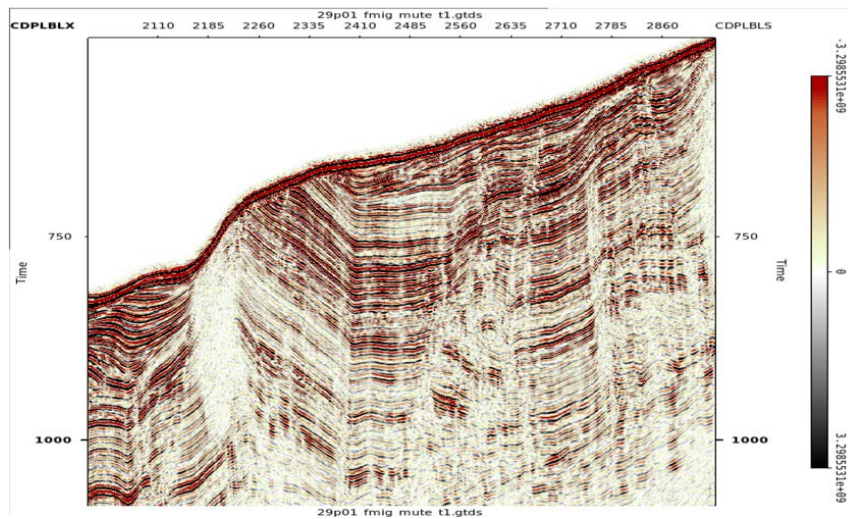


Figure B.12: Time slice – 1000ms (Sparker)



**Figure B.13:** Inline – 1755 Enlarged (Sparker)



**Figure B.14:** Crossline – 2746 Enlarged (Sparker)

## B.11 Sail Line Listing

Seq No	Line Name	Bearing	FGSP	LGSP
1		NTBP	NTBP	NTBP
2	1006A	132°	2952	4616
3	1594A	312°	2236	3898
4	1018A	132°	2952	4608
9		NTBP	NTBP	NTBP
6	1606B	312°	2952	4617
7	1030A	132°	2224	3889
8	1618A	312°	2952	3836
9	1042A	132°	1560	4351
10		NTBP	NTBP	NTBP
11	1630A	312°	5514	5297
12	1630B	312°	5121	943
13	1054A	132°	1481	4426
14	1642A	312°	5517	964
15	1066A	132°	1427	4483
16		NTBP	NTBP	NTBP
17	1654A	312°	5490	964
18		NTBP	NTBP	NTBP
19	1078A	132°	1399	2142
20		NTBP	NTBP	NTBP
21	1666A	312°	5507	977
22		NTBP	NTBP	NTBP
23	1090A	132°	1381	4607
24	1678A	312°	5497	948
25	1102A	132°	1343	2986
26	1690A	312°	5491	1457
27	1114A	NTBP	NTBP	NTBP
28		NTBP	NTBP	NTBP
29	1114B	NTBP	NTBP	NTBP
30		NTBP	NTBP	NTBP
31		NTBP	NTBP	NTBP
32		NTBP	NTBP	NTBP
33		NTBP	NTBP	NTBP
34	1582A	312°	5529	946
35		NTBP	NTBP	NTBP
36		NTBP	NTBP	NTBP
37	1114C	132°	1332	4737
38	1702C	312°	5540	4850
39	1702D	312°	4719	944
40	1126A	132°	1460	4824
41		NTBP	NTBP	NTBP
42	1714A	312°	5472	2638
43	1138A	132°	1256	4867
44		NTBP	NTBP	NTBP
45	1726A	312°	4830	950
46	1150A	132	1230	1769

47	1738A	312°	5490	948
48	1162A	132°	1193	4979
49	1750A	312°	5293	2000
50	1174A	132°	1162	5042
51	1762A	312°	5601	943
52	1186A	132°	1129	5102
53		NTBP	NTBP	NTBP
54	1198A	132°	1119	5102
55	1774A	312°	5482	947
56	1210A	132°	1033	5206
57	1786A	312°	5490	947
58	1222A	132°	1002	5299
59	1798A	312°	5490	946
60	1234A	132°	1127	5325
61	1810A	312°	5518	945
62	1246A	132°	887	5385
63	1822A	312°	5559	945
64	1258A	132°	914	5433
65	1834A	312°	5530	947
66	1270A	132°	982	5469
67	1846A	312°	5104	943
68	1282A	132°	990	5521
69	1858A	312°	5506	947
70	1294A	132°	966	5538
71	1870A	312°	5556	940
72	1450A	132°	910	5538
73	1882A	312°	5491	944
74	1150B	132°	1292	4940
75	1894A	312°	5573	943
76	1078B	132°	1388	4581
77	1906A	312°	5532	944
78	1462A	132°	919	5536
79	1918A	312°	5590	945
80	1474A	132°	930	5539
81	1930A	312°	5522	944
82	1486A	132°	949	5542
83	1942A	312°	5520	945
84	1306A	132°	955	5542
85	1954A	312°	5581	943
86	1318A	132°	920	5539
87	1966A	312°	5538	943
88	1330A	132°	970	5539
89	1978A	312°	5530	947
90	1342A	132°	936	5539
91	1990A	312°	5524	944
92	1354A	132°	917	5540
93	2002A	312°	5544	946
94	1366A	132°	1007	5540
95		NTBP	NTBP	NTBP
96	1810B	312°	4143	944
97	1378A	132°	980	5540
98	2014B	312°	5578	945
99	1390A	132°	963	5540

100	2026A	312°	5525	988
101	1402A	132°	968	5539
102	2038A	312°	5530	939
103	1414A	132°	989	5541
104	2050A	312°	5568	933
105	1426A	132°	920	5540
106	2062A	312°	5566	943
107	1438A	132°	885	5543
108	2074A	312°	5532	945
109	1498A	132°	962	5538
110	2086A	312°	5522	943
111	1510A	132°	973	5541
112	2098A	312°	5529	938
113	1522A	132°	943	5543
114	2110A	312°	5520	943
115	1306B	132°	960	2255
116	1750B	312°	2300	942
117	1234B	132°	970	2243
118	1690B	312°	2114	942
119	1282B	132°	915	4960
120	2122A	312°	5522	945
121	1378B	132°	952	5538
122	2134A	312°	5502	944
123	1534A	132°	953	5543
124	2146A	312°	5517	944
125	1546A	132°	900	5539
126	2146B	312°	5530	944
127	1570A	132°	995	5538
128	2158A	312°	5566	944
129	1558A	132°	972	3287
130		NTBP	NTBP	NTBP
131		NTBP	NTBP	NTBP
132		NTBP	NTBP	NTBP
133		NTBP	NTBP	NTBP
134		NTBP	NTBP	NTBP
135		NTBP	NTBP	NTBP
136	1558D	132°	4067	5537
137	2170A	312°	5528	945
138	1546B	132°	960	5537
139	2182A	312°	5522	1178
140	1546C	132°	1006	5539
141	2194A	312°	5558	947
142	1558E	132°	973	5539
143	2206A	312°	5543	5011
144	2206B	312°	4561	944
145	1438B	132°	949	5540
146	1726B	312°	5523	949
147	1222B	132°	988	5534
148	1846B	312°	5524	947
149	1330B	132°	978	5536
150	1714B	312°	5530	948

151	1210B	132°	1055	5402
152	2002B	312°	5562	946
153		NTBP	NTBP	NTBP
154	2194B	312°	1703	942
155	1222C	132°	1030	4469
156	1570B	132°	4917	5539
157	1882B	312°	5536	4386
158	1390B	132°	4402	5546
159	1750C	312°	5589	4206
160		NTBP	NTBP	NTBP
161	1570C	132°	3940	5542
162	1798B	312°	5571	4433
163	1498B	132°	5074	5540
164	1630C	312°	5502	5111
165	2206C	312°	5083	958
166	1450B	132°	978	2660
167	1822B	312°	2331	947
168	1114D	132°	1322	1686
169	2146C	312°	1325	946
170	1114E	132°	1311	1865
201		NTBP	NTBP	NTBP
202	4927A	315°	2049	973
203	4447A	135°	962	2047
204	4915A	315°	2042	974
205	4435A	135°	985	2049
206	4903A	315°	2064	973
207	4423A	135°	960	2048
208	4891A	315°	2057	974
209	4411A	135°	987	2047
210	4879A	315°	2039	974
211	4399A	135°	1003	2047
212	4867A	315°	2035	975
213	4387A	135°	983	2043
214	4855A	315°	2037	967
215	4375A	135°	987	2046
216	4843A	315°	2036	974
217	4363A	135°	982	2047
218	4381A	315°	2033	975
219	4351A	135°	983	2048
220	4819A	315°	2045	974
221	4339A	135°	983	2047
222	4807A	315°	2049	974
223	4327A	135°	979	2042
224	4795A	315°	2050	974
225	4315A	135°	975	2049
226	4783A	315°	2054	973

227	4303A	135°	969	2047
228	4771A	315°	2062	973
229	4303B	135°	964	2046
230	4771B	315°	2036	975
231	4291A	135°	991	2047
232	4759A	315°	2022	975
233	4279A	135°	1005	2047
234	4747A	315°	2039	975
235	4267A	135°	981	2048
236	4735A	315°	2035	976
237	4255A	135°	984	2046
238	4243A	315°	2044	975
239	4243A	135°	978	2047
240	4711A	315°	2058	974
241		NTBP	NTBP	NTBP
242	4699A	315°	2066	973
243	4231A	135°	962	2048
244	4687A	315°	2061	973
245	4219A	135°	950	2048
246	4675A	315°	2066	974
247	4219B	135°	997	2047
248	4663A	315°	2044	974
249	4207A	135°	972	2045
250	4651A	315°	2041	1564
251	4195A	135°	965	2048
252	4639A	315°	2058	964
253	4183A	135°	1110	2049
254	4627A	315°	2051	975
255	4171A	135°	970	2048
256		NTBP	NTBP	NTBP
257		NTBP	NTBP	NTBP
258		NTBP	NTBP	NTBP
259	4159B	135°	1033	2045
260	4615A	315°	2042	975
261	4147A	135°	977	2049
262	4603A	315°	2045	976
263	4135A	135°	979	2046
264	4591A	315°	2046	975
265	4123A	135°	978	2046
266	4579A	315°	2044	975
267	4111A	135°	1047	2046
268	4567A	315°	2046	972
269	4099A	135°	978	2048
270	4555A	315°	2056	973
271	4087A	135°	972	2048
272	4543A	315°	2055	973
273	4075A	135°	976	2049


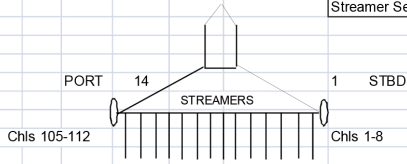
274	4531A	315°	2054	973
275	4063A	135°	977	2048
276	4519A	315°	2053	972
277	4051A	135°	975	2048
278	4507A	315°	2051	972
279	4039A	135°	976	2048
280	4495A	315°	2041	976
281	4027A	135°	977	2045
282	4483A	315°	2037	975
283	4015A	135°	976	2046
284	4471A	315°	2046	974
285	4003A	135°	978	2049
286	4459A	315°	2042	975
287	3991A	135°	976	2047
288	4627B	315°	2033	975
289	3979A	135°	978	2047
290	4591B	315°	2044	973
291	4195B	135°	971	2048
292	4555B	315°	2065	975
293	4183B	135°	983	2049
294	4891B	315°	2067	977
295	4111B	135°	957	2048
296		NTBP	NTBP	NTBP
297	4159C	135°	968	2054
298	3559B	315°	2043	975
299	4051B	135°	980	1902
300	3547A	315°	2065	975
301	4207B	135°	972	2046
302	3535A	315°	2047	975
303	4111C	135°	959	1993
304	3523A	315°	2047	976
305	3967A	135°	964	2047
306	3511A	315°	2027	974
307	3955A	135°	960	2048
308	3499A	315°	2053	974
309	3943A	135°	974	2049
310	3487A	315°	1886	973
311	3931A	135°	971	2049
312	3475A	315°	2082	973
313	3919A	135°	971	2048
314	3463A	315°	2052	974
315	3907A	135°	969	2050
316	3451A	315°	2054	973
317	3895A	135°	958	2047
318	3439A	315°	2029	975
319	3883A	135°	967	2046
320	3427A	315°	2050	975



321	3871A	135°	966	2047
322	3415A	315°	2039	976
323	3859A	135°	980	2046
324	3403A	315°	2062	976
325	3847A	135°	987	2047
326	3391A	315°	2041	975
327	3835A	135°	986	2049
328	3379A	315°	2048	974
329	3823A	135°	970	2050
330	3367A	315°	2032	974
331	3811A	135°	968	2047
332	3355A	315°	2058	973
333	3799A	135°	977	2048
334	2058A	315°	2058	975
335	3787A	135°	962	2050
336	3331A	315°	2055	973
337	3775A	135°	964	2047
338	3319A	315°	2057	975
339	3763A	135°	971	2047
340	3307A	315°	2049	975
341	3751A	135°	959	2047
342	3295A	315°	2053	975
343	3739A	135°	983	2047
344	3283A	315°	2036	975
345	3727A	135°	957	2047
346	3271A	315°	2063	975
347	3715A	135°	961	2047
348	3259A	315°	2055	973
349	3703A	135°	969	2049
350	3247A	315°	2054	973
351	3691A	135°	969	2049
352	3235A	315°	2050	970
353	3679A	135°	975	2049
354	3223A	315°	2052	973
355		NTBP	NTBP	NTBP
356	3667A	135°	971	2048
357	3211A	315°	2051	973
358	3655A	135°	967	2049
359	3199A	315°	2047	976
360	3643A	135°	961	2047
361	3187A	315°	2055	975
362	3631A	135°	971	2047
363	3175A	315°	2060	975
364	3619A	135°	977	2047
365	3163A	315°	2064	976
366	3607A	135°	976	2047
367	3151A	315°	2059	975

368	3595A	135°	970	2047
369	3487B	315°	2064	973
370	3583A	135°	971	2054
371	3499B	315°	2053	975
372	3571A	135°	976	2023
373	3379B	315°	2058	974
374	3643B	135°	963	2049
375	3139A	315°	2052	973
376	3823B	135°	966	2047
377	3127A	315°	2061	973
378	3895B	135°	970	2047
379	3115A	315°	2060	976
380	3751B	135°	971	2047
381	3103A	315°	2072	975
382	3943B	135°	966	1961
383	3091A	315°	2058	975
384	3031A	135°	977	2047
385	3079A	315°	2068	976
386	3019A	135°	970	2047
387	3067A	315°	2065	975
388	3007A	135°	969	2049
389	3055A	315°	2055	973
390	3571B	135°	979	2048
391	3043A	315°	2058	973
392	3775B	135°	969	2049
393	3235B	315°	2063	970
394	4351B	135°	973	2049
395	4591C	315°	2052	974
396	4075B	135°	962	2051
397	4519B	315°	2059	974
398	3631B	135°	953	2047
399	4927B	315°	2071	975
400	4135B	135°	988	2048

# B.12 Example Observers Log

FIELD LOG / OBSERVERS REPORT										Page 1 of 1
		Date: 01 November 2013	Line Number: 3271A		Water Depth(m): 500-800m					
		Client: Scripps	Line Azimuth: 315		Mean Velocity: NA					
		Area: San Onofre	Sequence No: 346		Vessel Speed: 4.0-4.5 Kts					
		Vessel: R/V New Horizon	Observers: James, Jayne		Sea State: <1m, Wind: NW 4.1 Kts					
<b>Recording System:</b>			<b>Source:</b>			<b>Streamers:</b>				
Model: Geometrics CNT-2		Low Cut Filter: NA		Type: Sparker		Type: GeoEel Solid				
Recording Format: SEG-Y		Slope: NA		Array Size: 3 Tips		Sensitivity: 20 µV/µBar				
Recording Media: Hard Disk		High Cut Filter: NA		Power(barM): NA		Streamers: 14				
Record Length: 2000 msec		Slope: NA		Tow Depth: 2.0 m		Chis/Streamer: 8				
Sample Rate: 2 kHz		Aux Ch 1: NA		Array Power: 2000 J		Total Chis: 112				
Preamp Gain: 18 dB		Aux Ch 2: NA		Shot Interval: 6.25 m		Group Interval: 6.25 m				
FTB Static: 0 ms		FTB Source: SPSU		Pressure: NA		Tow Depth: 2 m nominal				
						Streamer Separation: 6.25 m nom.				
<b>Physical Offsets:</b>										
Reference Point:		Stem								
CRP to Stem:		0 m								
Stem to Stbd Paravane:		104.5 m								
Stem to Port Paravane:		104.5 m								
Spread:		115 m								
Stem to Source:		71 m								
										
Recording File Name	Time UTC	Shot Point Number	FFID Number	Depth Stbd (m)	Depth Center (m)	Depth Port (m)	Water Depth (m)	Azimuth	Streamer Leakage	Remarks (SOL, EOL, sea state, problems, etc)
3271.sgy	1635	2063	3283	1.4	1.6	1.5	296	315	023	<b>SOL: 3271A SEQ: 346 UTC:1635</b>
3271.sgy	1703	1500	3846	1.2	1.6	1.5	311		023	Batteries: Port: 12.54V, Stbd: N/A Current: 3.00A
4137.sgy	1717	1209	4137	1.3	1.7	1.5	398		023	<b>File Change</b>
4137.sgy	1727	1000	4346	1.3	1.7	1.5	355		023	Batteries: Port: 12.59V, Stbd: N/A Current: 2.99A
4137.sgy	1728	0975	4371	1.3	1.7	1.6	362		023	<b>EOL: 3271A SEQ: 346 UTC:1728</b>

# B.13 Example Navigation Line Log

R/V New Horizon		DATE		11-Oct-13	
NAVIGATION LINE LOG		JULIAN DAY		284	
CLIENT: SRIPPS / Subsea Systems Inc.		SURVEY: SONGS 3-D HR Geophysical Survey, 2013		JOB # : 446	
<b>SURVEY AREA:</b> Southern Cal.		<b>DEPTH SOL:</b> 59.1 m <b>DEPTH EOL:</b> 49.1 m		<b>NAVIGATION SYSTEM USED:</b> NCS SubSea - NavPoint Version 1.1.0.0	
<b>SMG SOL:</b> 4 knots <b>SMG EOL:</b> 4.5 knots		<b>LINE NAME :</b> 1006A		<b>WEATHER</b> <b>WIND SOL :</b> <b>WIND EOL :</b>	
<b>FEATHER SOL :</b> <b>FEATHER EOL :</b>		<b>LINE BRG :</b> 132 °		<b>MAG DEC USED :</b> 12.13 °	
<b>SEQUENCE :</b> 2		<b>SEAS SOL :</b> <b>SEAS EOL :</b>		<b>SURVEY TYPE :</b> 3D P-Cable Geophysical Survey	
<b>PARTY CHIEF:</b> Mike Barth / Chuck Chamberlain <b>CHIEF NAVIGATOR:</b> Jesus Gaytan <b>NCS P.M.:</b> Jesus Gaytan		<b>NAVIGATOR:</b> Shane Traceski Dwayne Fontenot		<b>NAVIGATION PROCESSOR:</b> Abby Parish Micah Hall	
SP	T: (UTC)	EVENTS (NRP Pos.)	COMMENTS		
1902	00:23	FSP E: 444860.17 N: 3687425.90	Seq001 Test sequence, seq002 start of Job  Intermittent missed SP throughout line  No source GPS throughout line		
4121	01:14	LGSP E: 450124.87 N: 3682909.6		<b>NAVIGATION OFFSETS APPLIED (meters)</b> Shot Point Reference: NRP W1 Draft Correction: -3.60 NRP-COS: -70.0 CNG-CFG: -37.5 Groups per Streamer: 9 Group Interval: 6.25 Total Groups: 112 Shot Interval: 3.1 Vane wire length: 104.5 Paravane Separation: 115.0	
4121	01:14	LSP	EOL	<b>RAW FILE:</b> P294: 0002-1006A20131012002236.P294 P190: 0002-1006A20131012002236.P190	
NAVIGATION SYS-1 CNAV 200R		Ref. stations: CNAV RTG 098 W	NAVIGATION SYS-2 Trimble SPS 361	Ref. stations: SSAS Sta:138	NUMBER OF STREAMERS 14
COMPASSES KO'd Depths KO'd		S3,S6,S8,S9,S12 - no tail module S3,S6,S8,S9,S12 - no tail module		GENERAL COMMENTS:	Line Status: <b>Complete</b>

**Strms. @ 2.0 m**

## B.14 Example GeoEel Log

```
SONGS.1222c.log - Notepad
File Edit Format View Help
Beginning New Line - Line 1222c. Starting File Number is 1222
$ 1222c,00001004,20131024,002625.777 - Received at 00:26:19.56 for File 1222
File 1222 00:26:19.60 10/24/2013 1465 kbytes SAVED IN 1222.SG
$ 1222c,00001005,20131024,002627.193 - Received at 00:26:20.89 for File 1223
File 1223 00:26:20.91 10/24/2013 1461 kbytes SAVED IN 1222.SG
$ 1222c,00001006,20131024,002628.414 - Received at 00:26:22.20 for File 1224
File 1224 00:26:22.22 10/24/2013 1461 kbytes SAVED IN 1222.SG
$ 1222c,00001007,20131024,002629.724 - Received at 00:26:23.50 for File 1225
File 1225 00:26:23.53 10/24/2013 1461 kbytes SAVED IN 1222.SG
$ 1222c,00001008,20131024,002631.050 - Received at 00:26:24.82 for File 1226
File 1226 00:26:24.86 10/24/2013 1461 kbytes SAVED IN 1222.SG
$ 1222c,00001009,20131024,002632.298 - Received at 00:26:26.07 for File 1227
File 1227 00:26:26.11 10/24/2013 1461 kbytes SAVED IN 1222.SG
$ 1222c,00001010,20131024,002633.609 - Received at 00:26:27.39 for File 1228
File 1228 00:26:27.42 10/24/2013 1461 kbytes SAVED IN 1222.SG
$ 1222c,00001011,20131024,002634.903 - Received at 00:26:28.68 for File 1229
File 1229 00:26:28.72 10/24/2013 1461 kbytes SAVED IN 1222.SG
$ 1222c,00001012,20131024,002636.183 - Received at 00:26:29.96 for File 1230
File 1230 00:26:29.99 10/24/2013 1461 kbytes SAVED IN 1222.SG
$ 1222c,00001013,20131024,002637.478 - Received at 00:26:31.26 for File 1231
File 1231 00:26:31.28 10/24/2013 1461 kbytes SAVED IN 1222.SG
$ 1222c,00001014,20131024,002638.804 - Received at 00:26:32.59 for File 1232
File 1232 00:26:32.61 10/24/2013 1461 kbytes SAVED IN 1222.SG
$ 1222c,00001015,20131024,002640.145 - Received at 00:26:33.92 for File 1233
File 1233 00:26:33.95 10/24/2013 1461 kbytes SAVED IN 1222.SG
$ 1222c,00001016,20131024,002641.440 - Received at 00:26:35.21 for File 1234
File 1234 00:26:35.25 10/24/2013 1461 kbytes SAVED IN 1222.SG
$ 1222c,00001017,20131024,002642.766 - Received at 00:26:36.54 for File 1235
File 1235 00:26:36.58 10/24/2013 1461 kbytes SAVED IN 1222.SG
$ 1222c,00001018,20131024,002644.076 - Received at 00:26:37.85 for File 1236
File 1236 00:26:37.89 10/24/2013 1461 kbytes SAVED IN 1222.SG
$ 1222c,00001019,20131024,002645.356 - Received at 00:26:39.14 for File 1237
File 1237 00:26:39.17 10/24/2013 1461 kbytes SAVED IN 1222.SG
$ 1222c,00001020,20131024,002646.697 - Received at 00:26:40.48 for File 1238
File 1238 00:26:40.52 10/24/2013 1461 kbytes SAVED IN 1222.SG
$ 1222c,00001021,20131024,002648.008 - Received at 00:26:41.79 for File 1239
File 1239 00:26:41.81 10/24/2013 1461 kbytes SAVED IN 1222.SG
$ 1222c,00001022,20131024,002649.303 - Received at 00:26:43.07 for File 1240
File 1240 00:26:43.11 10/24/2013 1461 kbytes SAVED IN 1222.SG
$ 1222c,00001023,20131024,002650.660 - Received at 00:26:44.43 for File 1241
File 1241 00:26:44.47 10/24/2013 1461 kbytes SAVED IN 1222.SG
$ 1222c,00001024,20131024,002652.001 - Received at 00:26:45.78 for File 1242
File 1242 00:26:45.81 10/24/2013 1461 kbytes SAVED IN 1222.SG
$ 1222c,00001025,20131024,002653.296 - Received at 00:26:47.07 for File 1243
File 1243 00:26:47.11 10/24/2013 1461 kbytes SAVED IN 1222.SG
$ 1222c,00001026,20131024,002654.622 - Received at 00:26:48.40 for File 1244
File 1244 00:26:48.42 10/24/2013 1461 kbytes SAVED IN 1222.SG
$ 1222c,00001027,20131024,002655.948 - Received at 00:26:49.73 for File 1245
File 1245 00:26:49.77 10/24/2013 1461 kbytes SAVED IN 1222.SG
$ 1222c,00001028,20131024,002657.259 - Received at 00:26:51.04 for File 1246
File 1246 00:26:51.06 10/24/2013 1461 kbytes SAVED IN 1222.SG
$ 1222c,00001029,20131024,002658.585 - Received at 00:26:52.35 for File 1247
File 1247 00:26:52.39 10/24/2013 1461 kbytes SAVED IN 1222.SG
$ 1222c,00001030,20131024,002659.942 - Received at 00:26:53.71 for File 1248
File 1248 00:26:53.75 10/24/2013 1461 kbytes SAVED IN 1222.SG
$ 1222c,00001031,20131024,002701.299 - Received at 00:26:55.07 for File 1249
File 1249 00:26:55.11 10/24/2013 1461 kbytes SAVED IN 1222.SG
$ 1222c,00001032,20131024,002702.657 - Received at 00:26:56.43 for File 1250
File 1250 00:26:56.47 10/24/2013 1461 kbytes SAVED IN 1222.SG
$ 1222c,00001033,20131024,002704.045 - Received at 00:26:57.82 for File 1251
File 1251 00:26:57.86 10/24/2013 1461 kbytes SAVED IN 1222.SG
$ 1222c,00001034,20131024,002705.387 - Received at 00:26:59.17 for File 1252
File 1252 00:26:59.20 10/24/2013 1461 kbytes SAVED IN 1222.SG
$ 1222c,00001035,20131024,002706.744 - Received at 00:27:00.53 for File 1253
File 1253 00:27:00.55 10/24/2013 1461 kbytes SAVED IN 1222.SG
$ 1222c,00001036,20131024,002708.054 - Received at 00:27:01.84 for File 1254
File 1254 00:27:01.86 10/24/2013 1461 kbytes SAVED IN 1222.SG
$ 1222c,00001037,20131024,002709.349 - Received at 00:27:03.12 for File 1255
File 1255 00:27:03.17 10/24/2013 1461 kbytes SAVED IN 1222.SG
$ 1222c,00001038,20131024,002710.691 - Received at 00:27:04.46 for File 1256
File 1256 00:27:04.50 10/24/2013 1461 kbytes SAVED IN 1222.SG
$ 1222c,00001039,20131024,002712.001 - Received at 00:27:05.78 for File 1257
File 1257 00:27:05.81 10/24/2013 1461 kbytes SAVED IN 1222.SG
$ 1222c,00001040,20131024,002713.327 - Received at 00:27:07.10 for File 1258
File 1258 00:27:07.14 10/24/2013 1461 kbytes SAVED IN 1222.SG
```

## B.15 Example P190 Navigation Header

```

0090_1342.p190.txt - Notepad
File Edit Format View Help
H0100SURVEY AREA Nearshore San Diego, CA
H0101SURVEY DETAILS SONGS Pcable 2013
H0102VESSEL DETAILS R/V New Horizon
H0103SOURCE DETAILS Source 301
H0104STREAMER DETAILS Streamer 201 8 ch 1 1
H0104STREAMER DETAILS Streamer 202 8 ch 1 2
H0104STREAMER DETAILS Streamer 203 8 ch 1 3
H0104STREAMER DETAILS Streamer 204 8 ch 1 4
H0104STREAMER DETAILS Streamer 205 8 ch 1 5
H0104STREAMER DETAILS Streamer 206 8 ch 1 6
H0104STREAMER DETAILS Streamer 207 8 ch 1 7
H0104STREAMER DETAILS Streamer 208 8 ch 1 8
H0104STREAMER DETAILS Streamer 209 8 ch 1 9
H0104STREAMER DETAILS Streamer 210 8 ch 1 A
H0104STREAMER DETAILS Streamer 211 8 ch 1 B
H0104STREAMER DETAILS Streamer 212 8 ch 1 C
H0104STREAMER DETAILS Streamer 213 8 ch 1 D
H0104STREAMER DETAILS Streamer 214 8 ch 1 E
H0105OTHER DETAILS Stbd Tow Buoy 1 1
H0105OTHER DETAILS Port Tow Buoy 1 2
H0105OTHER DETAILS Stbd Vane 1 3
H0105OTHER DETAILS Port Vane 1 4
H0200SURVEY DATE 10/10/2013
H0201TAPE DATE 2013
H0202TAPE VERSION UK00A p1/90
H0203LINE PREFIX N/A
H0300CLIENT San Diego Edison
H0400GEOPHYSICAL CONTRACTOR Scripps Institute of oceanography
H0500POSITIONING CONTRACTOR NCS Subsea, Inc
H0600POSITIONING PROCESSING NCS Subsea, Inc
H0700POSITIONING SYSTEM NavPoint Integrated Navigation System
H0800COORDINATE POSITION Centre of Source
H0900OFFSET SYSTEM TO SOURCE 1 1 2 0.00 -50.00
H0901OFFSET SYSTEM TO S1R1 1 2 45.5 -97.40
H0901OFFSET SYSTEM TO S2R1 1 2 38.5 -100.7
H0902OFFSET SYSTEM TO S3R1 1 2 31.5 -103.6
H0903OFFSET SYSTEM TO S4R1 1 2 24.5 -106.0
H0904OFFSET SYSTEM TO S5R1 1 2 17.5 -107.9
H0905OFFSET SYSTEM TO S6R1 1 2 10.5 -109.2
H0906OFFSET SYSTEM TO S7R1 1 2 3.5 -109.9
H0907OFFSET SYSTEM TO S8R1 1 2 -3.5 -109.9
H0908OFFSET SYSTEM TO S9R1 1 2 -10.5 -109.2
H0909OFFSET SYSTEM TO S10R1 1 2 -17.5 -107.9
H0910OFFSET SYSTEM TO S11R1 1 2 -24.5 -106.0
H0911OFFSET SYSTEM TO S12R1 1 2 -31.5 -103.6
H0911OFFSET SYSTEM TO S13R1 1 2 -38.5 -100.7
H0911OFFSET SYSTEM TO S14R1 1 2 -45.5 -97.40
H0912OFFSET SYSTEM TO E/S 1 1 2 0.00 29.0
H0913OFFSET SYSTEM TO ANTENNA 1 2 0.0 0.0
H1000CLOCK TIME GMT -0.0 Hours
H1100RECEIVER GROUPS PER SHOT 112
H1400GEODETIC DATUM AS SURVEYED WGS84 WGS84 6378137.000 298.2572236
H1401DATUM SHIFT SURVEY TO WGS84 -0.0 -0.0-0.000-0.000-0.0000000
H1500GEODETIC DATUM AS PLOTTED WGS84 WGS84 6378137.000 298.2572236
H1501DATUM SHIFT PLOT TO WGS84 -0.0 -0.0 -0.0-0.000-0.000-0.0000000
H1510TOWNSHIP SYSTEM N/A
H1600DATUM SHIFT SURVEY TO PLOT 0.0 0.0 0.0 0.000 0.000 0.0000000
H1700VERTICAL DATUM Sea surface
H2600 Echosounder 1 transducer depth (z) 3.6
H1800PROJECTION TYPE 001 UTM North
H1810TOWNSHIP RELATIVE COORDS N/A
H1900PROJECTION ZONE 11N
H1910TOWNSHIP PRINCIPLE MERIDIANN/A
H2000GRID UNITS 1Metres 1.000000000000
H2001HEIGHT UNITS 1Metres 1.000000000000
H2002ANGULAR UNITS 1degrees
H2200LONGITUDE OF CM 129 0 0.000w
H2301GRID ORIGIN (LAT, LON) 0 0 0.000N129 0 0.000w
H2302GRID ORIGIN (E, N) 500000.00E 0.00N
H2401SCALE FACTOR 0.9996000000
H2402SCALE ORIGIN (LAT, LON) 0 0 0.000N129 0 0.000w
V1342A 1 000907332014.11N1173725.36W 441957.73688849.4 78.5291153430
E1342A 1 000907332013.47N1173724.53W 441979.03688829.7 78.5291153430
S1342A 11 000907332015.56N1173727.49W 441903.03688894.3 78.5291153430
T1342A 1 1000907332015.07N1173729.33W 441855.33688879.5 78.5291153430

```

## B.16 Final EBCDIC Headers

### Boomer Final Full PSTM Stack

```
C01 Client: Scripps/UNR
C02 Area: San Onofre, offshore Southern California, USA
C03 SONGS 3D Boomer Survey: Full Offset Stack Data with Filter
C04
C05 --- Acquisition Parameters -----
C06 Company, data          Scripps, October 2013
C07 Vessel                 R/V New Horizon
C08 Source                 Boomer, 3 plates, 0.5m depth
C09 Sp interval           3.125 m
C10 Record length         800 ms @ 0.25ms
C11 Format                  SEGY
C12 Cables                 14*50m, cable separation 6.25m, 2m depth
C13 Groups, grp int       8 (112 chns), 6.25m
C14
C15 --- Processing Parameters: Geotrace 5800411 November 2013 - April 2014 --
-
C16 1. Seg-y reformat
C17 2. Low cut filter 45Hz
C18 3. Resample to 1 ms (500 Hz Nyquist) with TAA filter
C19 4. Bad trace edits      5. De-noise, 2D SRME
C20 6. Sort into 3D bins    7. Apply 1480 m/s NMO
C21 8. 2D Stack (8 fold)   9. Deconvolution, Interpolation of empty bins
C22 10. Post Stack pre-migration noise attenuation (despike+fdna+fx)
C23 11. Post stack Kirchhoff migration
C24 12. Post migration dip filtering
C25 13. Amplitude balancing (Gain)
C26 14. SEGY
C27
C28
C29 --- Byte Positions -----
C30
C31 Cdp-y: 181-184 (local) Cdp-y: 185-188 (local)
C32 Easting: 189-192      Northing: 193-196      Inline: 205-208
C33 Crossline: 209-212    Cdp: 213-216      Cdplbl: 217-220
C34 Waterdepth: 221-224
C35
C36
C37 Survey spheroid: WGS84 Proj.: UTM Zone 11N
C38 3d survey origin: x: 438370.4 meters y: 3686647.4 meters
C39 angle: -42 degrees
C40 END EBCDIC
```

## Sparker Final Full PSTM Stack

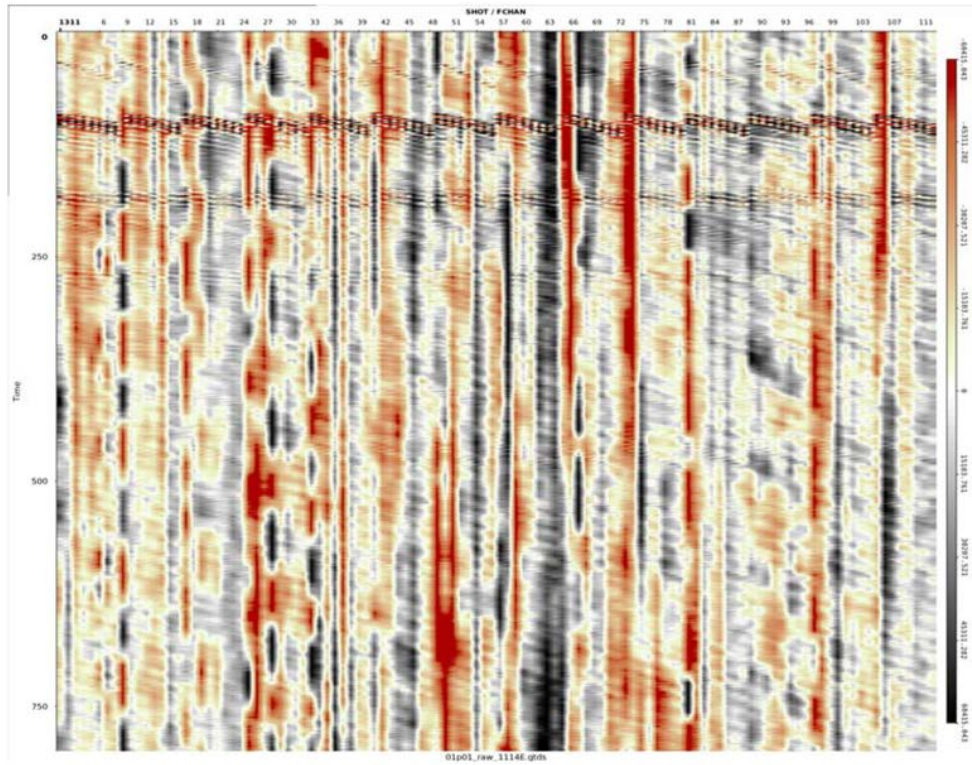
```
C01 Client: Scripps/UNR
C02 Area: San Onofre, offshore Southern California, USA
C03 SONGS 3D Sparker Survey: Full Offset Stack Data
C04
C05 --- Acquisition Parameters -----
C06 Company, data      Scripps, October 2013
C07 Vessel             R/V New Horizon
C08 Source             Sparker, 3 tips, 2m depth
C09 Sp interval       6.25 m
C10 Record length     2000 ms @ 0.5ms
C11 Format             SEGY
C12 Cables             14*50m, cable separation 6.25m, depth 2m
C13 Groups, grp int   8(112 chn), 6.25m
C14
C15 --- Processing Parameters: Geotrace 5800411 November 2013 - April 2014 --
-
C16 1. Seg-y reformat
C17 2. Low cut filter 45Hz
C18 3. Resample to 1 ms (500 Hz Nyquist) with TAA filter
C19 4. Bad trace edits      5. De-noise, 2D SRME
C20 6. Sort into 3D bins    7. Apply 1480 m/s NMO
C21 8. 2-D Stack, 1-D SRME 9. Interpolation of Empty Bins
C22 10. Post Stack pre-migration noise attenuation (despike+fdna+fxxy)
C23 11. Post stack Kirchoff migration
C24 12. TVF, Amplitude balancing (Gain)
C25 13. SEGY
C26
C27
C28
C29 --- Byte Positions -----
C30
C31 Cdp-x: 181-184 (local) Cdp-y: 185-188 (local)
C32 Easting: 189-192      Northing: 193-196      Inline: 205-208
C33 Crossline: 209-212   Cdp: 213-216      Cdplbl: 217-220
C34 Waterdepth: 221-224
C35
C36
C37 Survey spheroid: WGS84 Proj.: UTM Zone 11N
C38 3d survey origin: x: 435186.3 meters y: 3681633.1 meters
C39 angle: -45.52 degrees
C40 END EBCDIC
```



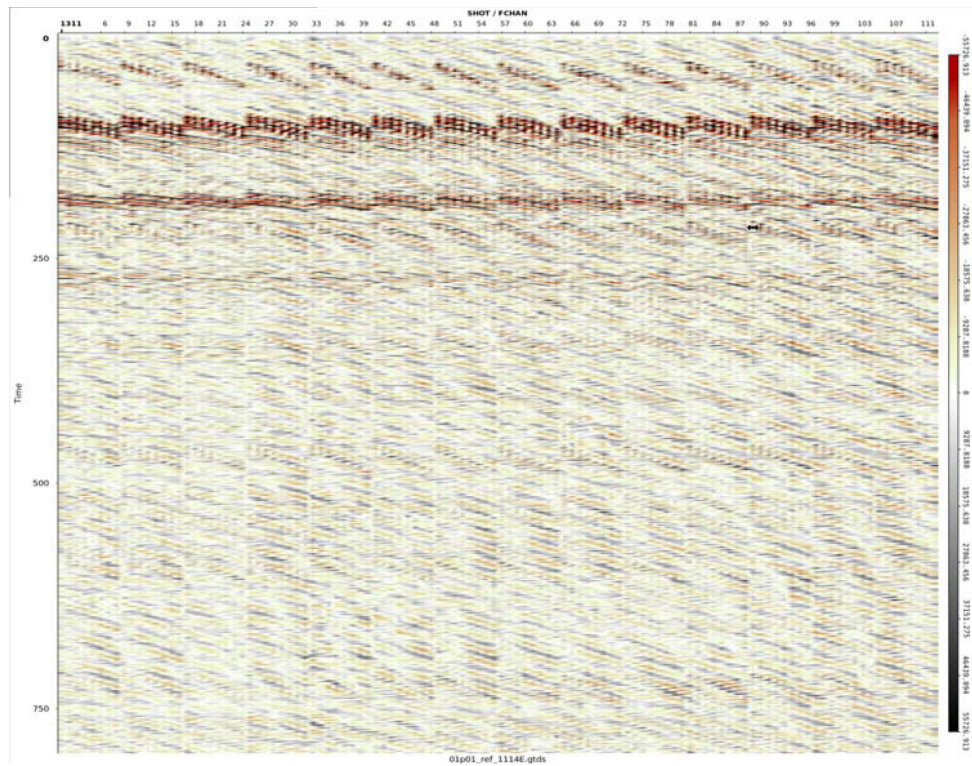
## **B.17 Seismic QC displays**

Example seismic QC displays included

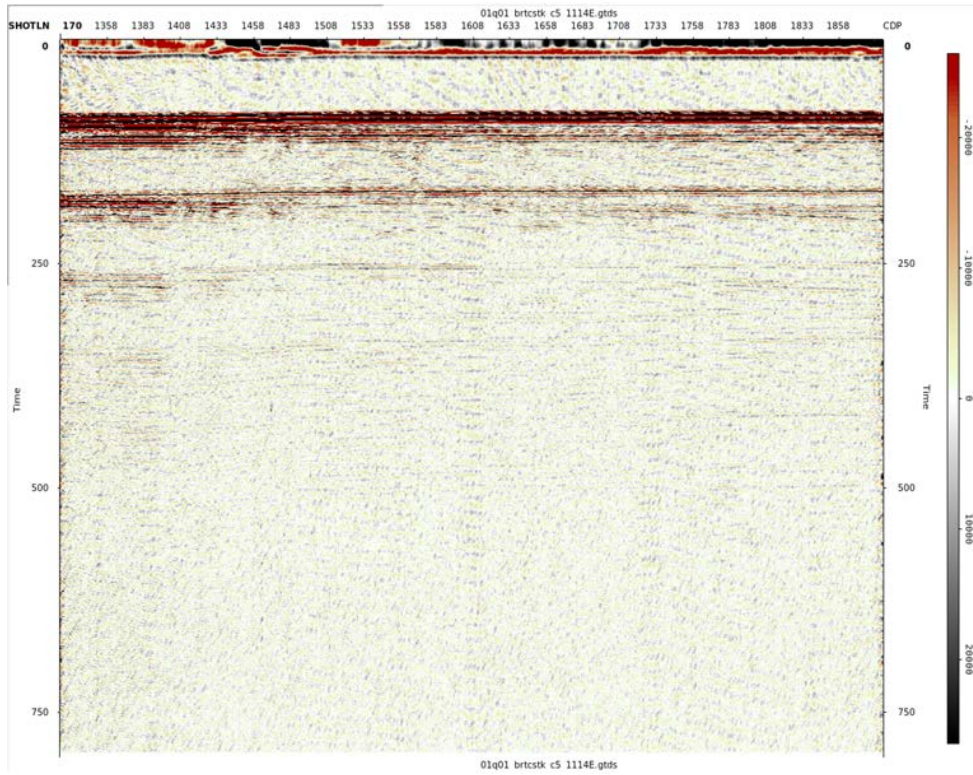
- Fig B.15 Raw Shots Display
- Fig B.16 Reformatted Shots Display
- Fig B.17 Brute Stack
- Fig B.18 Brute Stack Enlarged
- Fig B.19 Near Trace
- Fig B.20 Near Trace All
- Fig B.21 Whole Amplitude Map
- Fig B.22 Whole Frequency Map
- Fig B.23 Data Amplitude Map
- Fig B.24 Data Frequency Map
- Fig B.25 Ambient Amplitude Map
- Fig B.26 Deep Amplitude Map
- Fig B.27 Sparker Brute Stack
- Fig B.28 Sparker Brute Stack Enlarged



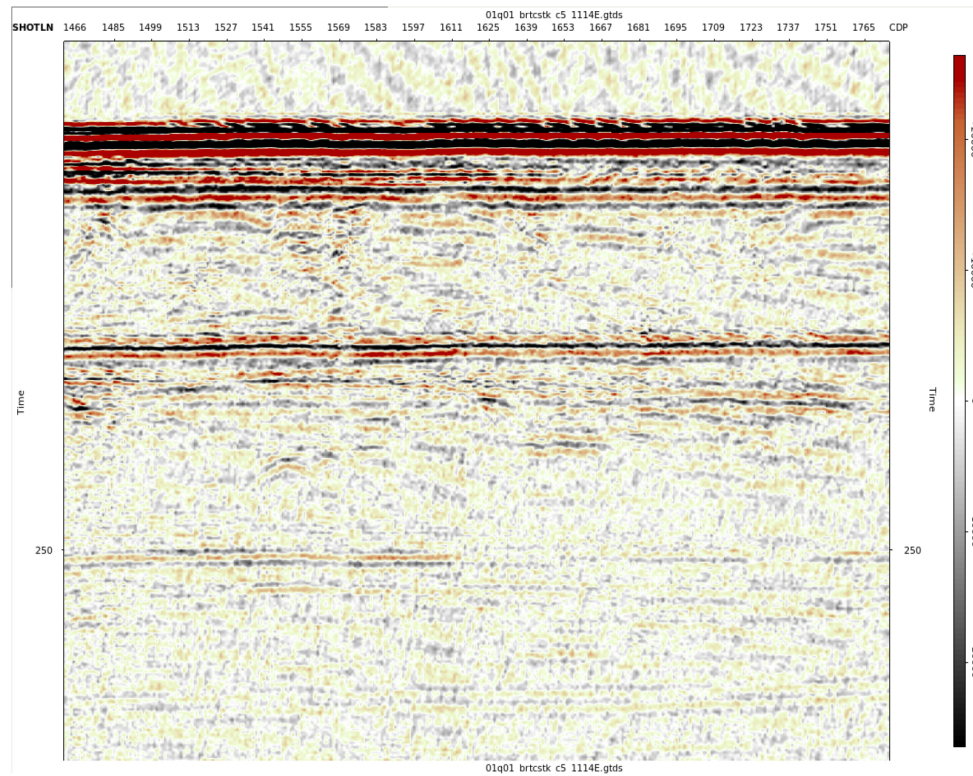
**Figure B.15:** Raw Shots Display (Line 1114E Cables 1-14)



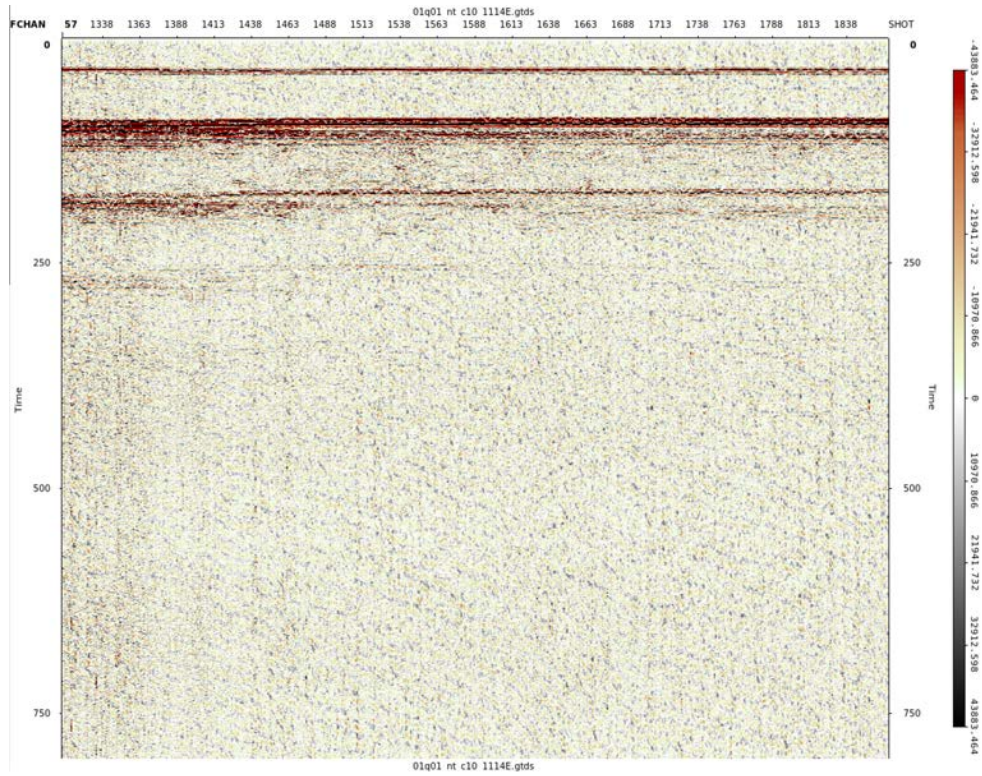
**Figure B.16:** Reformatted Shots Display (Line 1114E Cables 1-14)



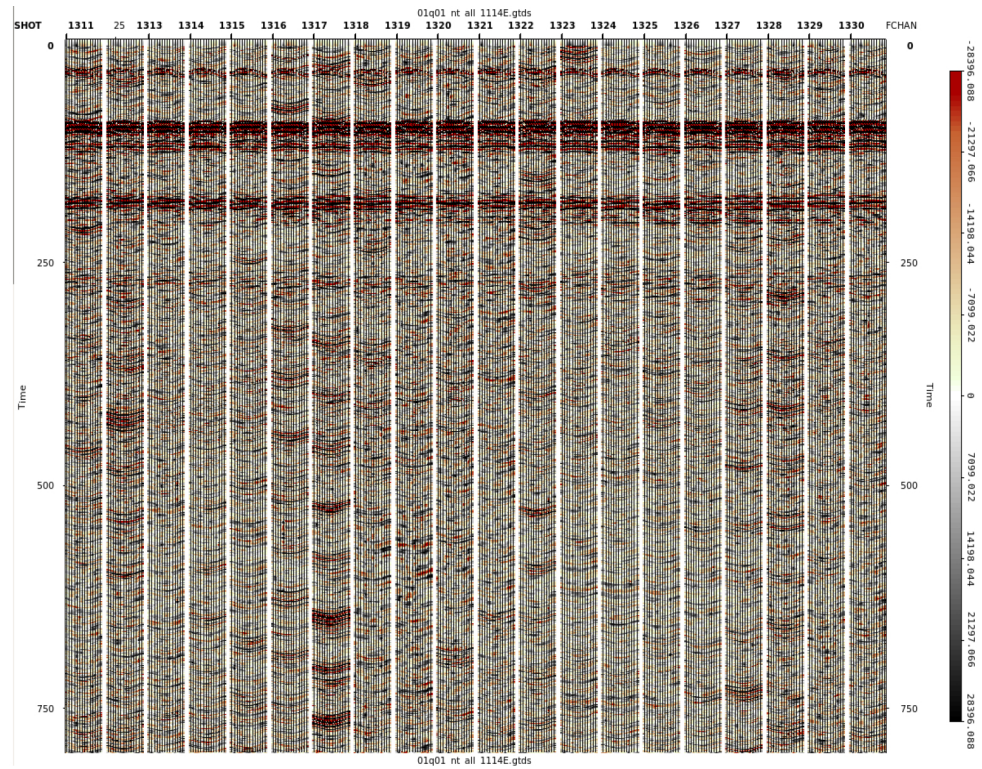
**Figure B.17:** Brute Stack (Line 1114E Cable 5)



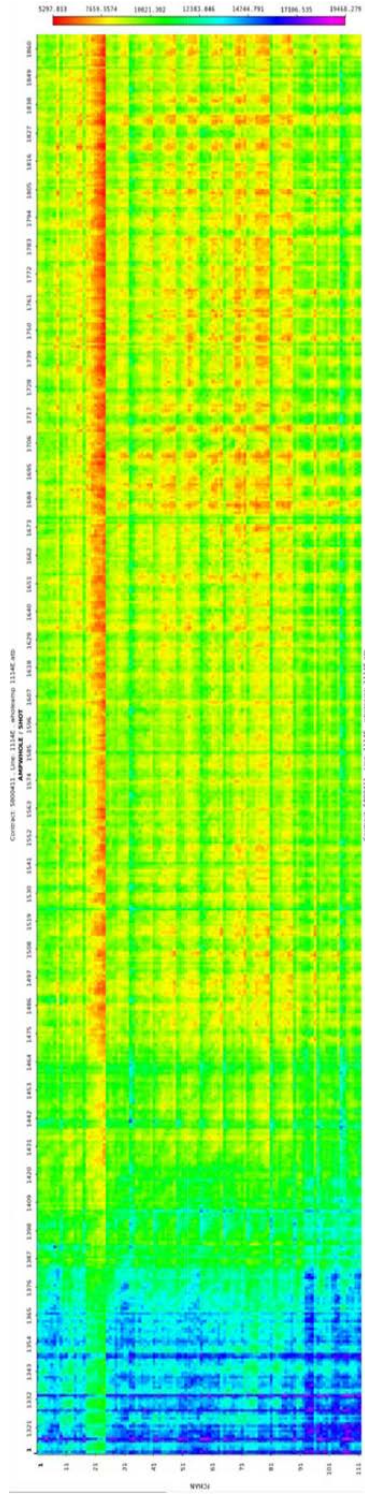
**Figure B.18:** Brute Stack Enlarged (Line 1114E Cable 5)



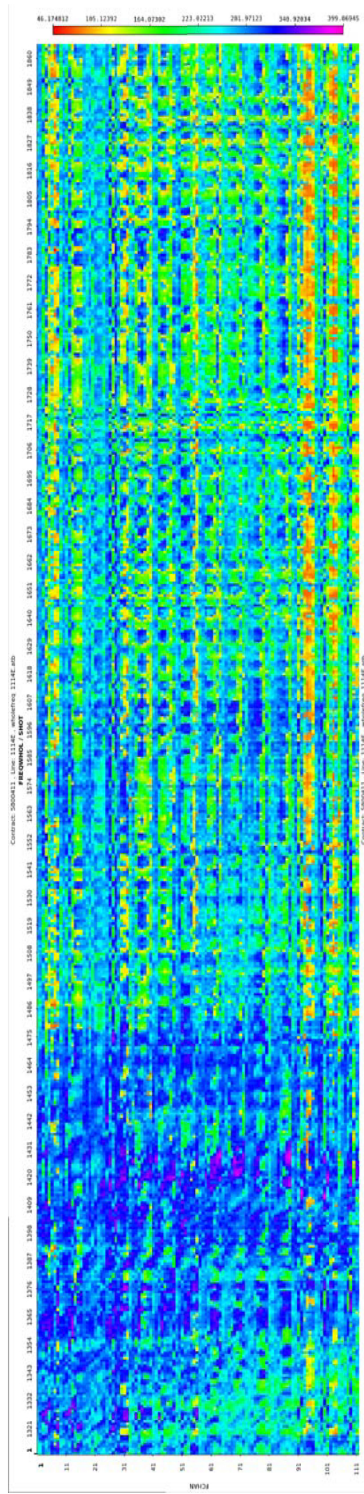
**Figure B.19:** Near Trace (Line 1114E Cable 10)



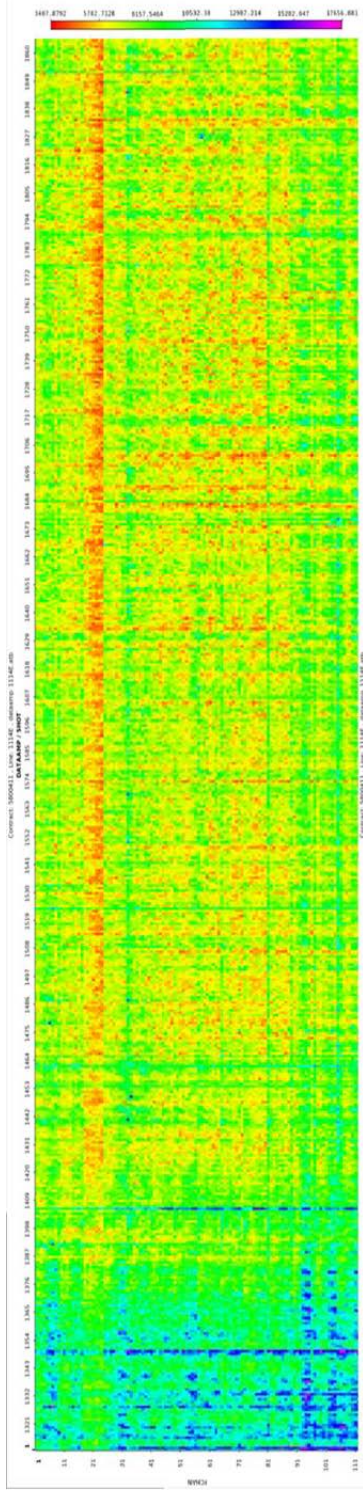
**Figure B.20:** Near Trace All Cables (Line 1114E Shots 1311-1330)



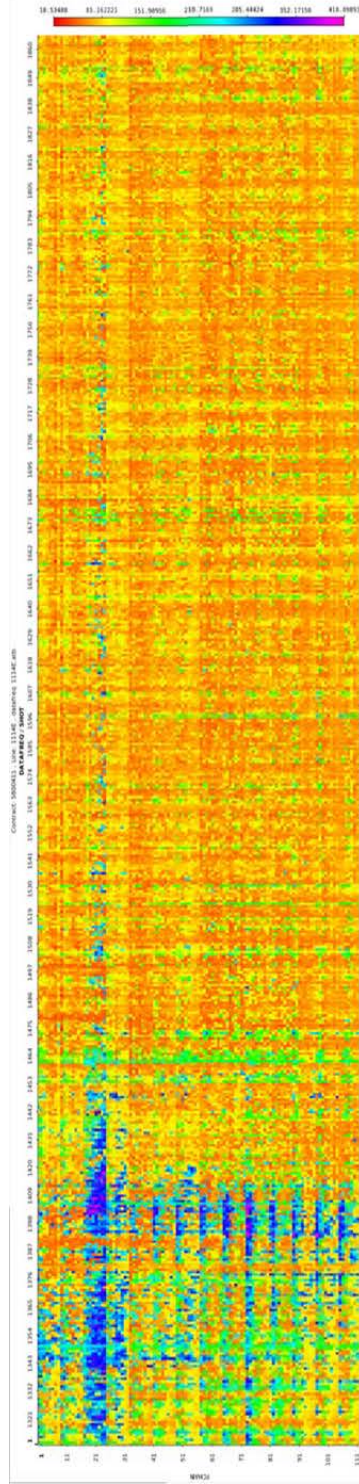
**Figure B.21: Whole Window Amplitude Map (Line 1114E)**



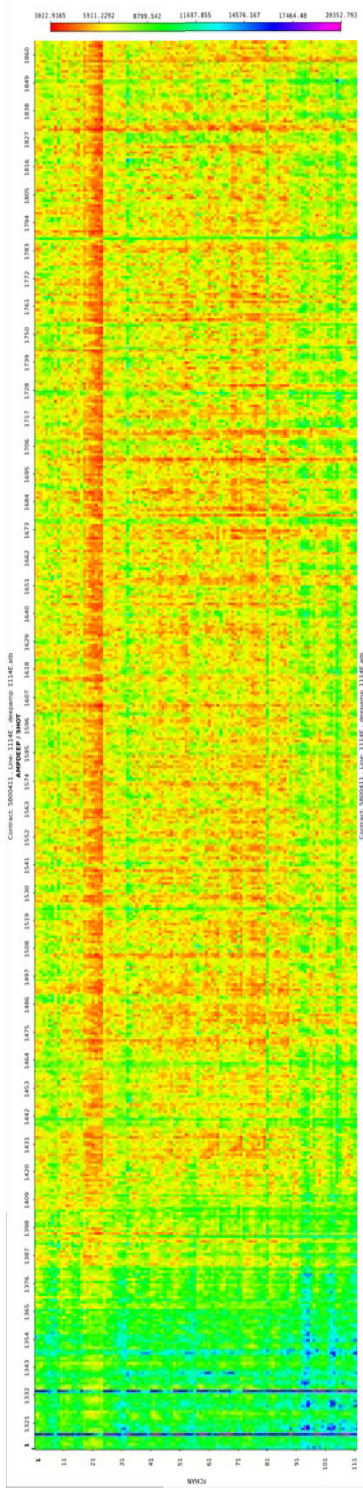
**Figure B.22: Whole Window Frequency Map (Line 1114E)**



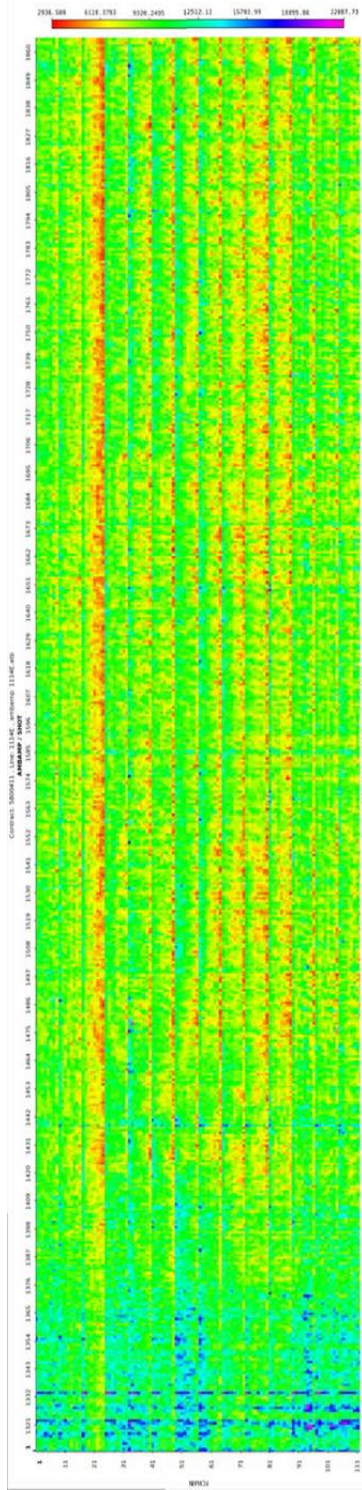
**Figure B.23: Data Window Amplitude Map (Line 1114E)**



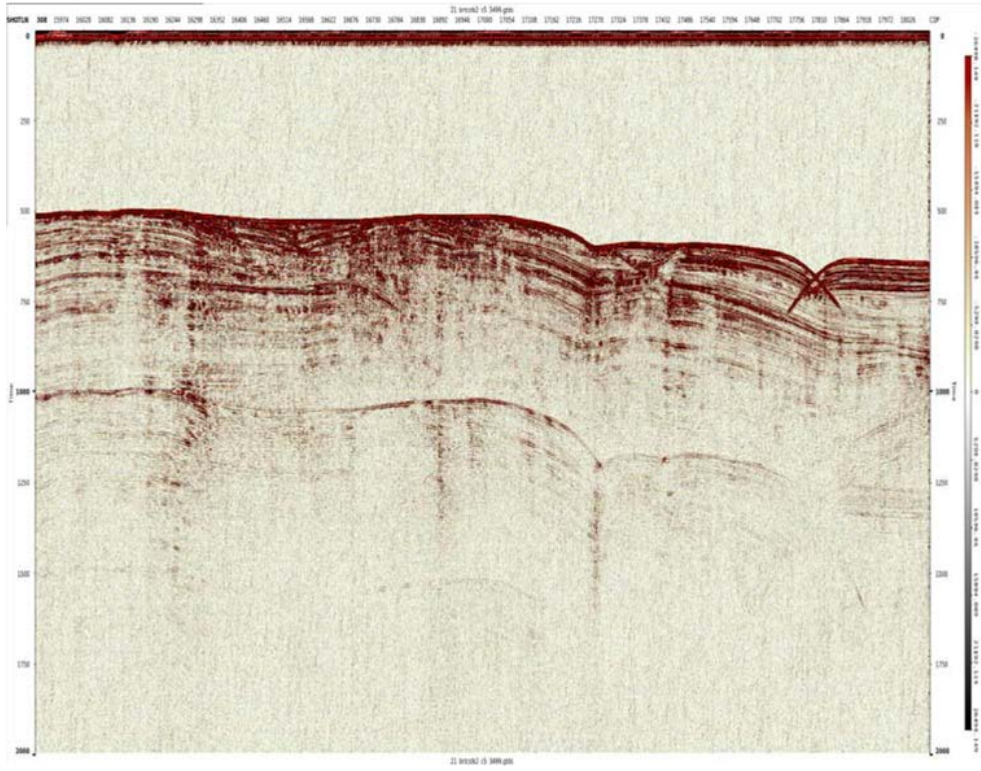
**Figure B.24: Data Window Frequency Map (Line 1114E)**



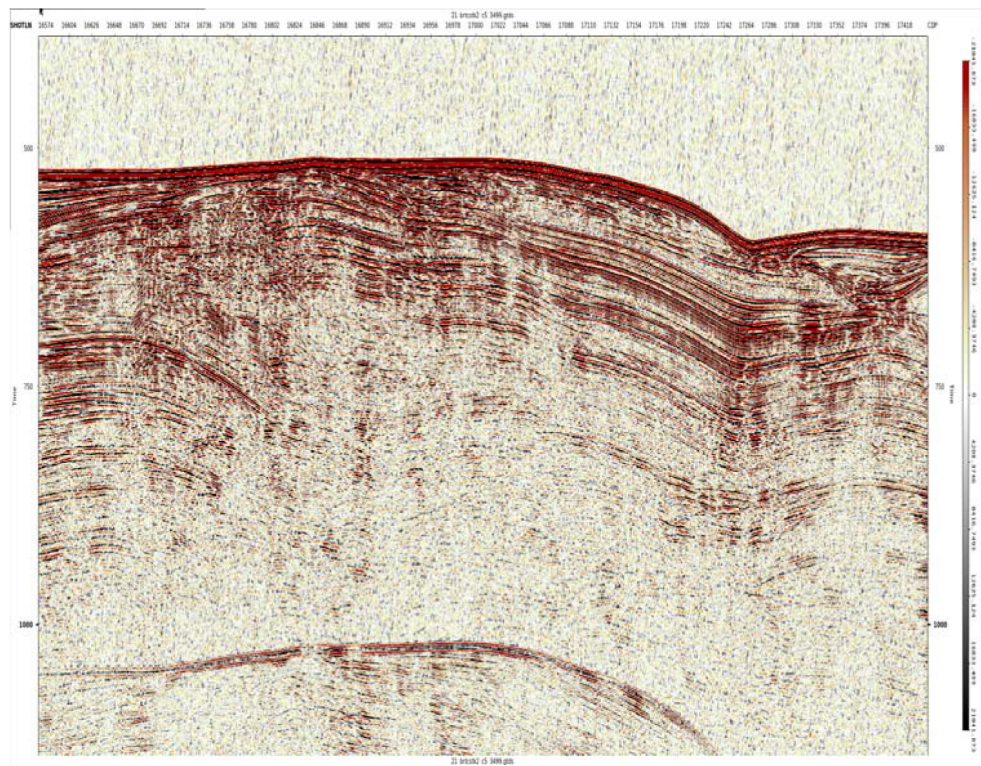
**Figure B.25: Ambient Amplitude Map (Line 1114E)**



**Figure B.26: Deep Amplitude Map (Line 1114E)**



**Figure B.27:** Sparker Brute Stack (Line 3499A Cable 5)



**Figure B.28:** Sparker Brute Stack Enlarged (Line 3499A Cable 5)



## **B.18 Acknowledgements**

This work, in full, is a processing report for data acquired on NH1323 developed by Geotrace, Inc., a Houston, Texas based exploration services company. The dissertation author was a science member of this survey cruise.

# References

- Abma, R., Sun, J., & Bernitsas, N. (1999). Antialiasing methods in Kirchhoff migration. *Geophysics*, 64(6):1783–1792.
- Alkhalifah, T. & de Hoop, M. V. (1996). Integral DMO in anisotropic media. In: *SEG Technical Program Expanded Abstracts 1996*, pages 491–494. Society of Exploration Geophysicists.
- Allen, P. A. (2008). Time scales of tectonic landscapes and their sediment routing systems. In: *Geological Society Special Publication (Vol. 296)*, pages 7–28.
- Anderson, J. G., Rockwell, T. K., & Agnew, D. C. (1989). Past and Possible Future Earthquakes of Significance to the San Diego Region. *Earthquake Spectra*, 5(2):299–335.
- Astiz, L. & Shearer, P. M. (2000). Earthquake locations in the inner Continental Borderland, offshore southern California. *Bulletin of the Seismological Society of America*, 90(2):425–449.
- Atwater, B. F., Carson, B., Griggs, G. B., Johnson, P. P., & Salmi, M. S. (2014). Rethinking turbidite paleoseismology along the Cascadia subduction zone. *Geology*, 42(9):827–830.
- Atwater, T. (1970). Implications of plate tectonics for the cenozoic tectonic evolution of western north america. *Bulletin of the Geological Society of America*, 81(12):3513–3536.
- Atwater, T. (1989). Plate tectonic history of the northeast Pacific and western North America. In: *The Eastern Pacific Ocean and Hawaii*, pages 21–72. Geological Society of America.
- Atwater, T. & Stock, J. (1998). Pacific-north america plate tectonics of the neogene southwestern united states: An update. *International Geology Review*, 40(5):375–402.
- Axen, G. J. & Fletcher, J. M. (1998). Late miocene-pleistocene extensional faulting, northern gulf of california, mexico and salton trough, california. *International Geology Review*, 40(3):217–244.
- Bahorich, M. S. & Farmer, S. L. (1995). 3-D seismic discontinuity for faults and stratigraphic features: The coherence cube. In: *1995 SEG Annual Meeting*, pages 93–96.
- Barrows, A. G. (1974). A review of the geology and earthquake history of the Newport-Inglewood structural zone, Southern California. California Division of Mines and Geology Special Report 114. Technical report, California Division of Mines and Geology.

- Becker, T. W., Hardebeck, J. L., & Anderson, G. (2005). Constraints on fault slip rates of the southern California plate boundary from GPS velocity and stress inversions. *Geophysical Journal International*, 160(2):634–650.
- Biasi, G. P. & Wesnousky, S. G. (2016). Steps and gaps in ground ruptures: Empirical bounds on rupture propagation. *Bulletin of the Seismological Society of America*, 106(3):1110–1124.
- Blaauw, M. & Christeny, J. A. (2011). Flexible paleoclimate age-depth models using an autoregressive gamma process. *Bayesian Analysis*, 6(3):457–474.
- Blum, M., Martin, J., Milliken, K., & Garvin, M. (2013). Paleovalley systems: Insights from Quaternary analogs and experiments. *Earth-Science Reviews*, 116(1):128–169.
- Bohannon, R. G. & Geist, E. (1998). Upper crustal structure and Neogene tectonic development of the California continental borderland. *Bulletin of the Geological Society of America*, 110(6):779–800.
- Brookshire, B. N., Lippus, C., Parish, A., Mattox, B., & Burks, A. (2016). Dense arrays of short streamers for ultrahigh-resolution 3D seismic imaging. *Leading Edge*, 35(7):594–599.
- Brothers, D. S., Conrad, J. E., Maier, K. L., Paull, C. K., McGann, M., & Caress, D. W. (2015). The Palos Verdes Fault offshore Southern California: Late Pleistocene to present tectonic geomorphology, seascape evolution, and slip rate estimate based on AUV and ROV surveys. *Journal of Geophysical Research: Solid Earth*, 120(7):4734–4758.
- Chopra, S. & Marfurt, K. (2007). Curvature attribute applications to 3D surface seismic data. *Leading Edge (Tulsa, OK)*, 26(4):404–414.
- Chopra, S. & Marfurt, K. J. (2005). Seismic attributes - A historical perspective. *Geophysics*, 70(5).
- Christie-Blick, N. & Driscoll, N. W. (1995). Sequence stratigraphy. *Annual Review of Earth & Planetary Sciences*, 23:451–478.
- Clark, K. J., Nissen, E. K., Howarth, J. D., Hamling, I. J., Mountjoy, J. J., Ries, W. F., Jones, K., Goldstien, S., Cochran, U. A., Villamor, P., Hreinsdóttir, S., Litchfield, N. J., Mueller, C., Berryman, K. R., & Strong, D. T. (2017). Highly variable coastal deformation in the 2016 MW7.8 Kaikōura earthquake reflects rupture complexity along a transpressional plate boundary. *Earth and Planetary Science Letters*, 474:334–344.
- Conrad, J., Brothers, D., Maier, K. L., Ryan, H., Dartnell, P., & Sliter, R. (2018). Right-lateral fault motion along the slope-basin transition, Gulf of Santa Catalina, Southern California. *SEPM Special Publication No. 110*, pages 1–17.
- Corbett, K. P., Friedman, M., Wiltschko, D. V., & Hung, J. H. (1991). *Controls on Fracture Development, Spacing, and Geometry in the Austin Chalk Formation, Central Texas: Considerations for Exploration and Production*. Dallas Geological Society.

- Covault, J. A. & Graham, S. A. (2010). Submarine fans at all sea-level stands: Tectono-morphologic and climatic controls on terrigenous sediment delivery to the deep sea. *Geology*, 38(10):939–942.
- Covault, J. A., Kostic, S., Paull, C. K., Ryan, H. F., & Fildani, A. (2014). Submarine channel initiation, filling and maintenance from sea-floor geomorphology and morphodynamic modelling of cyclic steps. *Sedimentology*, 61(4):1031–1054.
- Covault, J. A., Kostic, S., Paull, C. K., Sylvester, Z., & Fildani, A. (2017). Cyclic steps and related supercritical bedforms: Building blocks of deep-water depositional systems, western North America. *Marine Geology*, 393:4–20.
- Covault, J. A., Normark, W. R., Romans, B. W., & Graham, S. A. (2007). Highstand fans in the California borderland: The overlooked deep-water depositional systems. *Geology*, 35(9):783–786.
- Covault, J. A. & Romans, B. W. (2009). Growth patterns of deep-sea fans revisited: Turbidite-system morphology in confined basins, examples from the California Borderland. *Marine Geology*, 265(1-2):51–66.
- Covault, J. A., Romans, B. W., Fildani, A., McGann, M., & Graham, S. A. (2010). Rapid climatic signal propagation from source to sink in a southern California sediment-routing system. *Journal of Geology*, 118(3):247–259.
- Covault, J. A., Romans, B. W., Graham, S. A., Fildani, A., & Hilley, G. E. (2011). Terrestrial source to deep-sea sink sediment budgets at high and low sea levels: Insights from tectonically active Southern California. *Geology*, 39(7):619–622.
- Covault, J. A. & Sharman, G. R. (2019). Tectonostratigraphic Evolution of the Inner California Borderland: Template for Fill-and-Spill Sedimentation. In: *The Sedimentary Basins of the United States and Canada*, A. Miall, ed., (2nd ed.), chapter 12, pages 511–528. Elsevier.
- Covault, J. A., Shelef, E., Traer, M., Hubbard, S. M., Romans, B. W., & Fildani, A. (2012). Deep-Water Channel Run-Out Length: Insights from Seafloor Geomorphology. *Journal of Sedimentary Research*, 82(1):21–36.
- Crouch, J. K. (1979). Neogene tectonic evolution of the California Continental Borderland and western Transverse Ranges. *Bulletin of the Geological Society of America*, 90(4):338–345.
- Crouch, J. K. & Bachman, S. B. (1989). Exploration potential of the offshore Newport-Inglewood Fault. *AAPG Bulletin*, 73(4):p.536–.
- Crouch, J. K. & Suppe, J. (1993). Late Cenozoic tectonic evolution of the Los Angeles Basin and inner California borderland: a model for core complex-like crustal extension. *Geological Society of America Bulletin*, 105(11):1415–1434.

- Crutchley, G. J. & Kopp, H. (2018). Reflection and Refraction Seismic Methods. In: *Springer Geology*, pages 43–62. Springer.
- Damuth, J. E. & Olson, H. C. (2015). Latest Quaternary sedimentation in the northern Gulf of Mexico Intraslope Basin Province: I. Sediment facies and depositional processes. *Geosphere*, 11(6):1689–1718.
- Dartnell, P., Driscoll, N. W., Brothers, D. S., Conrad, J. E., Kluesner, J. W., Kent, G. M., & Andrews, B. D. (2015). Colored Shaded-Relief Bathymetry, Acoustic Backscatter, and Selected Perspective Views of the Inner Continental Borderland, Southern California. Technical report, United States Geological Survey.
- DeMets, C. & Dixon, T. H. (1999). New kinematic models for Pacific-North America motion from 3 Ma to present, I: Evidence for steady motion and biases in the NUVEL-1A model. *Geophysical Research Letters*, 26(13):1921–1924.
- Dixon, T., Farina, F., DeMets, C., Suarez-Vidal, F., Fletcher, J., Marquez-Azua, B., Miller, M., Sanchez, O., & Umhoefer, P. (2000). New kinematic models for Pacific-North America motion from 3 MA to present, II: Evidence for a "Baja California shear zone". *Geophysical Research Letters*, 27(23):3961–3964.
- Driscoll, N. W., Kent, G. M., & Bormann, J. (2013). Processed multi-channel seismic data (stacks and migrations) offshore California acquired during the R/V New Horizon expedition NH1320 (2013) using a sparker source: Academic Seismic Portal at UTIG, Marine Geoscience Data System.
- Ducassou, E., Migeon, S., Mulder, T., Murat, A., Capotondi, L., Bernasconi, S. M., & Mascle, J. (2009). Evolution of the Nile deep-sea turbidite system during the late quaternary: Influence of climate change on fan sedimentation. *Sedimentology*, 56(7):2061–2090.
- Ebuna, D. R., Mitchell, T. J., Hogan, P. J., Nishenko, S., & Greene, H. G. (2013). High-resolution offshore 3D seismic geophysical studies of infrastructure geohazards. In: *26th Symposium on the Application of Geophysics to Engineering and Environmental Problems 2013, SAGEEP 2013*, pages 311–320.
- Ehlig, P. L. (1977). Geologic report on the area adjacent to the San Onofre Nuclear Generating Station Northwestern San Diego County, California. Technical report, Southern California Edison Company.
- Eriksen, F. N., Berndt, C., Karstens, J., & Crutchley, G. (2015). P-Cable High Resolution 3D Seismic - Case Study and Recent Advances. *Society of Exploration Geophysicists*, pages 116–119.
- Field, E. H., Arrowsmith, R. J., Biasi, G. P., Bird, P., Dawson, T. E., Felzer, K. R., Jackson, D. D., Johnson, K. M., Jordan, T. H., Madden, C., Michael, A. J., Milner, K. R., Page, M. T., Parsons, T., Powers, P. M., Shaw, B. E., Thatcher, W. R., Weldon, R. J., & Zeng, Y. (2014). Uniform

- California Earthquake Rupture Forecast, version 3 (UCERF3) -The time-independent model. *Bulletin of the Seismological Society of America*, 104(3):1122–1180.
- Fischer, P. J. & Mills, G. I. (1991). The offshore Newport-Inglewood\Rose Canyon fault zone, California: Structure, segmentation, and tectonics. In: *Environmental Perils, San Diego Region. San Diego Association of Geologists for Geologic Society of America Meeting*, pages 17–36.
- Freeman, S. T., Heath, E. G., Guptill, P. D., & Waggoner, J. T. (1992). Seismic hazard assessment, Newport-Inglewood fault zone. *Engineering Geology Practice in Southern California*, 4:211–231.
- Gamberi, F., Rovere, M., Marani, M. P., & Dykstra, M. (2015). Modern submarine canyon feeder-system and deep-sea fan growth in a tectonically active margin (northern Sicily). *Geosphere*, 11(2):307–319.
- Goldfinger, C. (2009). Sub-Aqueous Paleoseismology. In: *Paleoseismology*, J. P. McCalpin, ed., pages 119–170. Elsevier.
- Goldfinger, C. (2011). Submarine Paleoseismology Based on Turbidite Records. *Annual Review of Marine Science*, 3(1):35–66.
- Goldfinger, C., Morey, A. E., Nelson, C. H., Gutiérrez-Pastor, J., Johnson, J. E., Karabanov, E., Chaytor, J., Eriksson, A., Winkler, M., Kalk, P., Camarero, A., Morri, C., Dunhill, G., Ramos, L., Raab, A., Pias, N., Pourmanoutscheri, M., Van Rooij, D., Amy, L., Liu, C. C., Moser, C., Etheridge, D., Stenner, H., Popham, C., McKee, C., McMillan, D., Crosby, C., Schmid, S., Gracia, E., Lovelady, S., Romsos, C., Rinterknecht, V., Robison, R., Casas, D., Charlet, F., Hinrichsen, B., Oxford, J., Marin, M., Mas, M., Montes, S., Villalonga, R., Vizcaino, A., Jimenez, S., Pedrosa, M., Perez, S., Perez, J., Turra, A., Lamas, D., Falcon, H., Baranco, A., Schwartz, D., Zoback, M. L., Fumal, T., & Niemi, T. (2007). Rupture lengths and temporal history of significant earthquakes on the offshore and north coast segments of the Northern San Andreas Fault based on turbidite stratigraphy. *Earth and Planetary Science Letters*, 254(1-2):9–27.
- Goldfinger, C., Nelson, C. H., & Johnson, J. E. (2003). Holocene Earthquake Records From the Cascadia Subduction Zone and Northern San Andreas Fault Based on Precise Dating of Offshore Turbidites. *Annual Review of Earth and Planetary Sciences*, 31(1):555–577.
- Grant, L. B. & Shearer, P. M. (2004). Activity of the offshore Newport-Inglewood Rose Canyon Fault Zone, Coastal Southern California, from relocated microseismicity. *Bulletin of the Seismological Society of America*, 94(2):747–752.
- Grant, L. B., Waggoner, J. T., Rockwell, T. K., & Von Stein, C. (1997). Paleoseismicity of the North Branch of the Newport-Inglewood fault zone in Huntington Beach, California, from cone penetrometer test data. *Bulletin of the Seismological Society of America*, 87(2):277–293.

- Hamling, I. J., Hreinsdóttir, S., Clark, K., Elliott, J., Liang, C., Fielding, E., Litchfield, N., Villamor, P., Wallace, L., Wright, T. J., D’Anastasio, E., Bannister, S., Burbidge, D., Denys, P., Gentle, P., Howarth, J., Mueller, C., Palmer, N., Pearson, C., Power, W., Barnes, P., Barrell, D. J., Van Dissen, R., Langridge, R., Little, T., Nicol, A., Pettinga, J., Rowland, J., & Stirling, M. (2017). Complex multifault rupture during the 2016 Mw 7.8 Kaikōura earthquake, New Zealand. *Science*, 356(6334).
- Hauksson, E. & Gross, S. (1991). Source parameters of the 1933 Long Beach earthquake. *Bulletin - Seismological Society of America*, 81(1):81–98.
- Hogarth, L. J., Babcock, J., Driscoll, N. W., Le Dantec, N., Haas, J. K., Inman, D. L., & Masters, P. M. (2007). Long-term tectonic control on Holocene shelf sedimentation offshore La Jolla, California. *Geology*, 35(3):275–278.
- Holmes, J. J., Driscoll, N. W., & Kent, G. M. (2019). High-Resolution 3D Seismic Imaging of Fault Interaction and Deformation Offshore San Onofre, California. In review.
- Ingersoll, R. V. (2008). Reconstructing southern California. In: *Ores and orogenesis: Circum-Pacific tectonics, geologic evolution, and ore deposits: Arizona Geological Society Digest 22*, pages 409–417. Arizona Geological Society.
- Inman, D. L. & Brush, B. M. (1973). The coastal challenge. *Science*, 181(4094):20–32.
- Jousset, P., Thierry, P., & Lambaré, G. (1999). Reduction of 3-D acquisition footprints in 3-D migration/inversion. In: *SEG Technical Program Expanded Abstracts 1999*, pages 1354–1357. Society of Exploration Geophysicists.
- Kaiser, A., Balfour, N., Fry, B., Holden, C., Litchfield, N., Gerstenberger, M., D’Anastasio, E., Horspool, N., McVerry, G., Ristau, J., Bannister, S., Christophersen, A., Clark, K., Power, W., Rhoades, D., Massey, C., Hamling, I., Wallace, L., Mountjoy, J., Kaneko, Y., Benites, R., Van Houtte, C., Dellow, S., Wotherspoon, L., Elwood, K., & Gledhill, K. (2017). The 2016 Kaikōura, New Zealand, earthquake: Preliminary seismological report. *Seismological Research Letters*, 88(3):727–739.
- Kalid, N. Z. A., Hamzah, U., & Samsudin, A. R. (2016). Seismic attributes and their application in faults interpretation of Kupe Field, Taranaki Basin, New Zealand. *Electronic Journal of Geotechnical Engineering*, 21(6):2169–2184.
- Kato, M., Imamura, E., Sakai-Kato, K., Nakajima, T., & Toyō’oka, T. (2006). Cationic amylopectin derivatives as additives for analysis of proteins in capillary electrophoresis. *Electrophoresis*, 27(10):1895–1899.
- Kennedy, M. P. & Tan, S. S. (2007). Geologic Map of the Oceanside 30’ x 60’ Quadrangle, California. Technical report, Department of Conservation, California Geological Survey.

- Kienast, S. S. & McKay, J. L. (2001). Sea surface temperatures in the subarctic Northeast Pacific reflect millennial-scale climate oscillations during the last 16 kyrs. *Geophysical Research Letters*, 28(8):1563–1566.
- Klotsko, S., Driscoll, N., Kent, G., & Brothers, D. (2015). Continental shelf morphology and stratigraphy offshore San Onofre, California: The interplay between rates of eustatic change and sediment supply. *Marine Geology*, 369:116–126.
- Kluesner, J. W. & Brothers, D. S. (2016). Seismic attribute detection of faults and fluid pathways within an active strike-slip shear zone: New insights from high-resolution 3D P-Cable™ seismic data along the Hosgri Fault, offshore California. *Interpretation*, 4(1):SB131–SB148.
- Kostic, S. (2011). Modeling of submarine cyclic steps: Controls on their formation, migration, and architecture. *Geosphere*, 7(2):294–304.
- Kovanen, D. J. & Easterbrook, D. J. (2002). Paleodeviations of radiocarbon marine reservoir values for the northeast Pacific. *Geology*, 30(3):243–246.
- Kranz, R. L. (1979). Crack-crack and crack-pore interactions in stressed granite. *International Journal of Rock Mechanics and Mining Sciences and*, 16(1):37–47.
- Le Dantec, N., Hogarth, L. J., Driscoll, N. W., Babcock, J. M., Barnhardt, W. A., & Schwab, W. C. (2010). Tectonic controls on nearshore sediment accumulation and submarine canyon morphology offshore La Jolla, Southern California. *Marine Geology*, 268(1-4):115–128.
- Lee, H. J. & Normark, W. R. (2009). *Earth Science in the Urban Ocean: The Southern California Continental Borderland*. Geological Society of America.
- Legg, M. R. (1991). Developments in understanding the tectonic evolution of the California Continental Borderland. *From shoreline to abyss: contributions in marine geology in honor of Francis Parker Shepard*, pages 291–312.
- Legg, M. R. & Kennedy, M. P. (1979). Faulting offshore San Diego and northern Baja California. In: *Earthquakes and other perils, San Diego region*, (1st ed.), pages 29–46. San Diego Association of Geologists.
- Lindvall, S. C. & Rockwell, T. K. (1995). Holocene activity of the Rose Canyon fault zone in San Diego, California. *Journal of Geophysical Research*, 100(B12).
- Lonsdale, P. (1991). Structural patterns of the Pacific floor offshore of Peninsular California. *The Gulf and Peninsula Province of the Californias*, pages 87–125.
- Lumley, D. E., Claerbout, J. F., & Bevc, D. (1994). Anti-aliased kirchhoff 3-d migration. In: *SEG Technical Program Expanded Abstracts 1994*, pages 1282–1285. Society of Exploration Geophysicists.
- Magistrale, H. (1993). Seismicity of the Rose Canyon Fault Zone near San Diego, California. *Bulletin - Seismological Society of America*, 83(6):1971–1978.



- Maier, K. L., Brothers, D. S., Paull, C. K., McGann, M., Caress, D. W., & Conrad, J. E. (2017). Records of continental slope sediment flow morphodynamic responses to gradient and active faulting from integrated AUV and ROV data, offshore Palos Verdes, southern California Borderland. *Marine Geology*, 393:47–66.
- Maier, K. L., Gales, J. A., Paull, C. K., Rosenberger, K., Talling, P. J., Simmons, S. M., Gwiazda, R., McGann, M., Cartigny, M. J., Lundsten, E., Anderson, K., Clare, M. A., Xu, J., Parsons, D., Barry, J. P., Wolfson-Schwehr, M., Nieminski, N. M., & Sumner, E. J. (2019). Linking direct measurements of turbidity currents to submarine canyon-floor deposits. *Frontiers in Earth Science*, 7.
- Maloney, J. M., Driscoll, N. W., Kent, G. M., Bormann, J., Duke, S., & Freeman, T. (2016). Segmentation and Step-Overs Along Strike-Slip Fault Systems in the Inner California Borderlands: Implications for Fault Architecture and Basin Formation. In: *Applied Geology in California*, pages 655–677. Applied Geology in California.
- Mayall, M., Jones, E., & Casey, M. (2006). Turbidite channel reservoirs—Key elements in facies prediction and effective development. *Marine and Petroleum Geology*, 23(8):821–841.
- Mayall, M. & Stewart, I. (2000). The Architecture of Turbidite Slope Channels. In: *Deep-Water Reservoirs of the World: 20th Annual*, pages 578–586. Society of Economic Paleontologists and Mineralogists.
- McHargue, T., Pyrcz, M. J., Sullivan, M. D., Clark, J. D., Fildani, A., Romans, B. W., Covault, J. A., Levy, M., Posamentier, H. W., & Drinkwater, N. J. (2011). Architecture of turbidite channel systems on the continental slope: Patterns and predictions. *Marine and Petroleum Geology*, 28(3):728–743.
- Meade, B. J. & Hager, B. H. (2005). Block models of crustal motion in southern California constrained by GPS measurements. *Journal of Geophysical Research: Solid Earth*, 110(3):1–19.
- Menard, Henry W. (1955). Deep-Sea Channels, Topography, and Sedimentation. *AAPG Bulletin*, 39.
- Milliman, J. D., Summerhayes, C. P., & Barretto, H. T. (1975). Quaternary sedimentation on the Amazon Continental Margin: A Model. *Bulletin of the Geological Society of America*, 86(5):610–614.
- Mineral Management Service (MMS) (1997). Oceanside seismic data set: Washington, D.C., U.S. Department of the Interior, Pacific Outer Continental Shelf CD97-01.
- Mitchum, R. M., Vail, P. R., & Thompson, S. (1977). Seismic Stratigraphy and Global Changes of Sea Level, Part 2: The Depositional Sequence as a Basic Unit for Stratigraphic Analysis: Section 2. Application of Seismic Reflection Configuration to Stratigraphic Interpretation. *Seismic Stratigraphy: Applications to Hydrocarbon Exploration AAPG Memoir 26*, pages 53–62.

- Mix, A. C., Lund, D. C., Pisias, N. G., Bodén, P., Bornmalm, L., Lyle, M., & Pike, J. (1999). Rapid climate oscillations in the northeast Pacific during the last deglaciation reflect northern and southern hemisphere sources. In: *Geophysical Monograph Series*, volume 112, pages 127–148. Blackwell Publishing Ltd.
- Moody, J. D. & Hill, M. J. (1956). Wrench-fault tectonics. *Bulletin of the Geological Society of America*.
- Mulder, T., Migeon, S., Savoye, B., & Jouanneau, J. M. (2001). Twentieth century floods recorded in the deep Mediterranean sediments. *Geology*, 29(11):1011–1014.
- Nakajima, T. & Kanai, Y. (2000). Sedimentary features of seismoturbidites triggered by the 1983 and older historical earthquakes in the eastern margin of the Japan Sea. *Sedimentary Geology*, 135(1-4):1–19.
- Nelson, A. R., Atwater, B. F., Bobrowsky, P. T., Bradley, L. A., Clague, J. J., Carver, G. A., Darienzo, M. E., Grant, W. C., Krueger, H. W., Sparks, R., Stafford, T. W., & Stuiver, M. (1995). Radiocarbon evidence for extensive plate-boundary rupture about 300 years ago at the cascadia subduction zone. *Nature*, 378(6555):371–374.
- Nicholson, C., Sorlien, C. C., Atwater, T., Crowell, J. C., & Luyendyk, B. P. (1994). Microplate capture, rotation of the western Transverse Ranges, and initiation of the San Andreas transform as a low-angle fault system. *Geology*, 22(6):491–495.
- Nishenko, S., Greene, H. G., Hogan, P., & Bergkamp, B. (2018). Geometry and late pleistocene displacement of the shoreline and oceanic fault zones, San Luis Obispo bay, California. *Bulletin of the Seismological Society of America*, 108(6):3225–3247.
- Normark, W. & Damuth, J. (1997). Sedimentary facies and associated depositional elements of the Amazon Fan. In: *Proceedings of the Ocean Drilling Program, 155 Scientific Results*. Ocean Drilling Program.
- Normark, W. R. (1970). Growth Patterns of Deep-Sea Fans. *American Association of Petroleum Geologists Bulletin*.
- Normark, W. R. (1986). Summary of drilling results for the Mississippi Fan and considerations for application to other turbidite systems. *Initial reports DSDP, Leg 96, Ft. Lauderdale to Galveston, Texas, 1983*, pages 425–436.
- Normark, W. R., Piper, D. J., Posamentier, H., Pirmez, C., & Migeon, S. (2002). Variability in form and growth of sediment waves on turbidite channel levees. *Marine Geology*, 192(1-3):23–58.
- Normark, W. R., Piper, D. J., Romans, B. W., Covault, J. A., Dartnell, P., & Sliter, R. W. (2009). Submarine canyon and fan systems of the California Continental Borderland. *Special Paper of the Geological Society of America*, 454:141–168.

- Pacific Gas and Electric Company (PG&E) (2014). Offshore Low-Energy Seismic-Reflection Studies in Estero Bay, San Luis Obispo Bay, and Point Sal Areas. Technical report, Pacific Gas and Electric Company.
- Paull, C. K., Ussler, W. I., Greene, H. G., Keaten, R., Mitts, P., & Barry, J. (2002). Caught in the act: The 20 December 2001 gravity flow event in Monterey Canyon. *Geo-Marine Letters*, 22(4):227–232.
- Pettingill, H. S. & Weimer, P. (2002). Worldwide deepwater exploration and production: Past, present, and future. *Leading Edge (Tulsa, OK)*, 21(4):371–376.
- Piper, D. J., Kontopoulos, N., Anagnostou, C., Chronis, G., & Panagos, A. G. (1990). Modern fan deltas in the western Gulf of Corinth, Greece. *Geo-Marine Letters*, 10(1):5–12.
- Piper, D. J. & Normark, W. R. (1983). Turbidite depositional patterns and flow characteristics, Navy Submarine Fan, California Borderland. *Sedimentology*, 30(5):681–694.
- Piper, D. J. & Normark, W. R. (2009). Processes That Initiate Turbidity Currents and Their Influence on Turbidites: A Marine Geology Perspective. *Journal of Sedimentary Research*, 79(6):347–362.
- Planke, S., Berndt, C., Mienert, J., Bünz, S., Eriksen, F., & Eriksen, O. (2010). P-Cable: New High-Resolution 3D Seismic Acquisition Technology. *EGU General Assembly Conference Abstracts*, 12(May 2014):13618.
- Planke, S., Eriksen, F. N., Berndt, C., Mienert, J., & Masson, D. (2009). P-Cable high-resolution seismic. *Oceanography*, 22(1):85.
- Platt, J. P. & Becker, T. W. (2010). Where is the real transform boundary in California? *Geochemistry, Geophysics, Geosystems*, 11(6).
- Posamentier, H. W., Erskine, R. D., & Mitchum, R. M. (1991). Models for Submarine-Fan Deposition within a Sequence-Stratigraphic Framework. In: *Seismic facies and sedimentary processes of submarine fans and turbidite systems*, pages 127–136. Springer.
- Prather, B. E. (2000). Calibration and visualization of depositional process models for above-grade slopes: A case study from the Gulf of Mexico. *Marine and Petroleum Geology*, 17(5):619–638.
- Prins, M. A. & Postma, G. (2000). Effects of climate, sea level, and tectonics unraveled for last deglaciation turbidite records of the Arabian Sea. *Geology*, 28(4):375–378.
- Rivero, C. & Shaw, J. H. (2011). Active folding and blind thrust faulting induced by basin inversion processes, InnerCalifornia Borderlands. *AAPG Memoir*, 94:187–214.
- Rivero, C., Shaw, J. H., & Mueller, K. (2000). Oceanside and thirtymile bank blind thrust: Implications for earthquake hazards in coastal Southern California. *Geology*, 28(10):891–894.

- Roach, L. D., Charles, C. D., Field, D. B., & Guilderson, T. P. (2013). Foraminiferal radiocarbon record of northeast Pacific decadal subsurface variability. *Journal of Geophysical Research: Oceans*, 118(9):4317–4333.
- Robert M. Mitchum Jr. (2003). Seismic Stratigraphic Expression of Submarine Fans: Chapter 7. In: *M 39: Seismic Stratigraphy II: An Integrated Approach to Hydrocarbon Exploration*, pages 117–136. American Association of Petroleum Geologists.
- Roberts, A. (2001). Curvature attributes and their application to 3D interpreted horizons. *First Break*, 19(2):85–100.
- Rockwell, T. K. (2010). The Rose Canyon fault zone in San Diego. In: *Fifth International Conference on Recent Advances in Geotechnical Earthquake Engineering and Soil Dynamics*, pages 1–9.
- Roden, R., Smith, T., & Sacrey, D. (2015). Geologic pattern recognition from seismic attributes: Principal component analysis and self-organizing maps. *Interpretation*, 3(4):SAE59–SAE83.
- Romans, B. W., Castellort, S., Covault, J. A., Fildani, A., & Walsh, J. P. (2016). Environmental signal propagation in sedimentary systems across timescales. *Earth-Science Reviews*, 153:7–29.
- Ryan, H. F., Conrad, J. E., Paull, C. K., & McGann, M. (2012). Slip rate on the San Diego trough fault zone, inner California Borderland, and the 1986 Oceanside earthquake swarm revisited. *Bulletin of the Seismological Society of America*, 102(6):2300–2312.
- Ryan, H. F., Legg, M. R., Conrad, J. E., & Sliter, R. W. (2009). Recent faulting in the Gulf of Santa Catalina: San Diego to Dana Point. *Special Paper of the Geological Society of America*, 454:291–315.
- Sahakian, V., Bormann, J., Driscoll, N., Harding, A., Kent, G., & Wesnousky, S. (2017). Seismic constraints on the architecture of the Newport-Inglewood/Rose Canyon fault: Implications for the length and magnitude of future earthquake ruptures. *Journal of Geophysical Research: Solid Earth*, 122(3):2085–2105.
- Shiki, T. (1996). Reading of the trigger records of sedimentary events - A problem for future studies. *Sedimentary Geology*, 104(1-4):249–255.
- Shiki, T., Kumon, F., Inouchi, Y., Kontani, Y., Sakamoto, T., Tateishi, M., Matsubara, H., & Fukuyama, K. (2000). Sedimentary features of the seismo-turbidites, Lake Biwa, Japan. *Sedimentary Geology*, 135(1-4):37–50.
- Singleton, D. M., Rockwell, T. K., Murbach, D., Murbach, M., Maloney, J. M., Freeman, T., & Levy, Y. (2019). Late-Holocene rupture history of the Rose Canyon fault in Old Town, San Diego: Implications for cascading earthquakes on the Newport–Inglewood–Rose Canyon fault system. *Bulletin of the Seismological Society of America*, 109(3):855–874.

- Sommerfield, C. K. & Nittrouer, C. A. (1999). Modern accumulation rates and a sediment budget for the Eel shelf: A flood-dominated depositional environment. *Marine Geology*, 154(1-4):227–241.
- Southon, J. R., Nelson, D. E., & Vogel, J. S. (1990). A record of past ocean-atmosphere radiocarbon differences from the northeast Pacific. *Paleoceanography*, 5(2):197–206.
- Stirling, M. W., Litchfield, N. J., Villamor, P., Van Dissen, R. J., Nicol, A., Pettinga, J., Barnes, P., Langridge, R. M., Little, T., Barrell, D. J., Mountjoy, J., Ries, W. F., Rowland, J., Fenton, C., Hamling, I., Asher, C., Barrier, A., Benson, A., Bischoff, A., Borella, J., Carne, R., Cochran, U. A., Cockroft, M., Cox, S. C., Duke, G., Fenton, F., Gasston, C., Grimshaw, C., Hale, D., Hall, B., Hao, K. X., Hatem, A., Hemphill-Haley, M., Heron, D. W., Howarth, J., Juniper, Z., Kane, T., Kears, J., Khajavi, N., Lamarche, G., Lawson, S., Lukovic, B., Madugo, C., Manousakis, I., McColl, S., Noble, D., Pedley, K., Sauer, K., Stah, T., Strong, D. T., Townsend, D. B., Toy, V., Villeneuve, M., Wandres, A., Williams, J., Woelz, S., & Zinke, R. (2017). The Mw7.8 2016 Kaikōura earthquake: Surface fault rupture and seismic hazard context. *Bulletin of the New Zealand Society for Earthquake Engineering*, 50(2):73–84.
- Stow, D. A. & Mayall, M. (2000). Deep-water sedimentary systems: New models for the 21st century. *Marine and Petroleum Geology*, 17(2):125–135.
- Stow, D. A. & Piper, D. J. (1984). Deep-water fine-grained sediments; history, methodology and terminology. *Geological Society Special Publication*, 15:3–14.
- Stuiver, M. & Polach, H. A. (1977). Reporting of <sup>14</sup>C data. *Radiocarbon*, 19(3):355–363.
- Stuiver, M. & Reimer, P. J. (1993). Extended <sup>14</sup>C data base and revised CALIB 3.0 <sup>14</sup>C age calibration program. *Radiocarbon*, 35(1):215–230.
- Sumner, E. J., Siti, M. I., McNeill, L. C., Talling, P. J., Henstock, T. J., Wynn, R. B., Djajadihardja, Y. S., & Permana, H. (2013). Can turbidites be used to reconstruct a paleoearthquake record for the central Sumatran margin? *Geology*, 41(7):763–766.
- Sweet, M. L. & Blum, M. D. (2016). Connections Between Fluvial To Shallow Marine Environments and Submarine Canyons: Implications For Sediment Transfer To Deep Water. *Journal of Sedimentary Research*, 86(10):1147–1162.
- Symons, W. O., Sumner, E. J., Paull, C. K., Cartigny, M. J., Xu, J. P., Maier, K. L., Lorenson, T. D., & Talling, P. J. (2017). A new model for turbidity current behavior based on integration of flow monitoring and precision coring in a submarine canyon. *Geology*, 45(4):367–370.
- Talling, P. J., Allin, J., Armitage, D. A., Arnott, R. W. C., Cartigny, M. J. B., Clare, M. A., Felletti, F., Covault, J. A., Girardclos, S., Hansen, E., Hill, P. R., Hiscott, R. N., Hogg, A. J., Clarke, J. H., Jobe, Z. R., Malgesini, G., Mozzato, A., Naruse, H., Parkinson, S., Peel, F. J., Piper, D. J. W., Pope, E., Postma, G., Rowley, P., Sguazzini, A., Stevenson, C. J., Sumner, E. J., Sylvester, Z., Watts, C., & Xu, J. (2015). Key Future Directions For Research On Turbidity Currents and Their Deposits. *Journal of Sedimentary Research*, 85(2):153–169.

- Talling, P. J., Masson, D. G., Sumner, E. J., & Malgesini, G. (2012). Subaqueous sediment density flows: Depositional processes and deposit types. *Sedimentology*, 59(7):1937–2003.
- Talling, P. J., Paull, C. K., & Piper, D. J. (2013). How are subaqueous sediment density flows triggered, what is their internal structure and how does it evolve? Direct observations from monitoring of active flows. *Earth-Science Reviews*, 125:244–287.
- ten Brink, U. S., Zhang, J., Brocher, T. M., Okaya, D. A., Klitgord, K. D., & Fuis, G. S. (2000). Geophysical evidence for the evolution of the California Inner Continental Borderland as a metamorphic core complex. *Journal of Geophysical Research: Solid Earth*, 105(B3):5835–5857.
- Thierry, P., Lambaré, G., & Xu, S. (1999). 3D common diffracting angle migration/inversion for AVA analysis. In: *SEG Technical Program Expanded Abstracts 1999*, pages 844–847. Society of Exploration Geophysicists.
- Triezenberg, P. J., Hart, P. E., & Childs, J. R. (2016). National Archive of Marine Seismic Surveys (NAMSS): A USGS data website of marine seismic reflection data within the U.S. Exclusive Economic Zone (EEZ): U.S. Geological Survey Data Release.
- U.S. Geological Survey (USGS) and California Geological Survey (CGS) (2006). Quaternary fault and fold database for the United States, accessed September 12, 2019, from USGS web site: <http://earthquake.usgs.gov/hazards/qfaults/>.
- Vail, P. R., Mitchum Jr, R. M., & Thompson III, S. (1977). Seismic Stratigraphy and Global Changes of Sea Level: Part 3. Relative Changes of Sea Level from Coastal Onlap: Section 2. Application of Seismic Reflection Configuration to Stratigraphic Interpretation. *AAPG Memoir*, 26:63–81.
- Warrick, J. A. & Farnsworth, K. L. (2009). Sources of sediment to the coastal waters of the Southern California Bight. *Special Paper of the Geological Society of America*, 454:39–52.
- Wei, E. A., Holmes, J. J., & Driscoll, N. W. (2019). Strike-slip transpressional uplift offshore San Onofre, California inhibits sediment delivery to the deep sea. In review.
- Wells, D. L. & Coppersmith, K. J. (1994). New empirical relationships among magnitude, rupture length, rupture width, rupture area, and surface displacement. *Bulletin - Seismological Society of America*, 84(4):974–1002.
- Wesnousky, S. G. (2006). Predicting the endpoints of earthquake ruptures. *Nature*, 444(7117):358–360.
- Wessel, P., Smith, W. H., Scharroo, R., Luis, J., & Wobbe, F. (2013). Generic mapping tools: Improved version released. *Eos*, 94(45):409–410.
- Wright, L. D., Friedrichs, C. T., Kim, S. C., & Scully, M. E. (2001). Effects of ambient currents and waves on gravity-driven sediment transport on continental shelves. *Marine Geology*, 175(1-4):25–45.

Xu, J. P., Swarzenski, P. W., Noble, M., & Li, A. C. (2010). Event-driven sediment flux in Hueneme and Mugu submarine canyons, southern California. *Marine Geology*, 269(1-2):74–88.